NASA Contractor Report

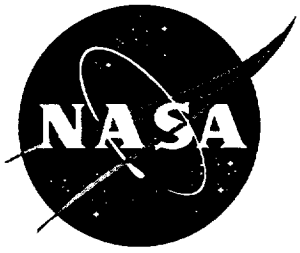

Shuttle Mission STS-50: Orbital Processing of High-Quality CdTe Compound Semiconductors Experiment

Final Flight Sample Characterization Report

Dr. David J. Larson, Jr.,* Dr. Louis G. Casagrande, and Dr. Don Di Marzio
Northrop Grumman Corporation, Inc., Bethpage, New York 11714-3580

Dr. J. Iwan D. Alexander
University of Alabama at Huntsville, Huntsville, Alabama

Dr. Fred Carlson and Dr. Taipo Lee
Clarkson University, Potsdam, New York

Dr. Michael Dudley and Balaji Raghathamachar
State University of New York at Stony Brook, Stony Brook, New York

*Principal Investigator; currently at State University of New York at Stony Brook, Stony Brook, NY

Contract NAS8-38147

September 1998

National Aeronautics and
Space Administration
George C. Marshall Space Flight Center
Marshall Space Flight Center
Alabama 35812

FOREWORD

ABSTRACT

The Orbital Processing of High-Quality Doped and Alloyed CdTe Compound Semiconductors program was initiated to investigate, quantitatively, the influences of gravitationally dependent phenomena on the growth and quality of bulk compound semiconductors. The objective was to improve crystal quality (structural and compositional) and to better understand and control the variables within the crystal growth production process. The empirical effort entailed the development of a terrestrial (one-g) experiment baseline for quantitative comparison with microgravity (μ-g) results. This empirical effort was supported by the development of high-fidelity process models of heat transfer, fluid flow and solute redistribution, and thermo-mechanical stress occurring in the furnace, safety cartridge, ampoule, and crystal throughout the melting, seeding, crystal growth, and post-solidification processing. In addition, analyses were conducted with respect to the sensitivity of the orbital experiments to the residual microgravity (μ-g) environment, both steady state and g-jitter.

CdZnTe crystals were grown in one-g and in μ-g. Crystals processed terrestrially were grown at the NASA Ground Control Experiments Laboratory (GCEL) and at the Grumman Corporate Research Center (GCRC), which is now Northrop Grumman Advanced Systems & Technology. Experiments in the GCEL developed optimized growth conditions for the flight experiments, experimentally empiricized the process models, and established a one-g baseline for the 15-mm OD crystals grown in the flight furnace. The 38-mm OD crystals grown at GCRC established a state-of-the-art commercial comparative baseline. Two μ-g crystals were grown in the Crystal Growth Furnace (CGF) during the First United States Microgravity Laboratory Mission (USML-1), STS-50, June 24 - July 9, 1992. The crystal growth parameters used on the USML-1 Mission were identical to those used in the CGF GCEL simulation furnace and those grown in the CGF Flight Unit.

It was anticipated that the μ-g environment would damp buoyancy (gravitationally dependent) convection, improving chemical homogeneity. More important for this investigation, it was anticipated that the near absence of hydrostatic pressure would reduce the hoop stresses experienced by the growing and cooling crystal, thus reducing the defect density within the flight samples. The one-g and μ-g samples were thus analyzed for chemical homogeneity, structural perfection, and opto-electronic performance (infrared transmission).

Macro segregation was predicted to be small in one-g and μ-g, using scaling analysis, with nearly diffusion-controlled growth. This was confirmed experimentally terrestrially in the 15-mm samples. Radial segregation was found to vary with fraction solidified through the shoulder region of the flight crystals, but to be nearly constant in the steady-state growth region. Residual strain, however, was significantly disturbed due to the asymmetric gravitational and thermal fields experienced by the USML-1 flight samples, which resulted in partial wall contact. Thermally symmetric fields were investigated in the follow-up flight experiment on USML-2 to improve this measurement.

FTIR transmission of both ground and flight materials was measured to be 63%, close to the theoretical value of 67%, and invariant from 2.5 to 20 μm (4000 to 500 wave numbers). This suggests that both the ground and flight materials were close to the stoichiometric composition. Infrared microscopy and x-ray measurements confirmed this conclusion in that the primary precipitates (inclusions) were Te, and their size (1-10 μm) and density suggested that both primary flight and ground-based samples experienced similar cooling rates and were close to stoichiometry.

The best regions of flight samples, however, were found to be much higher in structural perfection than the ground samples produced in the same furnace under identical growth conditions except for the gravitational level. Rocking curve widths were found to be substantially reduced, from 20/35 arc-sec (one-g) to 9/15 arc-sec (μ-g) for the best regions of the crystals. The value of 9 arc-sec equals the best reported terrestrially for this material. Morphologically, the ground samples were found to have a fully developed mosaic structure consisting of subgrains, macro- and micro-twinning, and regions of cross-slip. The flight samples, however, exhibited discrete dislocations without mosaic substructure in all areas. Defect density was reduced from 500,000-1,000,000 EPD (± 50%) (one-g) to 800 EPD (± 50%) (μ-g). The ≤ 500 EPD μ-g value is the lowest reported.

The thermo-mechanical process model suggested that the low dislocation density was due to the near absence of hydrostatic pressure in μ-g which allowed the melt to solidify with minimum wall content, thus reducing the thermo-mechanical stress transmitted to the crystal during growth and post-solidification cooling. The highest quality material was predicted to be on the periphery (free surface) of the boules, unlike the terrestrial samples where the best material is at the core. This was confirmed topographically and microstructurally.

Our follow-up experiment on USML-2 processed a flight sample in a thermally symmetric environment, with full wall contact. This will add to the comparative matrix and test further the validity of the process models.

CONTENTS

CONTENTS (cont'd.)

ILLUSTRATIONS

ILLUSTRATIONS (cont'd.)

1 -- INTRODUCTION & OBJECTIVES

CdZnTe is a technologically important member of the family of II-VI compound semiconductors. The most important application of CdZnTe is as a substrate for the epitaxial growth of HgCdTe infrared detectors. The requirements for large-area infrared devices have led to increased reliance on epitaxial processes to provide detector-grade HgCdTe active areas and a concomitant demand for high-quality substrates. CdZnTe is typically grown using unseeded, horizontal or vertical Bridgman crystal growth techniques.

HgCdTe epilayers are most commonly fabricated using liquid phase epitaxy (LPE). However, to achieve abrupt device/substrate junctions, epitaxial growth of HgCdTe has been driven to lower temperatures using chemical vapor deposition (CVD) or molecular beam epitaxy (MBE). These techniques minimize interdiffusion at the interface, but are much more sensitive to wafer quality, particularly at the surface.

One approach to minimizing interfacial strains and dislocation generation, propagation, and/or multiplication at the substrate/epilayer interface is to lattice-match the substrate and the epitaxial layer at the growth temperature. The lattice-matched substrate of choice for HgCdTe is CdZnTe. In addition, fast diffusion of Hg along dislocation cores has resulted in demand for the minimization of extended defects within the epilayers. The latter requires reduced defect densities in the substrates, as the extended defects are likely to propagate from the substrate surface into the epilayer.

The primary needs for these CdZnTe substrate applications are therefore: (1) increased structural perfection (reduced defect density and residual strain) within the bulk crystals and substrates and (2) more uniform lattice parameters (chemical homogeneity) within the substrates, which better match those of the specific HgCdTe composition at the epitaxial growth temperature. Our microgravity (μ-g) program addresses these needs.

The objective of this program is thus to investigate quantitatively the influences of gravitationally dependent phenomena on the growth and the quality of compound semiconductors as a means of improving crystal quality (structural and compositional) and to better understand and control the variables within the crystal growth process.

2 -- BACKGROUND

CdZnTe crystals were grown in one-g and in μ-g. Crystals grown terrestrially were processed at the NASA Ground Control Experiments Laboratory (GCEL) and at the Grumman Corporate Research Center (GCRC). Experiments in the GCEL developed optimized growth conditions for the flight experiments, experimentally empiricized the process models, and established a one-g baseline for the 15-mm OD crystals grown in the flight furnace. The 38-mm OD crystals grown at Grumman established a one-g state-of-the-art commercial comparative baseline. Two μ-g crystals were grown in the Crystal Growth Furnace (CGF) during the First United States Microgravity Laboratory Mission (USML-1), STS-50, June 24 - July 9, 1992. The crystal growth parameters used on the USML-1Mission in the CGF Flight Unit were identical to those used in the CGF GCEL simulation furnace.

2.1 CdTe/ZnTe PHASE RELATIONS

The CdTe binary compound is a single equiatomic phase, CdTe, with a congruent melting temperature of 1092°C as shown in Fig. 1. Secondary eutectic solidification reactions on each side of equiatomic CdTe occur at 449°C on the Te-rich side of stoichiometry and 324°C on the Cd-rich side. There is virtually no solubility of Cd in Te or Te in Cd. The addition of ZnTe to CdTe is crystallographically isostructural and the phase diagram calculated in this work, after data of Yu and Brebrick, is shown as Fig. 2. Clearly, there is increasing temperature of solidification and increasing separation of the liquidus and solidus lines with increasing ZnTe content. The Zn solute redistribution coefficient, K_0, for the CdTe/ZnTe pseudo-ternary phase diagram is shown as Fig. 3. For the compositional range to be investigated, nominally 0.04 mole fraction ZnTe alloys, the equilibrium redistribution coefficient, K_0, is expected to vary from 1.3 to 1.2.

The equilibrium redistribution coefficient, K_0, can be reduced significantly if gravitationally dependent convection can be damped, approaching diffusion-controlled growth conditions. Scaling analysis conducted at the University of Alabama at Huntsville (UAH) showed that even in one-g the regime of diffusion-controlled growth can be approached, for the CGF 15-mm-diameter samples, as shown in Fig. 4.

The 38-mm-diameter samples experienced significantly more convection because of the greater diameter and radial gradients; however, even in this case, the equilibrium redistribution coefficient, K_0, was reduced from 1.25 to an effective redistribution coefficient, K_e, of 1.10 by careful thermal control. This significantly reduced the amount of longitudinal macrosegregation in the commercially sized ingots in one-g.

2.2 CRYSTAL GROWTH FURNACES

The furnaces used in this program were the NASA Crystal Growth Furnace (CGF) in its flight and Ground Control Experiment Laboratory (GCEL) versions and the Grumman Programmable Multizone Furnace (PMZF). The latter was used to grow state-of-the-art commercial-size crystals for comparison with the smaller NASA crystals. The CGF furnaces grew CdZnTe crystals 15mm in outer diameter, whereas the PMZF grew 38-mm-diameter crystals. Both furnaces employed the seeded vertical Bridgman-Stockbarger crystal growth technique terrestrially, with an upper ampoule wall temperature of 1135°C and a lower ampoule

wall temperature of 980°C. The actual furnace wall settings differed because of differences in the furnace thermal masses and safety ampoule/cartridge assembly (SACA) configurations. The CGF GCEL configuration is shown as Fig. 5, and the flight furnace, integrated into the Spacelab racks is shown as Fig. 6. The Grumman PMZF is shown as Fig. 7. The ground furnaces are loaded horizontally and then rotated 90° into a vertical, thermally stabilizing orientation relative to the Earth's gravity vector.

CdZnTe crystals are typically grown using the Bridgman or modified Bridgman crystal growth technique. The technique we are employing is the seeded Bridgman-Stockbarger technique. This technique establishes hot and cold isothermal zones that bracket the solidification temperature, with a linear thermal gradient in between. The gradient is translated at a constant velocity down the length of the sample, directionally solidifying the sample from the cold (seed) end to the hot end. Either the sample or the furnace can be translated, and we have selected furnace translation because vibration associated with the translation is not mechanically coupled directly to the sensitive solidification interface.

The "external" samples were fabricated using the same growth method, and the Grumman Programmable Multizone Furnace (PMZF) operated in a low gradient configuration (<10°C/ cm). The PMZF material has been shown in an ARPA Infrared Materials Producibility Program to compare favorably with the best CdZnTe crystals grown terrestrially with FTIR transmission close to theoretical and defect densities less than 10,000.

2.3 ACCELERATION ENVIRONMENT

Our experience with spacecraft laboratory environments anticipated that the residual acceleration environment on board the First U. S. Microgravity Laboratory (USML-1) would deviate significantly from a condition of "zero gravity." Indeed, based on a consideration of gravity gradient and orbital attitude effects alone it was concluded, for USML-1 at 300 km in a quasi-circular orbit and a gravity gradient stabilized attitude, that the magnitude of the residual acceleration increases at 0.41×10^{-6} g/m from the spacecraft mass center in the so-called local vertical direction, and 0.136×10^{-6} g per meter in the direction perpendicular to the orbital plane. This results in a residual acceleration vector which is typically at a high angle relative to the geometrical and thermal axes of the growing crystals and demanded that non-axisymmetric calculations and terrestrial experiments be the basis for anticipating micro-g results. The effects of atmospheric drag, crew motions, attitude maneuvers, thruster firings, and structural vibrations also contribute significantly to the acceleration environment and can lead to instantaneous magnitudes in excess of 10^{-3} g.

It was desired for the USML-1 mission that the residual g-vector in orbit be aligned such that the experiments conducted within the CGF would experience a thermally and gravitationally stabilizing crystal growth environment. This demanded that the orbiter be flown in a specific orbital attitude, which became known as the "CGF attitude." The orbiter, CGF, and the calculated residual g-vector orientation in the CGF attitude are shown in Fig. 8. The calculated residual g-vector points down the axis of the flight furnace (gravitationally stabilizing), from the hot end towards the cold end (thermally stabilizing), which offered optimal scientific results.

2.4 PROCESS MODELING

The empirical effort was supported by the development of high-fidelity process models of heat transfer (Clarkson University [CU]); fluid flow and solute redistribution (UAH); and thermo-mechanical stress (CU, GCRC) occurring in the furnace, safety cartridge, ampoule, and crystal throughout the melting, seeding, crystal growth, and post-solidification processing. In addition, analyses were conducted (UAH) with respect to the sensitivity of the orbital experiments to the residual microgravity (μ-g) environment, both steady state and g-jitter. Figure 9 shows typical output from the thermal, thermo-solutal, and thermo-mechanical models, respectively. Specific examples of the model output will be included in the sections on experimental results to demonstrate the utility of these models in the planning, implementation, and interpretation of the flight and ground experiments. In addition, a section focusing on interactive model validation will be included as Section 7, and the UAH final report will be appended as the Appendix.

In addition to the models described above, a one-dimensional macrosegregation model at the Space Sciences Laboratory of the NASA Marshall Space Flight Center, SSL/MSFC, was employed to calculate macrosegregation within the 15-mm samples processed in the CGF. Figure 10 shows results of these calculations, with empirical ground truth, one-g, data superimposed. This is a diffusion-controlled model, and the agreement between the model and the empirical data suggests that the growth conditions, which were anticipated to be within the partial mixing regime, are close to diffusion controlled even in one-g. The mass transport coefficient that gave the best fit to the one-g data was 3×10^{-5} cm^2/s, which is a reasonable diffusion coefficient for this system.

A sensitivity analysis conducted using the same model suggested that further reduction of the mass transport coefficient had no great impact on the longitudinal macrosegregation results, as shown in Fig. 11, only shortening the initial transient. The terminal transient would be obscured by the quench and cooling operations. As a result, experimentation involving the investigation of diffusion controlled longitudinal macrosegregation in the microgravity environment was not compelling, since little change would be expected and so radial segregation was primarily considered.

Brown, et al., have predicted that as longitudinal macrosegregation diminishes, radial segregation can become much more significant, as shown in Fig. 12. It was planned, as a consequence, to quantitatively analyze the radial macrosegregation as an integral part of this program, anticipating that both the one-g and μ-g results would be generated in near-diffusion-controlled growth conditions.

2.5 CHARACTERIZATION

The CGF samples were characterized, and the results from one-g and μ-g were quantitatively compared with respect to chemical homogeneity and structural quality. These "internal" results were then quantitatively compared with the best results accomplished terrestrially as an "external" comparison." Characterization techniques employed in this study included x-ray double crystal rocking curve(DCRC), x-ray precision lattice parameter (XPLP), energy dispersive x-ray analysis (EDX), photoreflectance (PR), synchrotron white beam topography (SWBT) (Ref. 1), and synchrotron monochromatic beam topography (SMBT).

Both SWBT and SMBT were performed at the National Synchrotron Light Source (NSLS) at Brookhaven National Laboratory (BNL). The DCRC and XPLP measurements were made at Grumman using Blake Instruments custom systems, with Copper radiation and a spot size of ~1mm^2. The EDX and microprobe measurements were made at Marshall Space Flight Center.

PR was carried out at 300K using a He-Ne laser chopped at 200 Hz, a monochromator resolution of about 25 Å, and a typical spot size of ~1mm. The energy gap was determined from a lineshape fit using the low-field approximation (Ref. 3, 4); the zinc content (x) in Cd(1-x)Zn(x)Te was derived from the "calibration curve" of Ref. 2, assuming a constant energy shift in the curve to account for our use of 300K rather than 77K. For DCRC, XPLP, and PR, the sample was mounted on a micropositioner stage which allowed manual or automatic scanning over the sample surface. All samples were identically chemo-mechanically polished using a dilute Br-methanol solution (Ref. 5).

3 -- MICROGRAVITY RATIONALE

Since the days of Skylab and the Apollo-Soyuz Test Project, it has been recognized that an orbiting spacecraft may serve as a laboratory within which to carry out crystal growth experiments in a unique reduced gravity working environment. The attraction of this almost weightless environment to crystal growers may be explained simply. Under terrestrial conditions, gravitational acceleration imposes hydrostatic and buoyancy forces on the melt and growing crystal and crystal/melt interface that can be deleterious to the structural quality and chemical homogeneity of the product crystal. The orbital environment offers the opportunity to undertake bulk crystal growth experiments under conditions for which the gravitationally dependent hydrostatic and buoyancy forces are drastically reduced, thus offering the possibility of significantly increasing structural perfection and chemical homogeneity.

4 -- INVESTIGATION & TECHNICAL PLAN

As previously stated, the technical objectives of this program are to investigate, quantitatively, the gravitational influences (hydrostatic and buoyant) on the growth and quality of alloyed compound semiconductors, particularly CdZnTe, obtained using the modified Bridgman crystal growth technique. Flight experiments and supporting ground-based experiments were conducted.

In the ground-based experimental program, at the Crystal Growth Laboratory of the Grumman Corporate Research Center, we employed our advanced low-gradient programmable multizone furnace systems in order to minimize the thermo-mechanical stresses imposed on the growing CdTe crystal and during post-solidification processing. We applied our thermal model of this furnace system to anticipate the thermal environment imposed on the crystal growth ampoule and the longitudinal and radial thermal environments experienced by the growing crystal and melt. A finite element model of thermoelastic stress was developed in collaboration with Clarkson University that calculated the thermoelastic stress imposed on the growing or cooling CdTe crystal, and displayed the thermoelastic stress field imposed on each wafer selected from the real boules. These results were compared with the supporting experimental and literature studies, and it was determined that alloying of the CdTe was necessary to raise the allowable critical resolved shear stress (Ref. 6) within the growing crystal above the minimum thermoelastic stress levels imposed by the available furnace systems, on the ground and in flight. In addition to the thermoelastic stress studies, the influences of axisymmetric and non-axisymmetric gravitational and thermal fields were investigated for the flight samples.

The University of Alabama at Huntsville conducted time-dependent and steady state mass, heat, and momentum transport calculations in support of the one-g and micro-g experiments (Ref. 7). Computer codes developed at the Center for Microgravity and Materials Research have been used to examine the effect of the orientation and magnitude of the gravity vector on simplified models of directional solidification using the Bridgman-Stockbarger technique. In order to adapt these codes to the requirements of the specific solidification system under investigation, further development of these codes was necessary. The calculated radial and longitudinal macrosegregation distributions in the crystal in one-g and micro-g were the bases for planning the one-g experimental matrix and the flight experiment. The flight experimental results were quantitatively determined utilizing the previously described state-of-the-art characterization equipment in the Grumman Crystal Growth and BNL/NSLS Laboratories. The interpretation of these results was augmented by the furnace thermal models, the thermoelastic stress model, and the time-dependent fluid flow and solute redistribution model.

4.1 PROGRAM PLAN

The empirical effort entailed the development of one-g experiment baselines for quantitative comparison with the μ-g results. The efforts in one-g and μ-g were supported by high-fidelity process models of heat transfer, fluid flow and solute redistribution, g-sensitivity, and thermo-mechanical stress. The furnace, safety cartridge, ampoule, and sample, throughout the melting, seeding, crystal growth, and post-solidification processing were considered in these models.

The program management, experiment design, sample/ampoule development, fabrication and delivery, flight support operations, process model validation, and sample characterization, were conducted by the Grumman Corporate Research Center, under the direction of the

Principal Investigator, Dr. David J. Larson, Jr. The thermal and thermo-mechanical process models were developed at Clarkson University under the direction of Professor Frederick Carlson. G-sensitivity and fluid flow and solute redistribution models were developed and validated under the direction of Dr. J. Iwan D. Alexander of the Center for Microgravity and Materials Research of the University of Alabama at Huntsville. Dr. Donald Gillies of the Space Sciences Laboratory of the NASA Marshall Space Flight Center, assisted in the development, qualification and optimization of the sample/ampoule and flight experiment, in the quantitative prediction and characterization of macrosegregation, and quantitative characterization of precipitate content using infrared microscopy. Prof. Michael Dudley of the State University of New York at Stony Brook and Dr. Gabrielle Long of the National Institute of Science and Technology headed the white and monochromatic synchrotron topography imaging teams, SWBT and SMBT, respectively.

The process models were initially used to predict the impact of process parameter variation (trend analysis), allowing us to design critical one-g growth experiments and to anticipate μ-g sensitivity (g-jitter and residual g orientation). Subsequently, as the models were validated experimentally, correlation and optimization experiments in one-g and in μ-g were conducted. Finally, the experimentally validated models were utilized to assist in the interpretation of the μ-g results and the quantitative comparison of μ-g and one-g results.

DCRC, XPLP, and FTIR measurements at GCRC were conducted by Dr. Donald DiMarzio. IR microscopy and EPD studies were conducted by Dr. Louis Casagrande. Ampoule fabrication and chemo-mechanical polishing were conducted by Mr. Andre Berghmans.

5 -- EXPERIMENT DESCRIPTION

The experiment plan was to grow CdZnTe crystals in one-g and in μ-g under identical growth conditions except for the magnitude of the gravitational vector. It was anticipated that the μ-g environment would damp gravitationally dependent thermosolutal convection, improving longitudinal and radial chemical homogeneity (macrosegregation). More important for this investigation, however, was the near-absence of hydrostatic pressure in μ-g. This allowed the bulk liquid to minimize contact with the constraining ampoule walls, reducing the hoop stresses experienced by the growing and cooling crystal while maintaining thermal symmetry. It was anticipated that this might significantly reduce the defect density and residual strain within the μ-g samples. It was planned that the one-g and μ-g samples were to be carefully analyzed for chemical homogeneity (longitudinally and radially), and for structural perfection. Optoelectronic performance was also to be mapped using Fourier Transform Infrared (FTIR) measurements.

5.1 FURNACE THERMAL RESULTS

The Temperature/Time/Position history of the optimized ground and flight experiments were determined to be: heat-up rate (2°C/min), post-seeding thermal equilibration time (2 hr), solidification velocity (1.6mm/hr), applied thermal gradient (33°C/cm) and cool-down rate (2° C/min). These growth conditions gave the best quality crystals, highest crystallinity, and lowest defect density, that were consistent with the available flight time and the performance characteristics of the CGF.

5.2 SAMPLE AMPOULE CARTRIDGE ASSEMBLY

The Sample Ampoule Cartridge Assembly (SACA) is shown as Fig. 13 (a and b). This metallic containment device protected the furnace from caustic or toxic material release in case of an ampoule failure. In addition, the SACA provided support and alignment of the sample ampoule and the thermocouple instrumentation. The SACA consisted of a WC103 shell with non-reactive coatings on the inner and outer surfaces. This exterior of the SACA was found to change color and emissivity as a function of time at temperature. Since these color changes suggested significant emissivity changes that could significantly impact temperature distribution, this was investigated using the thermal model. The thermal model output is shown as Fig. 14, confirming that significant temperature changes do take place as a function of time. It was determined empirically, however, that the heat-up and equilibration time at temperature was sufficient to stabilize the emissivity and to provide a reproducible thermal environment for the sample to be processed.

5.3 INSTRUMENTATION/AMPOULE/SAMPLE CONFIGURATION

The sample ampoule and the surrounding instrumentation are shown schematically in Fig. 15. Six Type K (Chromel/Alumel) thermocouples were used. The thermocouple locations were at the base of the seed crystal, at the desired melt-back location on the seed crystal, at the shoulder of the ampoule, diametrically opposed thermocouples at the middle of the steady-state growth region, and at the end of the liquid zone. The ampoule was fused silica with a carbon

lining to minimize diffusion from the ampoule into the melt. The coating also was intended to provide a non-wetting interface so that the sample could disassociate itself from the wall (dewet) if possible during the flight experiment. In flight and ground ampoules, the carbon coating minimized stiction, the generation and transfer of stress, and the generation of structural defects.

The instrumentation thermocouples also served as safety devices in that if an ampoule was breached and CdTe was released into the SACA, the thermocouples were shown to fail well before the SACA would fail. These failure times and containment times were determined by complementary NASA safety studies.

6 -- EXPERIMENTAL RESULTS & DISCUSSION

One-g qualification and developmental tests were conducted in the CGF Ground Control Experiments Laboratory (GCEL) to confirm hardware designs for the sample/ampoule, ampoule/cartridge, and the interfaces between these components and instrumentation within the Sample/Ampoule Cartridge Assembly (SACA). In addition, timeline compatibility between the four experiments that were to run in series in the CGF on USML-1 and the flight timeline was confirmed. Lastly, the ground test results served to empiricize the process models and optimized the processing parameters for the flight experiment.

The final CGF ground sample, grown under the optimized process conditions, duplicated the anticipated flight conditions and served as a "ground truth" sample for quantitative comparison with the primary flight sample. Since we had the unexpected opportunity to conduct a second μ-g experiment with the flight back-up (secondary) sample, the "ground truth" experiment for the secondary sample was conducted post-flight. Analyses of these samples focused on chemical homogeneity, which was previously discussed, and the structural quality of the crystals, which will be discussed in a subsequent section.

In addition to the CGF "internal" baseline, an additional "external" baseline was established using the Programmable Multi-Zone Furnace at the Grumman Corporate Research Center. This furnace system employed lower thermal gradients (<10°C/cm) and slower heating and cooling rates (1°C/min) in order to minimize the thermo-mechanical stresses imposed on the sample during processing. These samples were 38 mm in diameter as compared to the CGF samples which measured 15 mm in diameter. In addition, one 15-mm-diameter sample was grown in the PMZF system to simulate the CGF growth conditions in the GCRC furnace and to confirm the design safety of the ampoule. These results were intended to serve as an external comparative baseline representative of the best CdZnTe produced terrestrially. CdZnTe PMZF material has been shown in the ARPA Infrared Materials Producibility Program to compare favorably with the best CdZnTe crystals grown terrestrially.

The USML-1 Mission was planned to process one primary sample, with a back-up sample in stowage outside the CGF Furnace. The primary sample was successfully processed, and due to the premature termination of one of the other experiments, a second flight experiment was possible, but of shorter duration. The furnace heat-up rate, seeding and thermal equilibration time, temperature profile, and cooling rate were identical for both experiments; the primary difference was the duration of the experiments. Since the samples were of identical lengths, this meant that the secondary sample was furnace cooled prior to the completion of solidification of the sample, and a substantial amount of material was solidified under non-plane-front growth conditions. The secondary sample served to confirm the successful seeding technique and to provide additional material from the shouldering region that solidified without wall contact.

Conducting the second experiment demanded unprecedented actions on the part of the crew, particularly: Payload Specialist Eugene Trinh to install the flexible glovebox on the CGF, which enabled the processed SACAs to be removed from the CGF; Alternate Payload Specialist Al Sacco to develop the SACA exchange procedures; and Payload Commander Bonnie Dunbar and Pilot Ken Bowersox who exchanged the SACAs, demonstrating for the first time in the U.S. program the ability to exchange potentially toxic materials in the closed environment of the Spacelab. These actions proved the feasibility of conducting similar necessary operations on Space Station, greatly increasing the productivity.

6.1 THERMAL

The samples on USML-1 were processed in the Crystal Growth Furnace (CGF) using the seeded Bridgman-Stockbarger method of crystal growth. Bridgman-Stockbarger crystal growth is accomplished by establishing isothermal hot zone and cold zone temperatures with a uniform thermal gradient in between. The thermal gradient spans the melting point of the material (1095°C). After sample insertion, the furnace's hot and cold zones are ramped to temperature (1175°C and 980°C, respectively), establishing a thermal gradient (33°C/cm) in between and melting the bulk of the sample. The furnace is then programmed to move farther back on the sample, causing the bulk melt to come into contact with the high-quality seed crystal, thus seeding the melt. The seed crystal prescribes the growth orientation of the crystal grown. Having seeded the melt, the furnace translation is reversed and the sample is directionally solidified at a uniform velocity (1.6 mm/hr) by moving the furnace and the thermal gradient over the stationary sample.

6.1.1 TEMPERATURE/TIME HISTORY

The temperature/time history of the ground and flight samples is shown in Fig. 16 and Fig. 17, respectively. The experiment durations of the Ground Truth and GCRC-1 flight samples are identical. The temperature/time history of the shortened duration flight experiment, GCRC-2, is shown as Fig. 18.

6.1.2 MELTING/SEEDING

The most critical step in the crystal growth process is the seeding operation. Much of the success or failure of the experiment will be determined by this step. The items of major concern are the quality of the seed used, the integrity of the seed during the heat-up and melting operation, the precision and stability of the melt-back, and the success of single crystalline regrowth from the seed through the shoulder region. Figures 19 and 20 illustrate the difference in melting behavior between one-g and μ-g experiments. It may be seen in Fig. 19 that, as melting in one-g is effected in the upper regions of the vertically oriented ampoule, the molten charge drains toward the cold end, causing a measurable thermal "surge" in the thermocouples at lower positions. This is strictly due to gravity and in the flight sample, Fig. 20, the absence of this "surge" should be noted.

This is a "good news/bad news" situation. In one-g, a thermal surge sufficient to melt the entire seed may develop -- clearly bad news! But this is a far more common event for large-diameter crystals, where the thermal mass of the charge greatly exceeds that of the seed, than for the small diameters used in the CGF experiments. Another undesirable possibility is that the molten material will quickly drain to the shoulder region and refreeze, possibly causing ampoule failure due to the expansion on solidification typical of most semiconductor materials. The thermal surge or draining and resolidification are not problems in μ-g, however, since in the near absence of hydrostatic pressure the molten charge is not forced to drain toward the cold end. The bad news in μ-g is that the molten charge is not forced in contact with the seed crystal and thus the experiment might proceed as an unseeded growth. Care is needed in the planning and execution of both ground and flight experiments.

The heat-up and melting sequence are shown enlarged in Fig. 21. It should be noted that the

endothermic melting reaction is clearly discernible from the thermocouple record. The apparent melting point for the thermocouple placed at the location of desired melt-back, and confirmed preflight to be in the correct position radiographically, was used as the melt-back temperature during the seeding operation. As such, this data point serves as an internal temperature calibration of the melting temperature, taking into account empirical errors due to instrumentation, accuracy, and/or software temperature conversion algorithms.

Once the seeding operation is initiated, the CGF furnace is moved, stepwise towards the seed crystal until it is decided that the melt-back interface location is coincident with the desired melt-back position on the seed crystal. In general, this was approximately one-third to one-half of the total seed length (20 mm) from the hot end. Typical stepwise seeding translation and thermal responses are shown in Fig. 22. It should be noted that the positional response is almost instantaneous, whereas the thermal response is considerably more sluggish. As a consequence, it is necessary to wait for thermal equilibrium to be reestablished before taking the next incremental step. Typically, seeding could be accomplished in two or three steps in less than one hour. The accuracy and reproducibility of this procedure and furnace were such that no seed crystals were inadvertently melted.

The seeding operation was supported by thermal modeling, and Fig. 23 shows the thermal model output for the final thermal profile selected for flight. The model predicted that the melt-back interface should be near planar. Figure 24 shows the melt-back interface on the exterior of a typical sample. The interface is clearly thermally symmetric on the periphery, and x-ray synchrotron topographs of the GCRC-2 flight sample confirmed that the melt-back interface was in fact very nearly a flat plane. These topographs will be presented in Section 6.5.7, "X-ray Synchrotron Bragg Contour Mapping."

6.1.3 CGF STABILITY

The temperature stability of a furnace is of concern during thermal equilibration after seeding in order to maintain a constant melt-back interface location without thermal "ratcheting," which can result in a compositionally and crystallographically disturbed regrowth interface. In addition, temperature stability is important to maintain compositional stability and the prescribed gradient environment during steady-state growth.

The temperature stability of the CGF GCEL furnace and for the identical flight experiment, GCRC-1, are shown in Fig. 25 and Fig. 26, respectively. It may be seen that the temperature stability is on the order of ±1.0°C in both cases. This is good, but certainly not exceptional. The temperature stability of the PMZF ground furnace, for comparison, was on the order of ± 0.2°C, without averaging, and much better than ±0.1°C, with averaging.

6.1.4 STEADY-STATE GROWTH

The steady state growth histories for the ground truth and GCRC-1 samples are shown in Fig. 27 and Fig. 28, respectively. The translation rates are identical, as are the heat-up rates, with the exception of the previously mentioned melting and draining phenomena. It was found in the course of the experiment that the furnace power consumption in orbit was on the order of 10% less than terrestrially. It is thought that this was due to the absence of the convective heat loss mechanism. The other difference that should be noted is the slightly steeper thermal gradient experienced by the flight sample. This, too, is thought to be related to the reduction of

gravitationally dependent convection.

6.1.5 COOLING/QUENCH

The programmed cooling of the ground and flight samples was planned to be identical. At the termination of the GCRC-1 steady-state growth, however, a net temperature rise was noted prior to the programmed cooling. The normal and GCRC-1 cooling curves are shown in Fig. 29 and Fig. 30, respectively. In addition to differences in the cooling rates, the possibility of differences in solidification temperature (thermal undercooling) was investigated. It was found in both flight and ground samples that little, or no, undercooling was exhibited, probably due to the presence of the grown crystal acting as a seed for the rapidly cooled region.

6.2 MICROGRAVITY ENVIRONMENT & MEASUREMENT

It was anticipated that if the residual g-vector pointed down the axis of the CGF, as desired, it would assist seeding and result in a thermally and gravitationally symmetric geometry that was thermally stabilizing for our experiment. The orientation of the calculated (anticipated) residual g-vector relative to the Spacelab and the CGF has been shown as Fig. 8. Inspection of the flight samples, to be discussed subsequently, suggested that this was not correct in the actual experiment. Thorough analysis of the acceleration data from the STS-50/USML-1 mission by UAH suggested that there was an unanticipated gravitational component that resulted in gravitational asymmetry at the CGF location. This was most likely due to the operation of the Shuttle Flash Evaporator System (FES), which operated on approximately a 28-hour cycle (14 hours on and 14 hours off). Figures 31(a) and 31(b) show the average orientation of the residual acceleration vector when FES was on, recorded by (a) OARE at the OARE location and extrapolated to the CGF location and (b) PAS on the Flight Deck and extrapolated to the CGF location. It is clear that this residual g-vector is significantly asymmetric relative to the CGF furnace bore axis, resulting in thermal and gravitational asymmetry in the flight samples.

6.3 SURFACE ANALYSIS

Optical examination of the surface topography of the primary flight sample, Fig. 32(a), shows that the areas in full contact with the ampoule wall mirror the surface topography of the wall and coating and appear visually to be very bright reflective surfaces. The topography of the free surfaces shows some thermal etching, but is relatively smooth and has the blue-grey appearance of most semiconductors. The region of partial wall contact, however, is a highly textured matte finish. The partial contact surface was found to be composed of a honeycomb of interconnected hexagonal cells that are nearly perfect hexagons nearest the region of full wall contact and which get progressively more elongated circumferentially as the liquid moves away from the wall. This pattern of partial wall contact is shown in Fig. 32(b).

6.3.1 X-RAY RADIOGRAPHY

Radiographs of the flight ampoules in their preflight condition are shown in Fig. 33. A macrophotograph of the processed flight ampoules is shown as Fig. 34, and radiographs of the

interior of the flight ampoules, post-flight, are shown in Fig. 35(a) (primary sample, GCRC-1) and Fig. 35(b) (secondary sample, GCRC-2). It should be noted that the bulk samples seen in Fig. 33, are separate from the seed crystals, although in physical contact with the seeds. When melted, the bulk liquid contacted the seed crystal, due to the residual gravitational vector and wetting forces, and since a liquid will always wet its own solid the seeding operation was successful in both instances.

Careful inspection of the radiographs in Fig. 35 shows that both of the crystals grown were separated from the ampoule wall in the shoulder region. This was anticipated and is referred to as "dewetting," although this term is not strictly correct. Wall contact was not reestablished until the full ampoule cross section is reached in the steady-state region of growth, and a significant pore, which is located on each shoulder, should be noted.

6.3.2 OPTICAL MACROSCOPY-BOULE

The color pattern and surface texture pattern on the surface of the GCRC-1 flight sample, shown in Fig. 36 (prior to sand blasting the surface), and GCRC-2 suggested that each sample solidified without wall contact throughout the shoulder region and that, when wall contact was resumed, it was only on one side of the ampoule. Partial wall contact would be expected to result from gravitational asymmetry, which was not anticipated, and was suspected of causing significant thermal asymmetry, possibly solutal asymmetry, and probably mechanical asymmetry. The thermal and thermo-mechanical models were modified, post-flight, to treat the asymmetric cases encountered, and Fig. 37 shows a typical output. Inspection of the thermal asymmetry, on the left, shows that the thermal disturbance was smaller than anticipated, due to the domination of radiative heat transfer at these elevated temperatures. Maximum radial gradients were on the order of 2°C/cm, with the free surface slightly hotter than the side with wall contact.

The thermo-mechanical stress experienced by the sample was calculated to be below the critical resolved shear stress at temperature of this material, unless there was stiction at the region of wall contact. This was found to be the case, empirically, and will be discussed in greater detail in a subsequent section.

6.3.3 X-RAY SYNCHROTRON TOPOGRAPHY-BOULE

Synchrotron White Beam Topography (SWBT) at a shallow glancing angle was used to evaluate the surface condition of the flight samples in the three regions of varying wall contact. The region of total wall contact gave very poor topographic images (not shown), imaging the carbon coated inner surface of the ampoule, suggesting high levels of surface strain. The regions of no wall contact, gave high-quality topographs which suggested that the residual strain levels were very low. Images of the defect structure in this region suggested the possibility that the defect density was very low and that dislocations present were discrete rather than in a fine subgrain or mosaic structure. The regions of no wall contact showed no sign of twinning at the surface. The regions of partial contact, however, showed strong evidence of cross slip, and occasional twinning. Deformation of this type was restricted to the regions of partial wall contact and suggested that the honeycomb surface structure may have acted as a series of stiction points for the solidification interface resulting in much higher local stresses and concomitant plastic deformation by dislocation and twinning mechanisms.

A topograph of a region of the primary sample that solidified with no wall contact is shown as Fig. 38, and a region of the same sample solidified with partial wall contact is shown as Fig. 39. Note the discrete dislocation pattern and low dislocation density in Fig. 38 and the high density of dislocations manifested as occasional twinning and extensive slip in Fig. 39.

6.4 SECTIONING PLANS

Having thoroughly analyzed the surfaces of the samples, the crystals were then oriented using x-ray Laue techniques and wafered such that the wafer surfaces were {111} planes, which is the industry standard for LPE substrates. Each flight sample was cropped to remove the portion of the sample that was not plane-front solidified. The GCRC-1 primary sample was sectioned on a {111} plane that was 15° to the growth axis of the crystal. The wafers from both samples were chemo-mechanically polished and etched with a lactic acid etchant that differentiated between the A and B faces; A (Cd, Zn) appearing dark and B (Te) appearing bright.

6.4.1 SCHEMATICS

Figure 40 shows, schematically, the GCRC-2 boule configuration and the wafering plan for flight sample. Each wafer was cut such that the wafer surface was a {111} crystallographic plane. The orientation of the slices relative to the regions of wall contact differed from sample to sample.

6.4.2 {111} WAFERS

The wafer arrays assembled from boules GCRC-1 and GCRC-2 are shown photographically in Fig. 41and Fig. 42, respectively.

6.5 WAFER ANALYSES

Each wafer was subjected to a comprehensive analysis. These analyses included FTIR, DCRC, XPLP; IR, and Optical microscopy; and Synchrotron White Beam Topography, Synchrotron Monochromated Beam Topography, and Bragg (Strain) Contour Mapping. It was anticipated that this spectrum of analyses would document the chemical and structural quality of the materials. Some results were found to be different in flight samples GCRC-1 and GCRC-2. This is most likely due to the significantly different temperature/time histories noted in section 6.1.1. As a result, examples from both sample sets of samples will be illustrated where differences occur, whereas only representative results will be presented where similar results were obtained.

6.5.1 FTIR MAPPING

FTIR transmission of both ground and flight materials was measured to be close to theoretical; 63% versus 66% (theoretical). This suggested that both the ground and flight materials were close to the stoichiometric composition. Infrared microscopy and x-ray measurements confirmed that the principal precipitates were Te and their size (1-10 μm), and

density suggested that both primary flight and ground-based samples experienced similar cooling rates and were close to stoichiometry.

A typical FTIR spectrum is shown as Fig. 43. It should be noted that the extended flat region of transmission and the high percentage of transmission are indicative of very high quality material. The present industry standard is 55% transmission, and the current objective is to move this value commercially to 60%. Transmission in the GCRC PMZF samples was close to 65% ±1.5% for all samples over a similar wavelength range. Clearly, the commercial standard was met throughout our investigation, strongly suggesting that our stoichiometric control during solidification and post-solidification processing is excellent.

6.5.2 DCRC MAPPING

The flight samples were found to be much higher in structural perfection than the ground samples produced in the same furnace under identical growth conditions except for the gravitational level. Rocking curve widths in the best regions of the samples were found to be substantially reduced, from 20/35 arc-sec (one-g) to 9/15 arc-sec (μ-g). The value of 9 arc-sec found in the GCRC-2 sample equals the best reported terrestrially for this material (Northrop Grumman PMZF and LBBF 38-mm and 64-mm boules, respectively).

X-ray synchrotron Bragg reflection topography confirmed that the GCRC-1 and GCRC-2 wafer surfaces are entirely {111}. However, in the GCRC-2 samples, shown in Fig. 44, there was 180° rotational twinning about the longitudinal axis. It may be seen, for the orientation shown, that the left third of the wafers are predominantly A faces, whereas the remainder consists of a single B face. It is thought that the left side of the wafer was the side that developed wall contact, but we have no reason to believe that this was a factor since the rotational twin nucleated in regions thought to have been free surfaces throughout.

Both flight samples were analyzed using DCRC mapping as a measure of residual strain in the crystal. The results suggest that the quality of the flight material, particularly in regions solidified without wall contact, and as judged by the full width half maximum (FWHM) of the {333} Bragg diffraction peak, is substantially better than that recorded for the ground truth samples. An area map of the FWHM for GCRC-2 flight wafer 7 is shown as Fig. 45. It should be noted that appreciable areas of the flight samples average FWHM values between 10 and 15 arc-sec, whereas the same regions in the ground truth samples averaged 20 to 35 arc-sec. The best regions of the GCRC-2 flight wafers, as indicated by the FWHM of the {333} rocking curve, are 9.2 arc-sec. This is fully comparable to the best material that has been grown on the ground, using the PMZF technology or any other commercial technology.

The GCRC-1 wafers showed a different strain pattern, as determined from the DCRC mapping. The XPLP measurements in Fig. 46 showed a near constant radial composition across the GCRC-1 wafers, as measured using XPLP. These results confirm that, in the steady state regions of this crystal, diffusion-controlled growth was achieved. The DCRC values at the same measurement points, however, told a much different story. These values, shown in Fig. 47, revealed a decided gradient in residual strain from the wall contact side to the free surface side of the GCRC-1 Wafer 3. Similar results were obtained for wafers sliced from further down the boule. This is consistent with the output of the thermo-mechanical stress model which predicted that the region of wall contact with stiction significantly exceeded the critical resolved shear stress at temperature, resulting in residual strain which is greatest at the wall and which diminishes on progressing toward the free surface.

The GCRC-2 strain distributions are different in part because of the manner in which the wafers were cut relative to the wall contact. In regions without wall contact, the best material is found close to the sample periphery. In the ground samples, and the previously discussed region of the GCRC-1 sample with wall contact, maximum strain and peak width were concentrated at the periphery where wall contact was noted. This suggests that, unlike the ground samples that were forced to be in mechanical contact with the ampoule walls during processing, the GCRC-2 flight sample was not, with a resultant significant reduction in strain. Post-flight modeling of this process confirms this hypothesis, with the stress experienced by the free surface significantly lower than that at the wall. This is shown in Fig. 48.

An additional difference between the highest quality regions of the flight samples and the ground-based samples appears in the shape of the DCRC peaks. Figure 49(a) shows a typical DCRC peak and Gaussian fit for a good region of a PMZF ground sample. The FWHM is about 20 arc-sec, but the fit at the base of the peak, the "tail" of the curve, is quite poor. This indicates that agreement between diffraction theory and real diffraction is not good. This deviation occurs because the "tails" of the curve represent the defect structure of the real samples and the defect distribution in these samples is not the ideal distribution that the theory assumes. Figure 49(b) shows the same peak and fit, except that it is plotted on a log plot which emphasizes the tails of the curve and focuses attention on the lack of agreement between theory and practice. Figure 50 is a ground sample from a complementary study, where the tails of the curve are well described by kinematic diffraction theory. This sample region had a fully developed mosaic substructure that conforms well to the description of an "ideally imperfect" crystal. Figure 51 shows a typical {333} rocking curve peak from a low-strain region of the GCRC-2 flight material. In this case, the tails of the curve are very well described by the Gaussian fit and, taken in concert with the low density of discrete dislocation regions imaged on the flight sample free surfaces, suggested the possibility that this material was "ideally perfect" material rather than the aforementioned "ideally imperfect" material that we commonly encounter terrestrially. The critical test for this hypothesis was to image the samples topographically in transmission, so that the dislocation structure was imaged directly. These results will be presented in a subsequent section.

6.5.3 PRECISION LATTICE PARAMETER MAPPING

Precision lattice parameter mapping of the wafers was intended to monitor the local variation of composition longitudinally and radially. The spatial resolution of this technique corresponded to the x-ray beam spot size, which was on the order of 0.5 to 1.0 mm^2. Sufficient counts under each x-ray peak were demanded to justify statistical significance and a good fit to the Gaussian distributions. Typically, the {333} peak and monochromatic Copper radiation were utilized for these measurements. Peak anisotropy and peak broadening will be reported under the DCRC results.

The most important PLP results confirmed that the flight samples solidified under diffusion-controlled growth conditions. The Zn concentration in the initial transient region of GCRC-1 is well described by the one-dimensional diffusion model, and the steady-state concentration achieved for the bulk growth corresponds to the bulk alloy concentration. In addition, the radial segregation determined along the central axis of the boule is nearly planar, suggesting a nearly planar solidification interface and minimal convective contributions to the macrosegregation. Typical examples are shown in Fig. 52 for the initial and steady-state longitudinal segregation

and in Fig. 46 for the radial segregation.

6.5.4 IR MICROSCOPY

The infrared microscopy was aimed at determining whether there was a significant difference in precipitate distribution between the ground and flight material. The precipitates being monitored were Te precipitates, consistent with the slight Te excess compositionally used in these experiments. This excess was intended to maximize the resistance of the material, as semi-insulating behavior is desirable in the substrate applications that are envisioned.

Two types of precipitates were monitored. The first, referred to in the literature as "inclusions," result from liquid precipitation and entrapment during solidification. Because this is a macroscopic phenomenon, these particles are large, i.e., 1 to 10 μm, and sometimes cause problems in real applications because of their size and irregular distribution. The second precipitates occur during cooling in the solid state. These precipitates are small, i.e., less than 1 μm, and uniformly distributed.

No difference was noted between the flight sample and ground truth distributions, although the literature had led us to anticipate that there might be a gravitational dependence. This result supports the FTIR results that the composition was similar in both cases, slightly Te-rich, and that no substantive differences existed in this respect, between the flight and ground materials. A typical IR Transmission Micrograph is shown as Fig. 53. The large triangular precipitate is a Te "inclusion," whereas the others are thought to be Te precipitates.

6.5.5 OPTICAL MICROSCOPY

Morphologically, the ground samples were found to have a fully developed mosaic structure consisting of subgrains and large regions of cross-slip, as shown in Fig. 54. The flight samples, however, exhibited discrete dislocations in all cases, and very low dislocation densities in many cases, with no mosaic substructure or cross-slip evident. The defect density was reduced from 500,000-1,000,000 (one-g) to 400-3000 EPD (μ-g) in the GCRC-1 and GCRC-2 samples, which are shown as Fig. 55a and Fig. 55b, respectively. The 500 EPD value is the lowest reported for this material to date and is a spectacular demonstration of the importance of removing wall contact as a source of stress during solidification and post-solidification processing.

6.5.6 X-RAY SYNCHROTRON TRANSMISSION TOPOGRAPHY

Samples of the flight and ground base materials were chemo-mechanically polished to 180 μm in thickness and were exposed to monochromatic synchrotron radiation. Only the flight sample could be brought into diffraction; insufficient transmission resulted in the absence of topographic imaging for the ground samples. This suggested the probability that the higher strain content of the ground samples prevented sufficient transmission, whereas the flight sample permitted transmission due to greater crystalline perfection and lower residual strain. Figure 56 clearly shows that the dislocations in this shoulder region of GCRC-2 are low in density and are discrete over large (relative) areas. The singular bright spots are thought to be Te precipitates, and the long straight lines are two variants of {111} twins. This micrograph confirms the discrete nature and low number density of dislocations in the flight material, as previously concluded from optical microscopy and the surface topographic studies.

6.5.7 X-RAY SYNCHROTRON BRAGG CONTOUR MAPPING

Bragg contour mapping uses the highly monochromatic x-ray source as a high-resolution interferometer. Small angular steps are taken across the angular range of a Bragg reflection, and the resulting regions that diffract at each setting are recorded on film or on an x-ray camera. These sequences can then be overlaid, and an image of the strain regions diffracting for each step can be generated. This appears as a series of strain contours, which can be quantitatively related to the thermo-mechanical models, or can be integrated to result in a full topographic image for comparison with optical or infrared images of the same regions. An example for a PMZF wafer is shown as Fig. 57. It is clearly seen that the high-strain regions are located at the periphery and anisotropically, as predicted by our model, but that there is also a large core of high-quality material, internally. This demonstrates the Strain Contour technique.

For the region of the seed crystal referred to earlier, another variation of this technique was utilized. An x-ray diffraction vector interacts with the strain tensor at the surface of the crystal, and strain images can be optimized by rotating the sample relative to the x-ray beam so that the strained feature of interest is perpendicular to the incident x-ray vector. An example of this is shown in Fig. 58a and Fig.58b for the seed region of GCRC-2. In Fig. 58b, the diffraction vector is perpendicular to the melt-back interface of the seed crystal, whereas in Fig. 58a the diffraction vector is perpendicular to the growth and geometrical axes of the seed/regrowth region of the sample. In the case of Fig. 57b, the melt-back interface is resolved clearly, and is shown to be the nearly planar interface anticipated by the thermal model and ground testing. In Fig. 57a, strain contours are clearly delineated as the regrowth approaches the shoulder, but the melt-back interface is diffuse. This example demonstrates that, to optimize a specific strain feature, using monochromatic synchrotron radiation, the best strain contrast will be obtained when the feature is normal to the diffracting beam.

7 -- PROCESS MODELING

The thermo-mechanical process model was used uniquely to predict the residual strain fields within the crystals grown. This was accomplished by first predicting the thermal fields experienced by the grown crystals and comparing the model predictions with the actual temperatures monitored during the crystal growth run. Once agreement was confirmed, the stresses experienced by the crystal were calculated using the thermo-mechanical process model developed at Clarkson University. The model predicted the stresses experienced within each boule. This stressed boule was then sliced on the computer exactly as the real boule had been empirically. The individual wafer slices, with superimposed residual stress fields, were then illustrated, for comparison with the strain images obtained using synchrotron topography. End effects were particularly important to depict rigorously. When done correctly, the correlation between the predicted excess stress images and the empirically determined strain images were dramatic evidence for the power of this new technique, and demonstrate that even an elastic model is valuable as a first approximation. Examples are shown for the residual stresses within wafers sliced from a model PMZF boule shown as Fig. 59. These slices coincided literally with slices taken from the real boule. Slice 13 was imaged using SMBT, Fig. 60, and the enlarged stress image from Fig. 59 is superimposed in Fig. 61. It is clear that major sub-grain features result directly from the stress field imposed during processing. We believe that this prediction/correlation is the first time that this has been accomplished for structural defects within a grown crystal, and is an example of the integrity of the models that we have developed.

Our follow-up experiment on USML-2 will process the flight sample in a thermally symmetric environment, with full wall contact, hopefully without stiction. This will add to the comparative matrix and test further the validity of the process models.

8 -- EXPERIMENT SUMMARY & CONCLUSIONS

FTIR transmission of both ground and flight materials showed that the infrared transmission was close to theoretical, 63% versus 66%, suggesting that the crystals grown were close to the stoichiometric composition in both the ground and flight experiments. Infrared microscopy confirmed that the principal precipitates were Te, and their size (<1-10 μm) and density suggested that the primary flight and ground base samples experienced similar cooling rates and were similar in composition.

Macrosegregation was predicted (using scaling analysis) to be low even in one-g crystals, and this was confirmed experimentally. Nearly diffusion controlled growth was achieved even in the partial mixing regime on the ground. Radial segregation was monitored in the flight samples and was found to vary with fraction solidified, but was disturbed due to the asymmetric gravitational and thermal fields experienced by the flight samples.

The flight samples were found to be much higher in structural perfection than the ground samples produced in the same furnace under identical growth conditions except for the gravitational level. The flight material was properly described as "ideally perfect" material from a diffraction standpoint, whereas ground material was described as ideally imperfect material. The rocking curve width of the best flight material matched the best achieved terrestrially, 9.2 arc-sec, using any growth technique. The dislocation density was reduced from 50-100,000 in the ground samples, to 500-2500 in the flight samples. The low dislocation density completely eliminated the dislocation substructure that is typical of all ground material. The dislocation reduction is thought to have resulted from the near-absence of hydrostatic pressure in μ-g, which allowed the melt to solidify with minimum or no wall content, resulting in very low stress being exerted on the crystal during growth and during post-solidification cooling.

9 -- ACKNOWLEDGMENT

We gratefully acknowledge financial support under NASA Contract NAS8-38147. Furthermore, we acknowledge the following Northrop Grumman personnel: Andre Berghmans, Frank Chin, and Nils Fonneland, who rendered valuable assistance in growing and characterizing the CdZnTe crystals. We also thank Dr. Louis Casagrande for valuable advice on polishing the wafers and Dr. Donald DiMarzio for assistance in making x-ray measurements. We also would like to acknowledge the technical contributions and generosity of Dr. Michael Dudley and Dr. Bruce Steiner in conducting synchrotron topography studies.

10 -- REFERENCES

1. J. Miltat and Dudley, Chapter 3 in Applications of Synchrotron Radiation, C. R. A. Catlow and G. N. Greaves (eds.), Blackie and Son Ltd, Glasgow, UK, 65-99 (1990).
2. J. J. Kennedy, P. Amirtharaj, Boyd, Qadri, R. C. Dobbyn, and G. Long, *J. Crystal Growth*, v. 86, 93 (1988).
3. D. E. Aspnes, *Surf. Sci.*, v. 37, 418 (1973).
4. F. H. Pollak and H. Shen, *J. Electronic Materials*, v.19 (5), 399 (1990).
5. L. G. Casagrande, D. DiMarzio, M. B. Lee, D. J. Larson, Jr., M. Dudley, and T. Fanning, *J. Crystal Growth*, v. 128, 576 (1993).
6. C. Parfeniuk, F. Weinberg, I. V. Samarasekera, C. Schvezov, and L. Li, *J. Crystal Growth*, v. 119, 261 (1992).
7. J. I. D. Alexander, "Orbital Processing of High-Quality CdTe Compound Semiconductors: Numerical Modelling and Acceleration Data Analysis," Final Report on Contract Number PO 21-69118, CMMR, University of Alabama at Huntsville, March 1994.

FIGURES

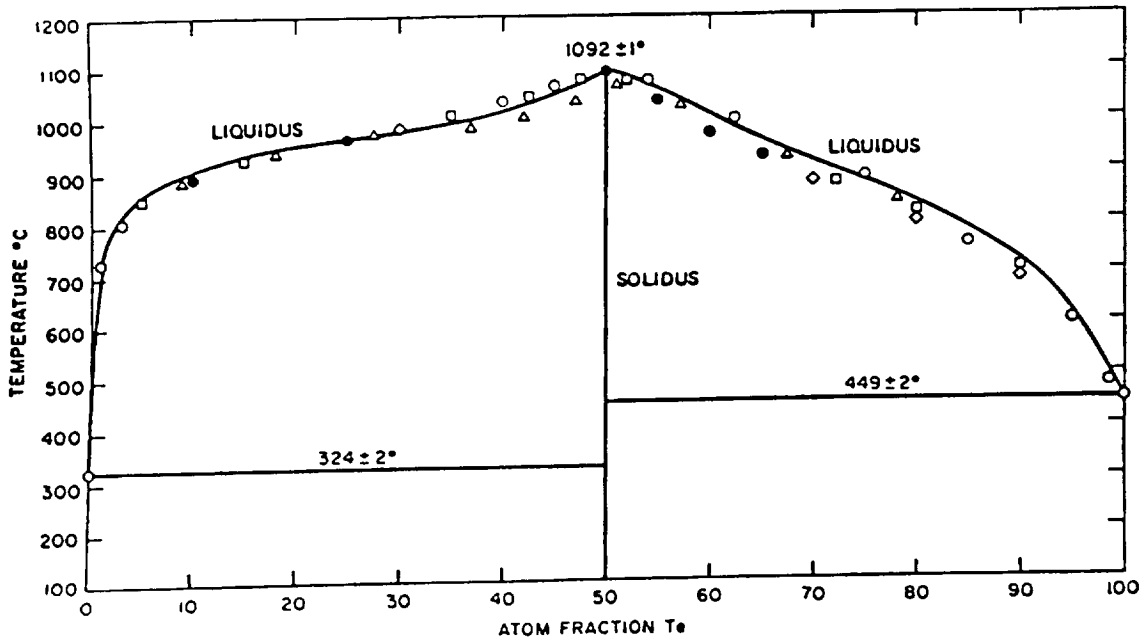

Fig. 1 Cd/Te Phase Diagram

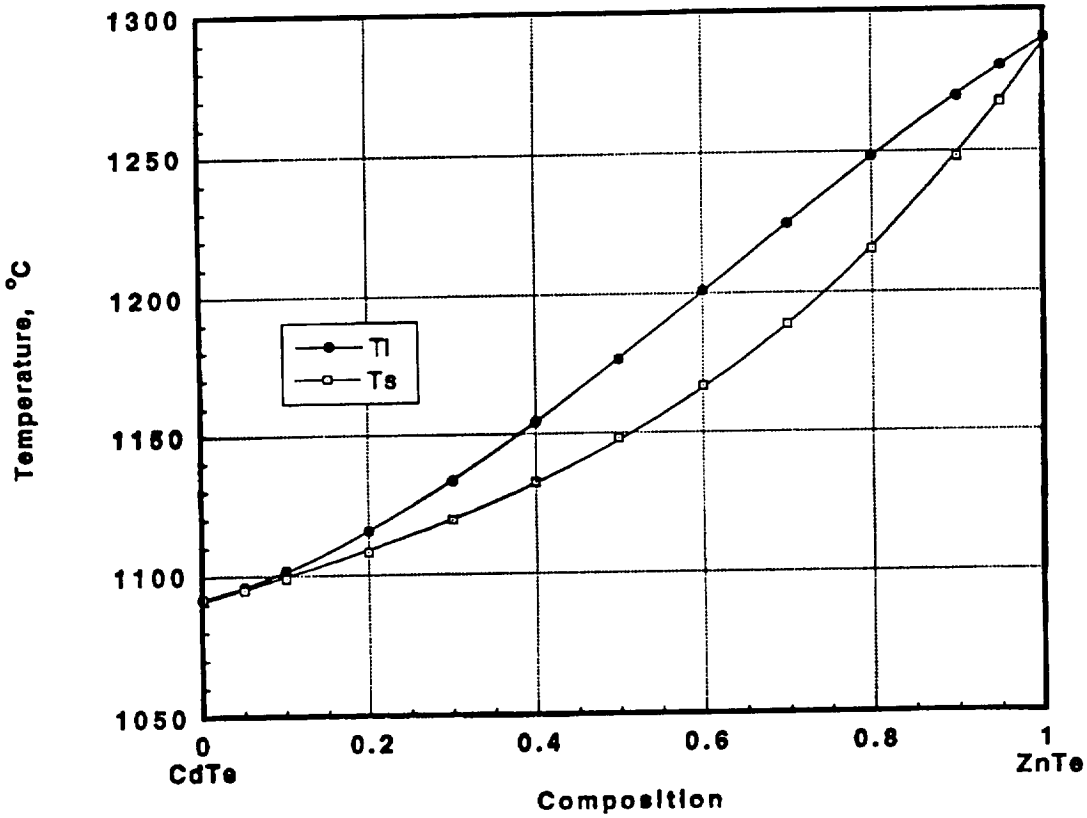

Fig. 2 CdTe/ZnTe Phase Diagram

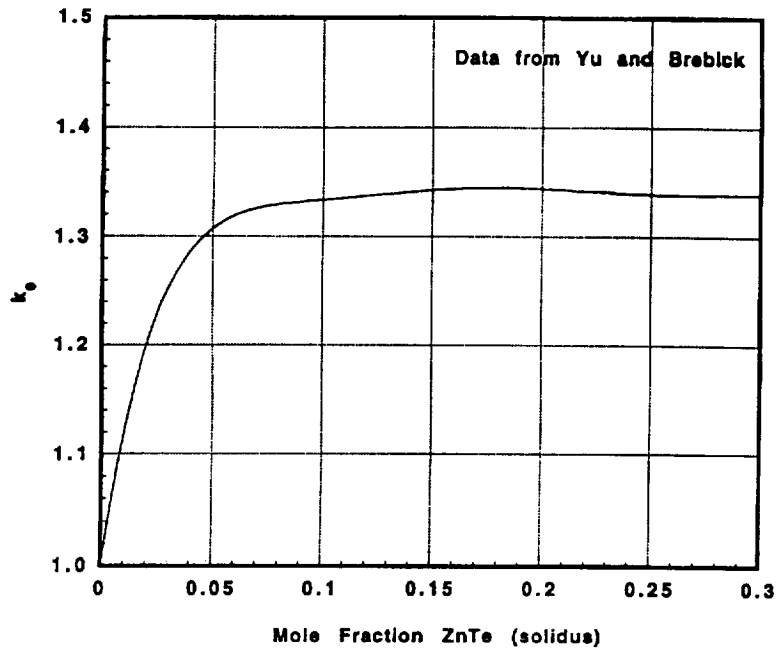

Fig. 3 Zn Redistribution Coefficient (k_o) in CdTe

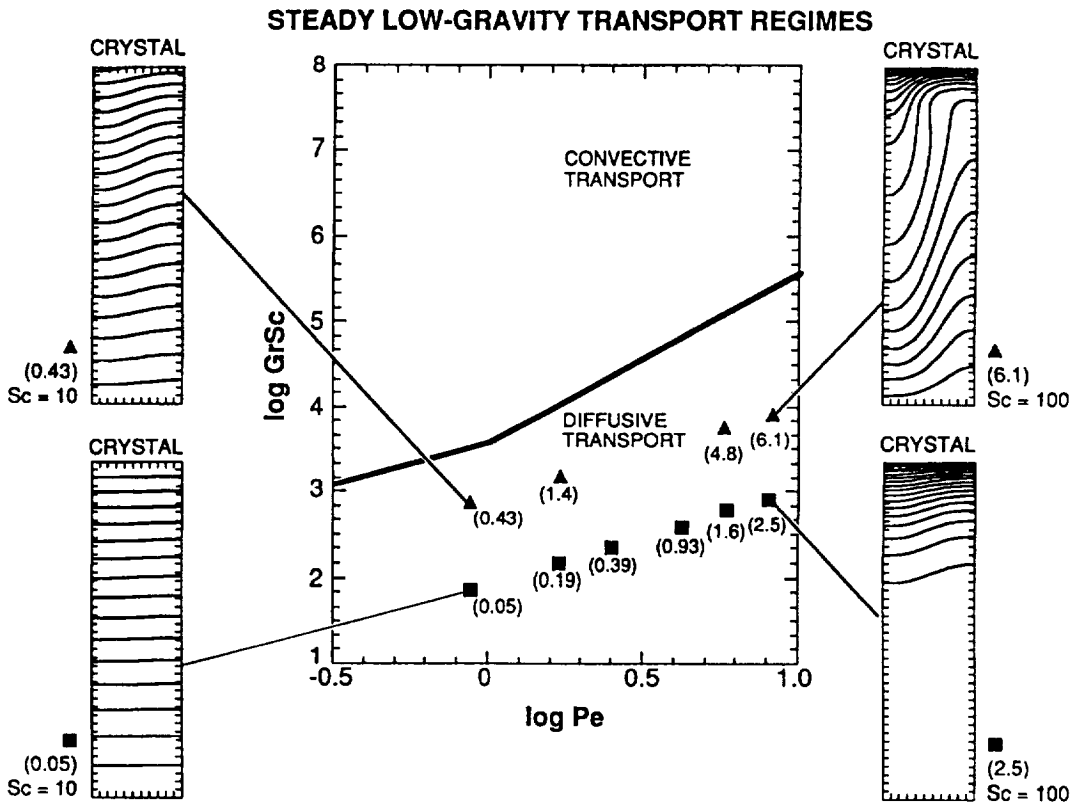

Fig. 4 Scaling Analysis Predicting Diffusion-Controlled Growth (in One-g (Δ) & Micro-g (□)

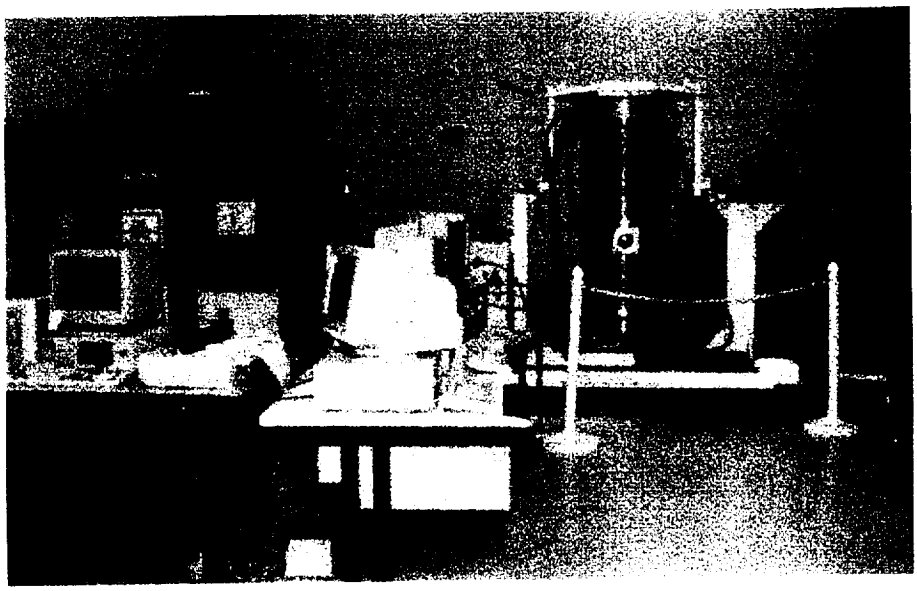

Fig. 5 NASA CGF Ground Control Experiments Laboratory

Fig. 6 NASA USML-1 Integrated CGF Flight Furnace System

Fig. 7 GCRC Programmable Multizone Furnace (PMZF)

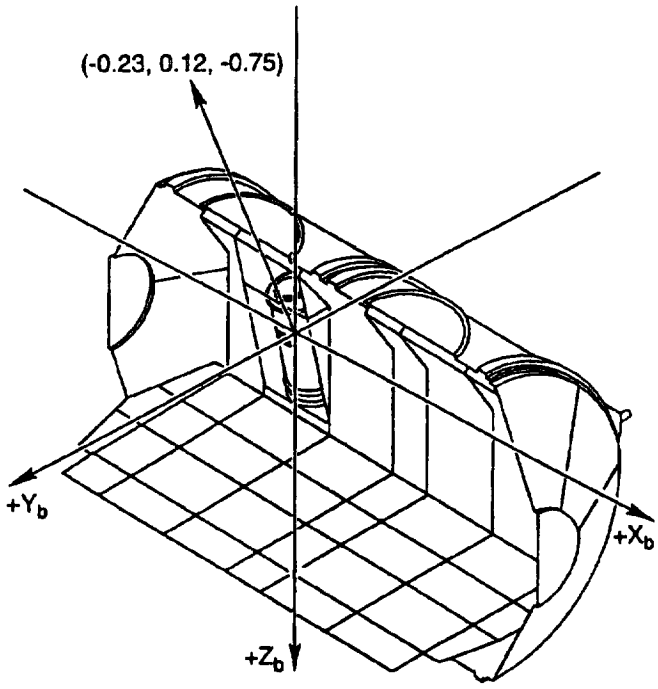

Fig. 8 STS50/USML-1/CGF Attitude & Anticipated Residual g-Vector Without the Flash Evaporator System

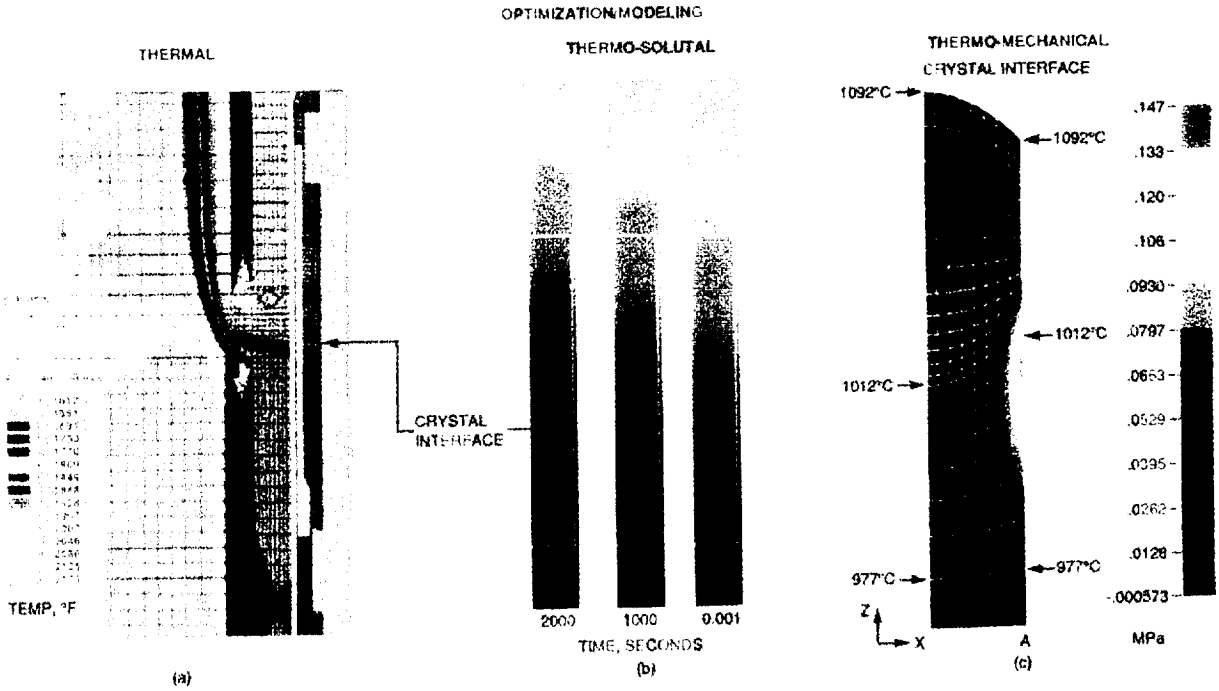

Fig. 9 Typical Process Model Outputs: (a) Thermal, (b) Thermo-solutal, & (c) Thermo-mechanical

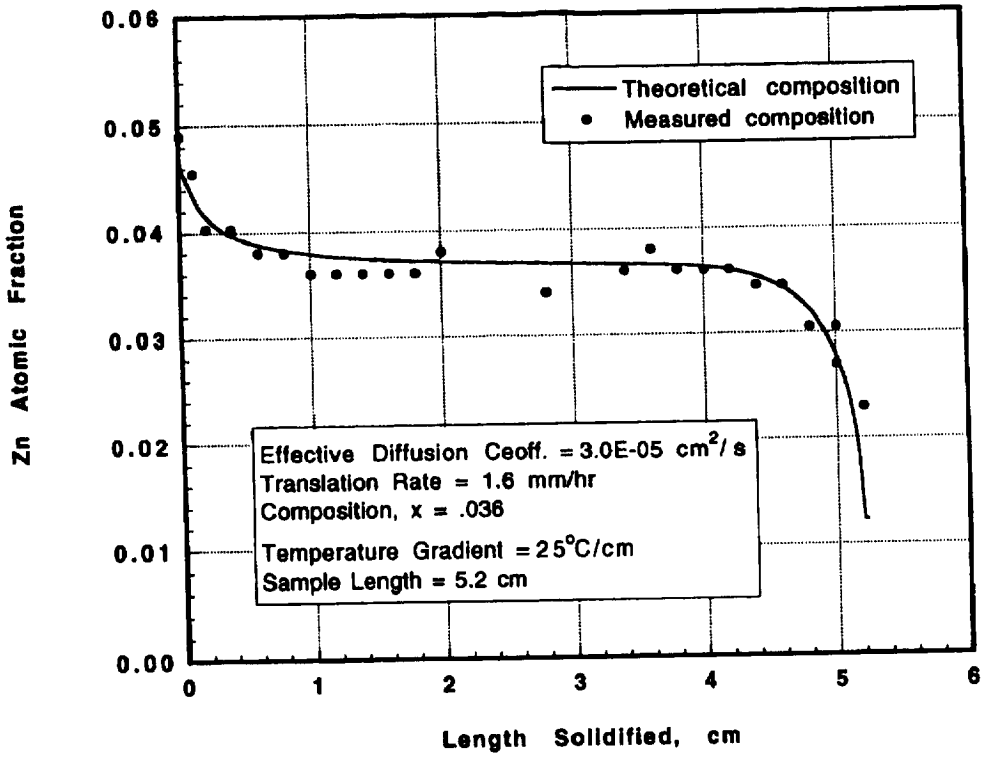

Fig. 10 One-g Best Fit to Longitudinal Macrosegregation

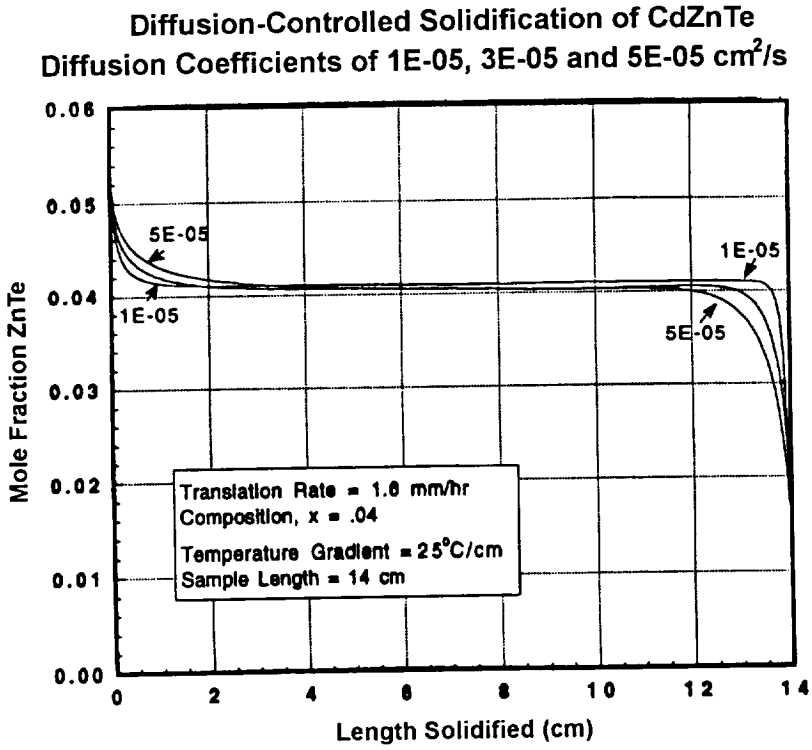

Fig. 11 Diffusion Coefficient Sensitivity Analysis

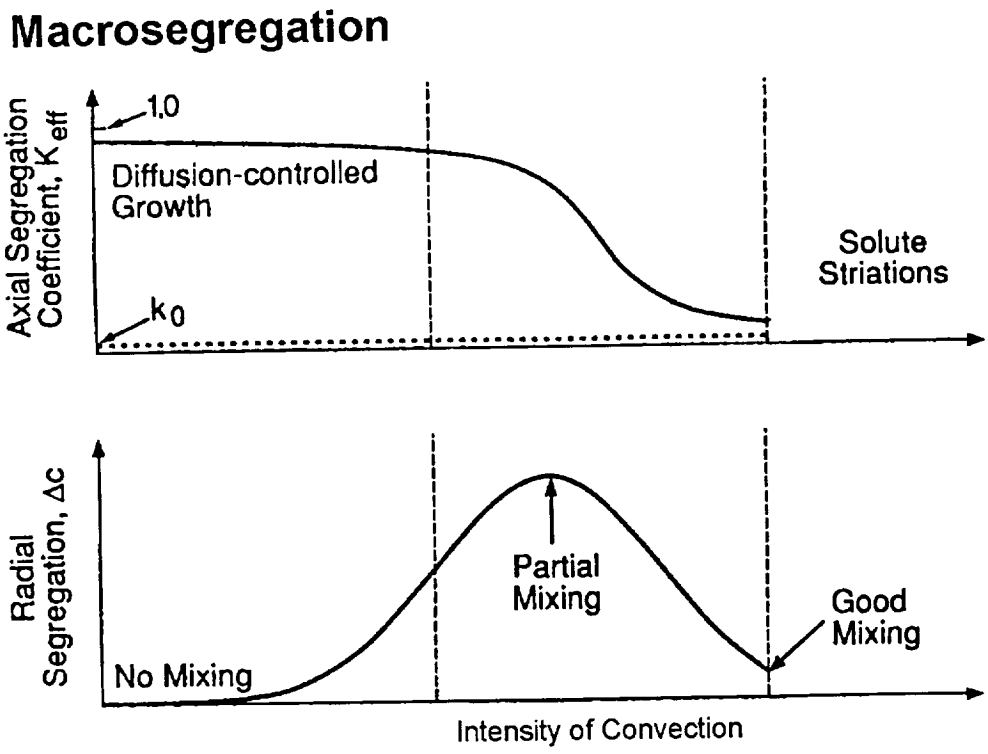

Fig. 12 Longitudinal & Radial Segregation, after Brown et al.

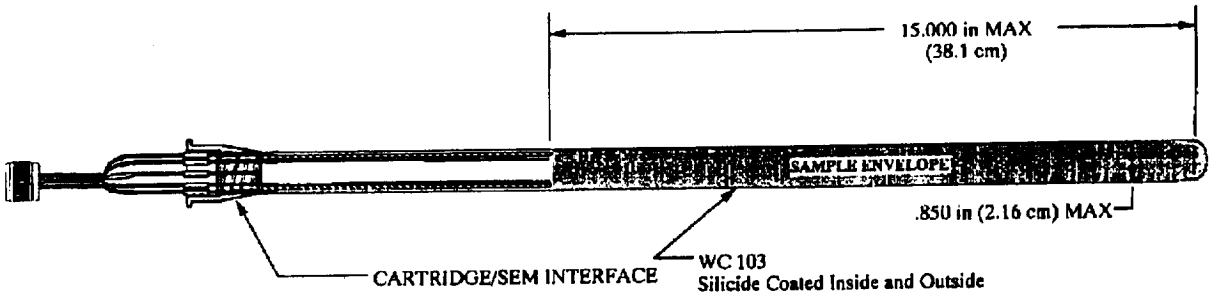

(a)

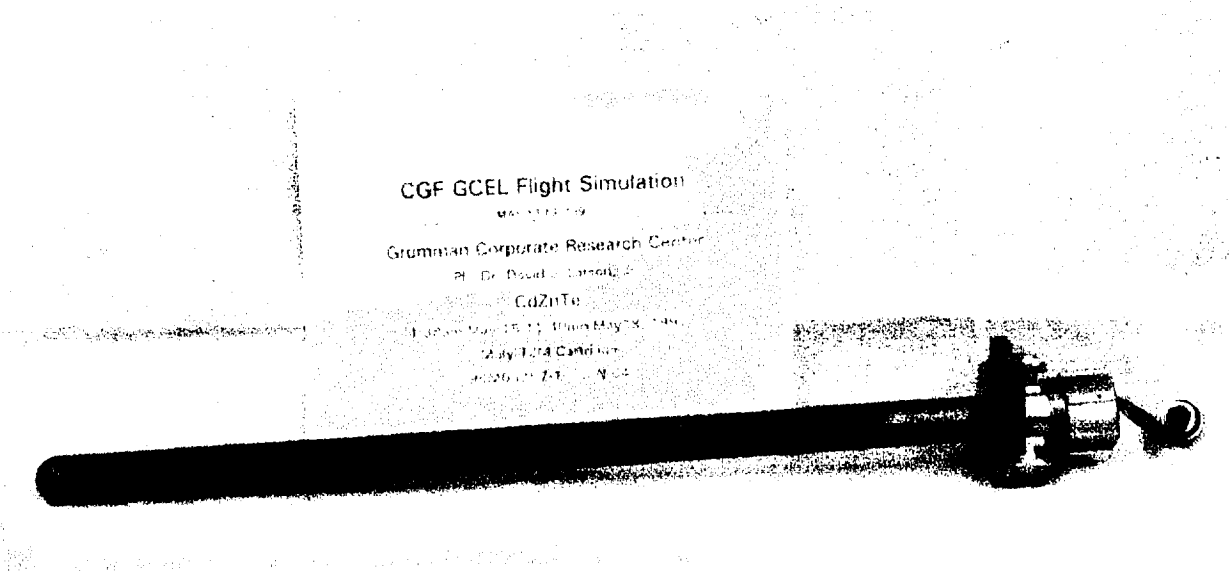

(b)

Fig. 13 (a) Sample Ampoule Cartridge Assembly (SACA) Schematic, (b) SACA, After Flight Simulation Test

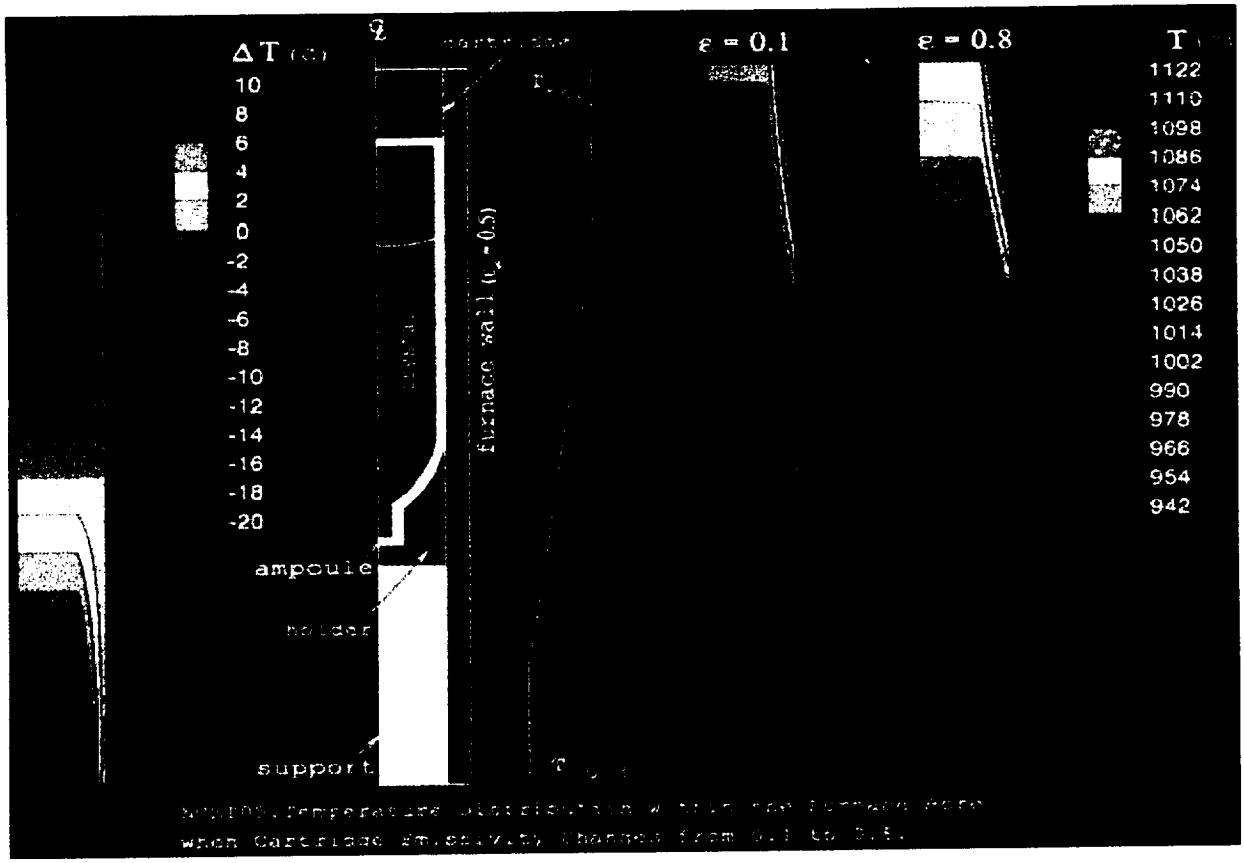

Fig. 14 Predicted Thermal Sensitivity to Emissivity Changes

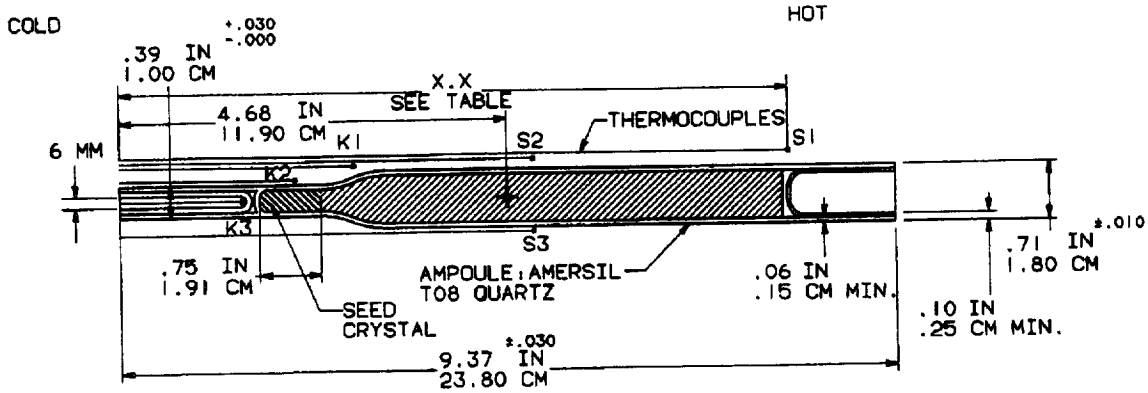

THERMOCOUPLE	X.X
S1	8.07 (205 MM)
S2	5.00 (127 MM)
S3	5.00 (127 MM)
K1	2.83 (72 MM)
K2	2.13 (54 MM)
K3	≤1.50 MAX(38.1 MM) BOTTOMED IN WELL

Fig. 15 Sample, Ampoule & Thermocouples

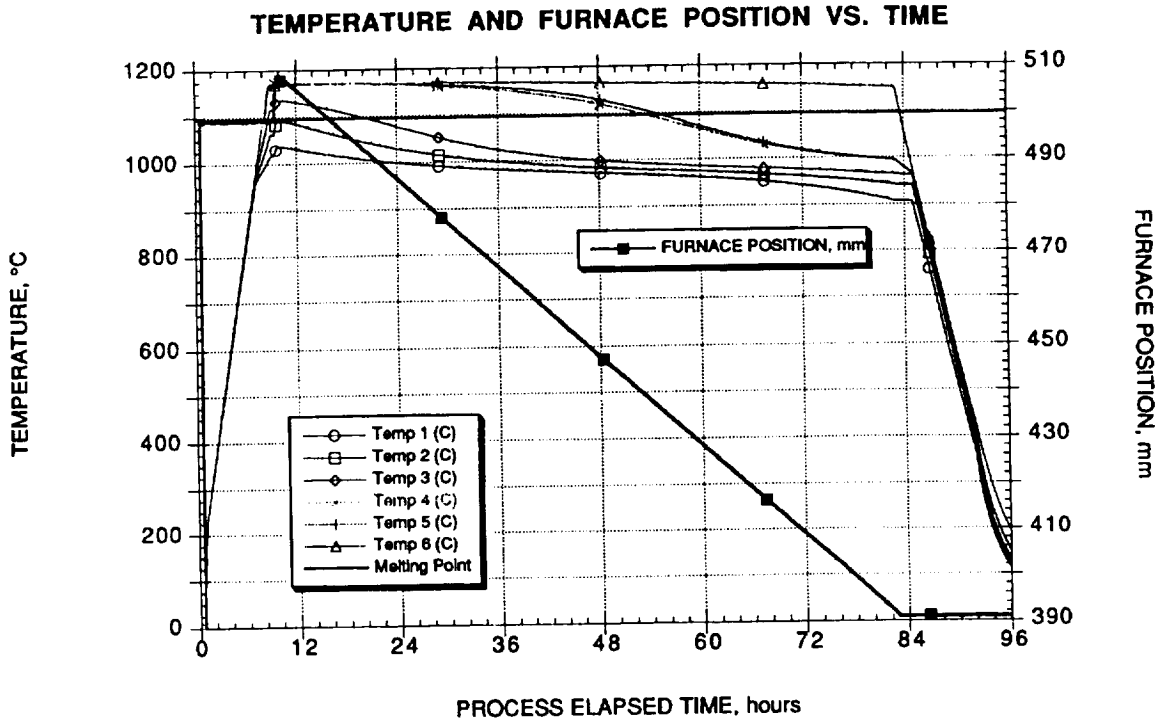

Fig. 16 Temperature/Time History for GCRC-1 (One-g)

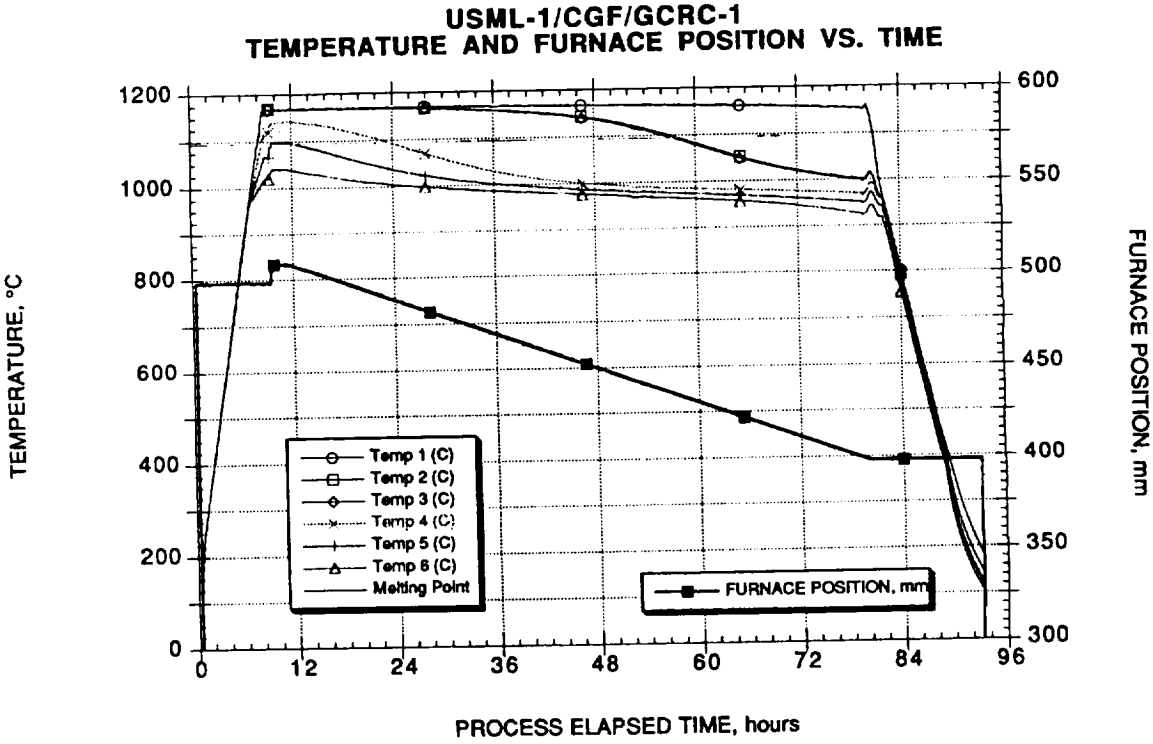

Fig. 17 Temperature/Time History for GCRC-1 (μ-g)

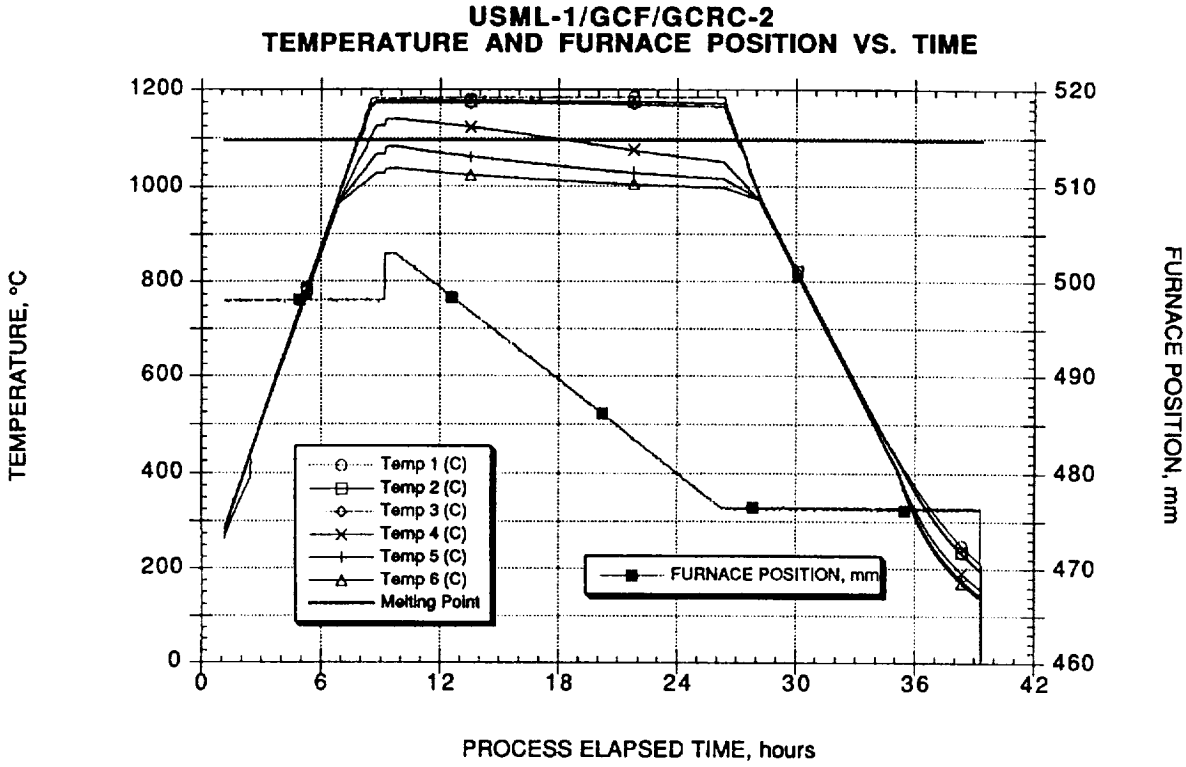

Fig. 18 Temperature/Time History for GCRC-2 (μ-g)

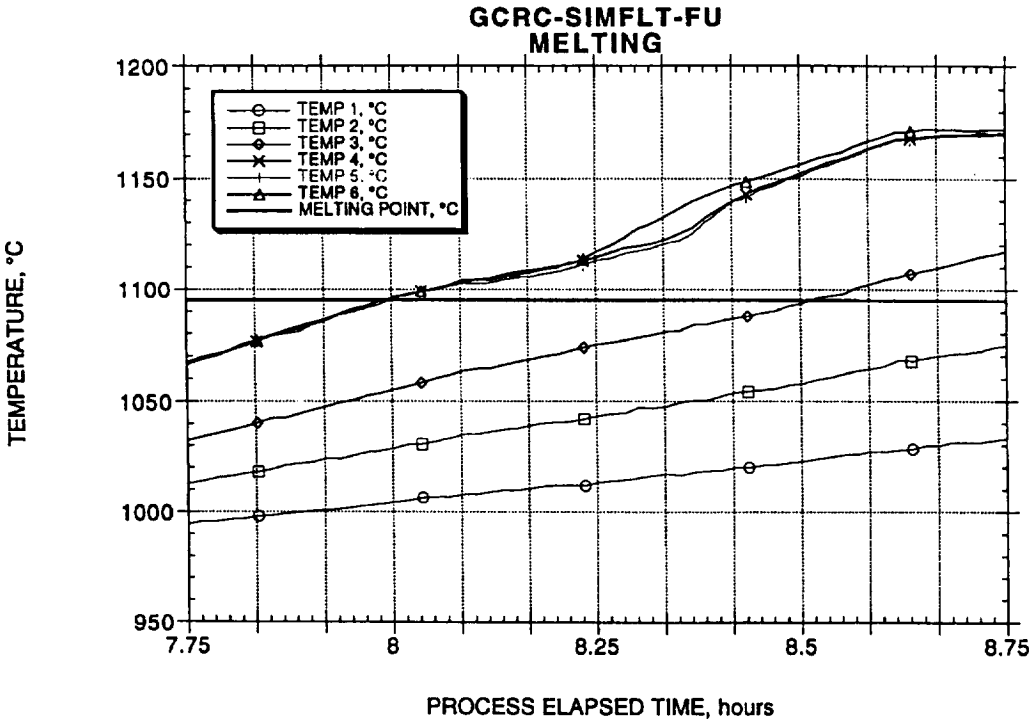

Fig. 19 Thermal Record of Melting in One-g

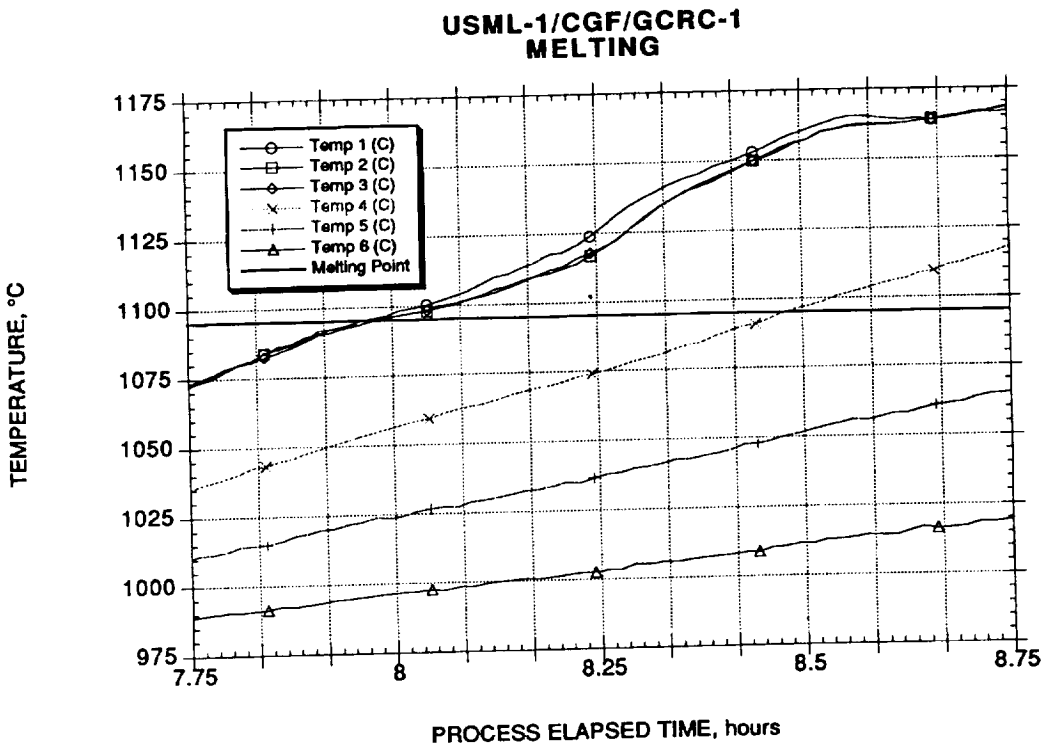

Fig. 20 Thermal Record of Melting in μ-g

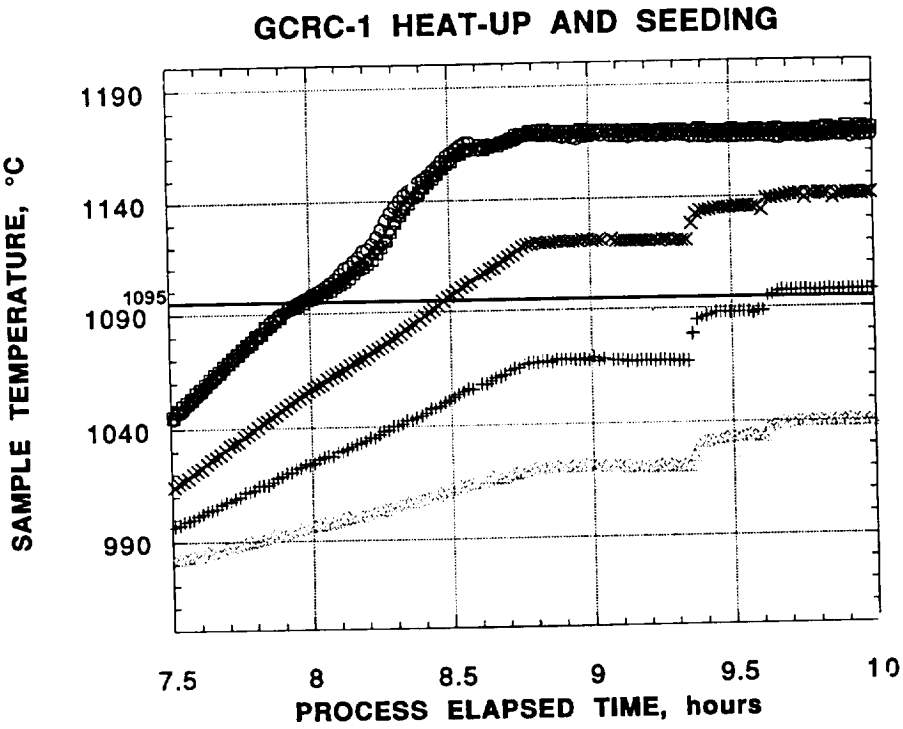

Fig. 21 Internal Melting Point (T_{mp}) Calibration

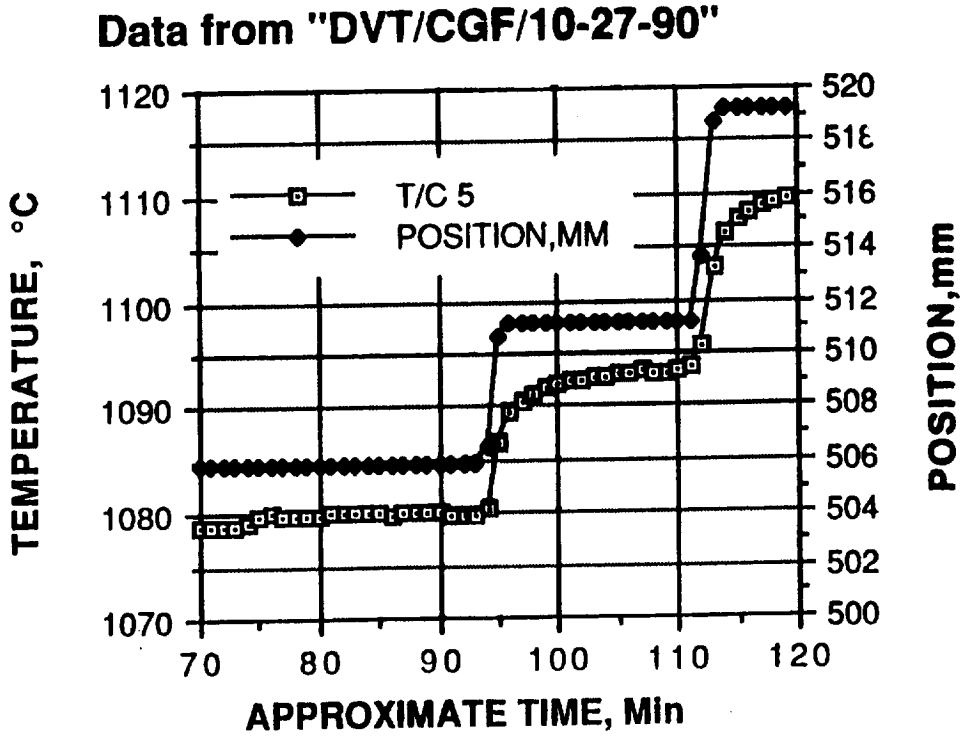

Fig. 22 Translation & Thermal Responses During Seeding

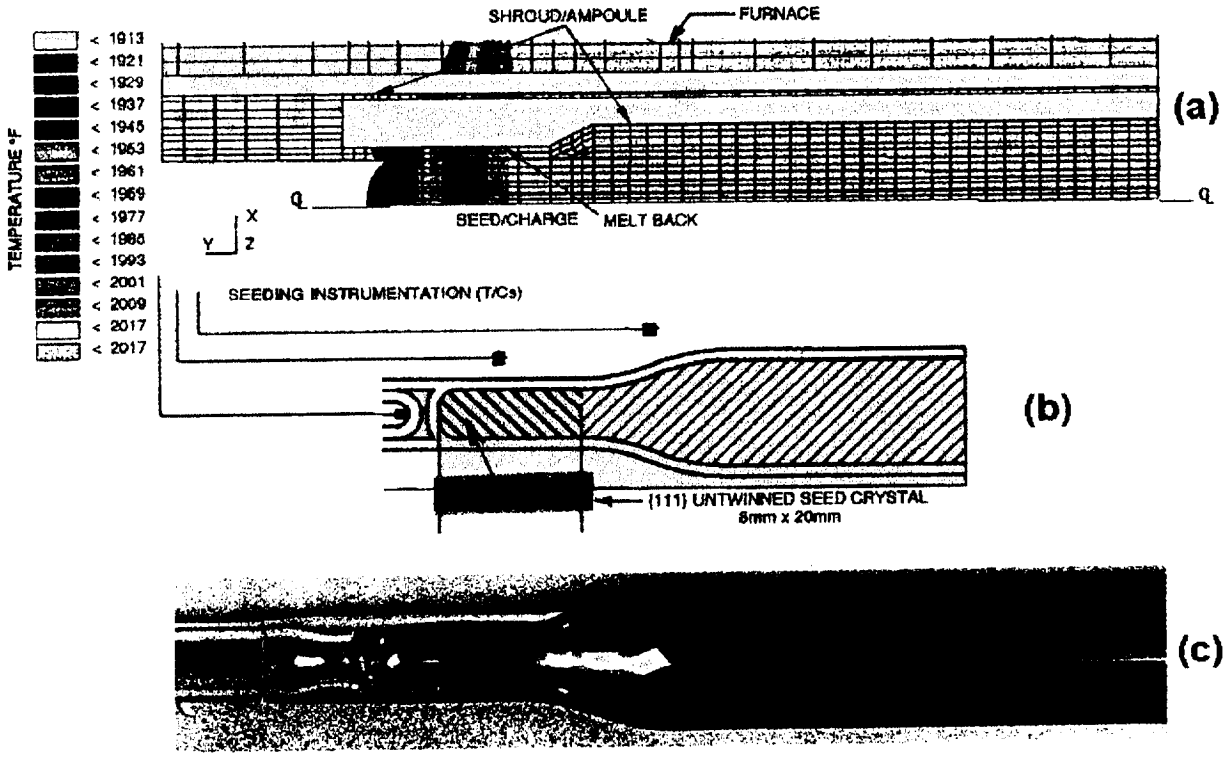

Fig. 23 Seeding/Thermal Model

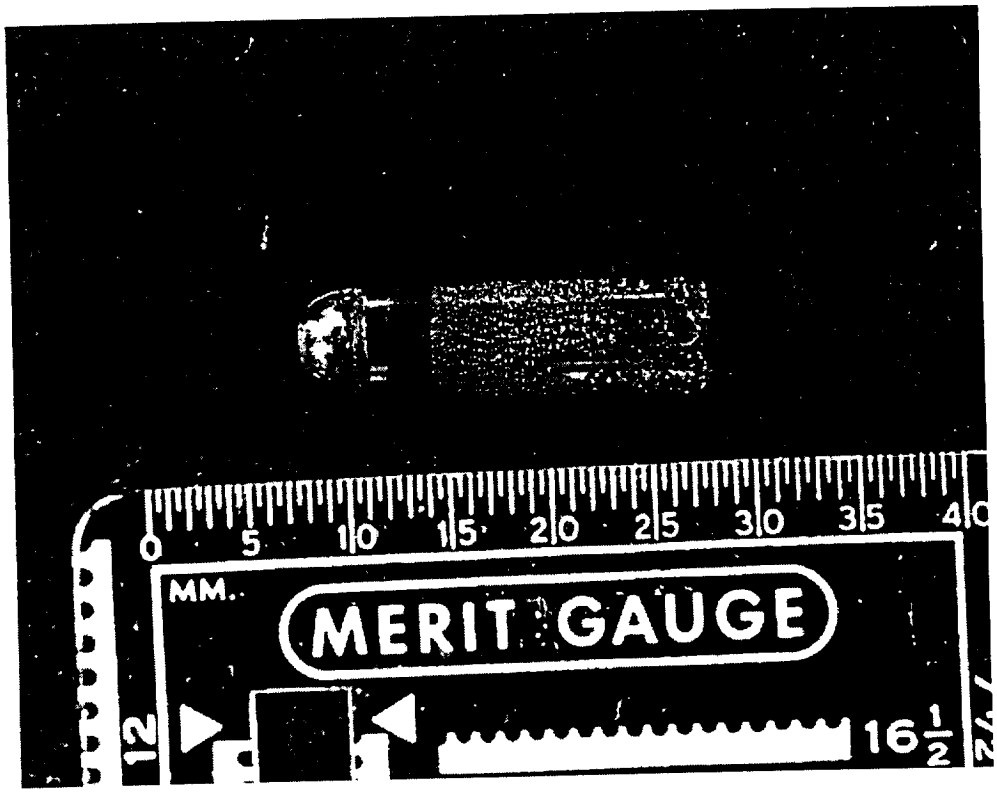

Fig. 24 Macrophotograph of Melt-back Interface on Seed

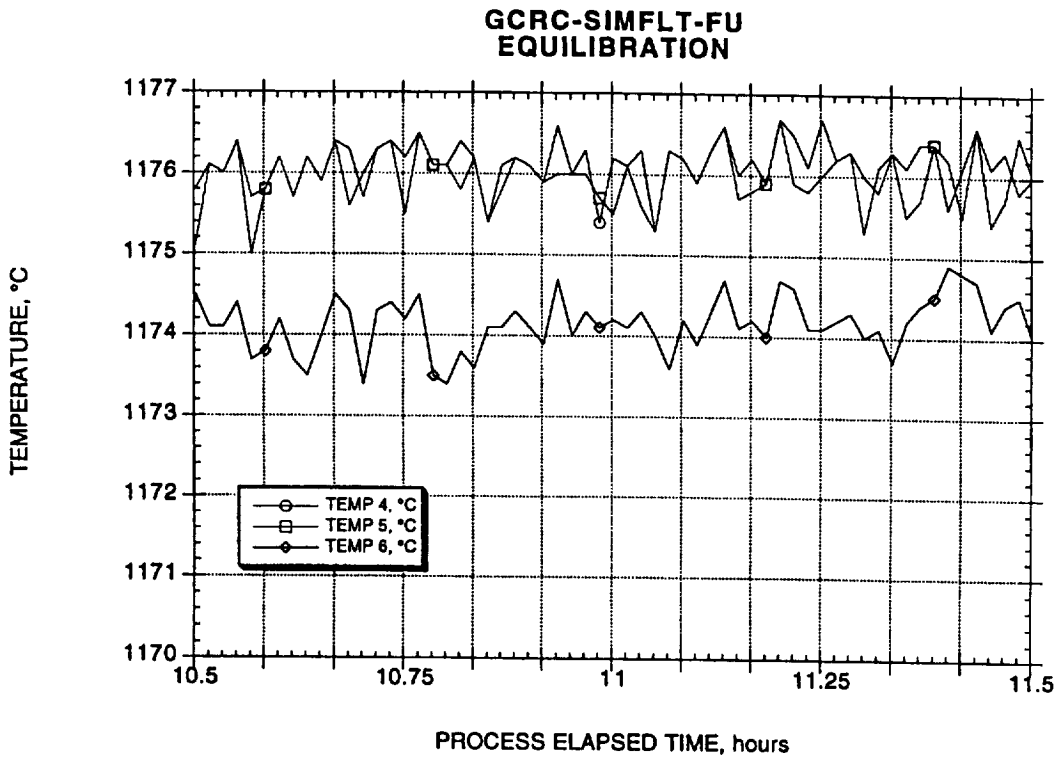

Fig. 25 Typical GCEL Temperature Stability

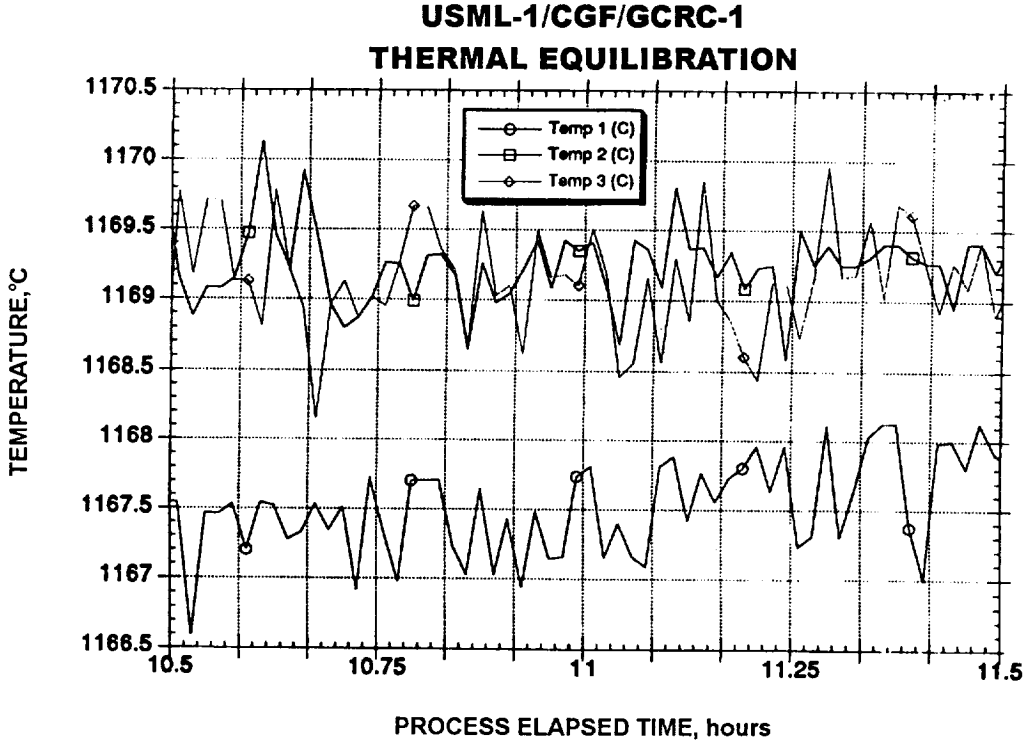

Fig. 26 Typical CGF (GCRC-1) Temperature Stability

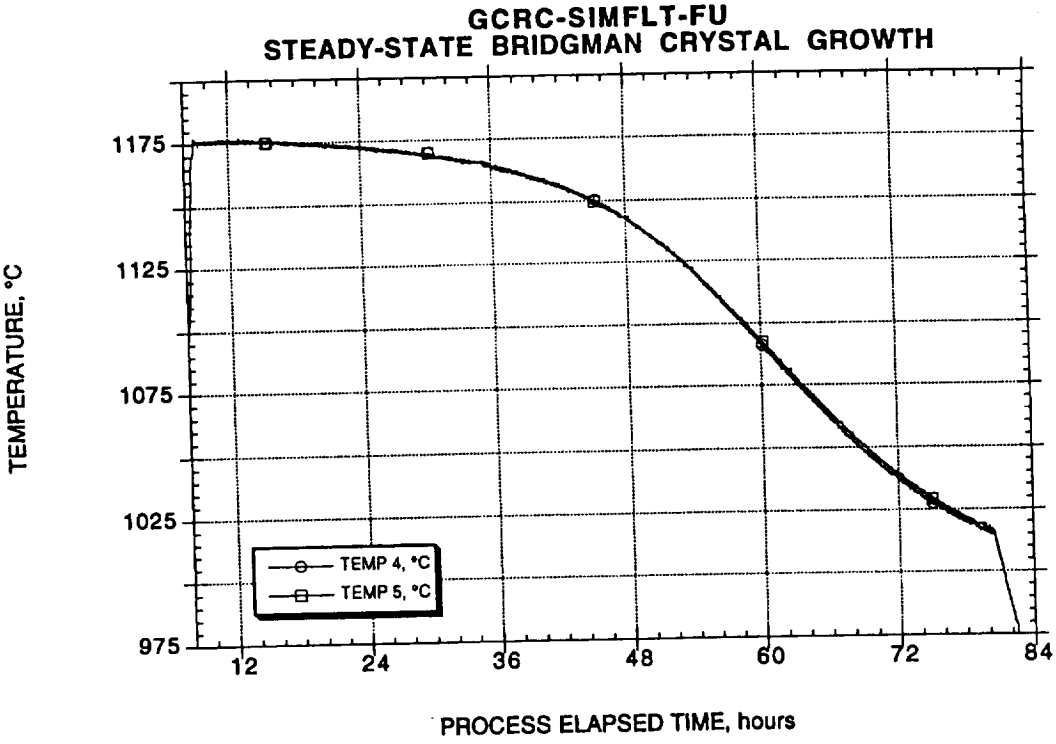

Fig. 27 Ground Truth Steady-State Growth

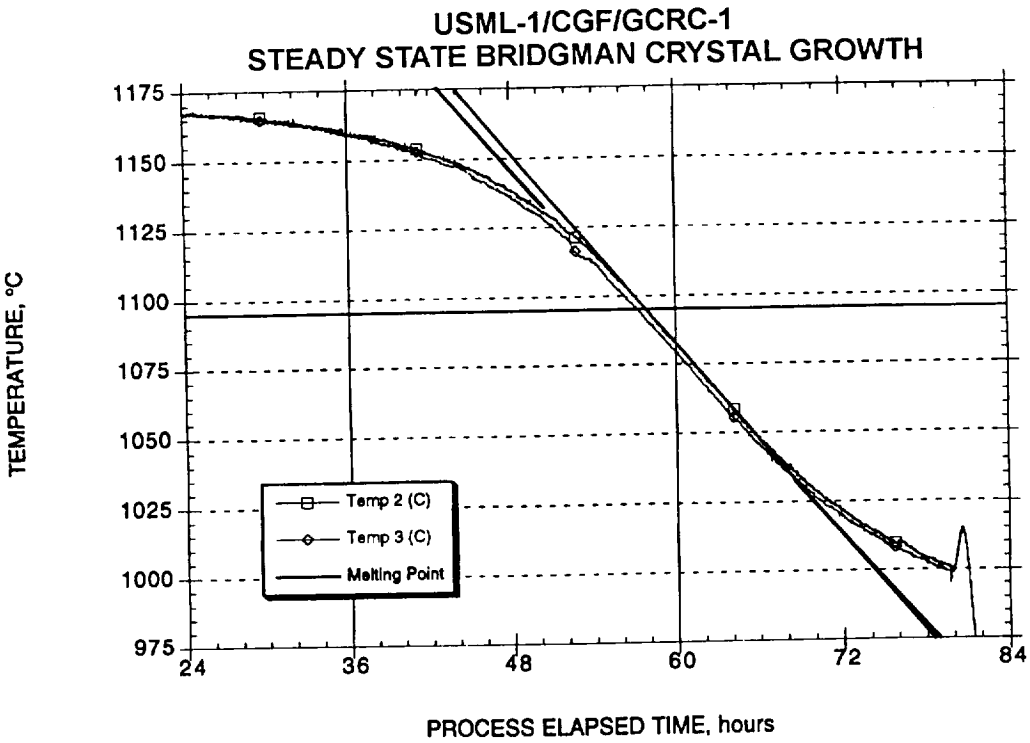

Fig. 28 Flight Sample Steady-State Growth

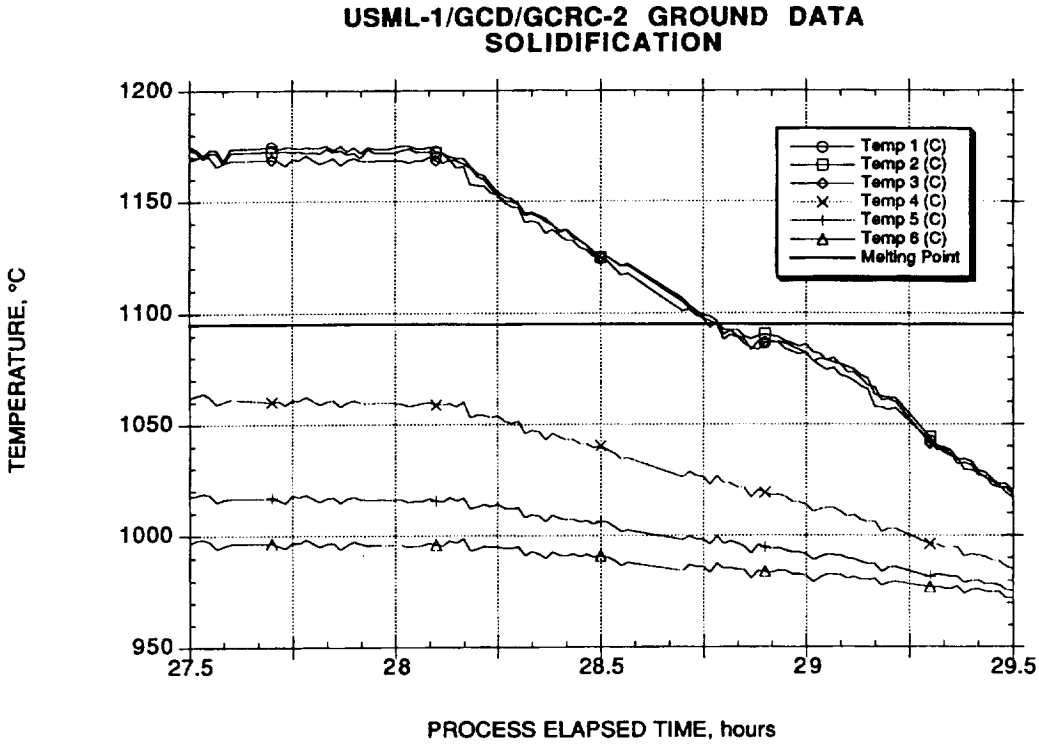

Fig. 29 Ground Truth Sample Cooling History

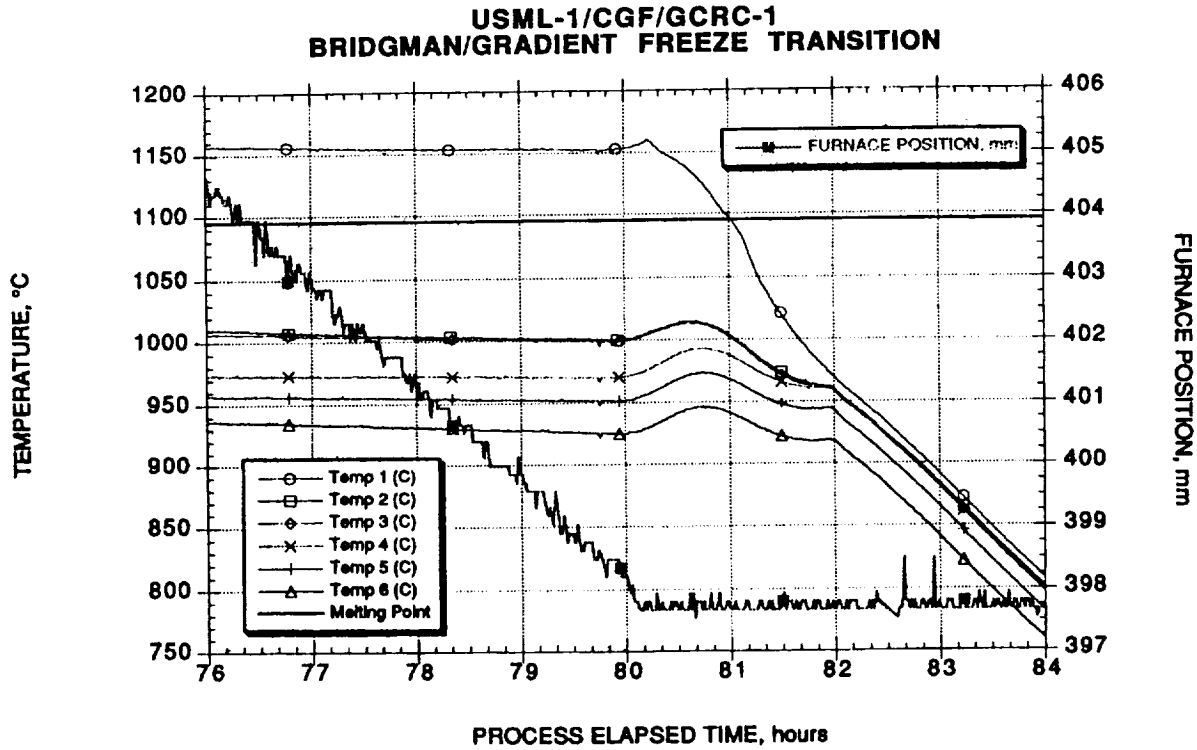

Fig. 30 Flight Sample Cooling History

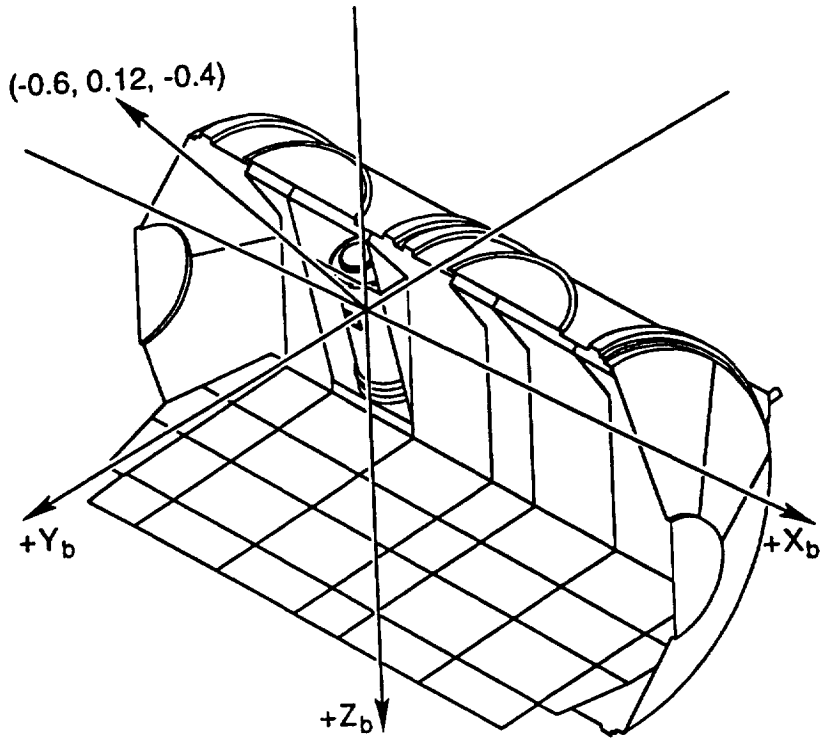

(a)

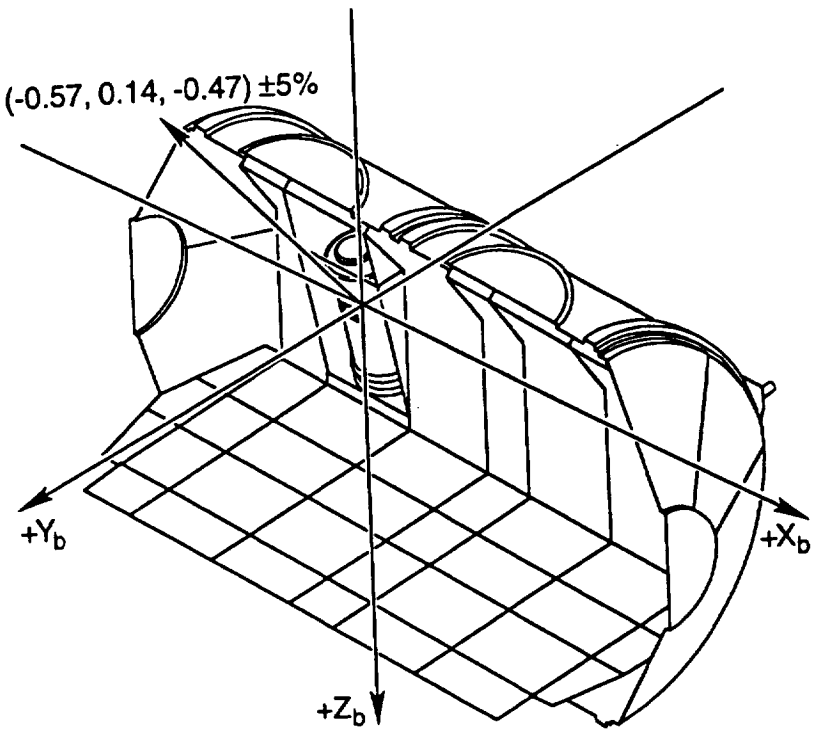

(b)

Fig. 31 Residual g-Vector at CGF, From: (a) OARE & (b) PAS

USML-1/CGF/GCRC-1
FLIGHT SAMPLE

(a)

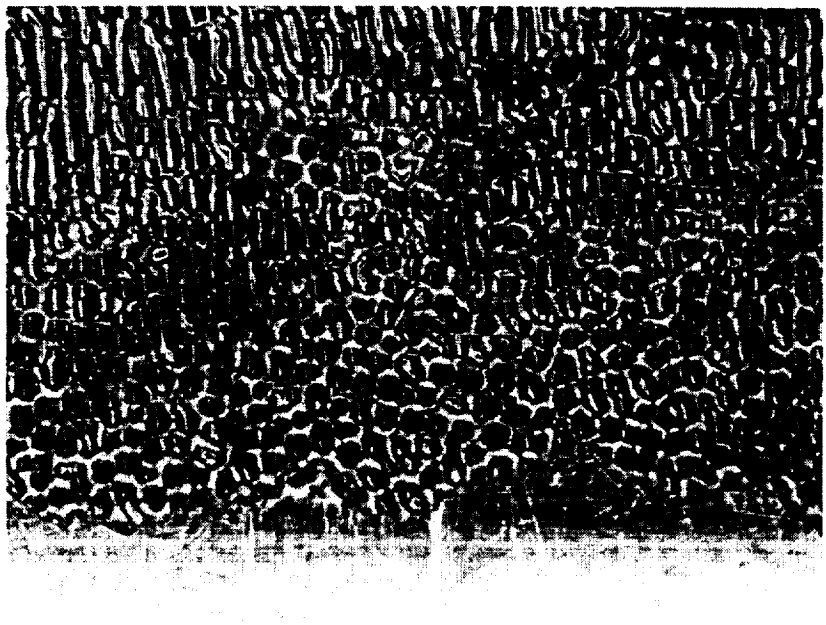

(b)

Fig. 32 (a) Surface Morphologies Showing Variations in Wall Contact;
(b) Enlargement of Partial Wall Contact Region

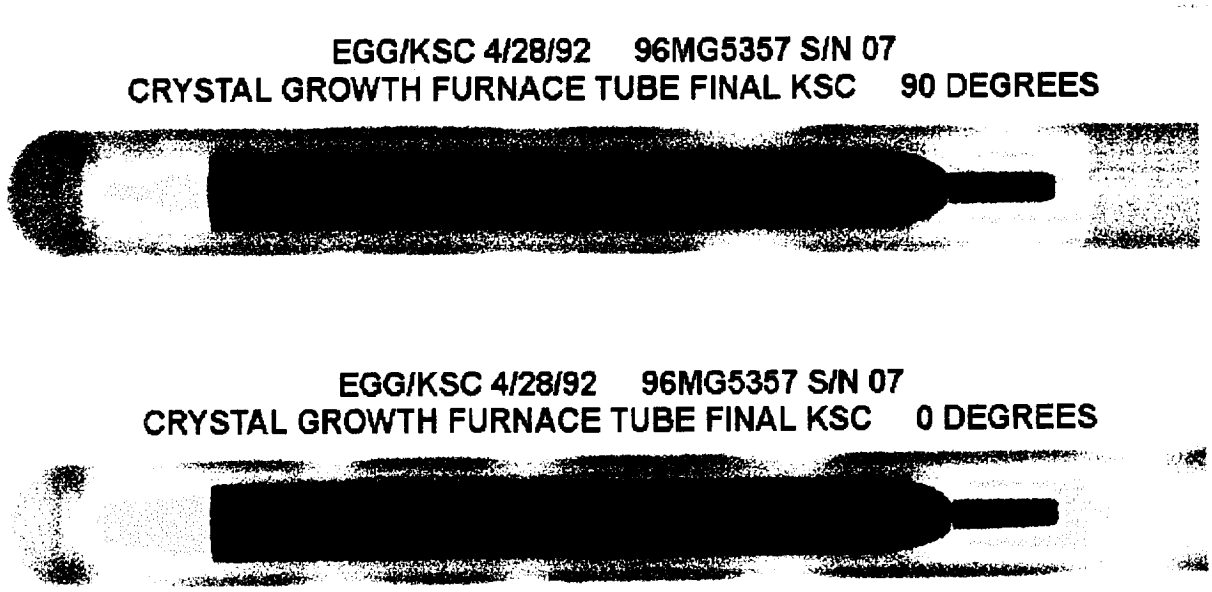

Fig. 33 Preflight Radiographs of the Flight Sample/Ampoules

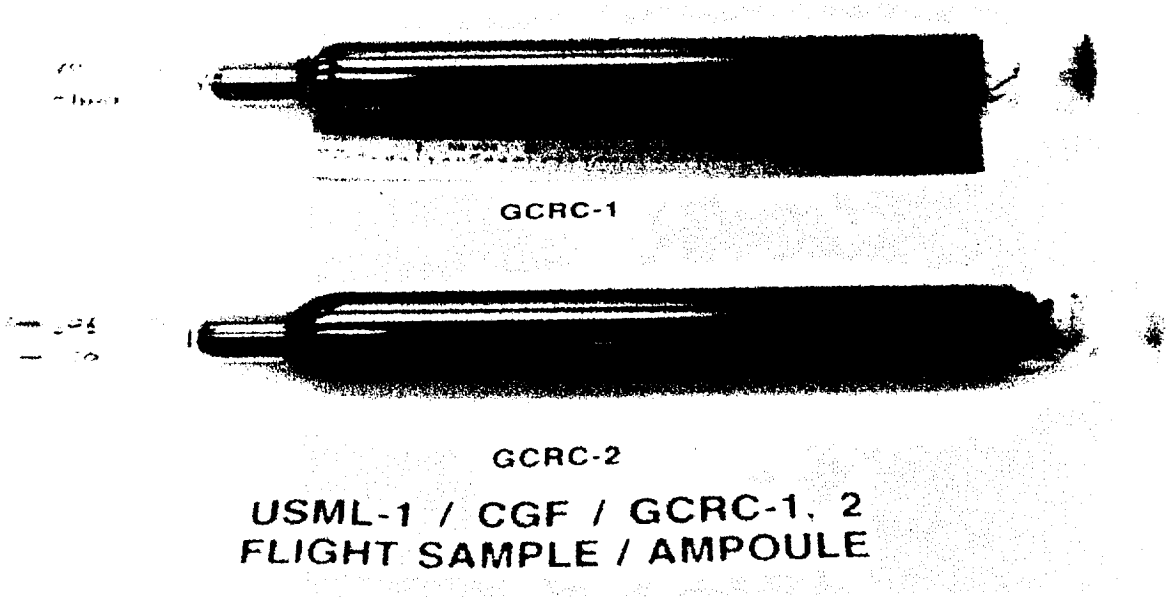

Fig. 34 Postflight Sample Ampoules

Fig. 35 Postflight Radiographs of the Flight Sample/Ampoules

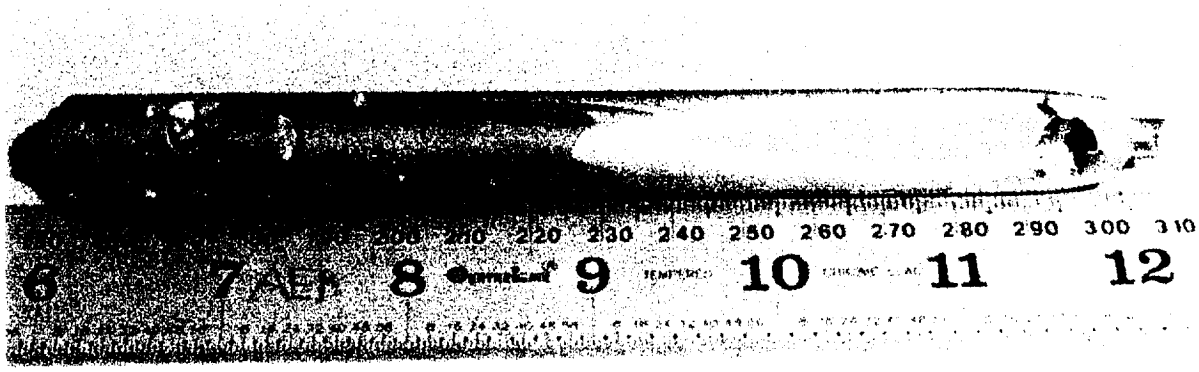

Fig. 36 GCRC-1 Boule Surface Morphology

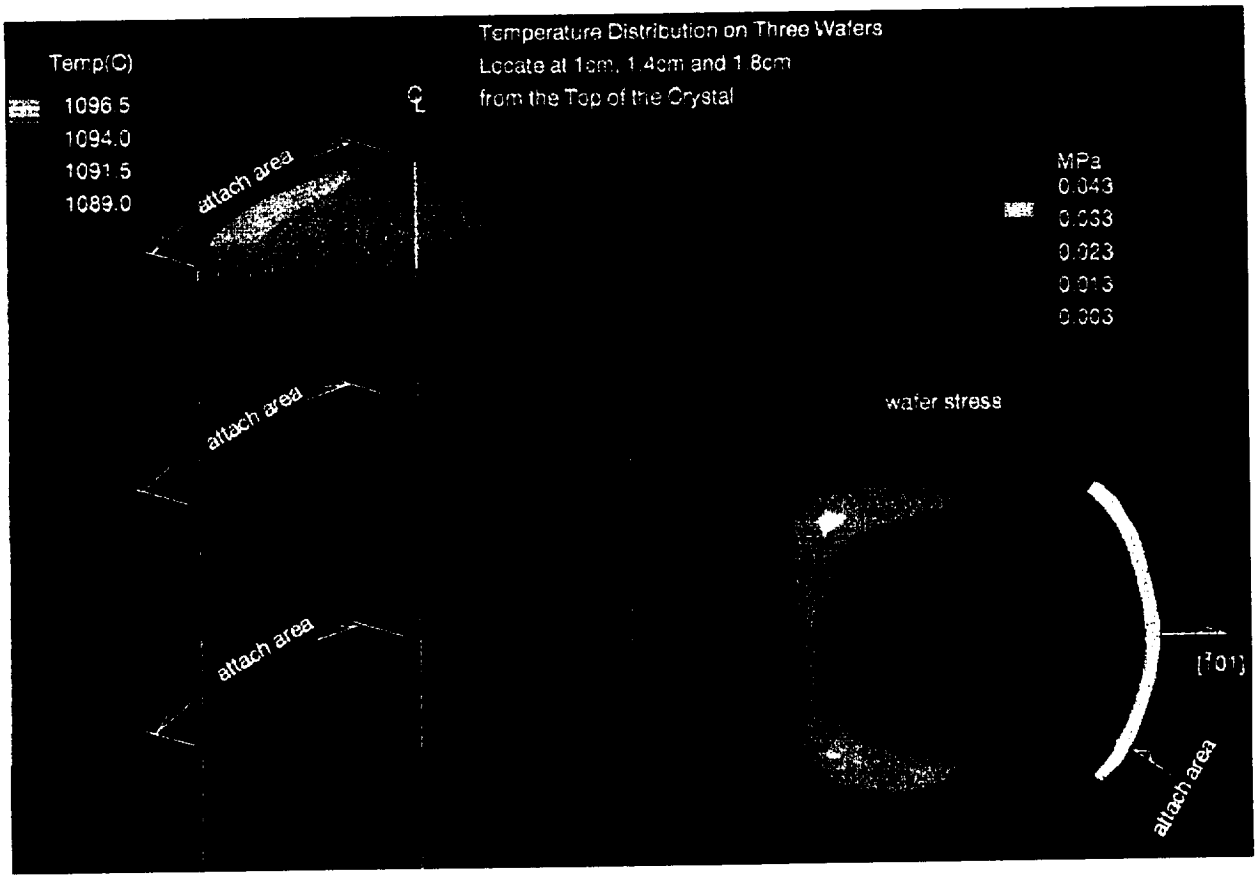

Fig. 37 Thermal Model of Asymmetric Thermal Distribution

Fig. 38 Free Surface Topograph of Flight Sample GCRC-1

Fig. 39 Partial Wall Contact Surface Topograph of Flight Sample

GCRCF2 µg Sample

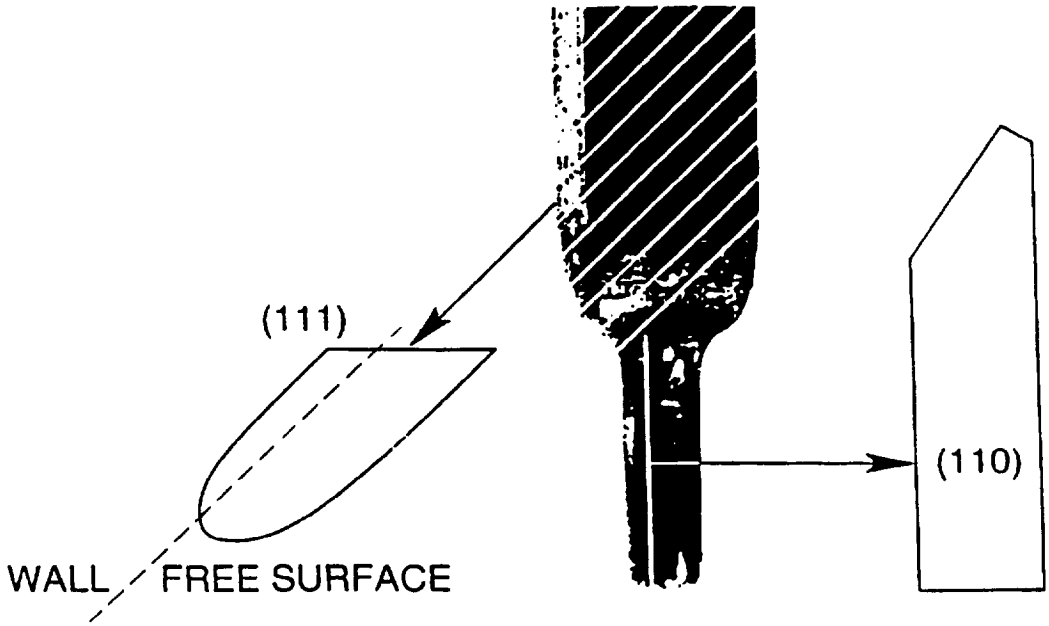

Fig. 40 GCRC-2 Wafering Schematic

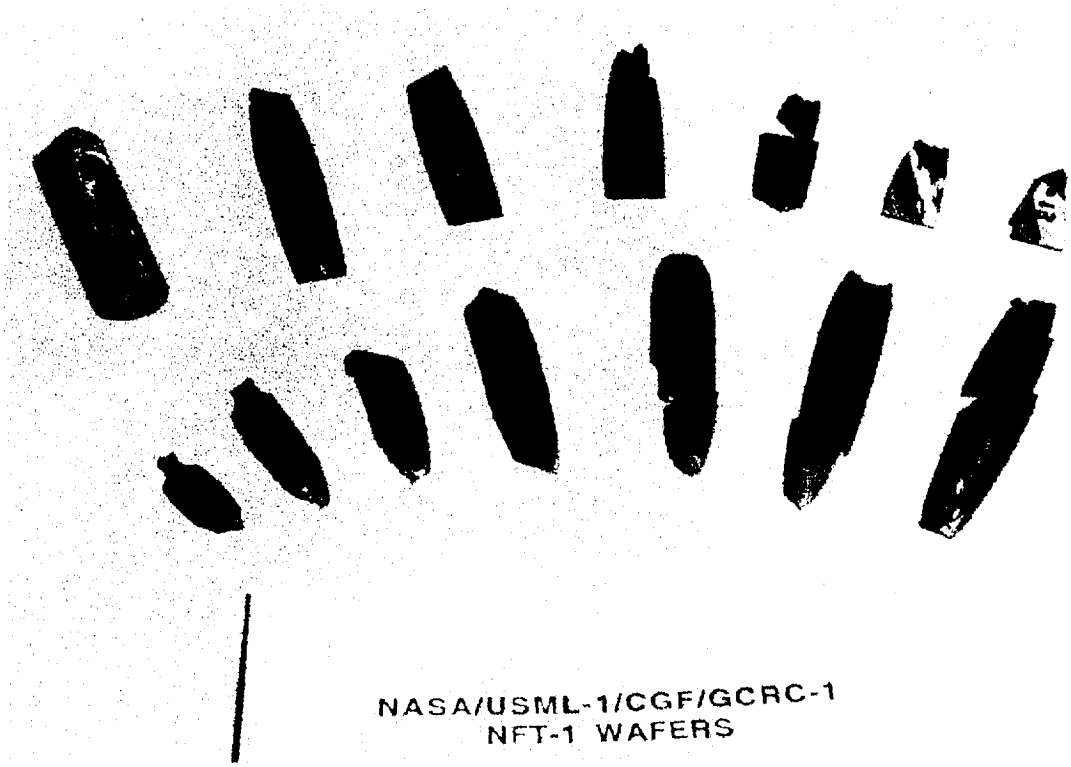

Fig. 41 Photograph of GCRC-1 {111} Wafers

Fig. 42 Photograph of GCRC-2 {111} Wafers

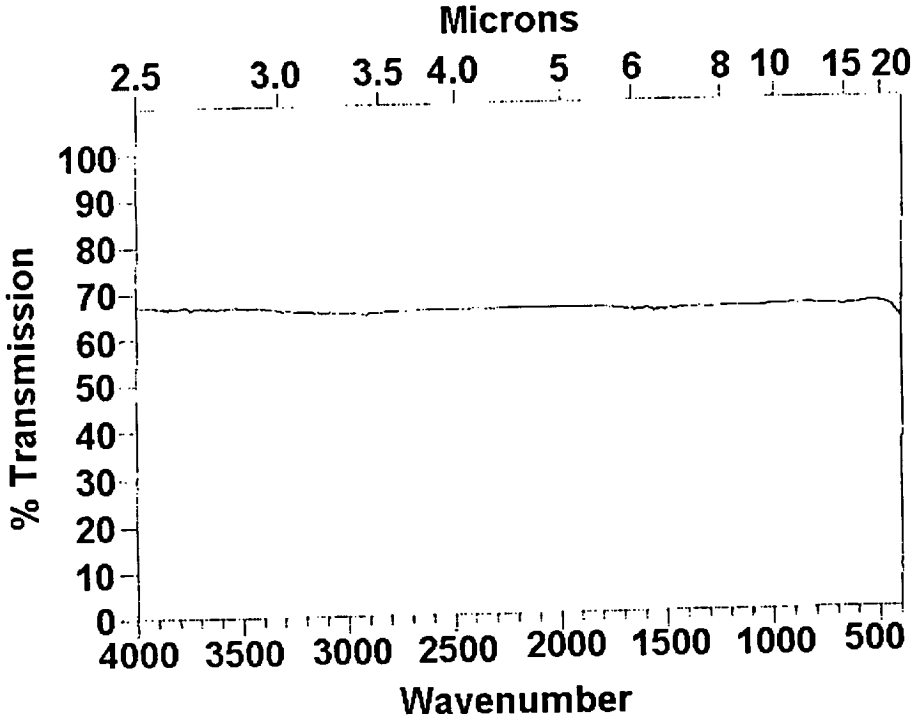

Fig. 43 Typical FTIR Transmission Spectrum

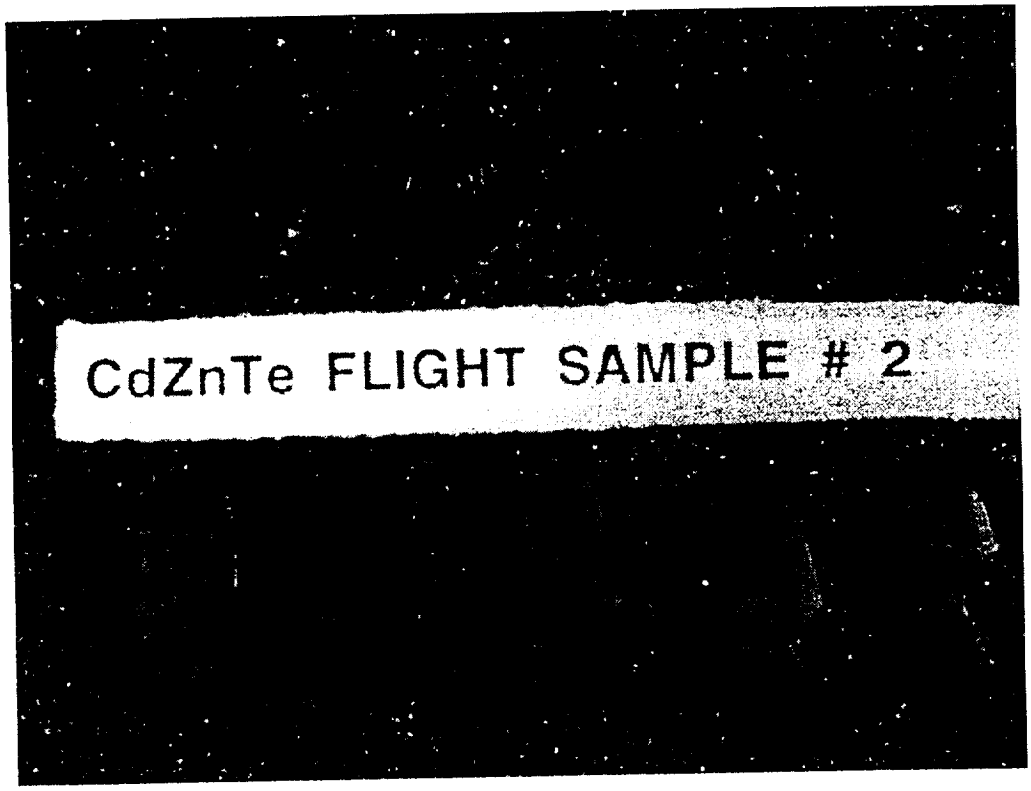

Fig. 44 GCRC-2 Etched Wafers Showing Rotational Twin

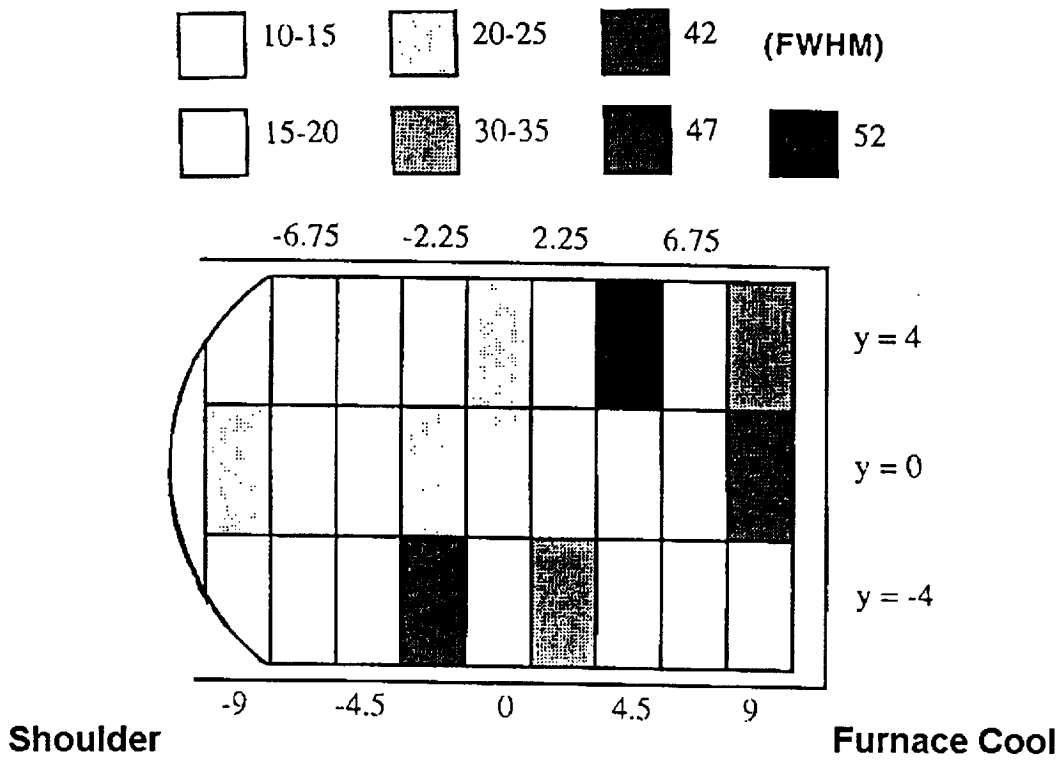

Fig. 45 GCRC-2 Wafer 7 DCRC Map

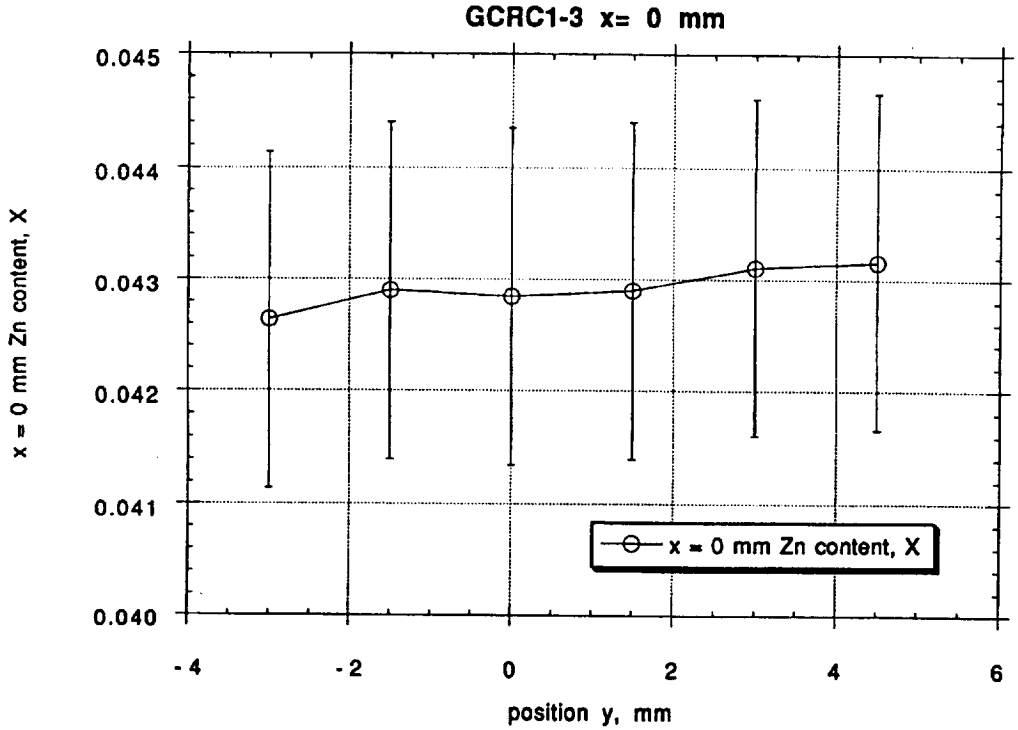

Fig. 46 GCRC-1 Wafer 3 Radial Segregation

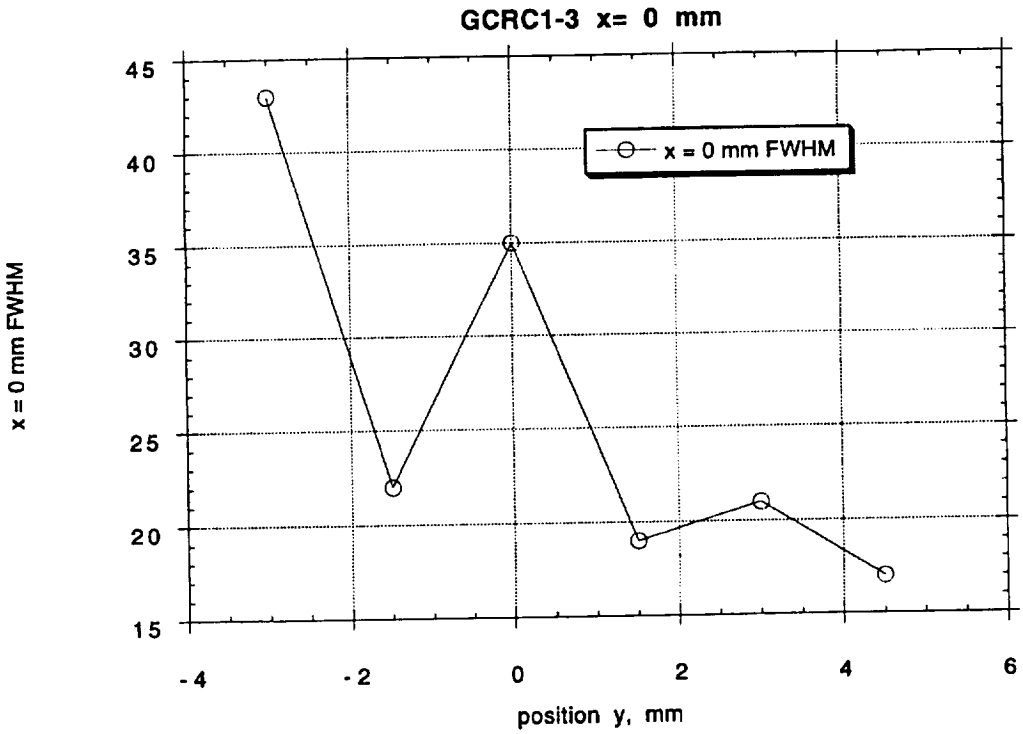

Fig. 47 GCRC-1 Wafer 3 Radial Residual Strain Map

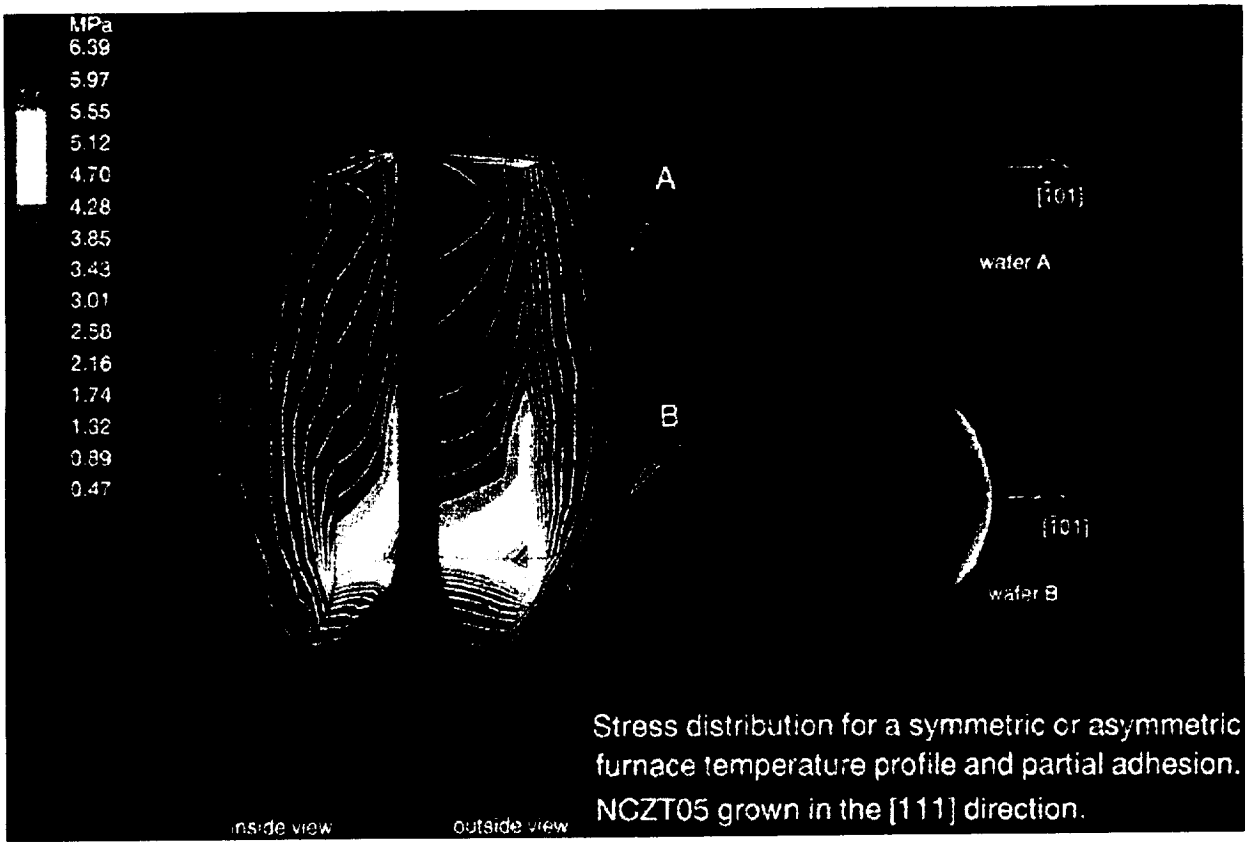

Fig. 48 Stress Distribution for Flight Sample with Partial Adhesion

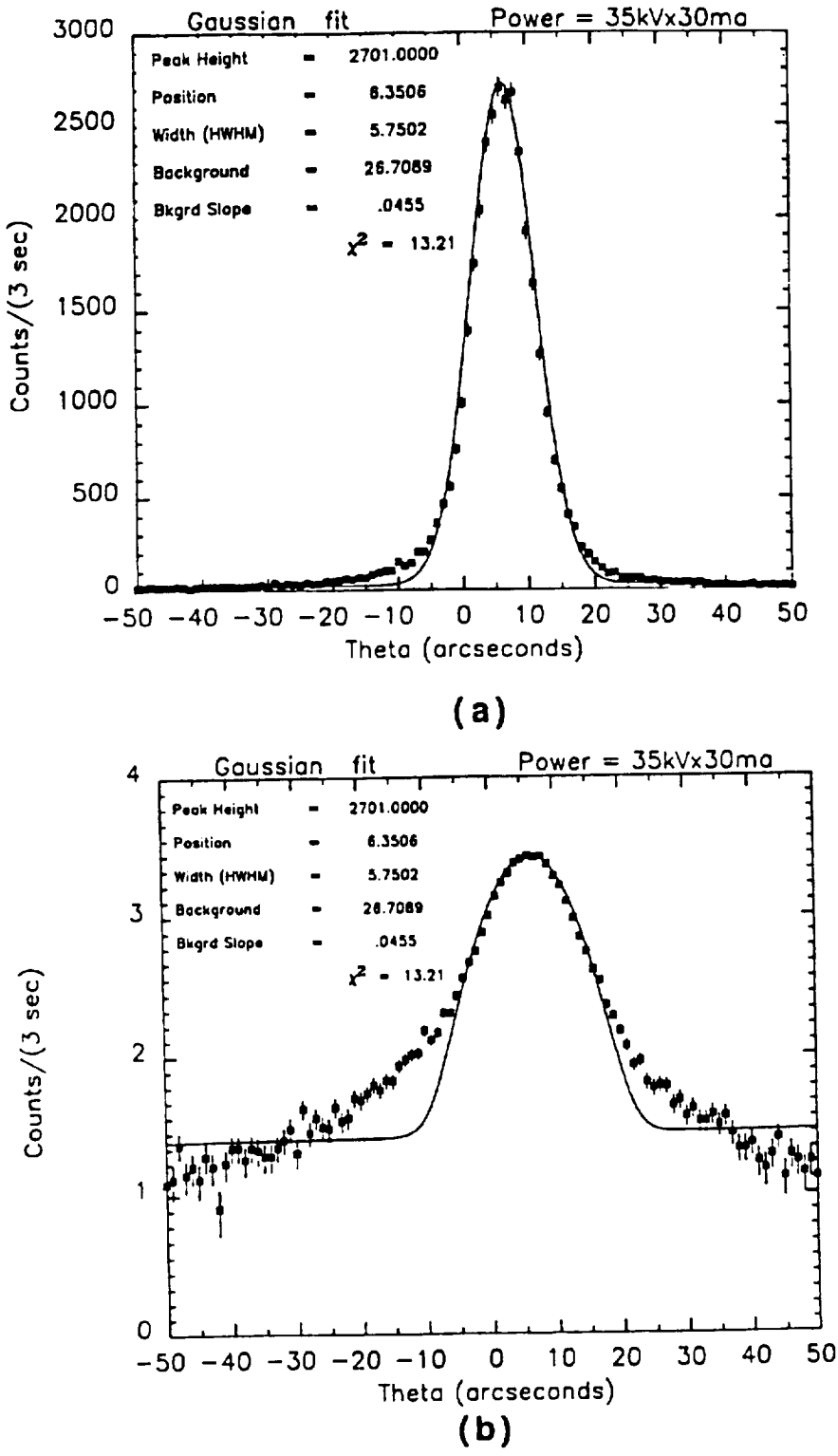

Fig. 49 Typical DCRC Curve from PMZF Material: (a) Linear, (b) Log

Peak Height	=	48186.6500
Position	=	-5.7064
Width (HWHM)	=	77.2925
Background	=	3934.9880
Bkgrd Slope	=	-10.5792

χ^2 = 21.12

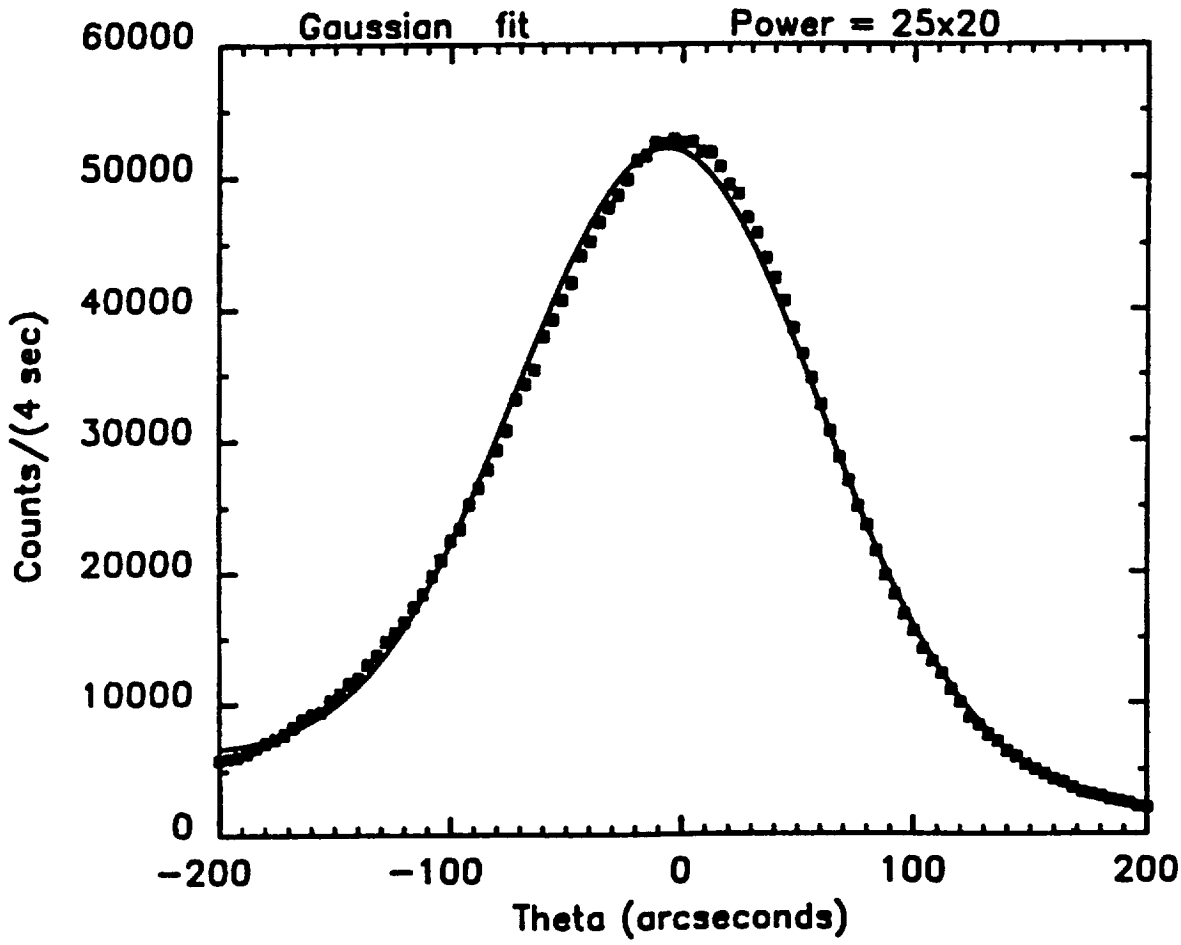

Fig. 50 Ideally Imperfect Rocking Curve Peak

Peak Height	=	1643.5000	±	.0000
Position	=	−40.7409	±	.1417
Width (HWHM)	=	10.1820	±	.1048
Background	=	13.5773	±	1.6134
Bkgrd Slope	=	−.0326	±	.0385

χ^2 = 2.96

X trans (Millimeter) = 8.2500

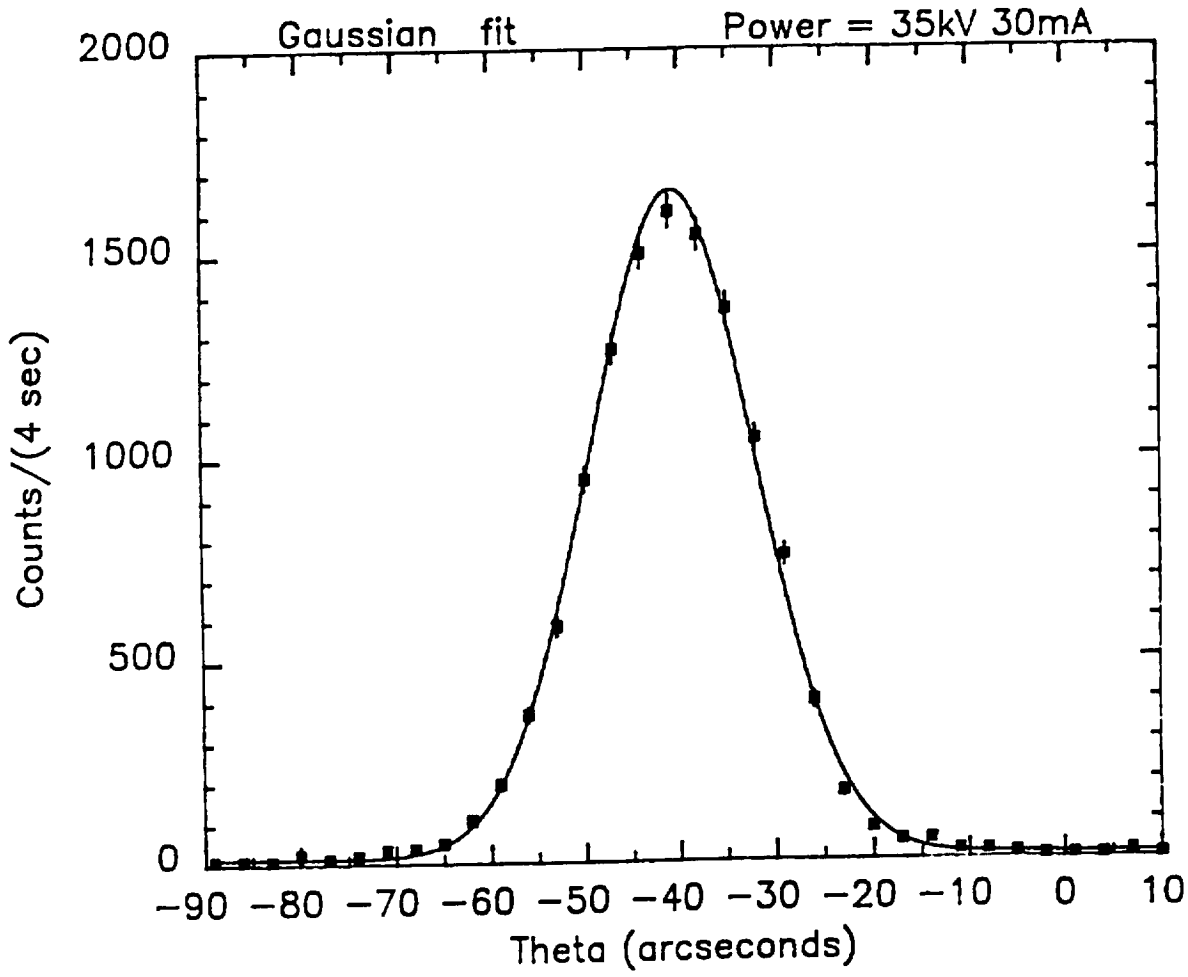

Fig. 51 GCRC-2 Ideally Perfect Rocking Curve Peak

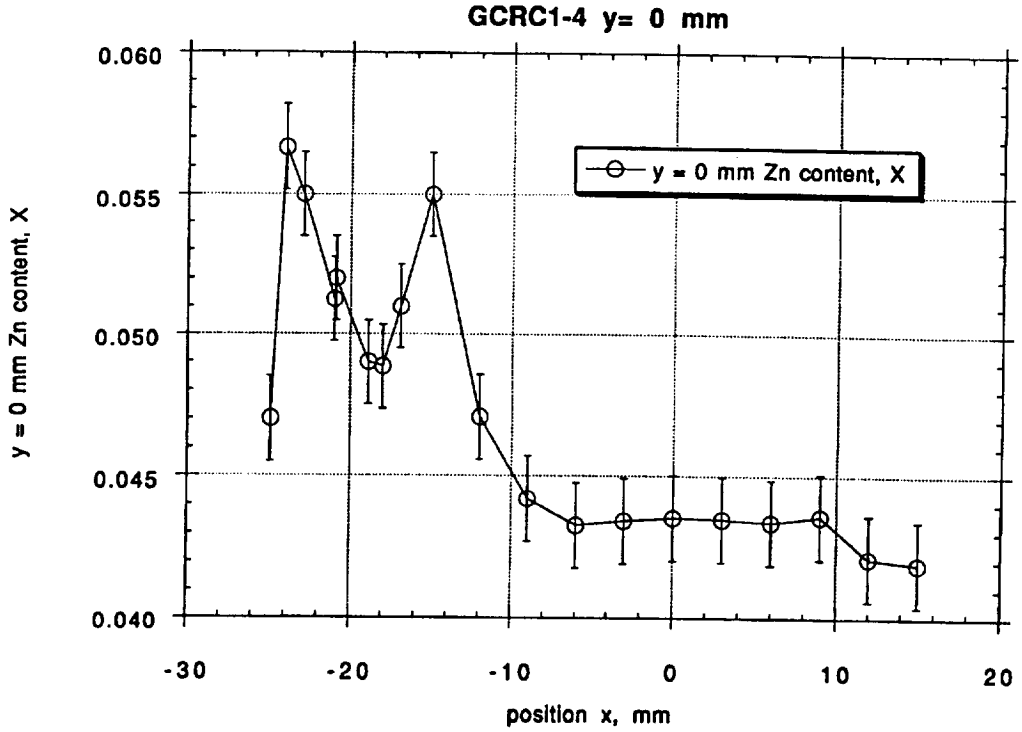

Fig. 52 Longitudinal Macrosegregation Data for GCRC-1

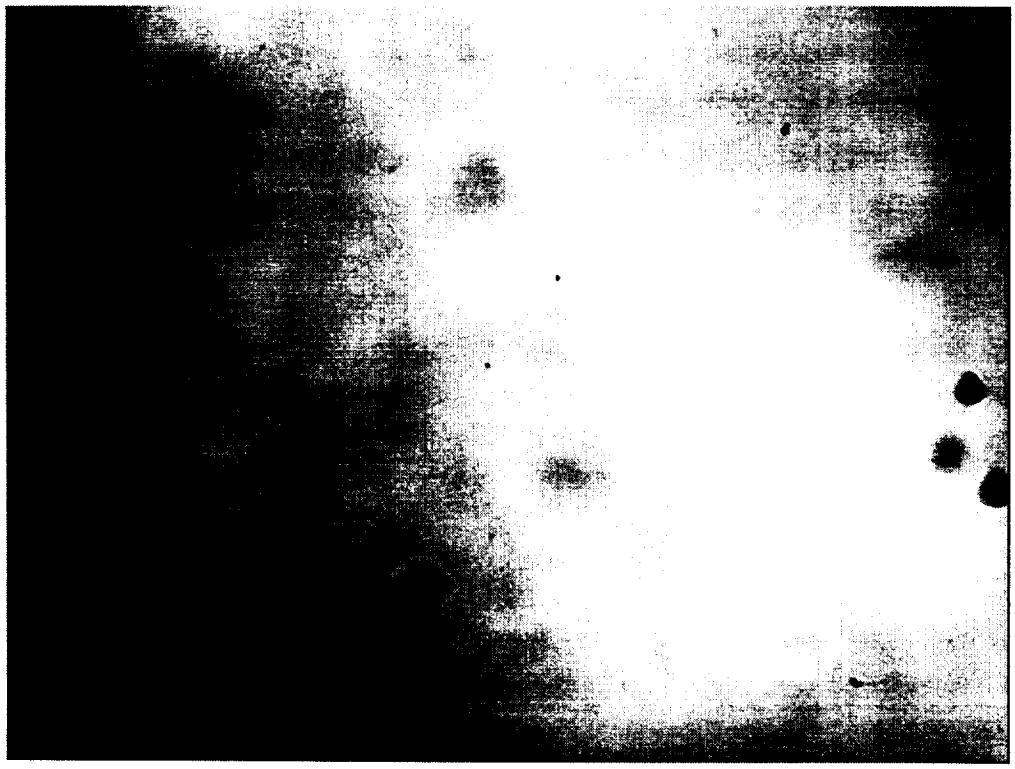

Fig. 53 IR Photomicrograph Showing Te Inclusions & Precipitates

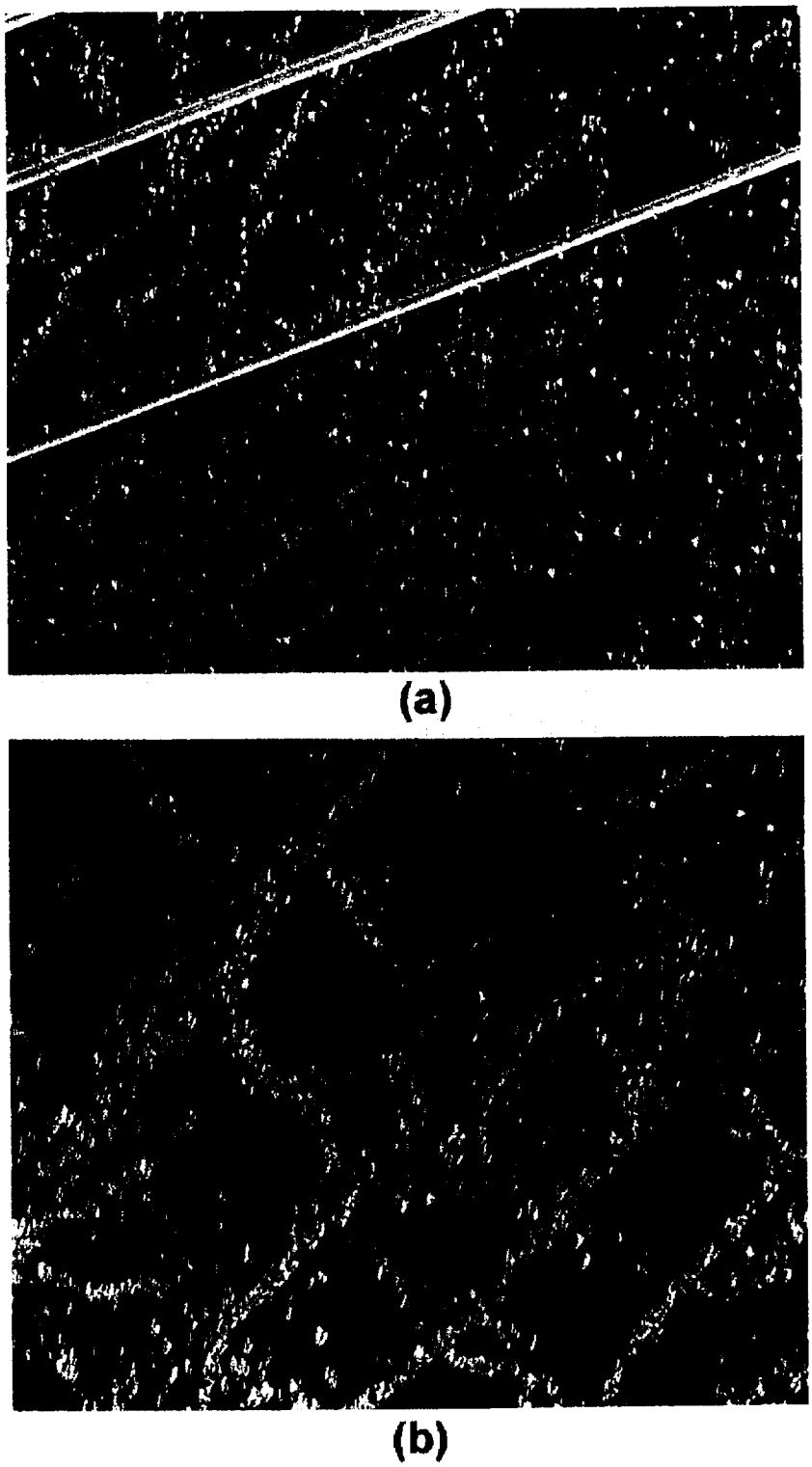

Fig. 54 One-g Microstructure Showing: (a) Microtwins, (b) Mosaic Structure

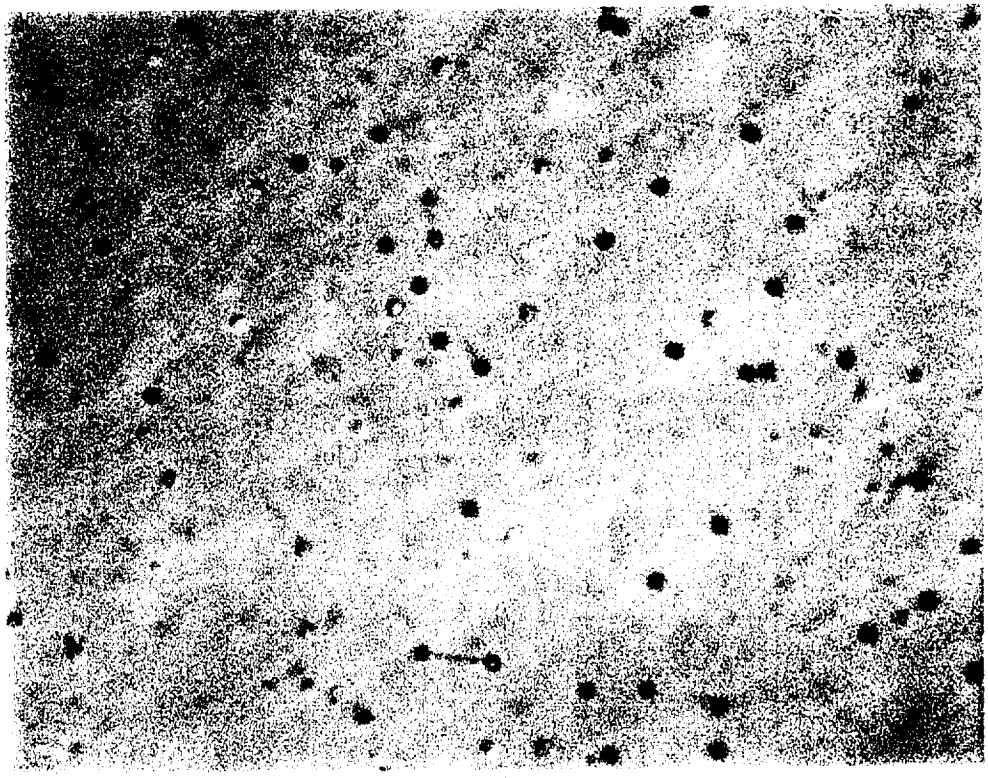

(a)

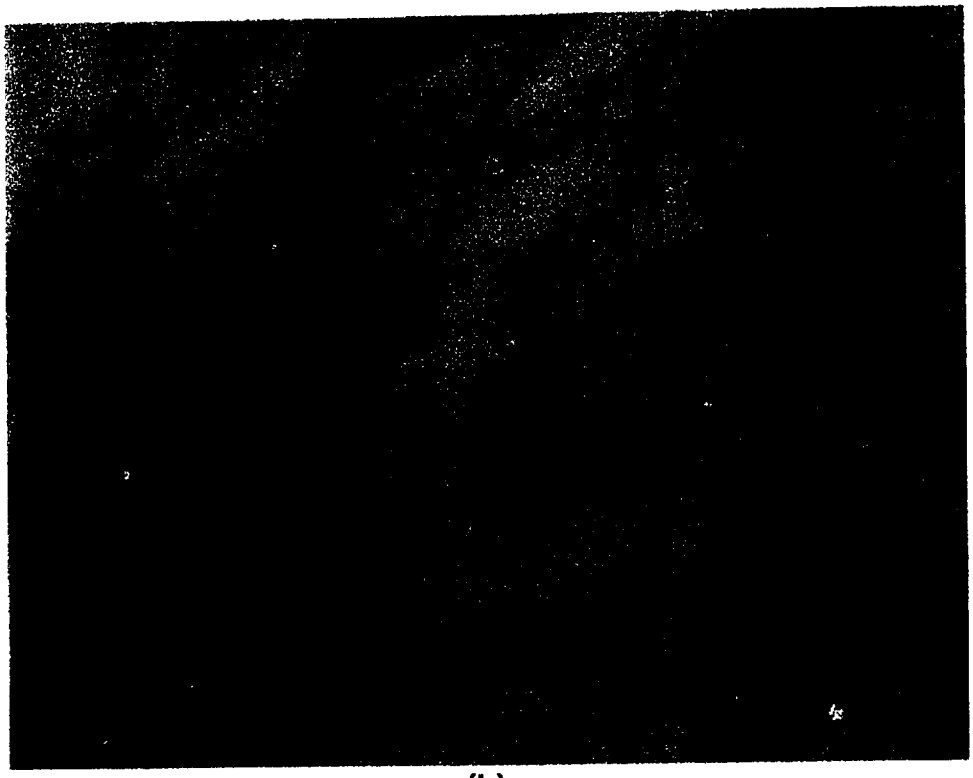

(b)

Fig. 55 GCRC-2 Flight Sample: (a) EPD ~2400; (b) EPD ~400

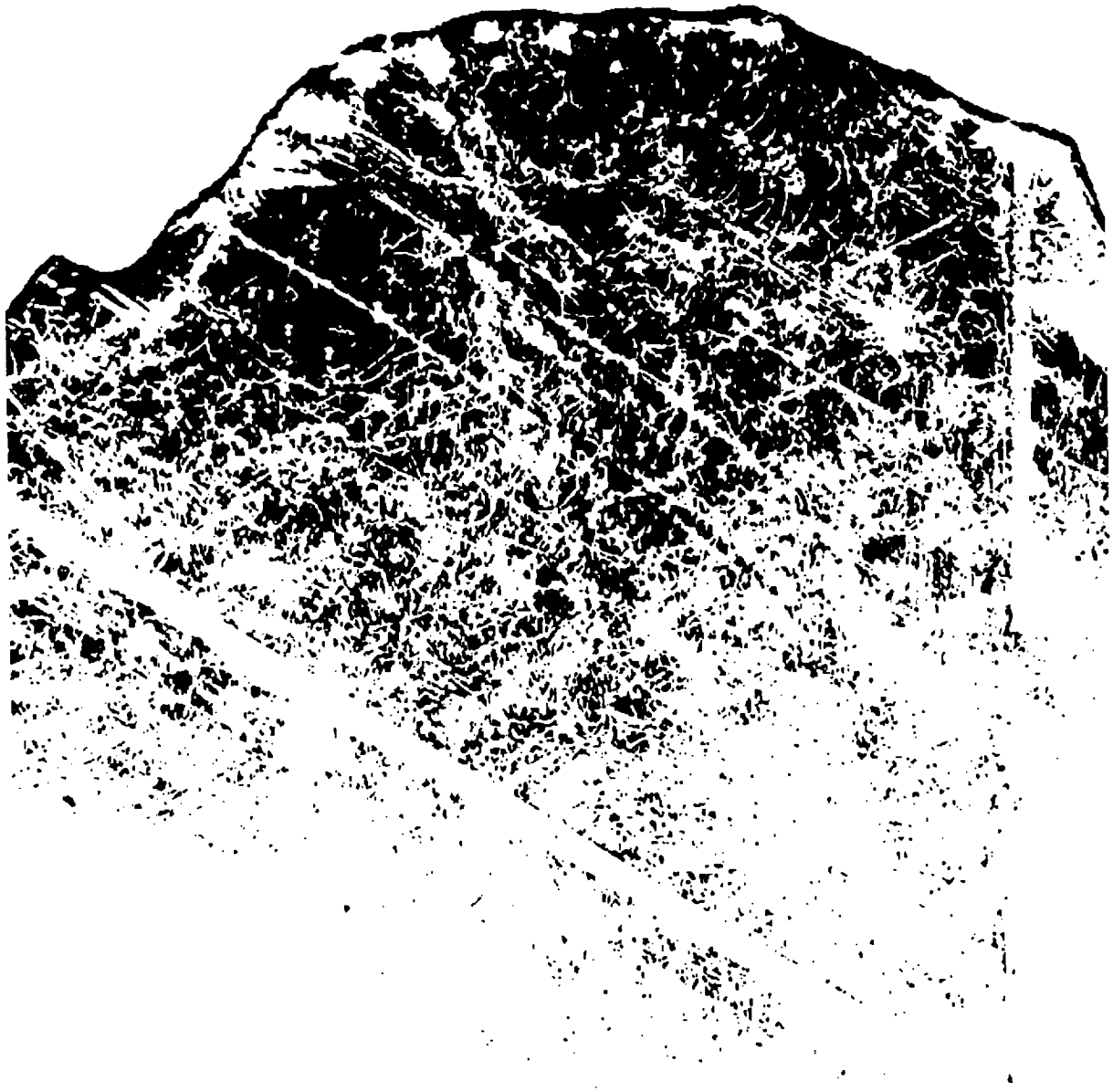

Fig. 56 Transmission SMBT Showing Dislocation Array in GCRC-2

Fig. 57 {422} Bragg Contour Image of One-g PMZF Sample

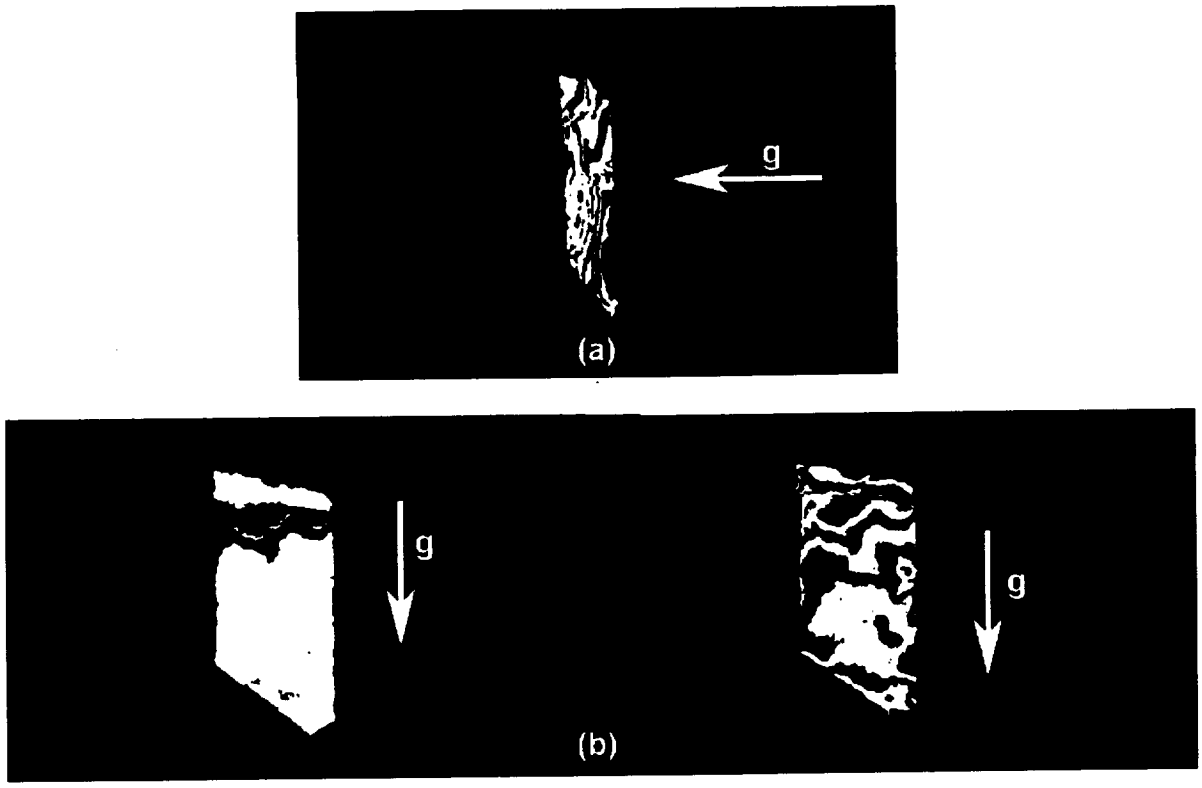

Fig. 58 GCRC-2 Seed SMB Topograph: (a) g = 0°; (b) g = 90°

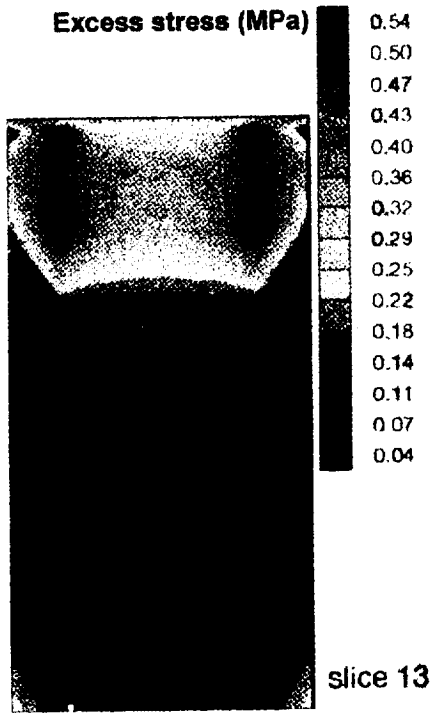

Fig. 59 Thermo-mechanical Model Output, Wafer 13

Fig. 60 SMB Topograph of Wafer 13

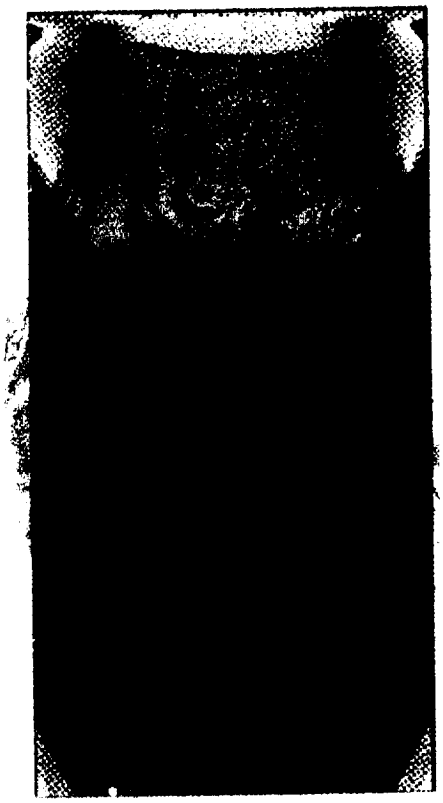

Fig. 61 Superposition of Figures 58 & 59 Showing Correlation

APPENDIX

Final Report for the Period of Performance

9/1/90-2/28/94

Contract number: P.O. 21-69118

Grumman Corporate Research Center, Bethpage, New York

ORBITAL PROCESSING OF HIGH QUALITY CdTe COMPOUND SEMI-CONDUCTORS: NUMERICAL MODELLING AND ACCELERATION DATA ANALYSIS

Prepared by

J. Iwan D. Alexander

Principal Investigator

Contributing Researchers:

S. Amiroudine
M.J.B. Rogers
A. Fedoseyev

CENTER FOR MICROGRAVITY AND MATERIALS RESEARCH

THE UNIVERSITY OF ALABAMA IN HUNTSVILLE

1. INTRODUCTION

The First United States Microgravity Laboratory (USML- 1) flew on Columbia on STS-50 from 25 June to 8 July 1992. The Grumman Corporate Research Center (GCRC) flew one of the four crystal growth experiments accommodated in the Crystal Growth Furnace. The GCRC experiment involved the growth of CdZnTe, a compound semiconductor, by directional solidification. As part of the GCRC team, led by Dr. D. Larson, the Center for Microgravity and Materials Research was responsible for pre-flight assessment of the sensitivity of transport conditions to residual acceleration (or g-jitter), for post-flight analysis of measured residual acceleration data and for preliminary research on mechanisms leading to detachment of the melt form the ampoule wall.

Accordingly, this report is split into six sections including this section. The second section describes the results of a study on the g-jitter acceleration-sensitivity of the transport of Zn in dilute CdTeZn melts. The third section deals with an analysis of the evolution of the average axial composition profile during solidification under zero-g conditions and comparison with the observed profile from one of the Grumman USML-1 flight samples. In the fourth section, the results of our analysis of USML-1 acceleration data is presented and discussed. The fifth section includes an analysis of possible modes of separation of the melt from the ampoule during growth under low-gravity accelerations. In the final section, a summary of publications and conference papers arising from work related to this project are listed.

2. *SENSITIVITY OF BRIDGMAN GROWTH OF CdZnTe TO LOW GRAVITY ACCELERATIONS*

2.1 Introduction

The work presented here is an examination of the sensitivity of species transport in solidifying CdZnTe melts to microgravity accelerations characteristic of low-earth-orbit spacecraft. In particular, the system under investigation is a model of the Grumman Corporate Research Center's CdZnTe experiment which was flown on USML-1 in July 1992. The bulk of the work described here was carried out as part of a preflight analysis. Additional post-flight analyses were carried out to assess effects of recorded microgravity disturbances (see ***section 3*** for a description of the microgravity environment on USML-1).

The motivation for this work stems from the knowledge that, depending on the orientation of the interface in the residual gravity field, buoyancy-driven convective effects in Bridgman-type crystal growth systems can still cause significant lateral composition variations in the crystal even at gravity levels 10^{-6} times that experienced on Earth [1-5]. For the CdZnTe system flown on USML-1, density gradients caused by thermal and compositional varitaions can result in buoyancy-driven convection pre- and post-flight estimates of residual acceleration effects were necessary. It has been demonstrated [5] that predictions based on scaling arguments can also be made provided there is sufficient specific knowledge of the system behavior under a range of conditions. Preferably, such knowlegde should be obtained from practical experience. In the absence of experimental results, such knowlegde can be obtained from numerical simulation.

For CdZnTe melts, as for most semiconductors the Prandtl number ($Pr = \nu/\kappa$) is less than unity. That is, the momentum diffusivity (or kinematic viscosity ν) is smaller than the thermal diffusivity, κ. In such systems, flows are driven throughout the melt interior by buoyancy forces. At low levels of residual acceleration (and, thus, small buoyancy forces) the resulting convection, as we shall see, has little effect on the transport of heat. However, the same cannot be said for species transport. In general, species or solute diffusion is much slower than momentum diffusion (i.e. $Sc = \nu/D$, where D is the solute diffusivity and is usually >1). In this case a sluggish residual flow can modify a diffusion field whenever the convective velocities are of the same order of magnitude as the diffusive velocities.

In order to assess the effects of low gravity acceleration we examine a simplified model of CdZnTe growth by directional solidification. The model, results and a discussion of the results are described in the following sections.

2.2 The model system

The 2D model system depicted in Fig. 1 represents the directional solidification of a dilute CdZnTe melt (4% ZnTe). Solidification takes place as an ampoule of width W is translated through a temperature gradient. The translation of the ampoule is simulated by

Property	dimension	Value	Source
Growth velocity (V_g)	[cms^{-1}]	5×10^{-5}	
Ampoule length	[cm]	6.86	*
Ampoule width	[cm]	1.5	
Kinematic viscosity (ν)	[$cm^2\ s^{-1}$]	4.35×10^{-3}	2,3,4,5
Thermal diffusivity (κ)	[$cm^2\ s^{-1}$]	1.08×10^{-2}	6
Solute diffusivity (D)	[$cm^2\ s^{-1}$]	?	
Schmidt number (Sc)	[ν/D]	10, 20, 30	
		50, 70, 100	
Distribution coefficient		1.2	1
Solute expansion coefficient (β_S)		0, 0.3	
Thermal expansion coefficient (β_T)	K^{-1}	5×10^{-4}	7

supplying a doped melt of bulk composition c_∞, and density ρ_m, at a constant velocity V_m at the bottom of the computational space (inlet), and withdrawing a solid of composition $c_s = c_s(\mathbf{x},t)$ from the top (crystal-melt interface). The temperature gradient is imposed at the walls and is modelled after temperature profiles predicted for the CGF furnace (see Appendix A). At the crystal-melt interface, located at a distance L from the inlet, the temperature is taken to be T_m, the melting temperature of the crystal. The boundaries of the hot zone are held at a higher temperature T_h. The interface is held flat since we wish to confine our attention to compositional non-uniformities caused by buoyancy-driven convection, rather than variations resulting from non-planar crystal-melt interfaces.

Table 1 (Zn) CdTe: Physical Properties

The values of the physical properties were taken from the following sources:

1. Based on estimates of the interface composition during steady growth and from the phase diagram.
2. V. M. Glazov, S. N. Chizhevskaya and S. B. Even'ev, Russian J. Phys. Chem. **43** (1969) 201.
3.. V. M. Glazov, S. N. Chizhevskaya and N. N. Glagoleva, Liquid Semiconductors, (Plenum Press, New York, 1969) p. 161.
   R. F. Brebrick, J. Crystal Growth **86** (1988) 39-48.
6. S. Sen, W. H. Konkel, S. J. Tighe, L. G. Bland, S. R. Sharma and R. E. Taylor, J. Crystal Growth **86** (1988) 111.
7. S. Mokatef, Journal of Crystal Growth **104** (1990) 883.

* The length is chosen from a consideration of our modelling of Teledyne Brown's thermal profile. An " inlet" condition at the top of the computational space accounts for the fact that we are neglecting finite ampoule size effects.

The governing equations are cast in dimensionless form using L, κ/L (κ is the melt's thermal diffusivity), $\rho_m \kappa^2/L^2$, T_h-T_m, and c_∞ to scale the lengths, velocity, pressure, temperature, and solute concentration. The dimensionless equations governing momentum, heat and solute transfer in the melt are then

$$\frac{\partial \mathbf{u}}{\partial t} + (\mathrm{grad}\mathbf{u})\,\mathbf{u} = -\mathrm{grad}p + \mathrm{Pr}\,\Delta\mathbf{u} + \left[\mathrm{Ra}\,\mathrm{Pr}\theta + \mathrm{Ra_s}\mathrm{Pr}C\right]\mathbf{g}(t), \tag{1}$$

$$\mathrm{div}\,\mathbf{u} = 0, \tag{2}$$

$$\frac{\partial \theta}{\partial t} + \mathbf{u}\cdot\ \mathrm{grad}\theta = \Delta\theta, \tag{3}$$

$$\frac{\mathrm{Sc}}{\mathrm{Pr}}\left(\frac{\partial C}{\partial t} + \mathbf{u}\cdot\ \mathrm{grad}\,C\right) = \Delta C, \tag{4}$$

where, $\mathbf{u}(\mathbf{x},t)$, $\theta = (T(\mathbf{x},t) - T_m)/(T_h - T_m)$ and $C = c_m(\mathbf{x},t)/c_m^\infty$ are dimensionless variables which respectively represent the velocity, temperature solute concentration. $\mathrm{Pr} = \nu/\kappa$, $\mathrm{Ra} = \beta(T_h\text{-}T_m)L^3g/\nu\kappa$, $\mathrm{Ra_s} = \beta_c c_\infty L^3 g/\nu\kappa$ and $\mathrm{Sc} = \nu/D$ are, respectively, the Prandtl, Rayleigh, solutal Rayleigh and Schmidt numbers, and ν is the kinematic viscosity and D the solute diffusivity. The term $\mathbf{g}(t)$ in (1) specifies the orientation of the gravity vector. The Rayleigh numbers are taken to be the value of Ra at the Earth's surface, thus the magnitude of $\mathbf{g}$ is the actual acceleration magnitude relative to 1 g. The effective Rayleigh numbers are, thus, the magnitudes of Ra $\mathbf{g}(t)$ and $\mathrm{Ra_s}\,\mathbf{g}(t)$.

The following boundary conditions apply at the crystal-melt interface (y=1)

$$\theta = 0, \quad \mathbf{u}\cdot\mathbf{N} = \frac{\mathrm{Pe_g Pr}}{\mathrm{Sc}}, \quad \mathbf{u}\wedge\mathbf{N} = 0, \quad \frac{\partial C}{\partial y} = \mathrm{Pe_g}\ (1\text{-}k)C, \tag{5}$$

where $\mathrm{Pe_g} = V_g L/D$ and $\mathbf{N}$ is the unit vector normal to the interface. We define the measure of compositional non-uniformity in the crystal at the interface to be the maximum lateral difference in concentration given by

$$\xi(t) = \frac{c_{s\max} - c_{s\min}}{c_{sav}}\%, \tag{6}$$

where c_s is the (dimensional) solute concentration in the crystal, and c_{sav} is the average concentration. The following boundary conditions are applied at the "inlet" (y=0)

$$\theta = 1, \quad \mathbf{u}\cdot\mathbf{N} = \frac{\mathrm{Pe_g Pr}}{\mathrm{Sc}}, \quad \mathbf{u}\wedge\mathbf{N} = 0, \quad \frac{\partial C}{\partial y} = \mathrm{Pe_g}\ (C\text{-}1). \tag{7}$$

At the side walls the conditions are

$$\mathbf{u}\cdot\mathbf{N} = \frac{Pe_g Pr}{Sc}, \quad \mathbf{u}\cdot\mathbf{e}_w = 0, \quad \mathrm{grad}C\cdot\mathbf{e}_w = 0, \tag{8}$$

with a temperatue distribution $\theta = \theta(y)$ on the walls. Here $\mathbf{e}_w$ is the normal to the ampoule wall, and **N** (the normal to the melt-crystal interface) is parallel to the ampoule wall. In this model, transient effects related to the gradual decrease in the melt length are ignored. It is thus implicit that the ampoule is sufficiently long for transient effects to be negligible [1-6].

When we undertook the bulk of this work, neither the value of the diffusivity of ZnTe CdZNTe melt was not known. Thus, we undertook a parametric study using values of the Schmidt number (the ratio of melt kinematic viscosity to dopant diffusivity) in the range $10 \leq Sc \leq 100$. We now believe (assuming that the viscosity is close to CdTe's viscosity) that a Schmidt number of 100 is closest to the truth since, when we compare simple 1D simulations to radial averages of experimental profiles a value of $3\text{-}4 \times 10^{-5}$ cm^2s^{-1} seems to give the best fit (see ***section 3***). We also assumed that the value of the solute expansion coefficient to be 0.3 (about the same as HgTe in CdHgTe melts [7]). The melt density thus decreases with increasing Zn concentration. Since zinc is preferentially incorporated into the crystal during growth the ZnTe concentration increases away from the growing crystal. In otherwords, it reinforces the decrease in density with increasing temperature. This has the effect of "damping" convection only when the steady acceleration vector is antiparallel to the growth direction.

2.3 Solution method

The governing equations were recast in the stream-function vorticity formulation and solved using a pseudo-spectral Chebyshev collocation technique [8,9] which incorporates the influence matrix method [9].

2.4 Steady acceleration

For steady accelrations of 10^{-6} g magnitude oreinted paralel and anti-parallel to the interface, the lateral composition nonuniformity was on the order of 0.01%. Thus, in practice for accelerations of these magnitudes and orientations, lateral or radial nonuniformity will be controlled by the devaition of the interface shape from planarity. Figure 2 shows the temperature field for a steady acceleration of 10^{-6} g. It is insensitive to the convective motion due to the low magnitude residual acceleration causing the motion and the low Prandtl number. Note that, in addition to the axial temperature gradient (~12.4 K cm^{-1}), a shallow lateral temperature gradient is present in the upper part of the melt region.

Figures 3-6 illustrate the velocity and solute fields for two cases where the steady residual acceleration is parallel to the crystal melt interface. For purely diffusive conditions (i.e. no convective motion), the velocity vectors would all be the same length and perpendicular to the crystal-melt interface. Furthermore, the isoconcentrates and crystal-melt interface would be parallel. At 10^{-5} g (see Fig. 3b) a single convective cell has formed. For the choice of thermal and solute expansion coefficients used here the solute contribution to

buoyancy is not important. The motion of the liquid reflects the influence of the temperature field on the density. The cooler denser liquid sinks parallel to the crystal-melt interface in the acceleration direction. The isoconcentrates in the melt are distorted. The resulting composition non-uniformity, ξ, observed at the interface is 4.8% for Sc=10. At accelerations less than 10^{-5} g the strength of the cell diminishes as the convective velocities become comparable in size to the crystal growth rate. At 10^{-6} g (see Fig. 3a), there is a barely perceptible deflection of the velocity vectors from a purely longitudinal flow.

The solute fields, associated with the flows depicted in Fig. 3 are shown in Figs. 4 -6 for different Schmidt numbers. Table 2 gives the magnitudes of the non-uniformity at the interface in each case. For small Schmidt numbers, ξ is ten times higher for 10^{-5} g than for 10^{-6} g. For the cases examined here, the non-uniformity increases with Schmidt number. Note that for the purely diffusive case, the isoconcentrates are parallel to the flat crystal-melt interface and the concentration increases exponentially with increasing distance from the crystal. Deviations from this diffusive profile result from convective transport in the melt. The effect of increasing Sc is then twofold :

1 - Even in the absence of convection, the concentration gradient is increased.

2 - The effect of convection is most significant for higher Sc.

As far as the second effect is concerned, for a fixed Grashof number there will be a value of Sc at which ξ reaches a maximum. This has been demonstrated in earlier work by our group (for low gravity situations) and also by others [10,11].

If the results are expressed in terms of a "Favier-Camel" type transport diagram (see Fig. 7), our results clearly place us in a diffusive transport regime. At fixed Sc, as the acceleration is increased, we see that the system is moving toward the so-called convective-diffusive transition. At fixed Gr, the parametric study also shows that the system first moves parallel and then away from the convective-diffusive transition. As Sc increases the system will move further into the diffusive regime. As mentioned above, the nonlinear dependence of lateral compositional non-uniformity on Sc has been documented in other systems [12-14]. It can be simply explained upon consideration of the fact that at a fixed value of Gr, the flow has some ability to penetrate into the solute gradient zone. The degree to which convection is able to influence transport within this region will diminish as Sc becomes large since the width of the steep concentration gradient zone will decrease as Sc increases. This reflects a decrease in the solute diffusivity. Clearly, for $10 \leq Sc \leq 100$, the isoconcentrates shown in Figs. 4-6 show that the flows predicted for 10^{-5}-10^{-6} g will always have the ability to penetrate into this zone for the cases we have examined owing to the fact that at these growth rates the concentration gradient is relatively shallow.

2.5 Time-dependent acceleration

In order to understand the effect of the orientation of time-dependent acceleration on Zn transport during solidification, we have examined the effects of a number of simple and complex time-dependent acceleration profiles. In all but the extreme cases, we found the

compositional uniformity to be relatively insensitive. The results examined in detail below correspond to Sc=10, and the acceleration is sinusoidal with magnitude 10^{-3} g and frequency 10^{-2} Hz.

Table 2
Compositional non-uniformity ξ. The acceleration is parallel to the crystal-melt interface.

Residual acceleration (g)	**Schmidt (Sc)**	**Non-uniformity (ξ[%])**
10^{-6}	10	0.05
	20	0.19
	30	0.39
	50	0.93
	70	1.6
	100	2.3
10^{-5}	10	0.43
	20	1.4
	70	4.8
	100	6.1

For all the cases discussed here (and others examined to date), the non-uniformity at the interface was found to be very small, on the order of 1%, for the acceleration considered. For the case of CdTe:Zn, various orientations of the acceleration vector were considered. The system was found to produce significantly different responses according to the acceleration orientation.

Acceleration parallel to the interface

The temperature field (see Fig. 8) shows little distortion owing to the low characteristic thermal diffusion time, and gently oscillates with the frequency of the driving force. Note that, as for the Ge:Ga cases reported in [12] there are radial as well as axial temperature gradients.

Figure 9 shows the segregation as a function of time with the corresponding maximum velocities. There is a long transient in the segregation (2500 seconds). The non-uniformity increases until the velocity transient is over. Note that at these times the segregation is modulated at the same frequency as the acceleration. After t=800s, a second peak appears. The magnitudes of the original and the new peak gradually approach one another. This is also seen in Fig. 9. This behavior can be explained as follows. The isoconcentrates initially oscillate preferentially to one side (one maxima per period) because they have been driven to one side by the velocity transient. Since during the transient there will have been net rotation of the fluid in one direction, the compositional non-uniformity will reach a maximum toward the

end of the velocity transient. Once the fluid behaves regularly the solute field slowly adjusts to this state. The compositional non-uniformity gradually reduces and reaches a significantly smaller value after an elapsed time on the order of the characteristic diffusion time τ_D.

The velocity transient is short (see Figs 9b-c). Figure 10 shows the velocity field for 25, 50, 75 and 100 seconds. The velocity is in phase with the driving force owing to the low Strouhal number (see later discussion). Note that the vector plots are not to the same scale.

Acceleration tilted five degrees with respect to the interface

In this section, the effects of orienting **g** in other directions are examined. The first case is for an acceleration oriented 5 degrees with respect to the interface.

Figure 11 illustrates the segregation with the corresponding maximum velocities as a function of time. Clearly, there are some differences in comparison to the case when the gravity is parallel to the interface. In the maximum velocity profiles (see Figs 11b-c), note that the velocity is approximately in phase with the driving force. This is consistent with the low value of the Strouhal number. However, the peaks do not have the same magnitude. This suggests that a mean flow has been generated which has a clockwise direction. This is attributed to the fact that for cases of non-parallel g (non-axisymmetric), the vertical component of this acceleration results in the generation of a mean flow (see discussion in the next section). Note that, near the interface, the density is higher. Therefore, as can be deduced from Figs. 11b-c, the mean flow has a clockwise direction.

The net circulation of the flow in one direction builds up a mean non-uniformity which is slightly greater than that obtained for parallel acceleration. The segregation profile is shown in Fig. 11a. As for the parallel acceleration case, a second peak appears at about 600 s. However, the magnitude of the first peak decreases with time whereas the magnitude of the second peak increases and eventually dominates. The initial motion of the fluid drives the solute to one side. A maximum in interface concentration develops on this side and is modulated at 10^{-2} Hz as the fluid oscillates. After the fluid transient is over, the solute slowly diffuses to the other side until the spatial and temporal concentration distribution is compatible with the regularly oscillating velocity field. Since, in this case, a clockwise mean flow has developed, the transient concentration maximum is shifted such that a maximum appears on both sides but is larger on the right side due to the mean flow.

Figure 12 shows the concentration field at 25, 50, 75 and 100 s. Note that there is a maximum on one side and the concentration field oscillates about this continuously increasing maximum. At longer times, the mean flow causes a non-symmetric oscillation. Figure 13 shows the concentration field at 725, 750, 775 and 800 s. The non-uniformity at the interface at this time is small (see Fig. 11a) and,as expected, solute is oscillating from side to side. This is also reflected in the concentration field of Fig. 14 at 2025, 2050, 2075 and 2100 s.

Acceleration oriented 45 degrees with respect to the interface

In order to further investigate the previous results, the cases of gravity oriented $\pi/4$ and $3\pi/4$ degrees with respect to the vertical axis have been studied and analyzed. Depending on this orientation, the axial component of the density gradient will tend to

diminish or augment the fluid flow. Simply by analyzing the density gradient and taking into account the orientation of the acceleration the direction of the mean flow can be ascertained as follows. Figure 15 shows this schematically. In Fig 16a, the gravity is always parallel to the interface. At earlier times, the flow has an anti-clockwise direction because it is initially driven in this direction from a state of rest and takes a short time to relax to a regularly oscillating condition. At longer times, the buoyancy forces which characterize each half of the oscillation cycle are equal in magnitude but opposite in sign. Under these conditions, and because the flow Reynold's number is small, no mean flow is expected unless temperature oscillations are large.

Now consider gravity to be oriented with γ in the range $\pi/2 \leq \gamma \leq \pi$ with respect to the vertical axis (see Fig 15b). The associated flow can be viewed as responding to the components of the instantaneous acceleration acting parallel and perpendicular to the interface. During the first half of the period the instantaneous acceleration acting parallel to the interface dominates the flow and results in an anti-clockwise roll. The instantaneous perpendicular component acts on the fluid on the right side so as to retard its vertical motion. During the second half of the period, the instantaneous acceleration acting parallel to the interface dominates the flow and results in a clockwise roll. The instantaneous perpendicular component now increases the velocity of the downward moving fluid on the right side while the motion of the rising fluid on the left side is retarded. After the velocity transient is over, an average clockwise motion of the fluid develops.

Figure 16 illustrates the non-uniformity and the corresponding maximum velocities as a function of time when g is oriented at $3\pi/4$ with respect to the vertical axis of the ampoule. As expected, the maximum magnitude of the velocities for the first half of the period is smaller than that for the second half. This causes the clockwise direction of the flow. The compositional non-uniformity behaves in a manner similar to that for the 0.55π case. The reversal in the direction of the oscillation of the dopant concentration occurs at about 400 s. It then oscillates to the other side due to the clockwise direction of the mean flow.

Fig 17 shows the concentration field at 100, 150, 350, 400, 500 and 1000 s. Note that the non-uniformity is quite small near the interface; it oscillates on one side of the ampoule until about 400 s (see also Fig. 16), and subsequently oscillates on the other side as the composition field reaches dynamic equilibrium with the velocity field.

In Fig. 15c, the acceleration is oriented with γ in the range of $0 \leq \gamma \leq \pi/2$. For the first half of the period, the acceleration component parallel to the interface again results in a counterclockwise roll. The vertical component, however, now enhances the downward motion of the fluid on the left side while slowing the rising fluid on the right hand side. During the second half of the period, the vertical acceleration component retards all vertical fluid motion. This eventually results in an average counterclockwise fluid motion.

Fig. 18 illustrates the case when g is oriented $\pi/4$ with respect to the vertical axis of the ampoule. Note the first peak in the maximum velocity profiles is the largest and results in

the counterclockwise direction of the mean flow. The concentration field for one period at 25, 50, 75 and 100 seconds is shown in Fig. 19.

Time-average of the transport equation

As a first approximation, the time-average of the basic equations of conservation can be written by considering the primitive variables as a sum of a mean and fluctuating part. The mean conservation equations are then obtained by taking the time-average of the dimensionless equations. Thus, the mean transport equation can be determined by considering the time-average of equation (4).The occurrence of a mean transport effect (manifested in the finite mean value of ξ in Fig. 9.) can be explained by the following argument. Our results show that the velocity field and composition fields behave approximately like

$$\mathbf{u} = \frac{Pe_g Pr}{Sc}\mathbf{N} + \mathbf{u}_c(x)\sin(\omega t+\varphi_v), \quad c = c_0(\mathbf{x}) + c_1(\mathbf{x})\sin(\omega t + \varphi_D),$$

where $\mathbf{u}_c$ represents the velocity due to buoyant convection, $c_0(\mathbf{x})$ is a mean composition profile (which in the absence of the oscillating flow would correspond to a one-dimensional diffusion profile), $c_1(\mathbf{x})$ is the oscillating part of the composition and ϕ_v and ϕ_D are the velocity and solute phase differences with respect to the oscillating acceleration. The contribution of the oscillating flow to the mean transport can be estimated by taking the time average of the term $(\mathbf{u}\cdot\nabla)c$ over one period of the acceleration. The time average of the product of the oscillatory parts of the velocity and composition fields then yields a non-vanishing term given by

$$(\mathbf{u}_c\cdot\nabla)c_1\langle\sin(\omega t + \phi_v)\sin(\omega t+\phi_D)\rangle = \frac{1}{2}\cos(\phi_v - \phi_D)(\mathbf{u}_c\cdot\nabla)c_1 .$$

Here the time average over one period ($2\pi/\omega$) is denoted by $\langle\ \rangle$. Thus, in this case, unless the velocity and composition fields oscillate at exactly 90° out of phase there will be some contribution to mean transport even though the mean velocity is practically zero. Note that, it is *sufficient* but not *necessary* that the orientation of **g** breaks the symmetry of the buoyancy field. Indeed, inspection of the equations reveals that mean flow is possible even when the acceleration is parallel to the gradient of the density. This will certainly occur for Pr>1 and also for Sc>1 whenever thermal and/or solutal expansion coefficients and wherever thermal and solutal gradients are large enough to contribute significantly to the density gradient. The higher Prandtl (Schmidt) number fluids will tend to yield oscillating temperature (composition) fields. Time averaging the buoyancy field will now yield a mean body force that must produce a mean flow. The magnitude of this flow will depend on the significance of the oscillating thermal and solutal contributions of the solute field. Small amplitude oscillations tend to yield insignificant contributions. This is evident in the results presented earlier, and is also seen in results of previous work [12].

Generation of mean flows

For an oscillating body force $\mathbf{g}(t)$, the following situations can result in the generation of a mean flow :

1) For high Prandtl numbers, Pr, the temperature field will, for sufficiently large Gr, exhibit oscillations. Under these conditions, the temperature field might, for example, behave as,

$$\theta = \bar{\theta}(x) + \hat{\theta}(x) \sin(\omega t + \varphi_\kappa),$$

where $\bar{\theta}$ is the mean temperature and $\hat{\theta}$ is the amplitude of the oscillation of the temperature. The time average of the body force is then :

$$\left\langle Gr^* \, Pr^2 \left[\bar{\theta} + \hat{\theta} \sin(\omega t + \varphi_\kappa)\right] \sin \omega t \right\rangle \approx Gr^* \, Pr^2 \, \hat{\theta} \left\langle \sin(\omega t + \varphi_\kappa) \sin \omega t \right\rangle,$$

which is non-zero. A non-zero mean body force will generate a mean flow. Note that here $Gr^* = Gr \, g/g_0$ represents the effective Grashof number and φ_κ is the phase due to thermal diffusion effects.

2) $Gr^* >> 1$: A time average of the convective momentum transport $\langle \mathbf{u} \cdot \text{grad}\, \mathbf{u} \rangle$ may also generate mean flow terms for high Gr^* oscillating flows.

3) Orientation of the body force. As we have seen in the previous section the orientation of $\mathbf{g}(t)$ with respect to the temperature field can also result in mean flow generation whenever the oscillating body force breaks the symmetry of the temperature field.

2.6 Symmetry breaking Flow transitions

In our investigation of transport under steady acceleration levels approaching terrestrial conditions we found that for an axial acceleration parallel to the growth direction with Ra= 282,203, a quasi-steady solution with two symmetric co-rotating cells was obtained. This persisted for some time and then the rate of change of vorticity exhibited a rapid increase. This occurred as the flow underwent a transition from a symmetric flow with co-rotating cells to a single-cell non-symmetric flow. Similar behavior has been observed in other 2D models [15,16] and we are currently collaborating with researchers at the Institute for Fluid Mechanics in Marseille, France, on an investigation of flow transitions of this type (see reference [15] for recent results). In a different system (Ge:Ga) and for a melt aspect ratio (L/W) of 1 we have observed such a transition at Ra~5000. However, to date we have observed such transitions only in 2D models. For a cylidrical ampoule such transitions can occur for cases where the cylider is is "heated-from-below" and for perfectly conducting walls or perfectly insulating walls. Further work is necessary to determine whether the CdTe:Zn system might exhibit such behavior during ground-based experiments. Should this be the case, a 3D calculation would be necessary to get a better idea of the solutal and thermal Rayleigh numbers at which this occurs in 3D systems.

2.7 Summary

Our work to date has determined that transport under expected Spacelab low gravity conditions will be dominated by diffusive transport. Given the planned attitude motion of the Orbiter and the location of the experiment relative to the gravity-gradient, centrifugal, and predicted range of atmospheric drag acceleration, it is unlikely that the compositional uniformity will be even marginally sensitive to quasi-steady residual acceleration and should not respond adversely to typical unsteady and transient disturbances except under extreme circumstances. It will however, be susceptible whenver quasi-steady accelerations (characteristic of residual acceleration arising from gravity gradient and atmospheric drag) are greater than 10^{-6}g and are oriented parallel to the melt crystal interface. For the cases of residual accelerations associated with vibration, the frequency, amplitude and spatial orientation of the acceleration vector appear to play an important role in determining the response of the system. For example, for residual accelerations where the acceleration oscillates about positive and negative of a fixed direction in the system, the orientation of this direction relative to the density gradient determines whether a mean flow is generated in the system. The mean flow produces a mean compositional nonuniformity.

During the course of our work we observed three basic aspects of transport phenomena not previously recognized:

1) If the vibration direction breaks the symmetry of the buoyancy field, then a mean flow will be produced which, under extreme conditions as far as spacelab conditions are concerned, can lead to a compositional nonuniformity in the crystal.

2) For sinusoidally oscillating accelerations, even when the mean flow is negligible, a mean compositional nonuniformity arises when the phase difference ϕ_V-ϕ_D, between the oscillating velocity and composition fields, is different from 90°. 2) For oscillatory g-jitter, if the orientation of the g-jitter vector does not lie parallel to a symmetry axis of the density field, then the driving force is inherently asymmetric and a mean flow will result.

3) For steady axial acceleration, as terrestrial conditions are approached, a transition from symmetric to a non-symmetric flow was observed. Whether this can be expected under more realistic conditions remains to be determined.

2. 8 References

[1] J. I. D. Alexander, J. Ouazzani and F. Rosenberger, Proc. 3rd International Colloquium on Drops and Bubbles, AIP Conference Proceedings **197**, ed. Taylor G. Wang (American Institute of Physics, New York, 1988) p.112.

[2] J. I. D. Alexander and J. Ouazzani, Proc. 6th International Conference on Num. Methods in Laminar and Turbulent Flow, C. Taylor, P. Gresho, R. L. Sani and J. Haüser (eds.) (Pineridge, Swansea, 1989) p.103.

[3] J. I. D. Alexander, J. Ouazzani and F. Rosenberger, J. Crystal Growth **97** (1989) 28.

[4] V. I. Polezhaev and A. I. Fedyoshkin, Izvestiya Akad. Nauk. SSSR, Mekhanika Zhidkosti i Gaza **3** (1980) 11.

[5] P. R. Griffin and S. Mokatef, Appl. Microgravity Techn. **2** (1989) 128.

[6] C. J. Chang and R. A. Brown, J. Crystal Growth **63** (1983) 343.

[9] A.J. Pearlstein, unpublished manuscript, 1993.

[8] R. Peyret, The Chebyshev Multidomain Approach to Stiff Problems in Fluid Mechanics, Proceedings of ICOSAHOM 89, June 26-29, 1989, Como (Italy).

[9] U. Ehrenstein and R. Peyret, Int. J. Numerical. Meth. Fluids **9** (1989) 499.

[10] C. J. Chang and R. A. Brown, J. Crystal Growth **63** (1983) 343.

[11] P. M. Adornato and R. A. Brown, J. Crystal Growth 80 (1987) 155.

[12] J. I. D. Alexander, S. Amiroudine, J. Ouazzani and F. Rosenberger, J. Crystal Growth **113** (1991) 21.

[13] J. I. D. Alexander, J. Ouazzani and F. Rosenberger, J. Crystal Growth **97** (1989) 285.

[14] A. Rouzaud, D. Camel and J.J. Favier, J. Crystal Growth **73** (1985) 149.

[15] P. Larroude, J. Ouazzani and J.I.D. Alexander, in press, European Journal of Fluid Mechanics, 1994.

[16] M.D. Impey, D.S. Riley And A.A. Wheeler, Physics of Fluids A, 3 (1991) 535.

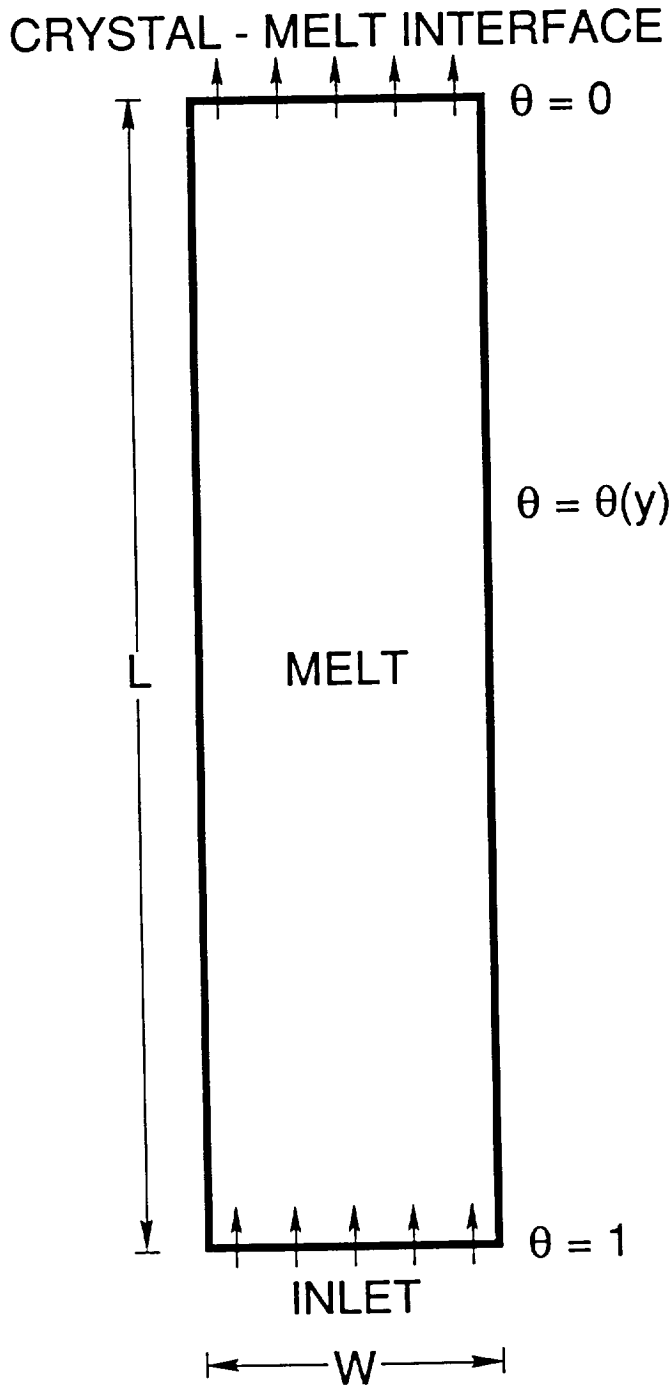

FIG. 1

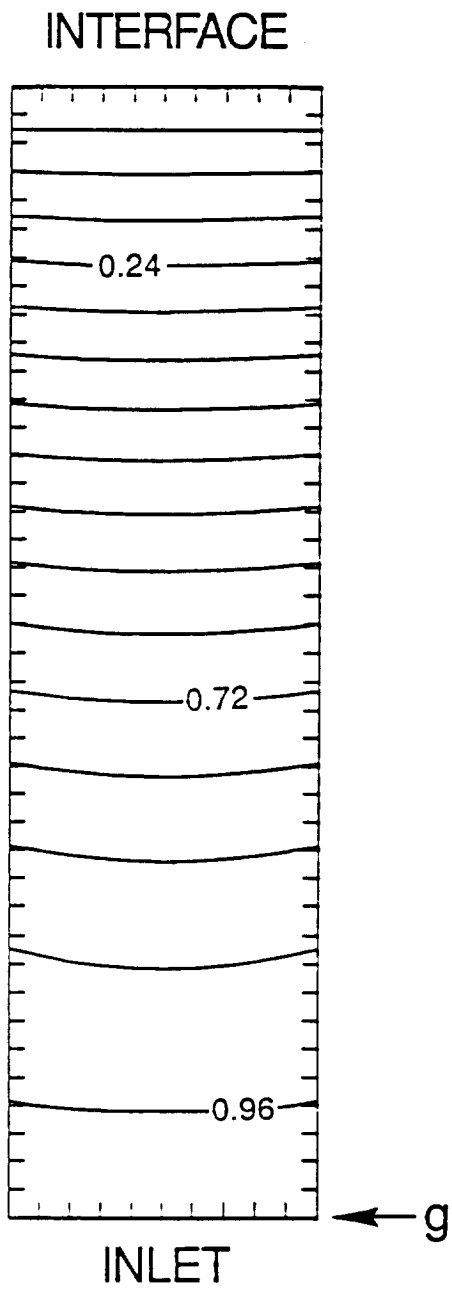

Figure 2 The dimensionless temperature field for 2D calculations corresponding to operating conditions given in Table 1.

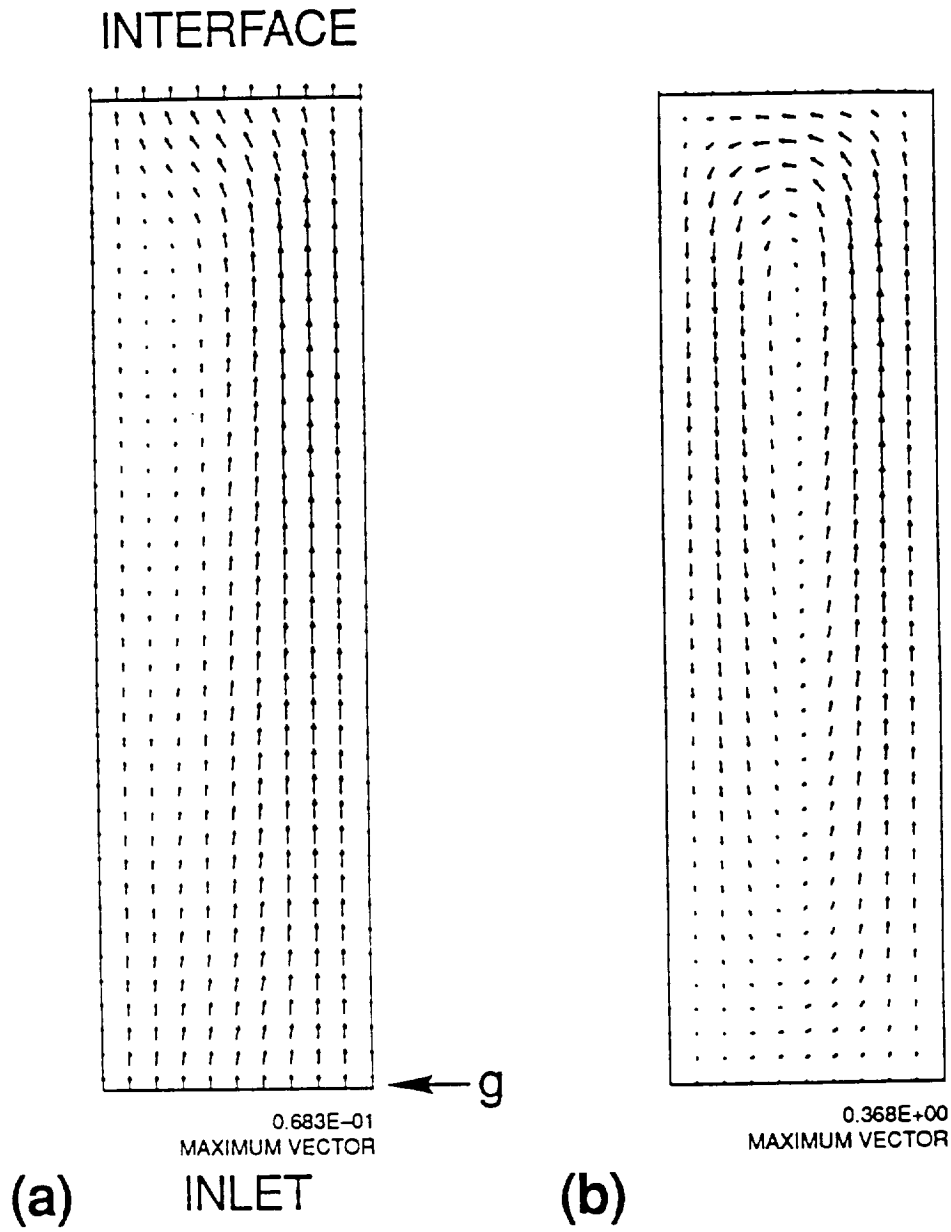

Figure 3 Velocity fields caused by a steady acceleration with magnitude a) 10^{-6} g and b) 10^{-5} g oriented parallel to the crystal-melt interface.

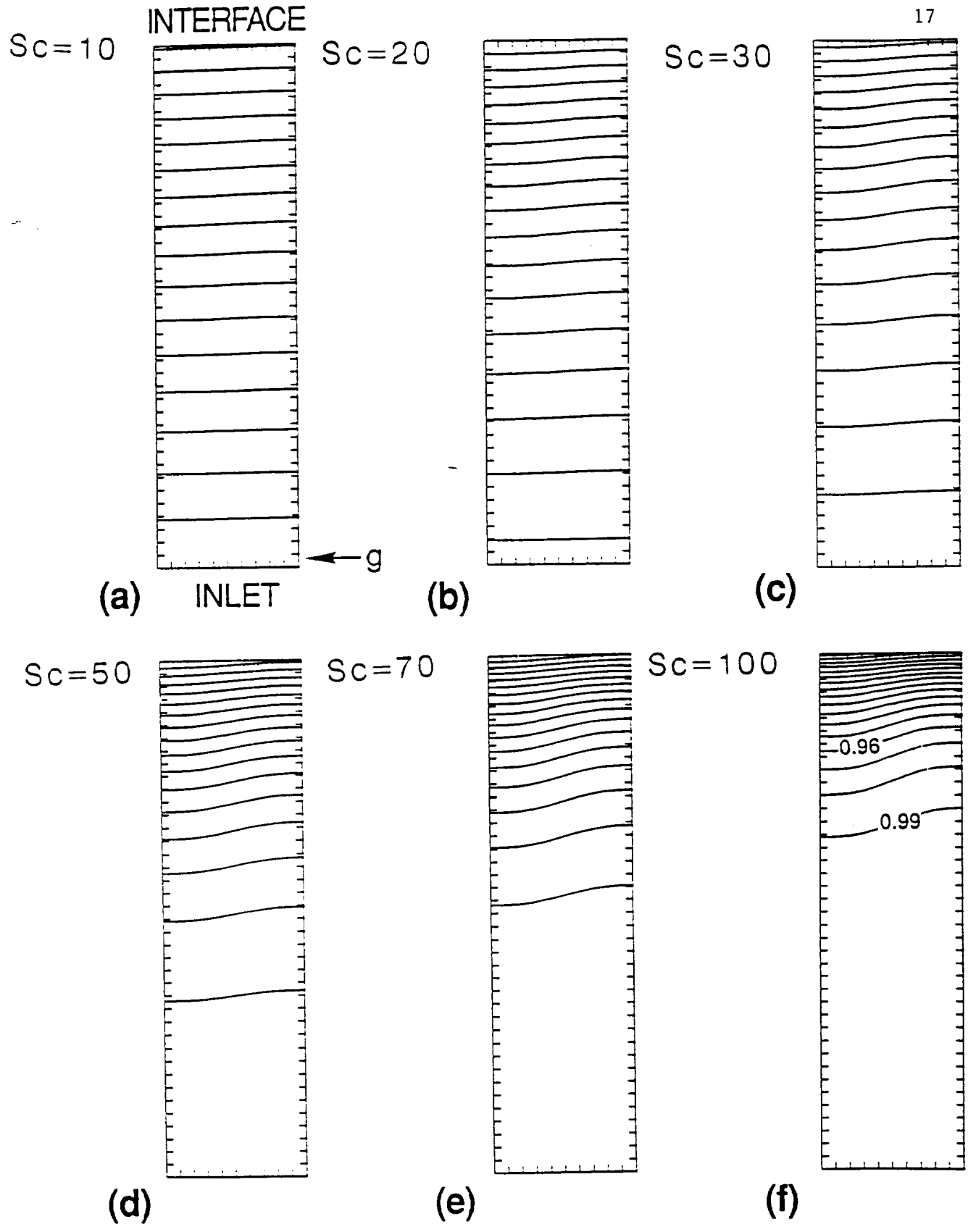

Figure 4 The solute field for different Schmidt numbers a) Sc=10 b) Sc=20 c) Sc=30 and d) Sc=50 e) Sc=70 f) Sc=100 for a steady acceleration of 10^{-6}g oriented parallel to the crystal-melt interface.

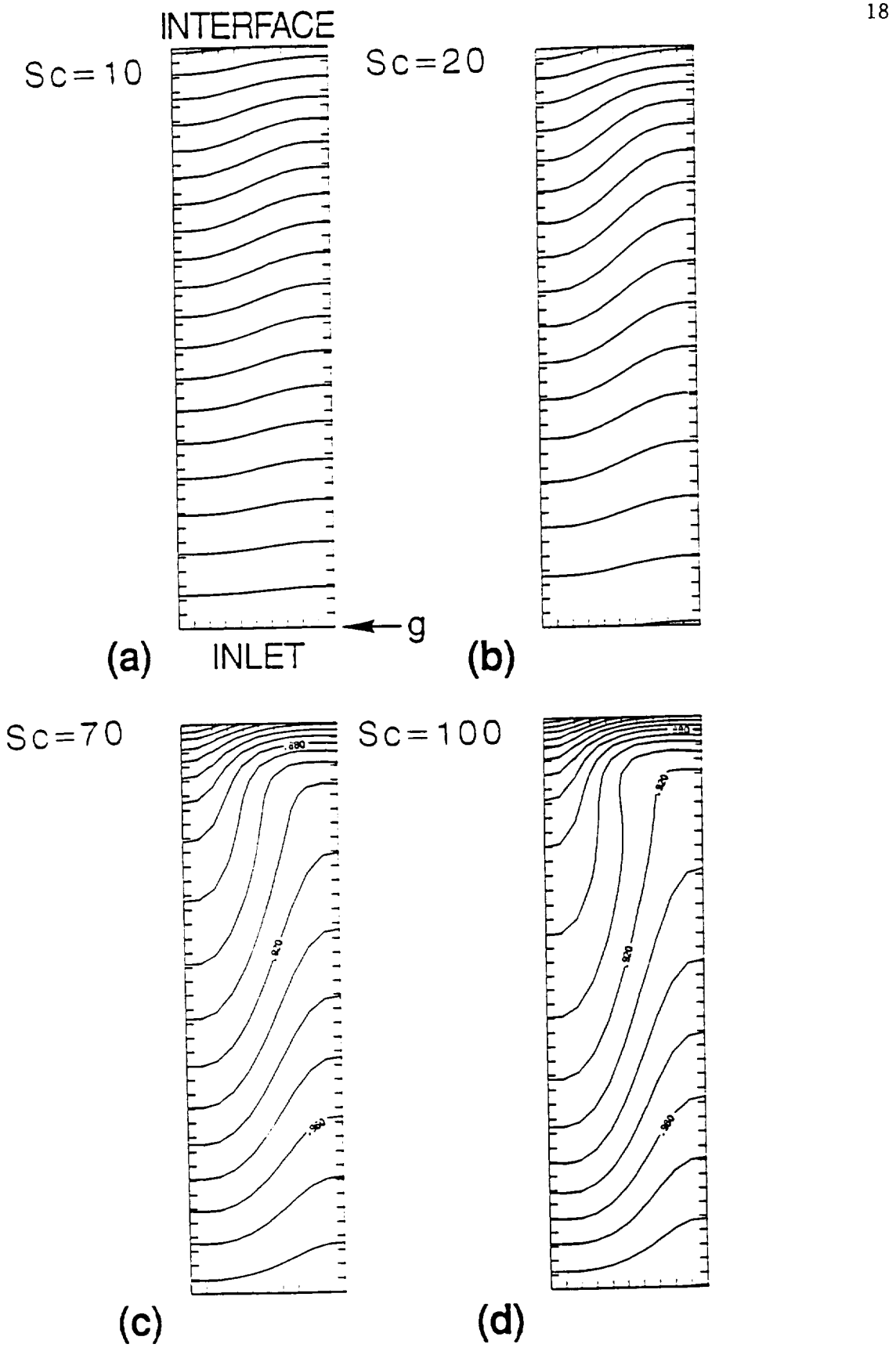

Figure 5 The solute field for different Schmidt numbers a) Sc=10 b) Sc=20 c) Sc=70 and d) Sc=100 for a steady acceleration 10^{-5} g oriented parallel to the crystal-melt interface.

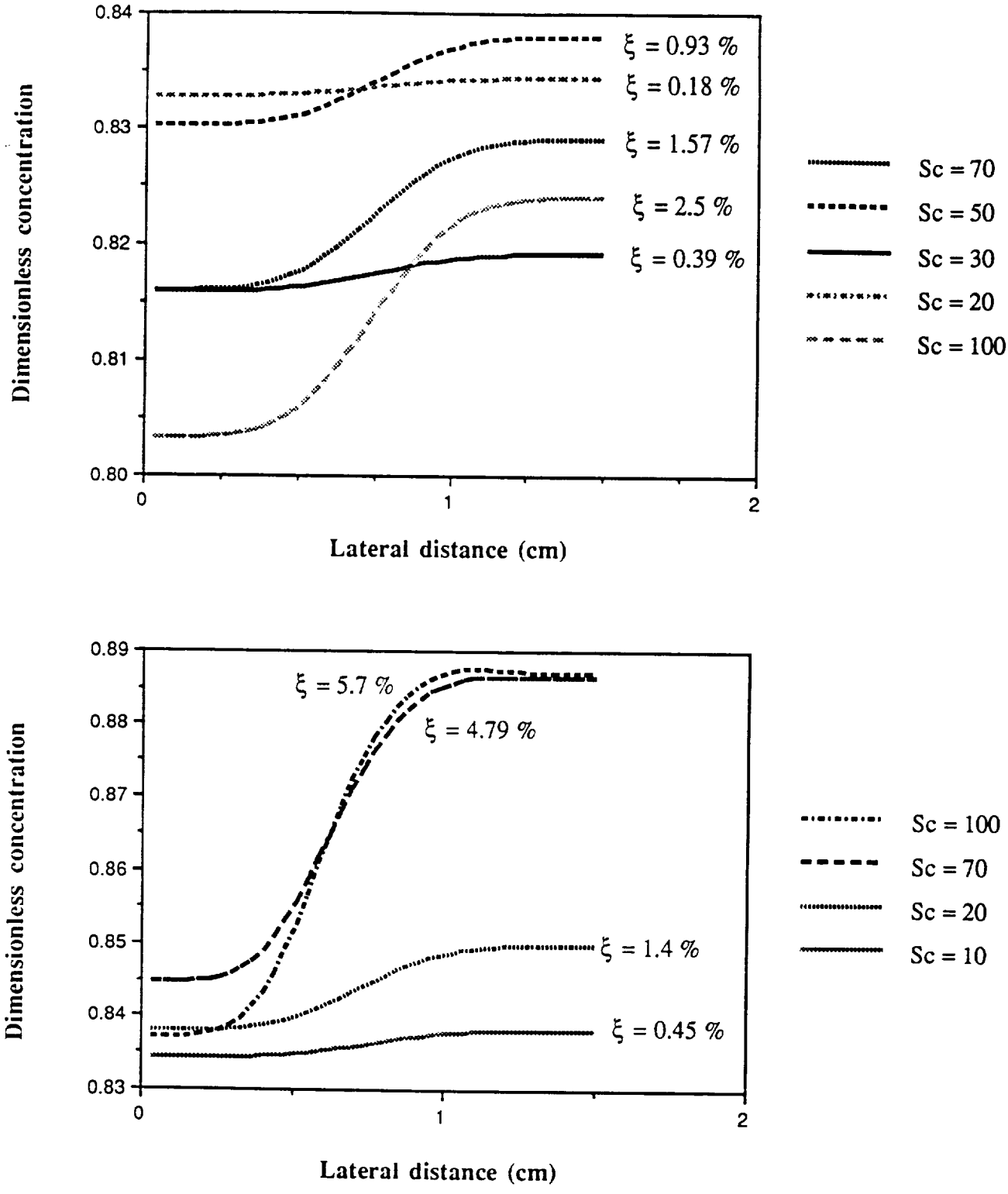

Figure 6 Dimensionless concentration as a function of lateral distance for different Schmidt numbers for steady accelerations a) 10^{-6} g b) 10^{-5} g parallel to the crystal-melt interface.

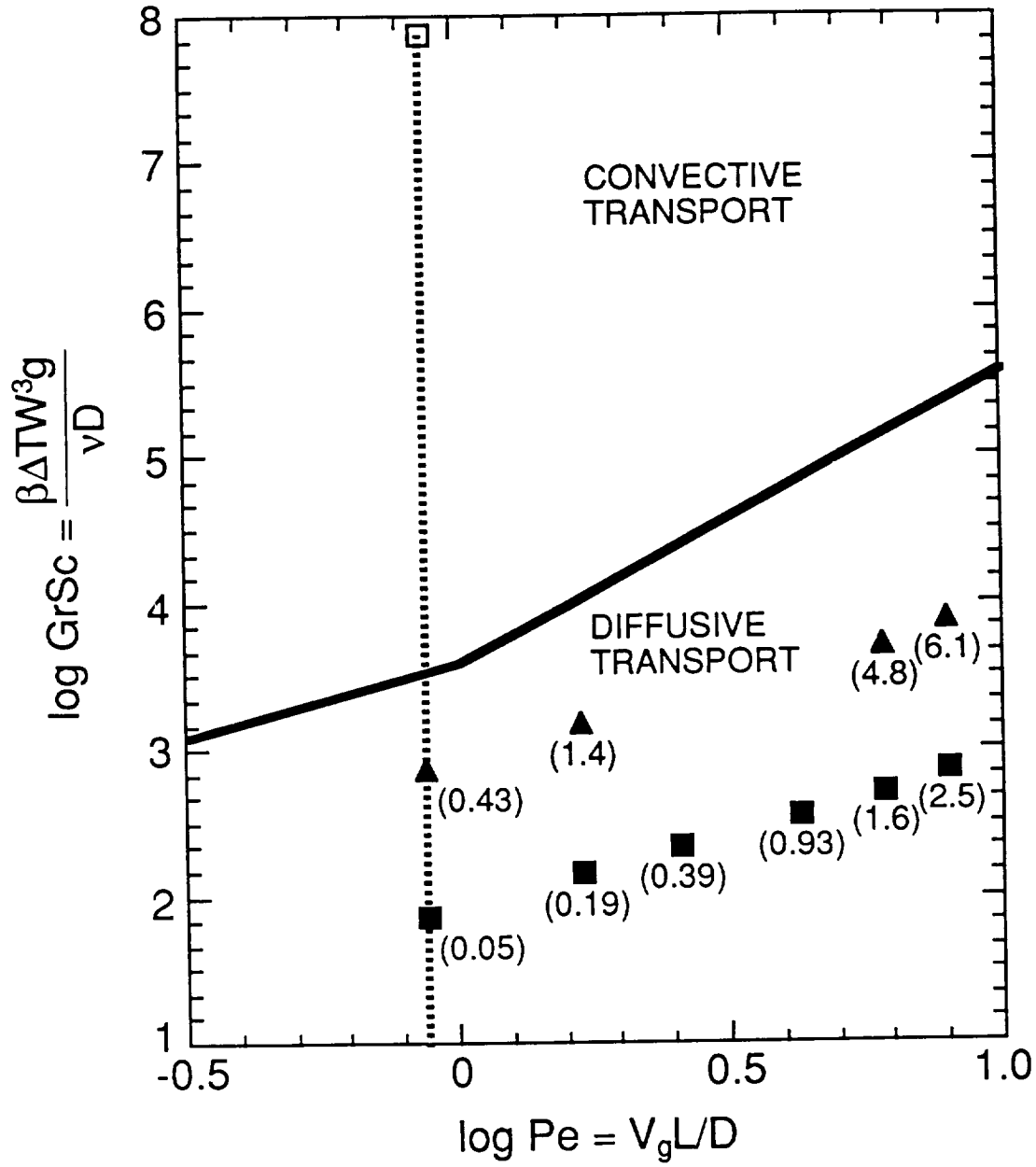

Figure 7 Favier-Camel type transport regime diagram. The thick solid line shows the estimated position of the convective-diffusive transition based on an order of magnitude analysis [13]. The open square corresponds to 1 g(Sc=10), and the filled triangles and squares to 10^{-5} and 10^{-6} g conditions respectively.

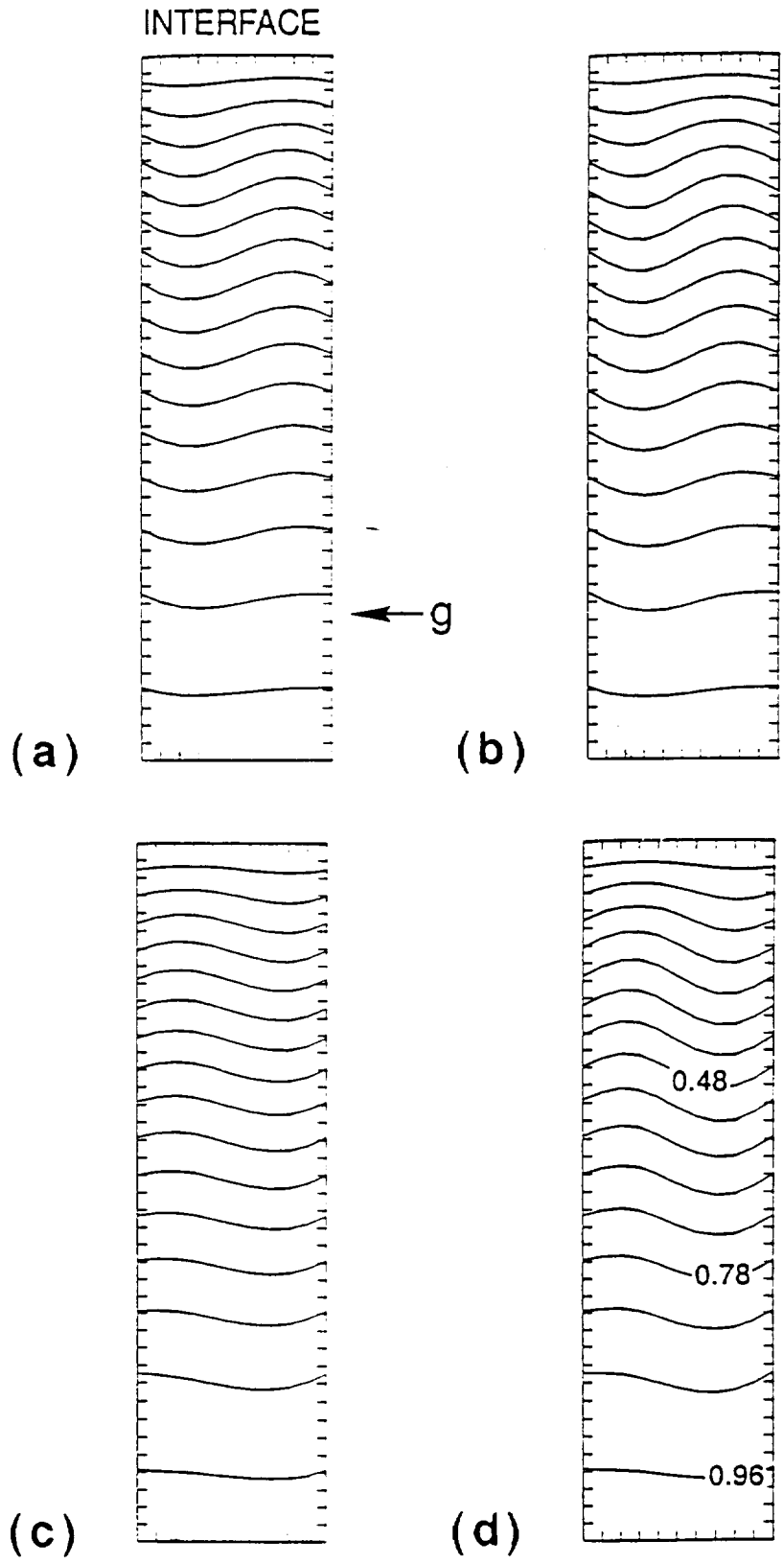

Figure 8 Temperature field at a) 25 b) 50 c) 75 and d) 100 seconds caused by a sinusoidal acceleration with magnitude 10^{-3} g and frequency 10^{-2} Hz oriented parallel to the crystal-melt interface.

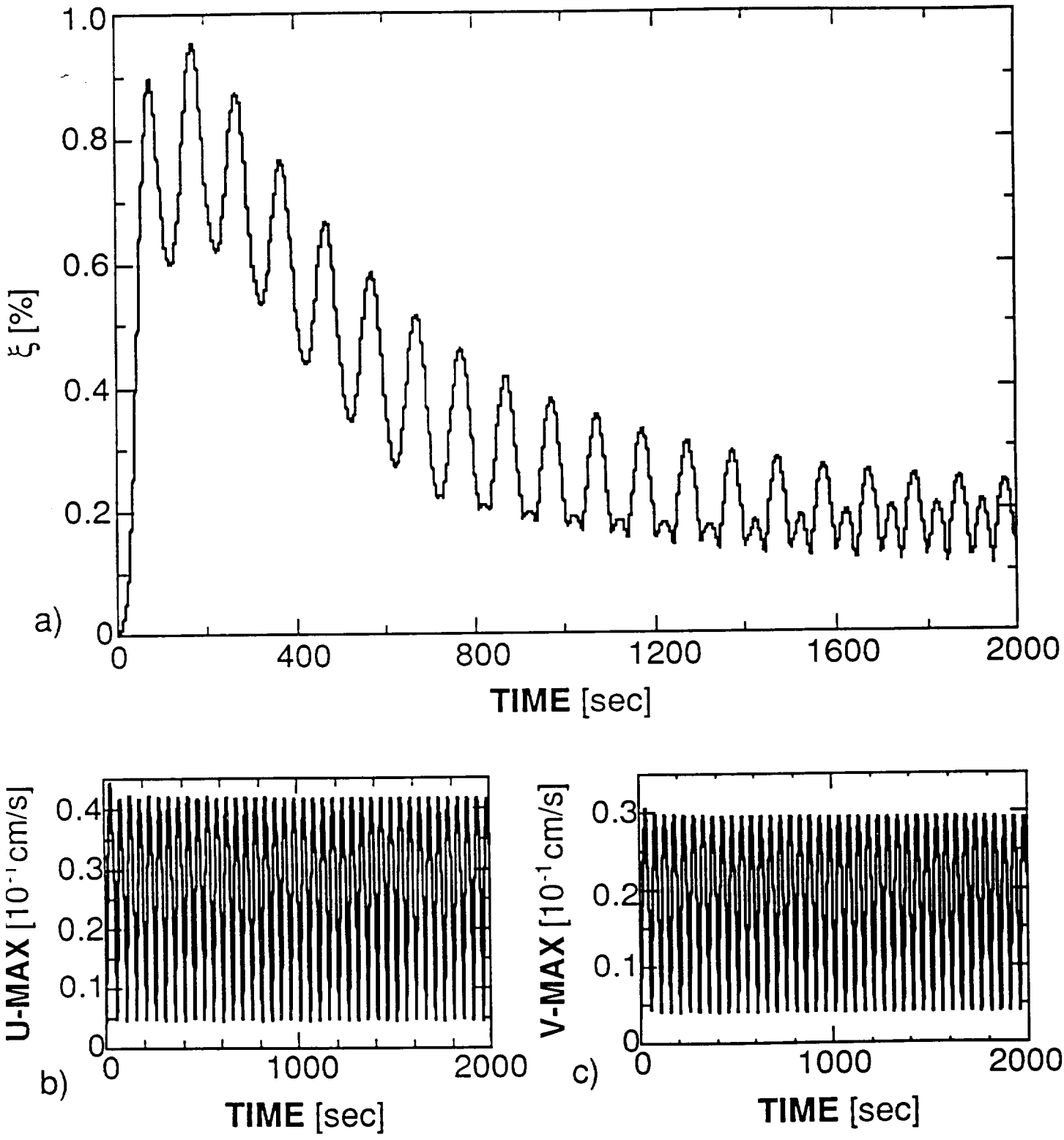

Figure 9 a) Compositional non-uniformity and Maximum b) u-velocity c) v-velocity function of time for a sinusoidal acceleration with magnitude 10^{-3} g and frequency 10^{-2} Hz oriented parallel to the crystal-melt interface.

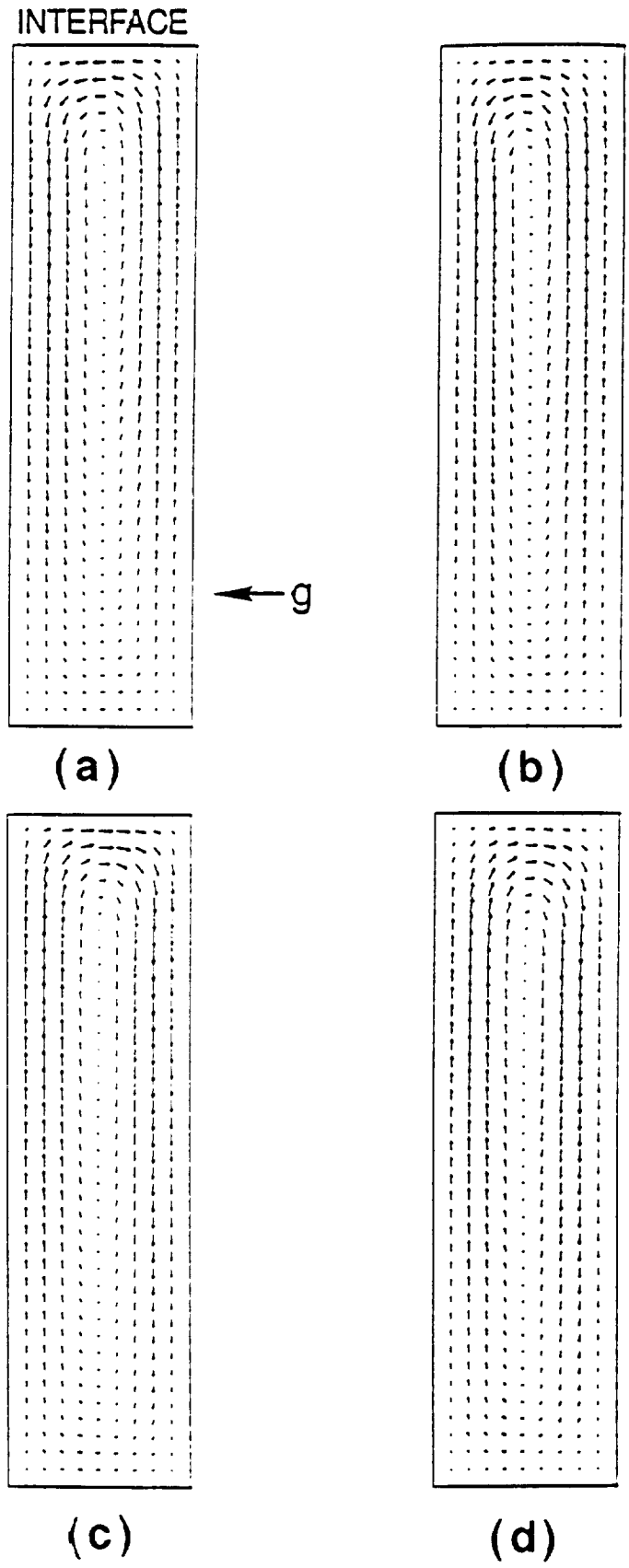

Figure 10 Velocity fields at a) 25 b) 50 c) 75 and d) 100 seconds caused by a sinusoidal acceleration with magnitude 10^{-3} g with frequency of 10^{-2} Hz oriented parallel to the crystal-melt interface.

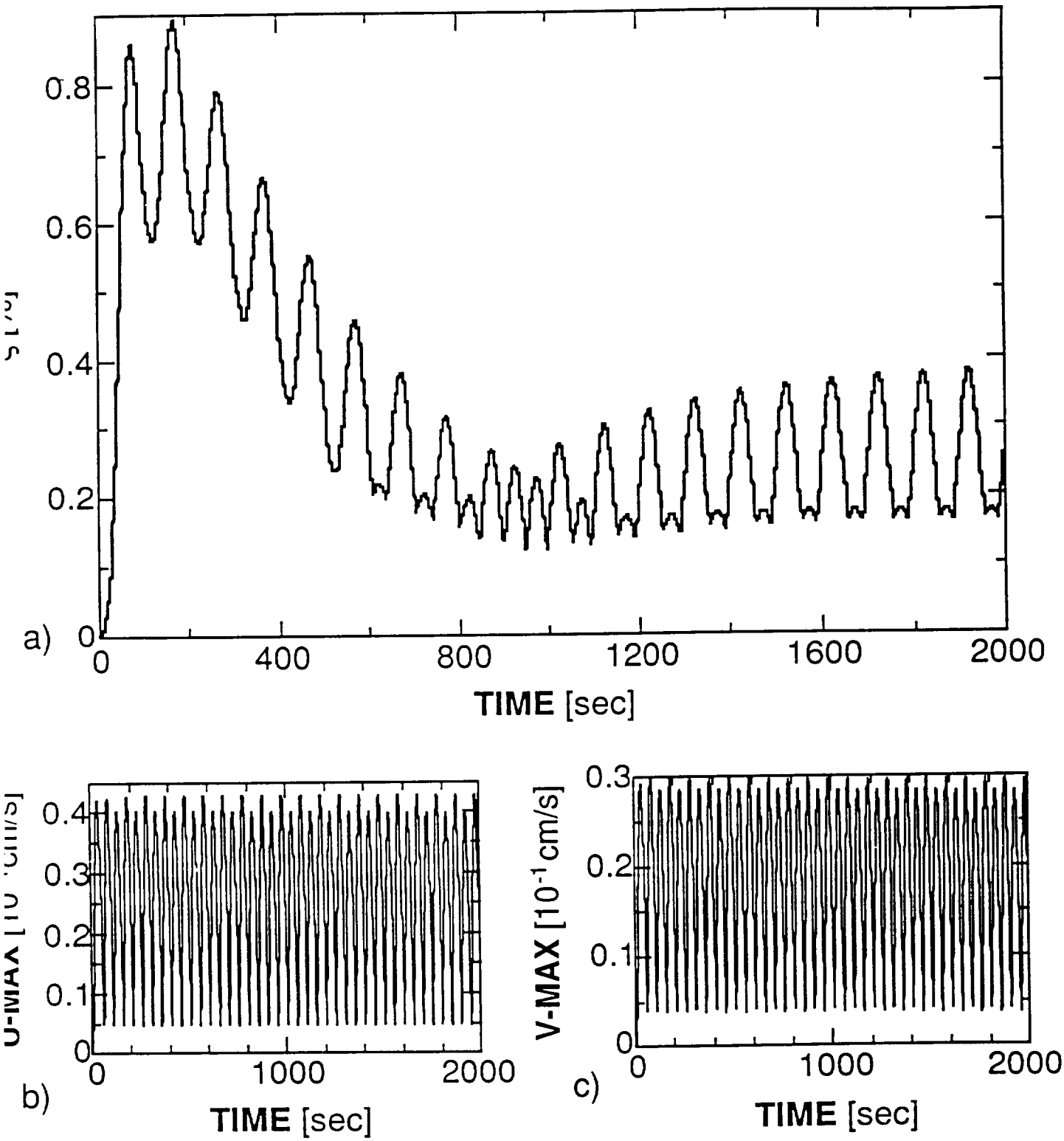

Figure 11 a) Compositional non-uniformity and maximum b) u-velocity c) v-velocity function of time for a sinusoidal acceleration with magnitude 10^{-3} g and frequency 10^{-2} Hz oriented 5 degrees with respect to the crystal-melt interface.

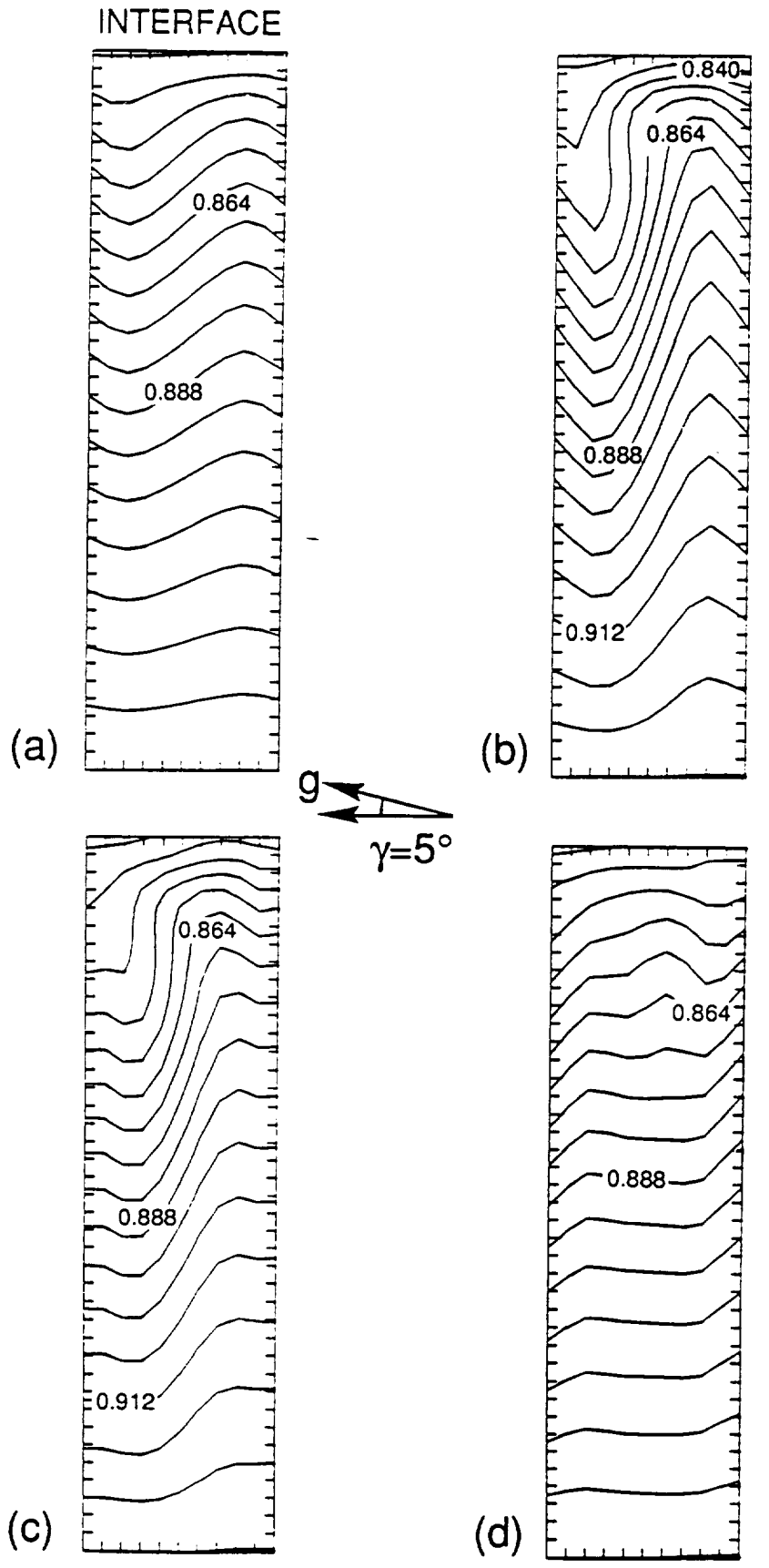

Figure 12 The solute field at a) 25 b) 50 c) 75 and d) 100 seconds for a sinusoidal acceleration with magnitude 10^{-3} g and frequency 10^{-2} Hz oriented five degrees with respect to the crystal-melt interface.

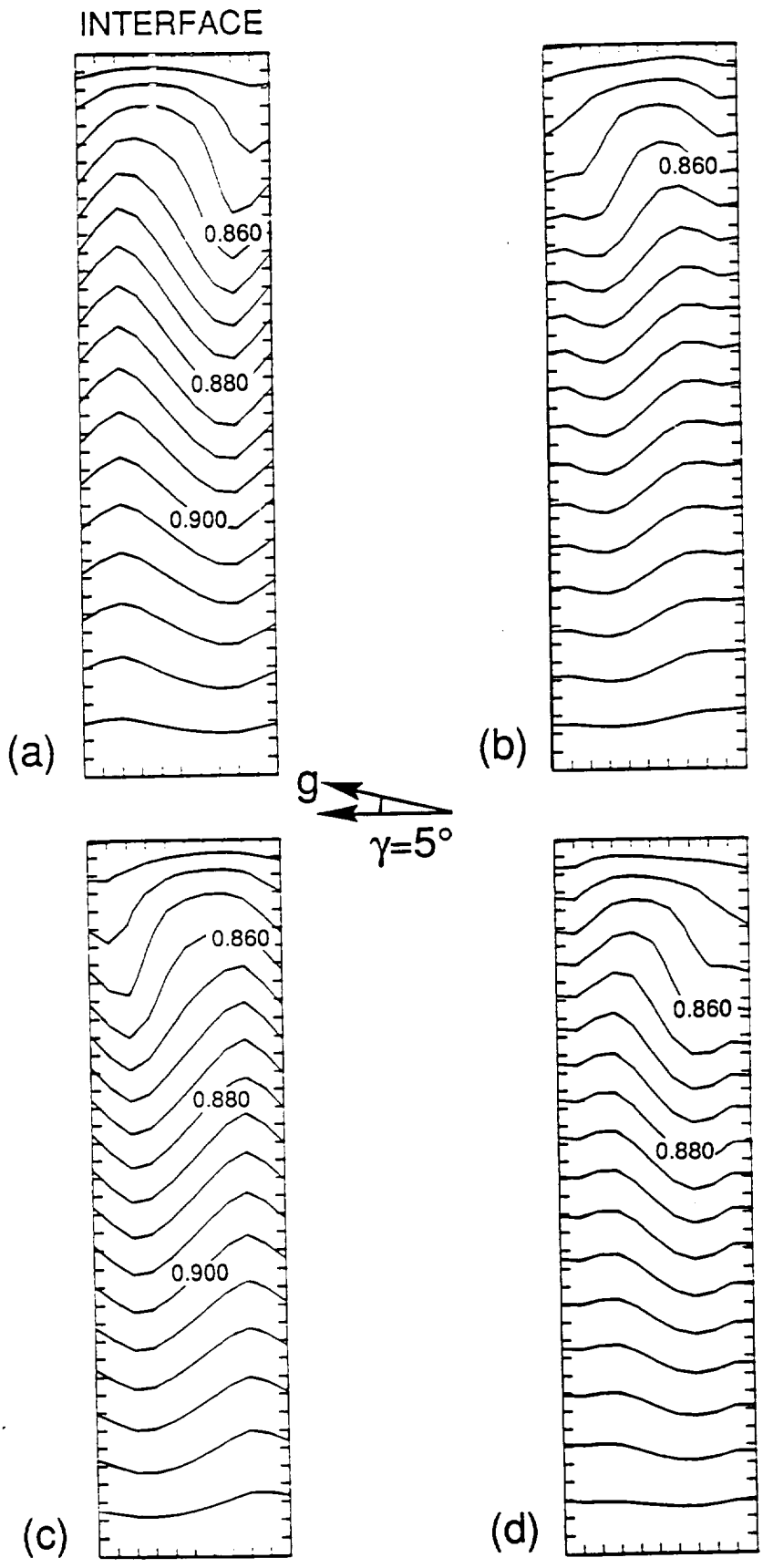

Figure 13 The solute field at a) 725 b) 750 c) 775 and d) 800 seconds for a sinusoidal acceleration with magnitude 10^{-3} g and frequency 10^{-2} Hz oriented five degrees with respect to the crystal-melt interface.

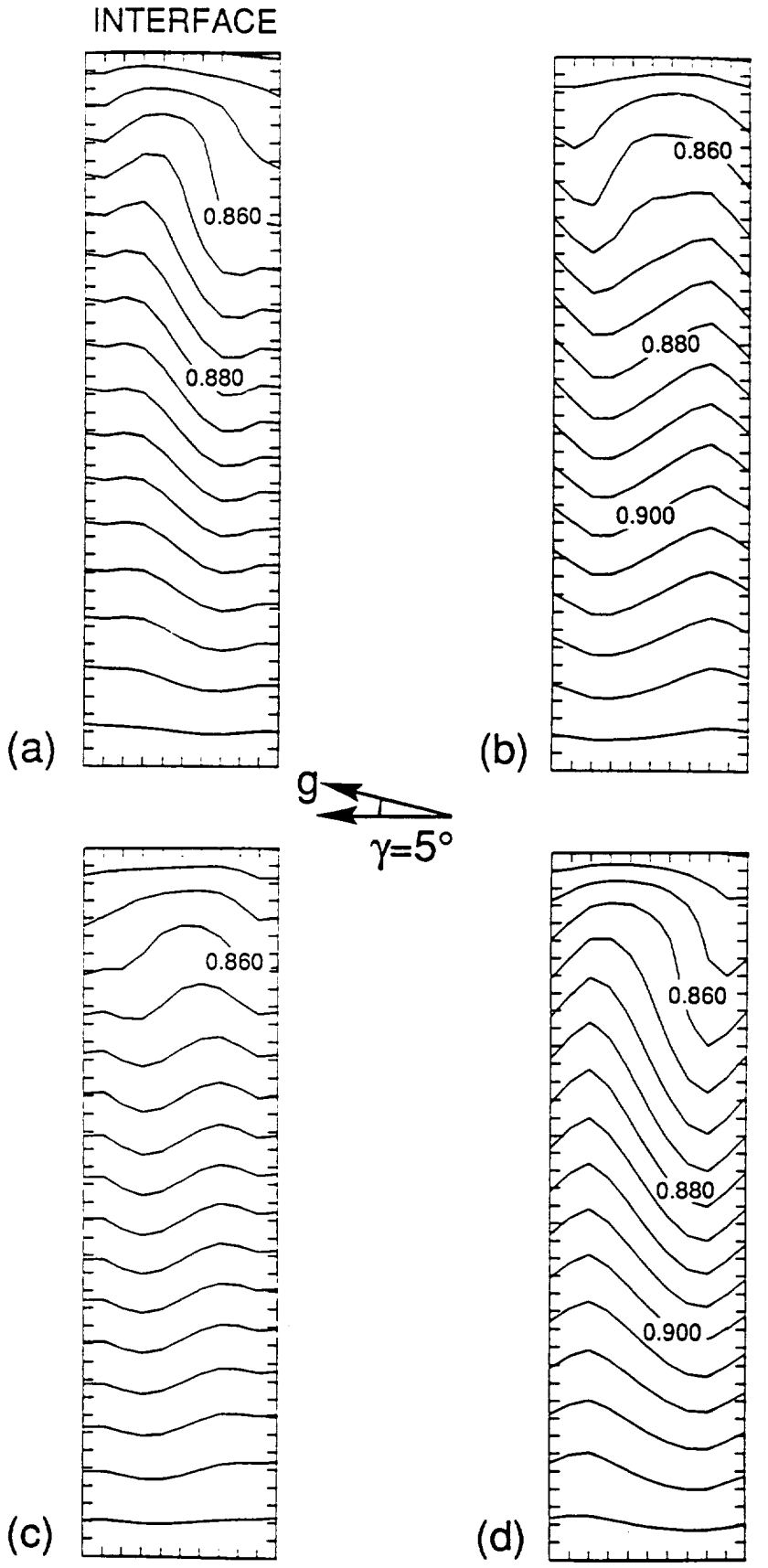

Figure 14 The solute field at a) 2025 b) 2050 c) 2075 and d) 2100 seconds for a sinusoidal acceleration with magnitude 10^{-3} g and frequency 10^{-2} Hz oriented five degrees with respect to the crystal-melt interface.

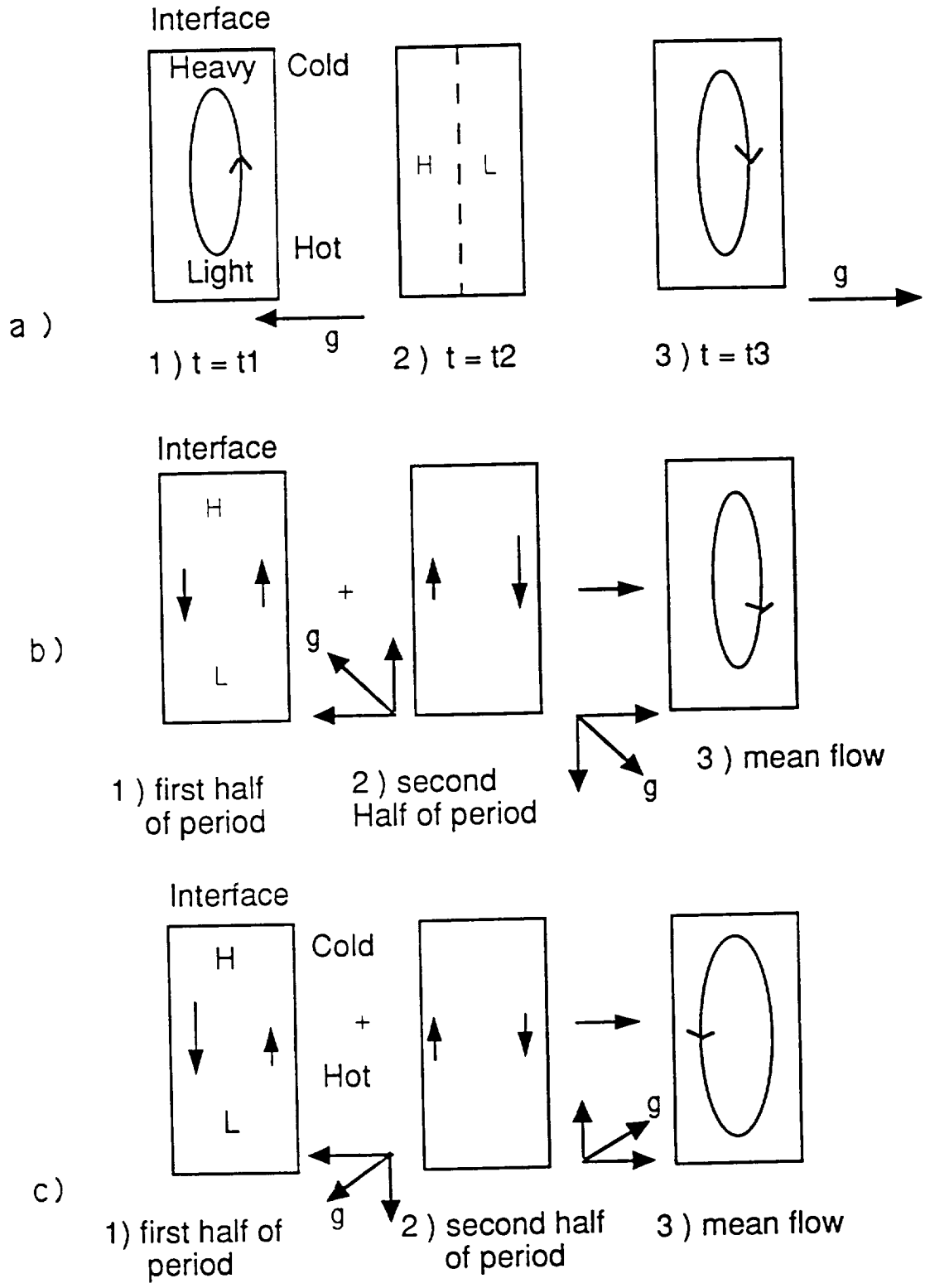

Figure 15 Direction of flows and mean flows during directional solidification for cases when the acceleration is oriented a) $\gamma = \pi/2$

b) in the range of angles $\pi/2 \leq \gamma \leq \pi$

c) in the range of angles $0 \leq \gamma \leq \pi/2$

with respect to the vertical axis.

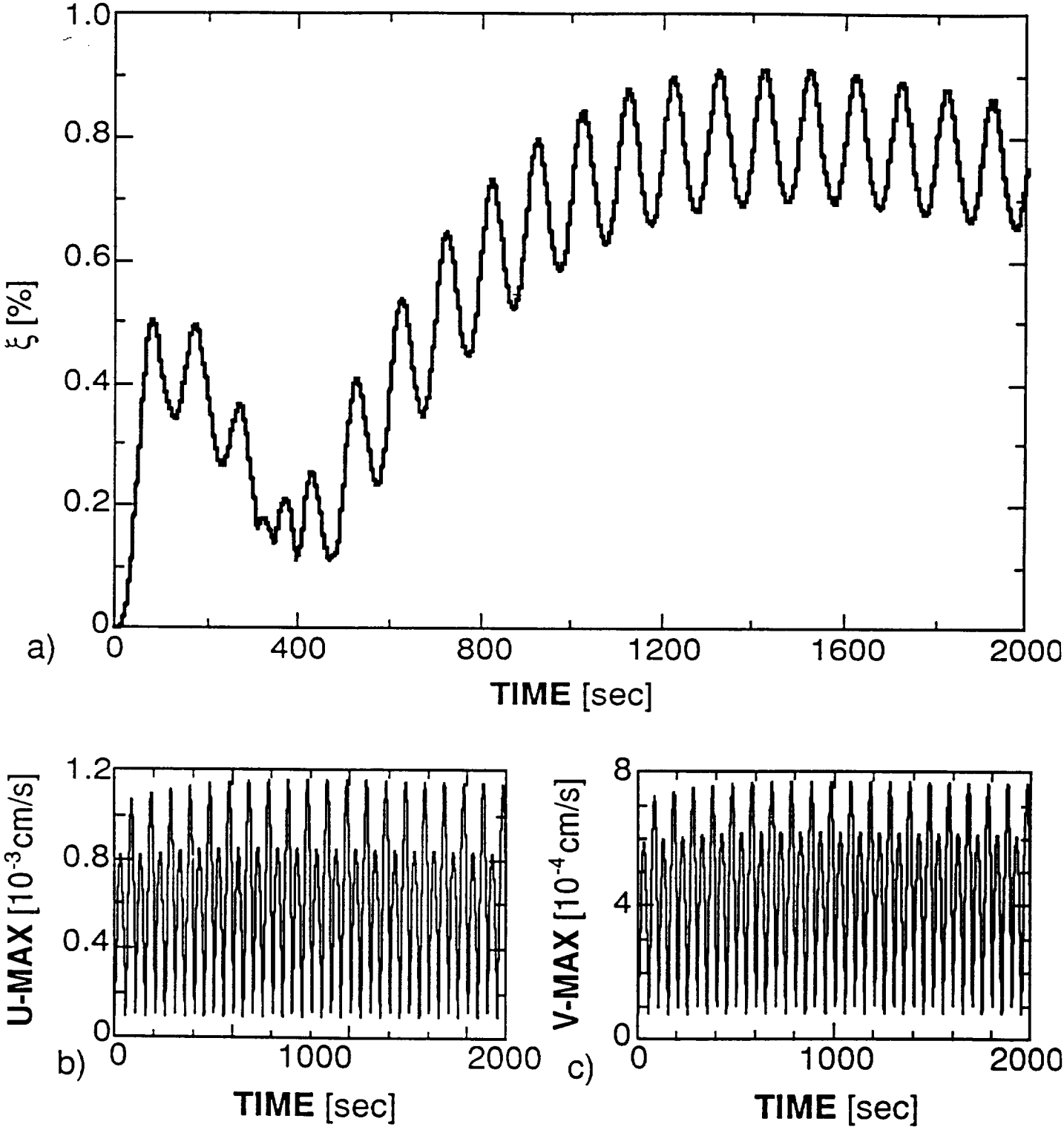

Figure 16 a) Compositional non-uniformity and maximum b) u-velocity c) v-velocity function of time for a sinusoidal acceleration with magnitude 10^{-3} g and frequency 10^{-2} Hz oriented 135 degrees with respect to the vertical axis.

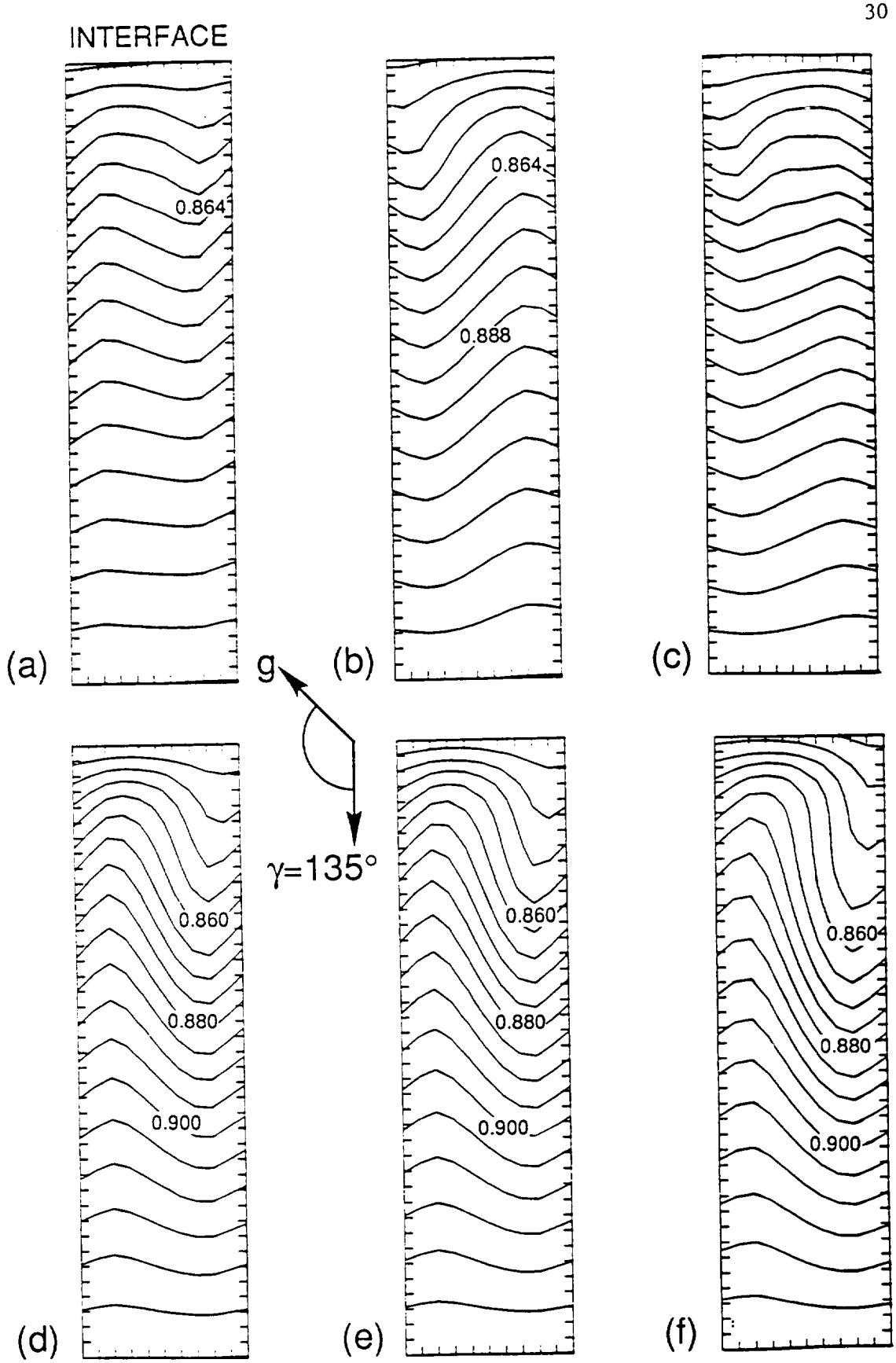

Figure 17 The solute field at a) 100 b) 150 c) 350 and d) 400 e) 500 f) 1000 seconds for a sinusoidal acceleration with magnitude 10^{-3} g and frequency 10^{-2} Hz oriented 135 degrees with respect to the vertical axis.

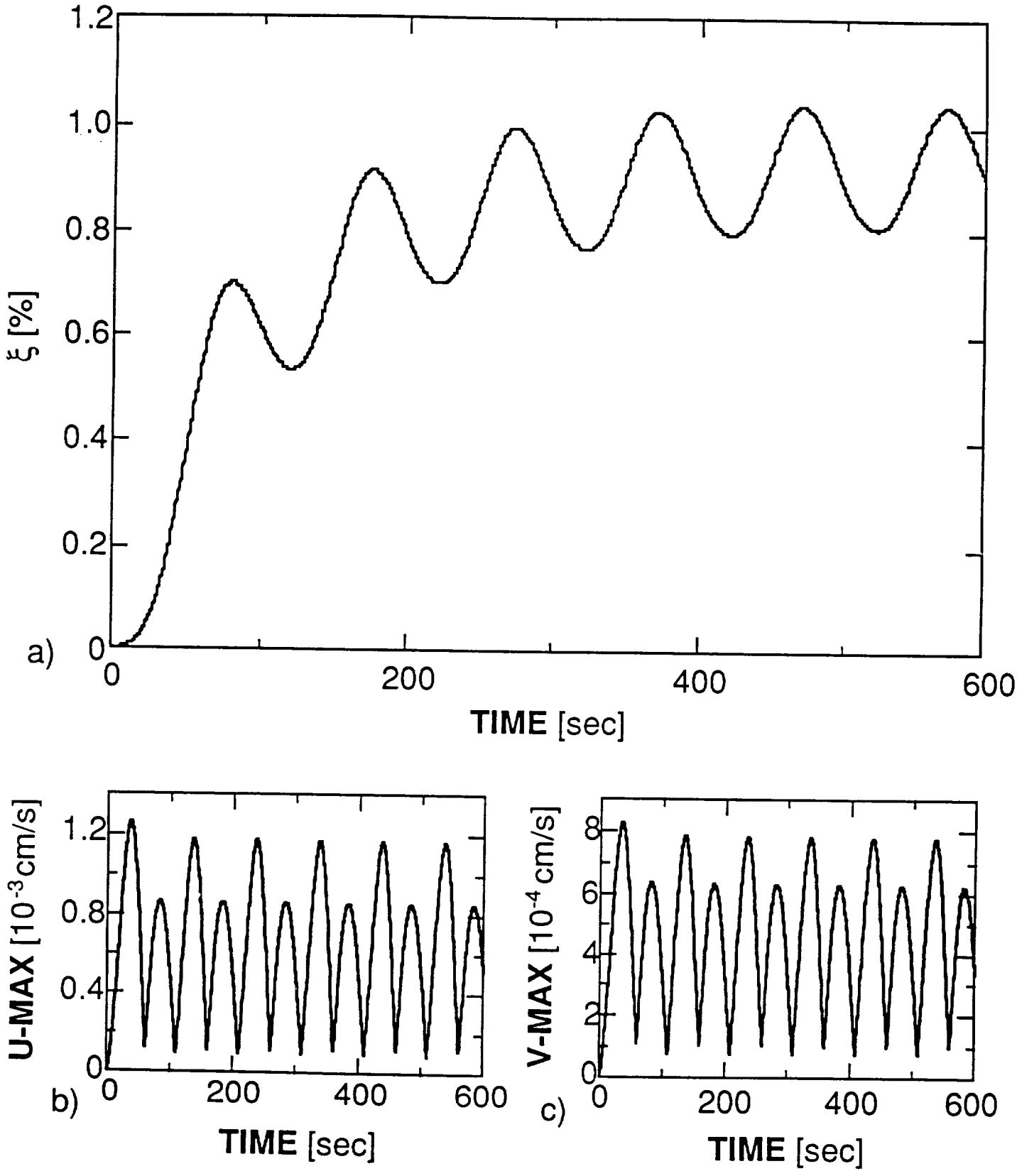

Figure 18 a) Compositional non-uniformity and maximum b) u-velocity c) v-velocity function of time for a sinusoidal acceleration with magnitude 10^{-3} g and frequency 10^{-2} Hz oriented 45 degrees with respect to the crystal-melt interface.

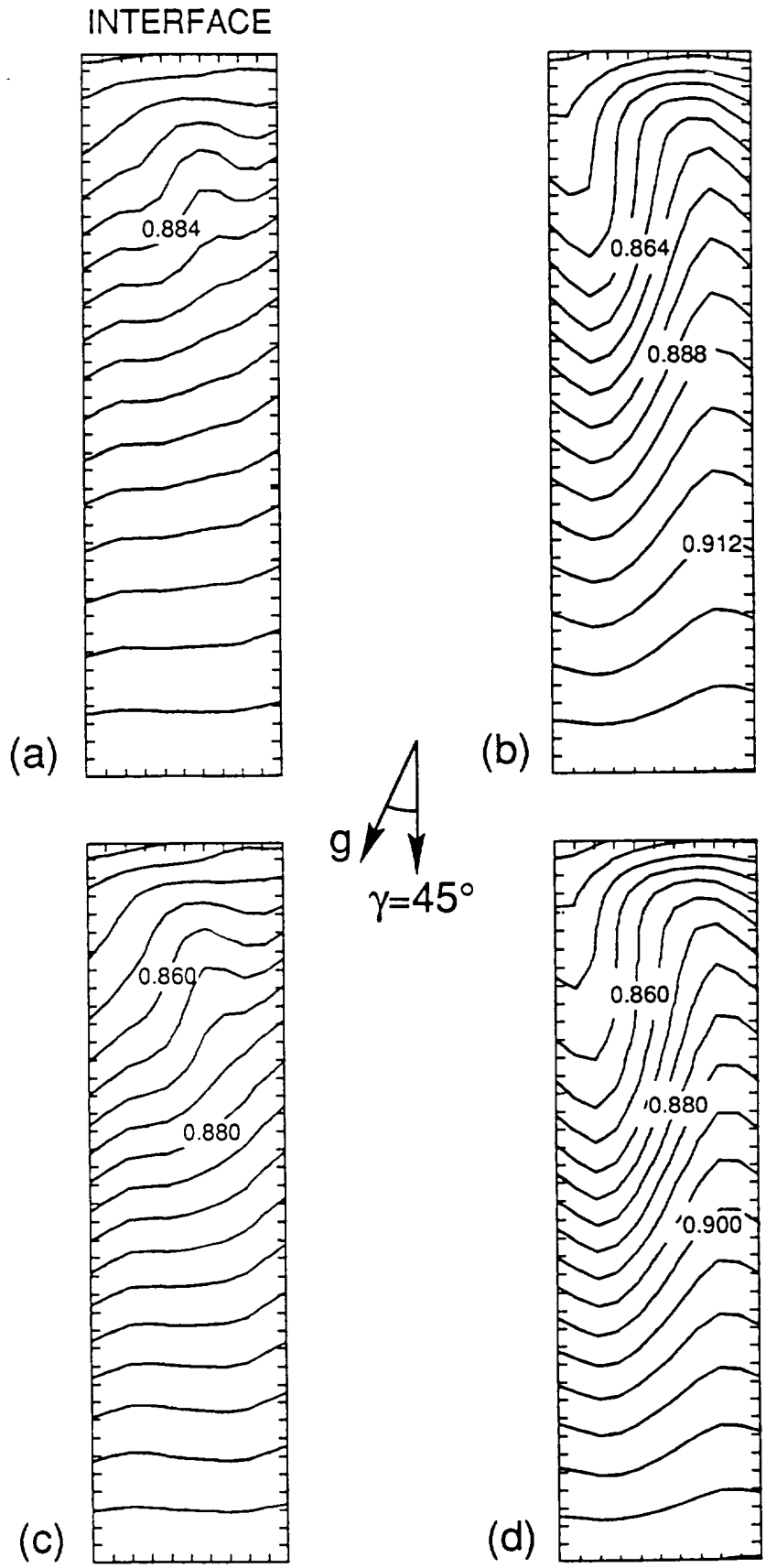

Figure 19 The solute field at a) 25 b) 50 c) 75 and d) 100 seconds for a sinusoidal acceleration with magnitude 10^{-3} g and frequency 10^{-2} Hz oriented 45 degrees with respect to the vertical axis.

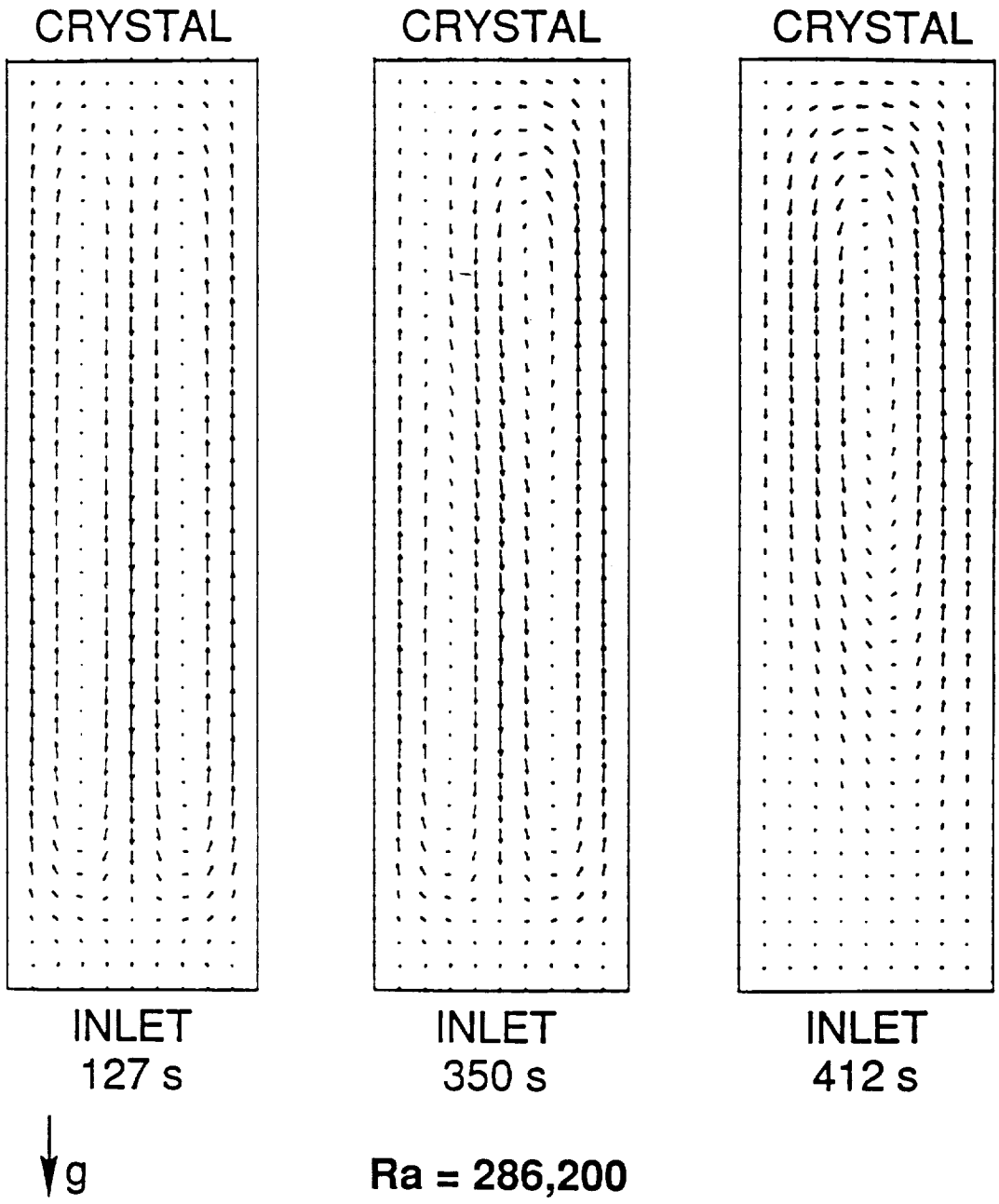

Figure 20 Transition from a two-cell symmetric flow to a single cell flow.

3. *COMPARISON OF A DIFFUSION MODEL WITH PRELIMINARY RESULTS*

3.1 Introduction

In this section we compare the results of a 1D model with preliminary results of compositional analysis carried out at Marshal Space Flight Center [1]. The model equations are exactly those proposed by Clayton et al. et al. [2]. The limitations of 1D diffusion models are well-known and have been discussed at length in the literature (for references see [3]). Nevertheless, they can still be of use in a preliminary analysis of flight data. The reason for this is that for the weakly convective conditions predicted in ***section 2.***, the average axial composition profile is close to the classical diffusion profile *even when there is significant lateral nonuniformity in melt composition.* Thus, a fit of averaged experimental profiles to an unsteady 1D diffusion model can give a reasonable estimate of the diffusion coefficient. This allows us to narrow the range of Schmidt numbers for the $Cd_{0.96}Zn_{0.04}Te$ melt. Since we only have electron microprobe compositional analyses of the flight sample #2 we cautiously estimate the diffusion coefficient to be between 3 - 4×10^{-5} cm^2s^{-1}. (The lower value has been independently obtained by Gillies et al. [1] from averaged data taken from ground samples.) If we assume the viscosity to be that of CdTe, this places our estimate of the Schmidt number in the range 100-150 .

3.2 Results

The compositional data from flight sample #2 is shown in Fig. 1. Note the abrupt changes in composition at 10.1 mm and 15.2 mm. We carried out a set of calculations to see if these changes could correspond to rate changes. The results are shown in Figs. 2-7. Three rate changes were examined. Fig.1 corresponds to a rate change from 1.6 mm/hr to 8 mm/hr, Fig. 2 from 1.6 mm/hr to 16 mm/hr and Fig.3 from 1.6 mm/hr to 32 mm/hr. Note that the concentration changes following each change of rate are sharp, in contrast to those exhibited in Fig. 1. This may reflect that the model assumes an immediate response to changing thermal conditions, for example a local deviation from the expected temperature gradient due to the proximity of a free surface, or that latent heat release is not accounted for by the model. This question can only be properly addressed with a model that accounts for the deviation of the interface shape from planarity and that accounts for latent heat release at the advancing crystal surface.

3. 3 References

[1] D. Gillies, S. L. Lehoczky, F.R. Szofran, D.J. Larson, C.-H. Su , Y.-G. Sha and H.A. Alexander, Growth and Characterization of Materials for Infra-red detectors, SPIE Vol. 2021, 1993.

[2] J.C. Clayton, M.C. Davidson, D.C. Gillies and S. L. Lehoczky, JCG 60 (1982) 374.

[3] J.I.D. Alexander and F. Rosenberger, in Low gravity fluid dyanmics and trasnport phenomena, J.L. Koster and R.L. Sani eds., Vol. 130 Progress in Astronautics and Aeronautics (AIAA, Washington D.C., 1990)

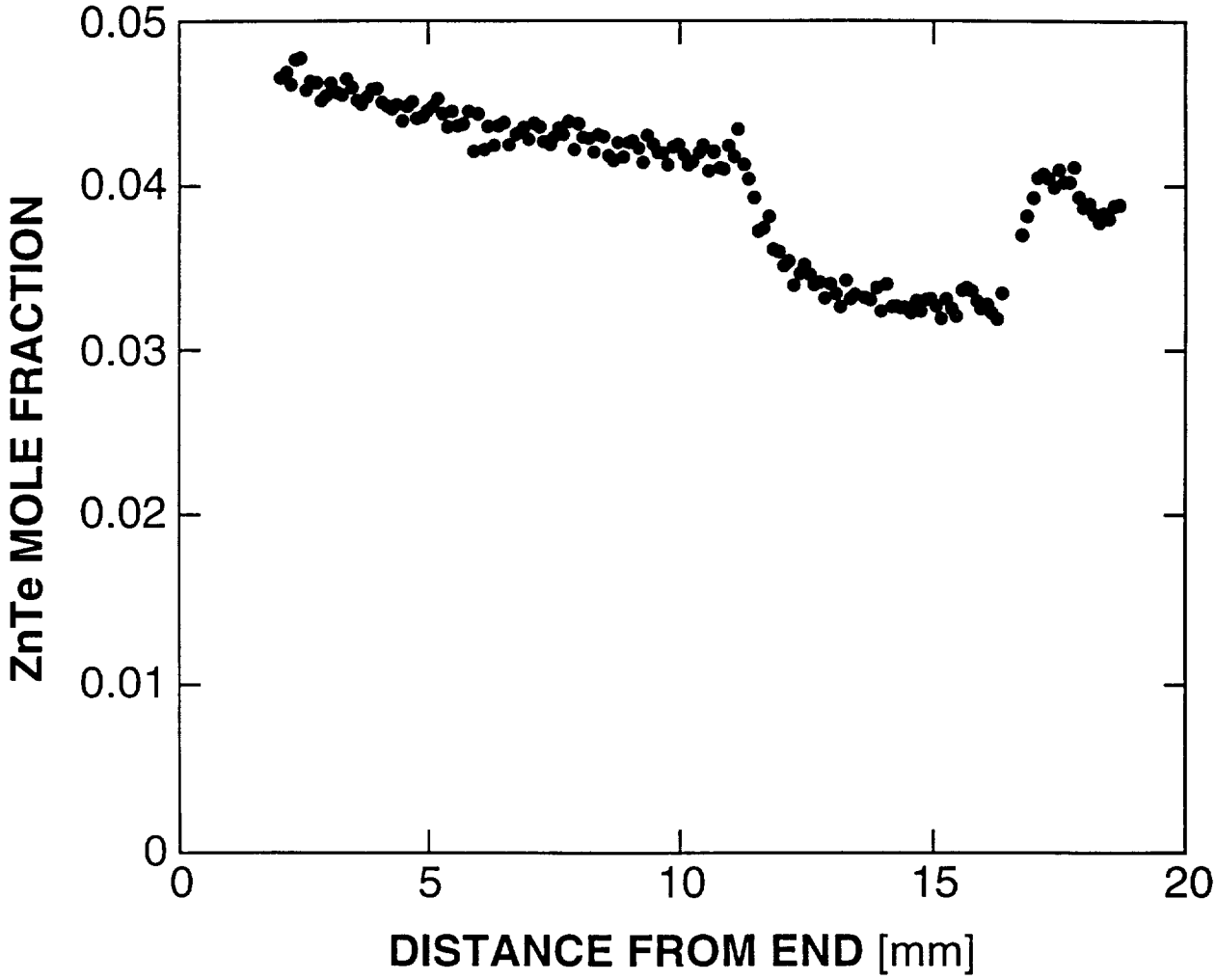

Figure 21a Composition profile of GCRC #2. (Courtesy of D.L. Gillies, MSFC).

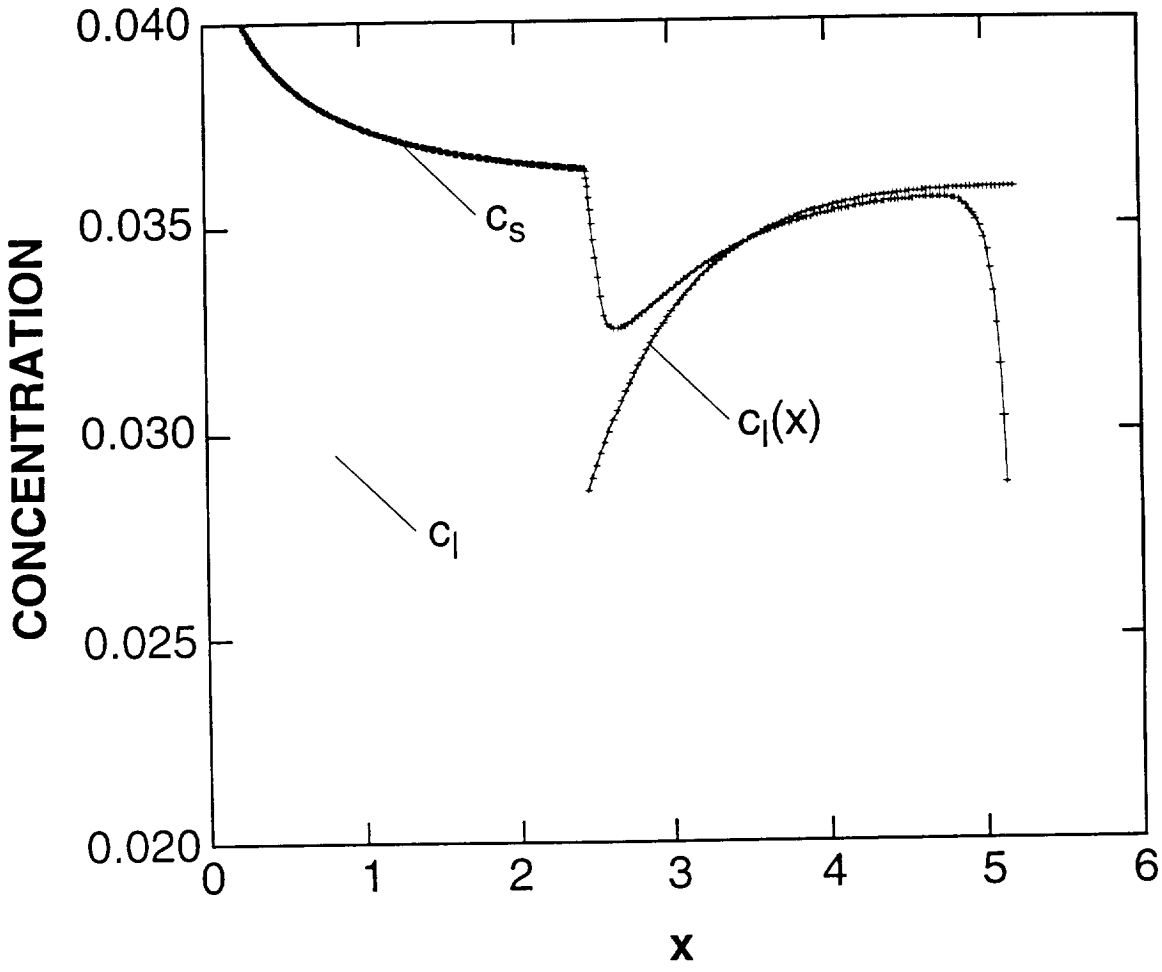

Figure 21b Response to a growth rate change from 1.6 mm/hr to 8 mm/hr (× 5)

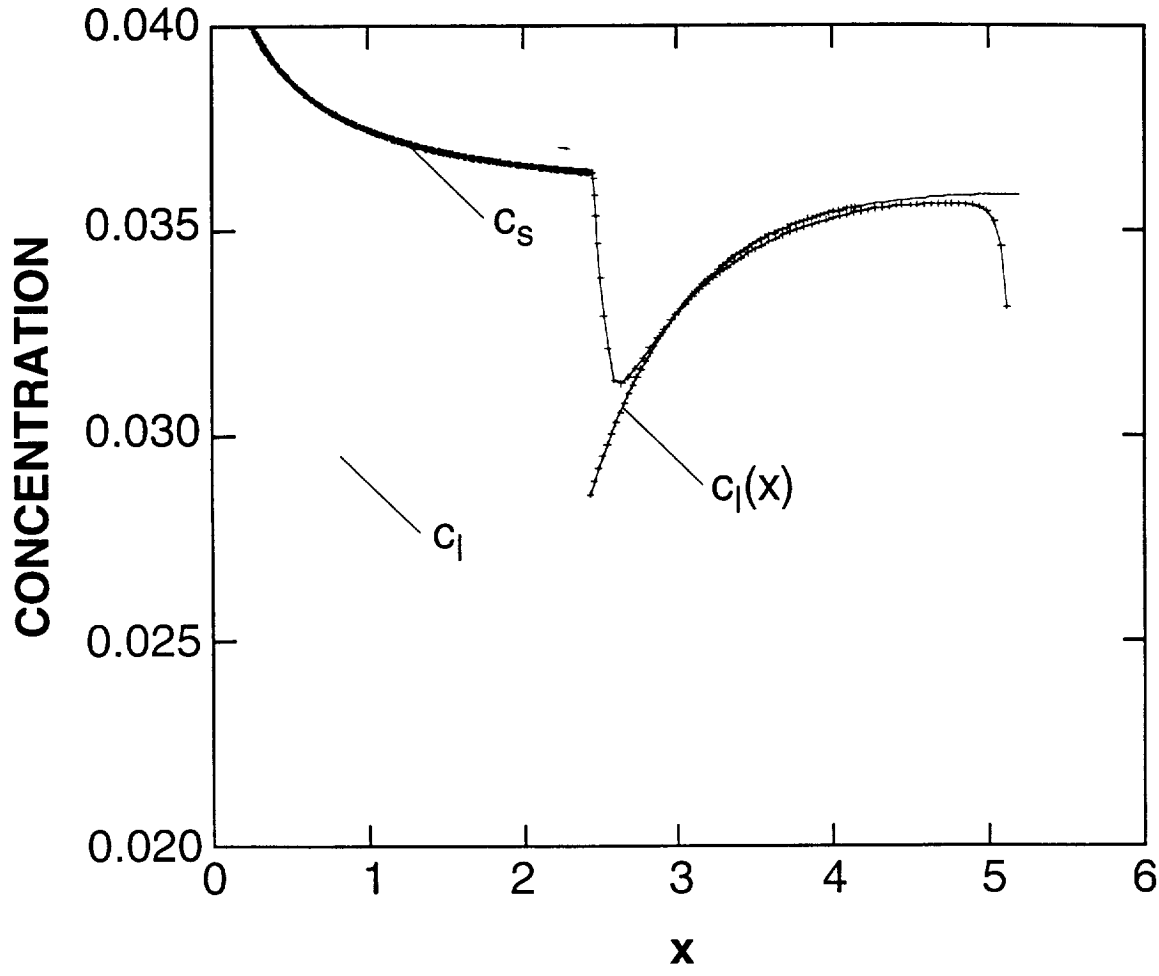

Figure 22 Response to a growth rate change from 1.6 mm/hr to 16 mm/hr (× 10)

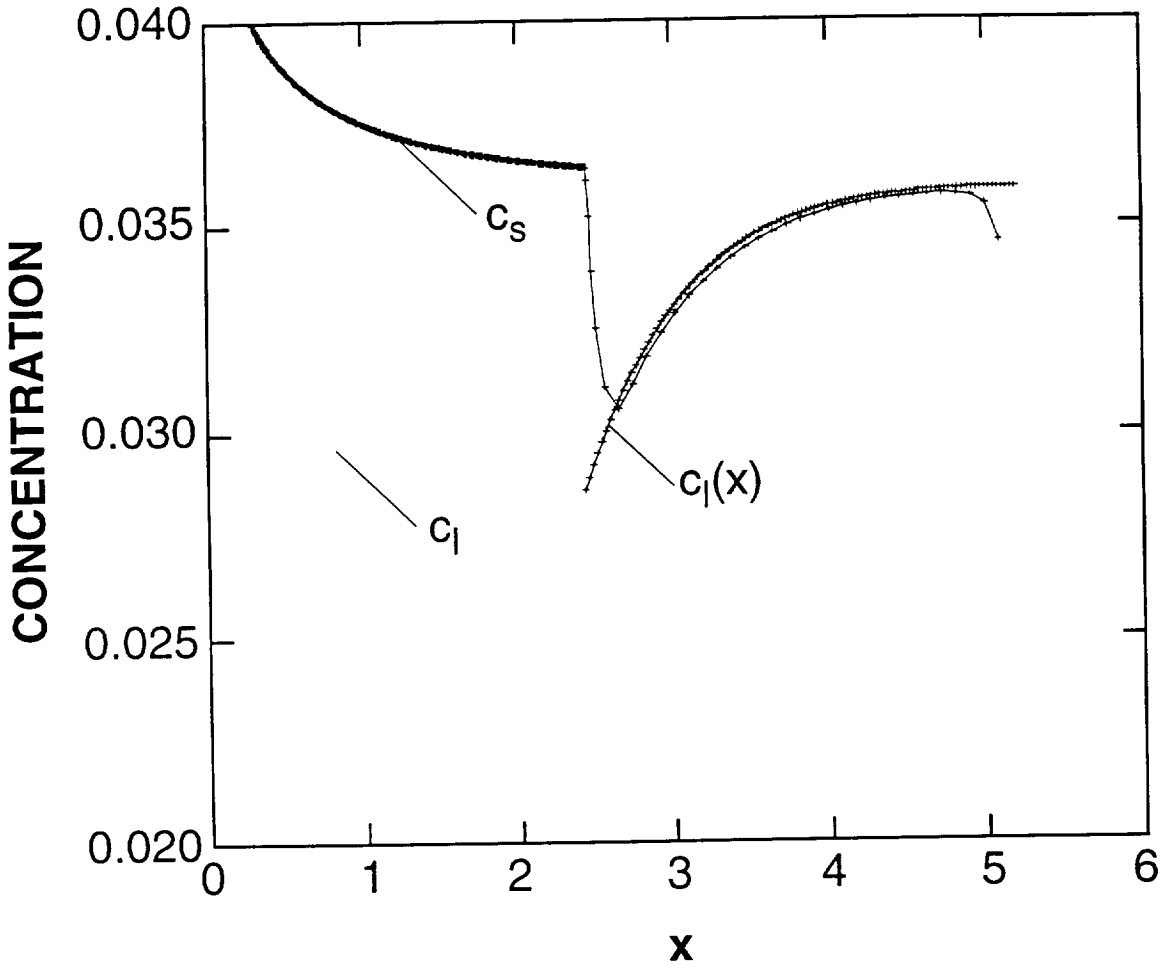

Figure 23 Response to a growth rate change from 1.6 mm/hr to 32 mm/hr (× 20)

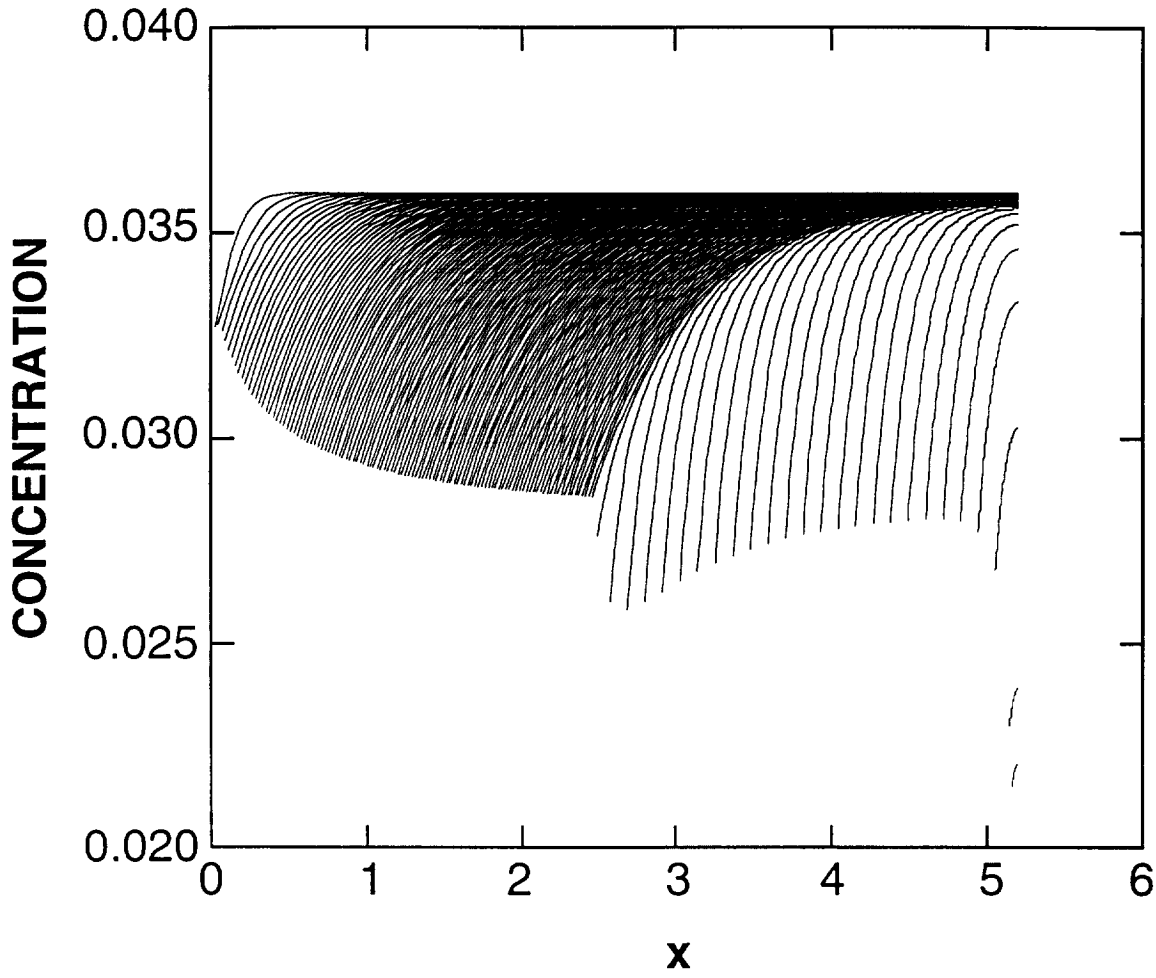

Figure 24 Liquid concentration profiles at successive times corresponding to Fig. 21b

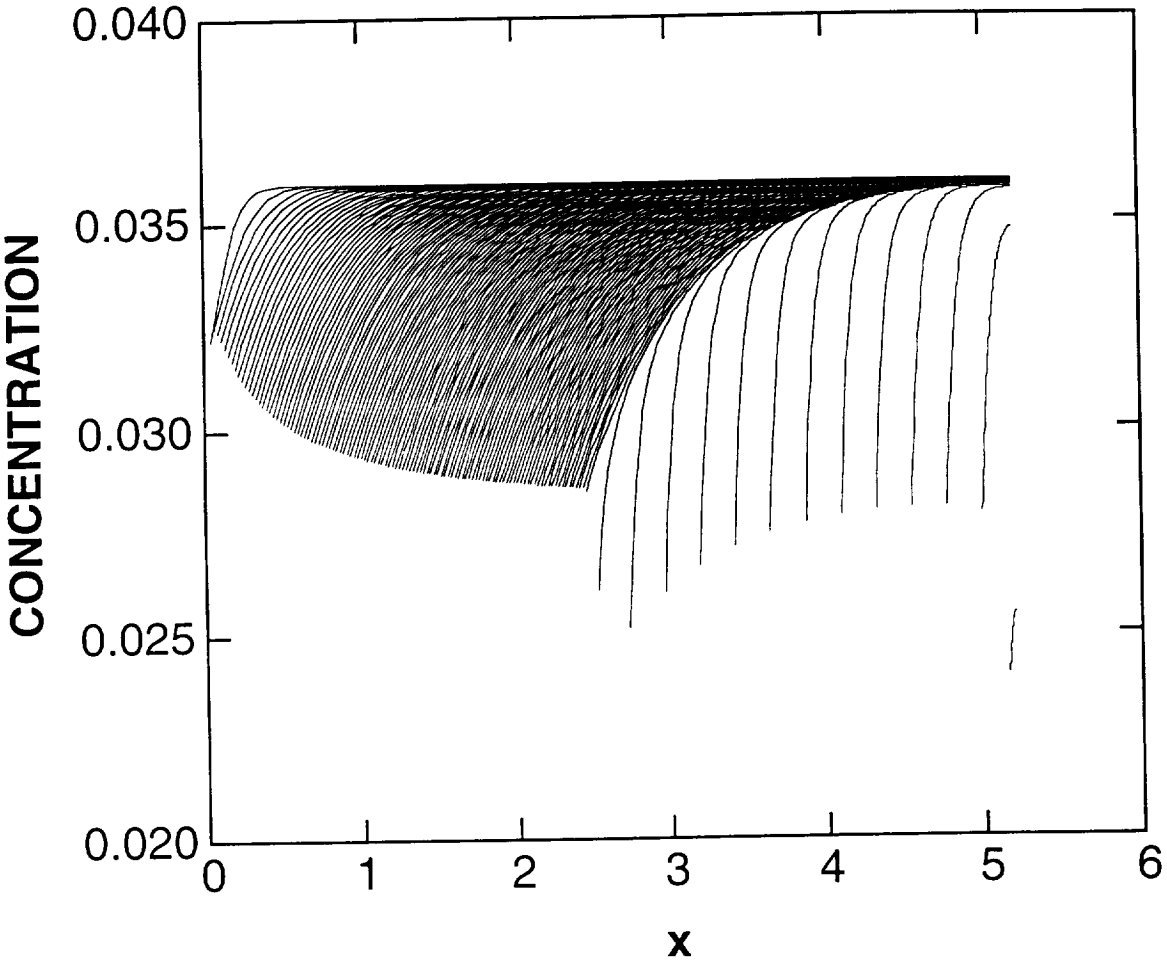

Figure 25 Liquid concentration profiles at successive times corresponding to Fig. 22

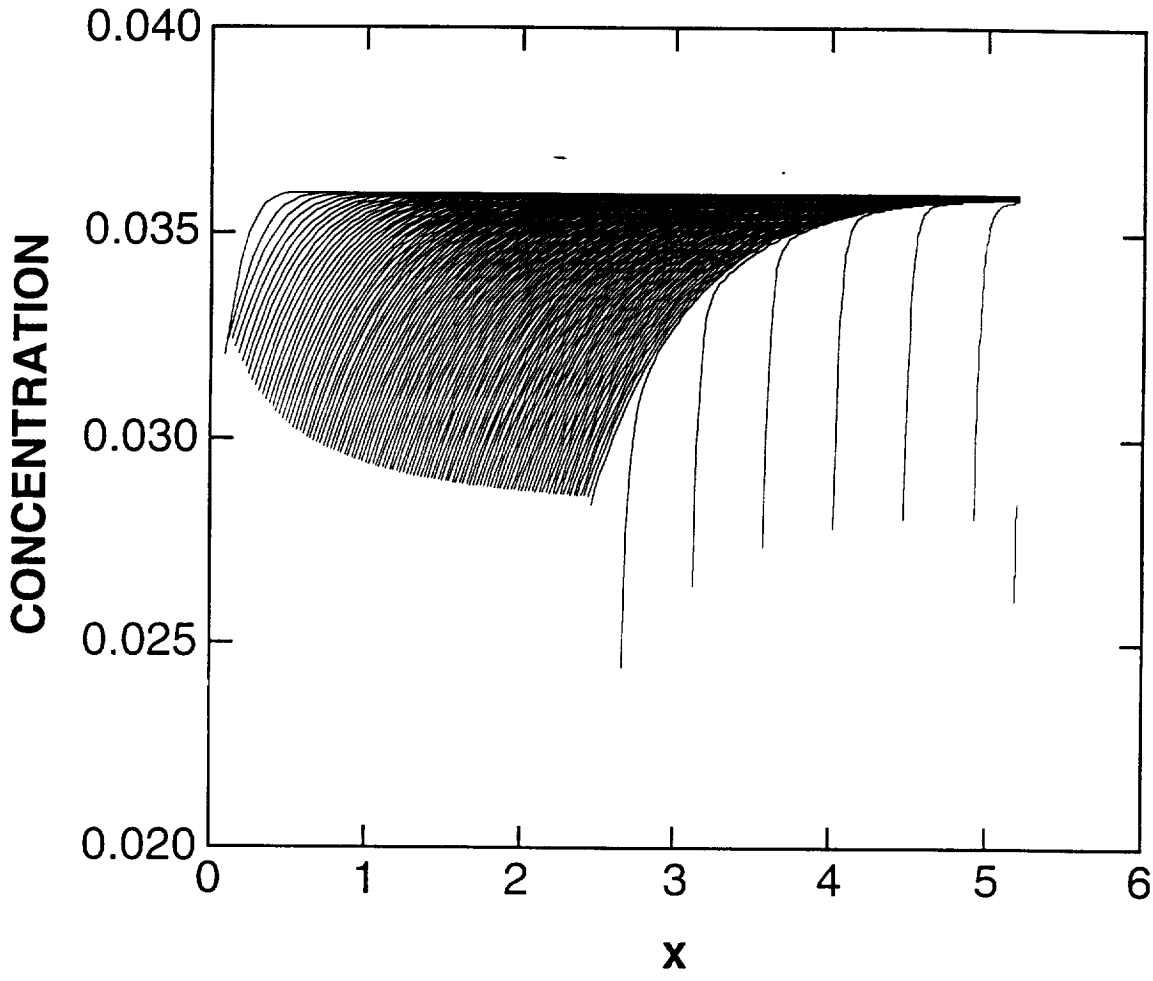

Figure 26 Liquid concentration profiles at successive times corresponding to Fig. 23

4. *QUALITATIVE ANALYSIS OF MELT/AMPOULE WETTING CONDITIONS*

4.1 Ampoule-melt and crystal-ampoule wetting conditions

There are three mechanisms that can lead to loss of contact between a melt and ampoule, and a crystal-melt surface and the ampoule [1]. For the CdZnTe microgravity experiment, loss of contact probably occurred due to two of these mechanisms. The reasons for this are outlined below. The first is the formation of macroscopic voids in the ampoule. The second is the so-called dewetting process most recently advanced by Duffar et al. [1]. A melt solidifying in a partly tapered ampoule may undergo loss of contact in the immediate vicinity of the crystal-melt interface (see section ***4.3***). Although this will generally be a transient phenomenon, it may persist for some time if conditions for necking are satisfied, particularly if it is coupled with the microscopic dewetting process discussed in section ***4.2***. Obviously these conclusions are qualitative and are based on simple geometric and thermodynamic arguments. More complicated phenomena, such as contact line dynamics at the ampoule-melt contact, may also have to be accounted for explicitly.

4.2 Crystal-melt-ampoule wall contact under low gravity conditions

During directional solidification the melt, particularly under low gravity conditions, the melt may locally lose contact with the ampoule wall. As a result, solidification may take place without the constraint of the ampoule wall. For crystals that expand upon freezing, e.g., semiconductors, this leads to a reduction of the stress caused by the constraining ampoule wall. The general mechanisms that might lead to loss of contact are discussed by Duffar et al. [1] and are summarized below. This is taken as a starting point for discussing the solidification of semiconductors in tapered ampoules and possible mechanisms for maintaining loss of wall contact near the growth front. Then, the extent to which these mechanisms may apply to CdZnTe solidification is estimated based on limited thermodynamic data and from qualitative evaluations of previous experiments.

4.3 "Loss-of-contact " mechanisms

4.3.1. Free Volume, bubble and void formation: The formation of voids, bubbles and other free volumes in semiconductor melts seems to be a thermodynamically and mechanically unavoidable situation. Under low gravity conditions, these bubbles will generally not migrate to a common location. They are formed due to such diverse sources as sample volume variations, sample filling defects, degassing and under conditions when the liquid will separate into zones due to capillary instability. The following discussion will deal with the latter. The behavior of liquids in partially filled containers has been addressed in a preliminary fashion by Sen and Wilcox [2,3]. They carried out an experimental study to examine the phenomenon of loss of contact between partially wetting and non-wetting liquids and containers under low gravity conditions. Their results are discussed below.

Stability of the melt volume

The first thought that comes to mind when considering total melt detachment from a cylindrical ampoule wall under low gravity conditions is that the melt volume may assume a prolate cylindrical shape. We know from extensive work on liquid columns or bridges that the stability of a cylindrical liquid column depends on its volume, V, aspect ratio $\Lambda = L/2R$, where L is the column length and R is the radius, and on the contact angles made by the bridges with their solid supports (in this case the crystal). For the case of a non-wetting melt, one can envisage the formation of such a volume (depicted schematically in Fig. 27). However, the shape stability will be limited by capillary instability once the aspect ratio of the melt becomes sufficiently large. We already know that for melts having volumes = $\pi R^2 L$, the maximum value of the aspect ratio Λ_{max} is π. For other volumes and depending on the growth angle θ_s, the value of Λ_{max} may increase or decrease.

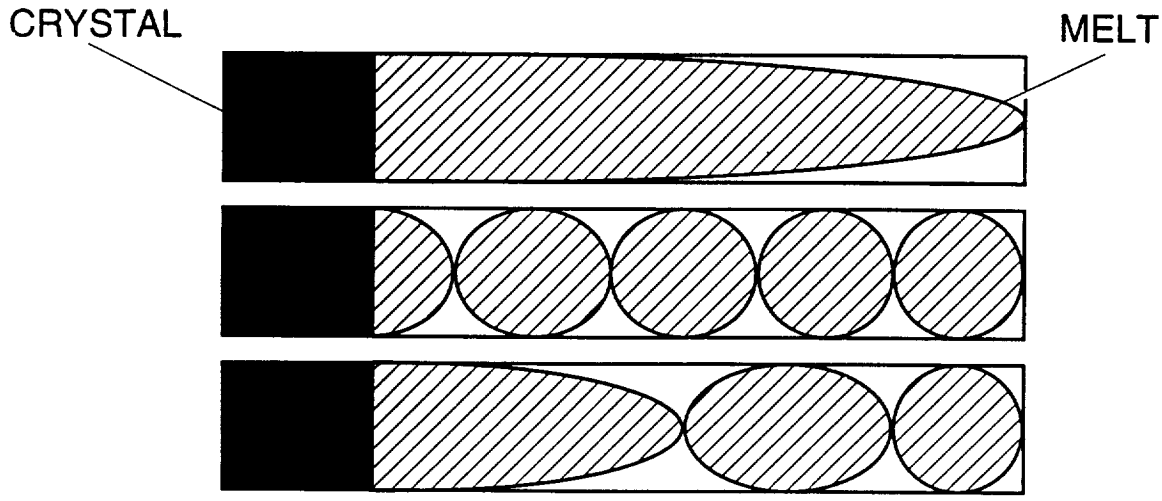

Fig. 27. Schematic depiction of melt volume following complete or partial loss of wall contact

The maximum stable melt length can be increased by allowing for a significant difference between melt ampoule volume (see Fig. 28). However, a significant increase beyond $L/D = \pi$, requires volumes greater than the right circular cylindrical volume that could be contained within the bridge and, thus, would be impractical for a solidification experiment. In addition, it must be assured that the melt is anchored at both at the crystal and at the far end. For melt lengths greater than Λ_{max}, or simply not sufficiently well anchored, the liquid will break up into zones. The number of zones and their shape will depend on the volume of the melt relative to the available space in the ampoule. In addition, the wetting properties of the melt and ampoule appear to be crucial. For example, Sen and Wilcox [2] observed that for partially wetting melts the liquid broke up into zones. The extent to which the bulk of the surfaces of these zones will wet the ampoule wall depends on the wetting angle θ_w. For non-wetting melts, contact may be lost along the bulk of the zone provided that the third fluid phase (for example a vapor) is able to displace the melt.

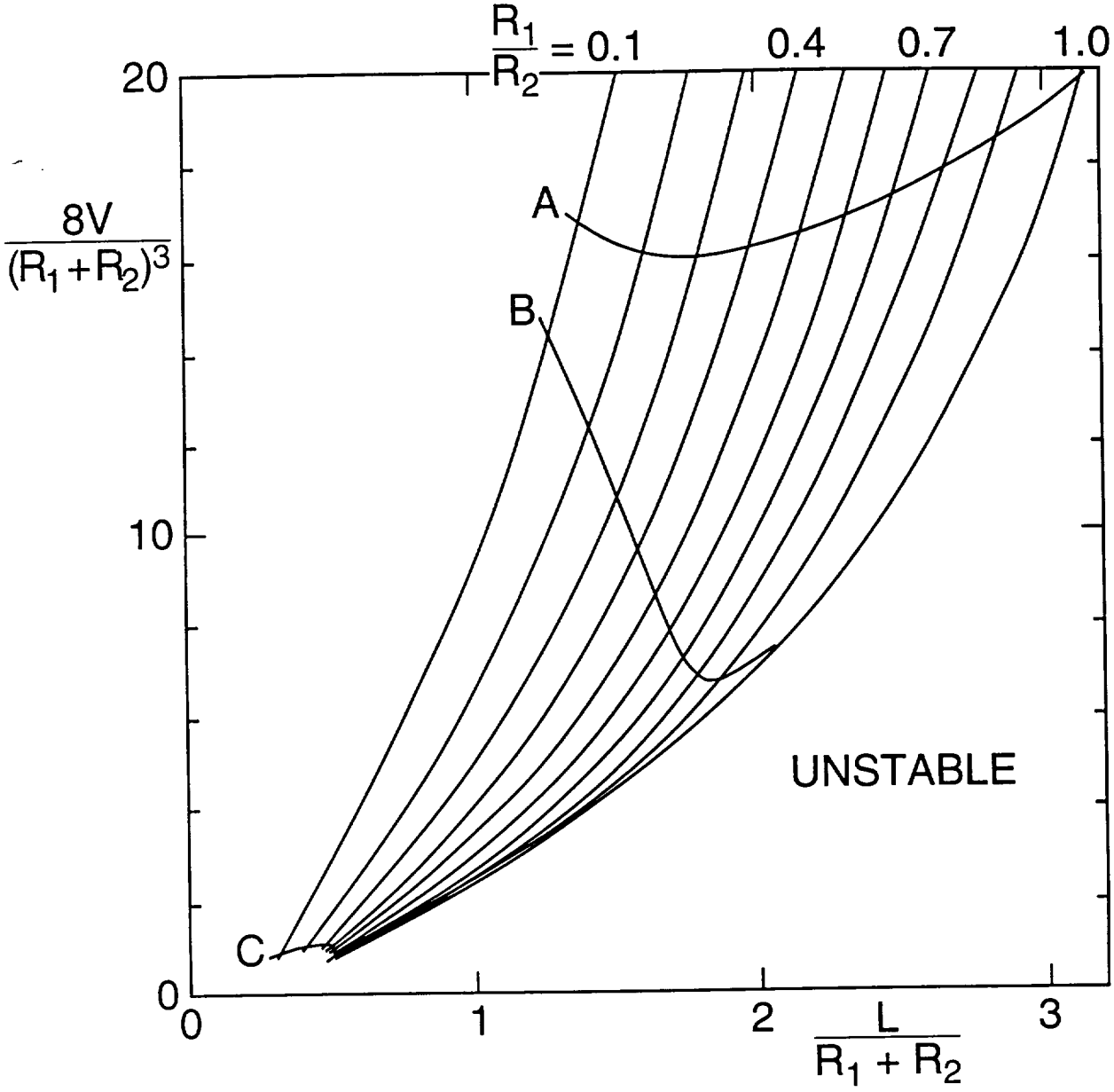

Fig. 28 Influence of Bond number on the stability limits of liquid bridges between unequal disks[7].

Any residual acceleration will also affect the melt volume. The quasi-steady component of acceleration may push the melt such that partial wall contact is established. Sen and Wilcox [2,3] examined different ampoule shapes and found that a triangular cross section ampoule provided the most regular contact free conditions. They ascribed this to the ease with which the third phase could move around the ampoule. They also conjectured that it could be possible for a non-wetting phase to completely lose contact with the wall.

4.3.2. "Dewetting" [1] : Dewetting refers to the loss of melt-ampoule contact immediately ahead of the growth surface due to the presence of surface roughness on the

inner ampoule wall. According to a recent model [1], dewetting must occur in the presence of a rough ampoule surface and will depend on the growth angle θ_s and the wetting angle θ_w. In addition, a more sophisticated, and very likely more realistic model must consider the dynamics of the receding melt-ampoule contact line and the consequences for the contact angle θ_w.

It is necessary that composite wetting occur between the ampoule and the melt as a precursor to dewetting. The condition that composite wetting occur is [1]

$$l/R \leq -2\cos(\theta_w - r), \tag{1}$$

where $R = \sigma/\rho gh$, σ is the surface tension, g is the acceleration due to gravity, h is the characteristic height of the liquid above the surface in the acceleration direction and ρ is the density of the melt. The angle r is shown in Fig. 29. It is measured with respect to the perpendicular to the macroscopic ampoule wall and characterizes the steepness of the asperite. Under zero gravity conditions it is easier to obtain composite wetting since l/R tends to zero. Note that for a quasi-steady acceleration with a magnitude g, not oriented axially, the composite condition may only be satisfied locally.

Composite wetting can be simply explained by considering the rough surface to be composed of microscopic asperites. For sharp asperites (see Fig. 29), the local equilibrium condition at a sharp edge shows that when the solid angle δ is greater than π, the liquid cannot penetrate to the corner. For smooth asperites, the contact angles satisfies the well known condition [4]

$$\gamma_{MV}\cos\theta_w = \gamma_{VA} - \gamma_{MA}. \tag{2}$$

where γ is the surface energy of the melt-vapor (MV), vapor ampoule (VA) and melt-ampoule (MA) respectively. When smooth asperite sides are steep, the wetting angle θ_w may not be accommodated in the groove so the melt loses contact with the wall. For sharp asperites, the microscopic contact angle may take values in the range $\theta_w+\delta > \theta > \theta_w$ (see Fig. 29).

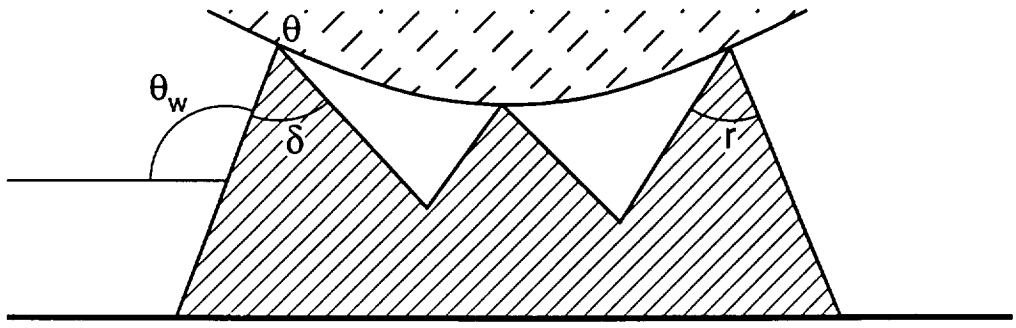

Fig. 29 The melt-ampoule contact angle at an asperite.

Once composite wetting is established, the process of dewetting described by Duffar et al.[1] occurs in much the same way as for the necking process. Possible contributing processes are not covered explicitly in their paper and are currently being studied at the CMMR. Whatever the details of the process, however, it seems reasonable, given the available experimental data, to assume that dewetting of melts occurs in association with ampoule roughness.

It should also be emphasized that the idea of dewetting is developed under the assumption that the melt partially wets the ampoule, i.e., the contact angle is less than π. For non-wetting melts, the removal of the constraint of gravity leaves open the possibility that loss of melt-ampoule contact occurs independently of the above mechanisms as discussed in *4.3.1*

The last mechanism that can be considered is necking, and although necking does not occur in most semiconductor melts which expand upon solidification it is worth reviewing the process since it gives some insight into what may happen at a tapered ampoule.

4.3.3. Necking [1,5] : Shrinkage of a solid upon solidification, resulting in a higher density solid than the adjacent melt can lead to the phenomenon of necking, i.e., a considerable reduction in the crystal radius relative to the initial seed. This occurs with some metals. If shrinkage occurs, then the behavior of the melt at the ampoule-crystal-melt contact line will be determined by the wetting angle θ_w made by the melt with the ampoule, and the angle of solid wetting θ_s or growth made by the melt with its own solid (see Fig. 30). If the sum $\theta_w + \theta_s > \pi$, then the melt will tend to draw the crystal away from the ampoule wall at angle $\alpha' = \pi - (\theta_w + \theta_s)$ with the growth direction. The introduction of a tapered ampoule with a taper angle, β, will result in a reduction in the tendency to draw the crystal away from the wall. That is, necking will occur only if $\theta_s - \beta + \theta_w > \pi$. For most semi-conductors, however, solid expansion rather than contraction occurs upon solidification. Thus, for the right circular cylindrical ampoule shown in Fig. 30, a semiconductor crystal will generally remain in contact with the wall. Obviously, necking will be a mechanism for maintaining loss of contact between the ampoule and the melt-crystal surface. However, if a semiconductor crystal is grown in an ampoule with a tapered geometry (see Fig. 31), then the loss of contact may occur. It can be maintained provided that the expansion of the freezing as it leaves the "seed holder" and enters the tapered section does not continue to force contact with the wall. That is, if the angle γ is less than the taper angle β, then loss of contact may be initiated. The extent of the melt region that loses contact and the time (or distance solidified) for which this can be maintained will depend on the difference β-γ, the growth angle θ_s and the wetting angle θ_w. For a shallow taper, with $\beta > \gamma$ and $\theta_s + (\gamma - \beta) + \theta_w > \pi$, necking can occur. (Necking is more difficult to initiate than for cases where the solid shrinks upon freezing). Note that for the dewetting mechanism discussed earlier, necking can occur if the dewetted area propagates several asperites ahead of the growth interface provided that $\theta_s - r + \theta_w > \pi$, where r is the

angle shown in Fig. 29. For CdTe melts on graphite coated quartz[6], the wetting angle θ_w is about 108 degrees at the melting temperature.

However, the above "mechanism" assumes that the ampoule surface is smooth, that the melt contact line recedes smoothly and that the contact angles θ_w and θ_s always have the same value. For rough surfaces, the contact line has a tendency to be locally pinned at certain irregularities and will generally allow for a range of angles than a single one. Even for smooth surfaces there may be a certain deformation of the surface that is allowed before the melt-ampoule contact line moves.

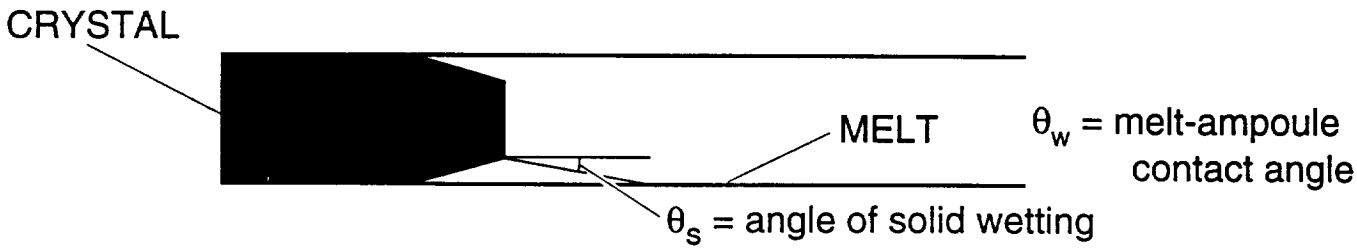

Fig. 30 Relationship between angle of solid wetting and contact angle for a necking crystal. Note that θ_s is measured with respect to the growth direction and θ_w with respect to the ampoule wall.

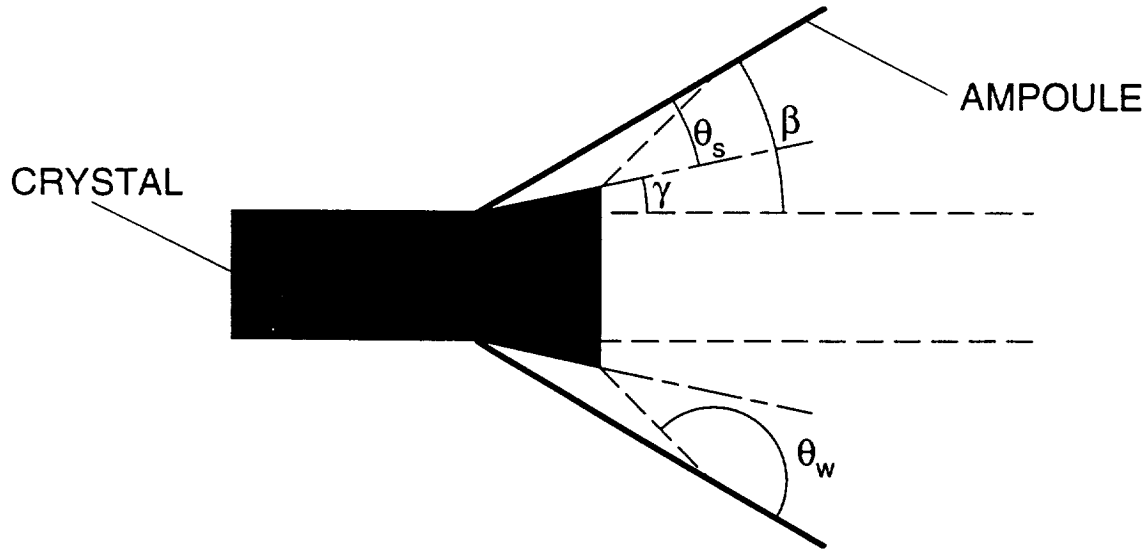

Fig. 31 Loss of contact in a tapered geometry

4.4 References

[1] T. Duffar, I. Paret-Harter and P. Dusserre, J. Crystal Growth **100** (1990) 171.

[2] R. Sen and W.R. Wilcox, J. Crystal Growth **74** (1986) 591.

[3] R. Sen and W.R. Wilcox, J. Crystal Growth **78** (1986) 129.

[4] J. C. Slattery, *Interfacial Transport Phenomena* (Springer-Verlag, Berlin, 1990) pp. 1159.

[5] V. S. Zemskov, M.R. Raukhman and I.N. Belokurova, *Proc. 4th European Symp. on Materials Sciences under Microgravity* , Madrid, April 1983, [ESASP-191 (1983) 325].

[6] R. Shetty and W.R. Wilcox, J. Crystal Growth **100** (1990) 51.

[7] I. Martinez, J.M. Haynes, and D. Langbein, in *Fluid Sciences and Materials Science in Space*, ed. H. Walter (Springer-Verlag, Berlin, 1987) p. 53.

5. *LOW GRAVITY ACCELERATION ENVIRONMENT IN USML-1*

5.1 Introduction

The First United States Microgravity Laboratory (USML- 1) flew on Columbia on STS-50 from 25 June to 8 July 1992. Three accelerometer systems measured and recorded data during the mission. The Orbital Acceleration Research Experiment (OARE) is a triaxial electrostatic accelerometer package with complete on-orbit calibration capabilities [1-3]. It is designed to characterize the Orbiter's aerodynamic behavior in the rarefied-flow flight regime through measurement of low frequency (<5 Hz), low magnitude accelerations. The Space Acceleration Measurement System (SAMS) was developed to monitor and measure the low-gravity environment of MSAD-sponsored science payloads on the Orbiter [4,5]. SAMS consists of up to three remote triaxial sensor heads connected to a main unit by cables. The sensors use a pendulous proof-mass and force-rebalance coil system to measure acceleration. Both OARE and SAMS record the acceleration of the Orbiter with respect to a frame of reference fixed to the accelerometer sensor. The Passive Accelerometer System (PAS) was designed to measure the quasi-steady residual acceleration caused by a combination of atmospheric drag and the gravity gradient. The system is used to determine the residual acceleration environment experienced by experiments with respect to a frame of reference fixed to the Orbiter. Acceleration is computed indirectly using a modified form of Stokes' Law using the recorded motion of a small steel proof mass along an oriented tube filled with liquid.

5.2 Experiment Locations

The experiment carrier for USML- 1 was the Spacelab. The Orbiter center of gravity was about (1091.9", -0.4", 374.0") halfway through the mission. The Passive Accelerometer System (PAS) measured the quasi-steady acceleration environment of the Flight Deck and Spacelab on USML- 1. A description of the PAS and PAS results is given elsewhere in this document Three SAMS heads recorded data in the Spacelab in Racks 3, 9, and 12, see Table 1 for locations. The OARE sensor was located at (1153.28", -1.33", 317.81"). Note that all locations are given in Orbiter structural coordinates, see Fig. 32. Quasi-steady accelerations and vibrations measured by these accelerometers are discussed in the following section.

5.3 Disturbance Sources and Resultant Acceleration Levels

The two main components of the low-gravity environment of the Orbiter are quasi-steady accelerations and vibrations caused by oscillatory and transient sources. These two components are discussed below in general and specific sources present during USML-1 are outlined.

Quasi-steady accelerations: The three major, predictable components of the quasisteady acceleration environment of orbiting laboratories are aerodynamic drag, gravity gradient, and rotational (tangential and radial) effects. These contributions are discussed at length in the literature [6-8]. Modelling of these effects at the CGF location on USML-1 indicate that predicted total contributions were between 7x10-8 g and 9x10-8 g in X-body, between 2x10-7 and 3x10-7 g in Y-body, and between -8x10-7 and -3x10-7 g in Z-body, see Fig.33. Quasi-steady accelerations have a frequency component on the order of 10-4 Hz, consistent with the orbital period.

An additional acceleration in the same magnitude range was identified in OARE and PAS measurements taken during USML-l. A component of this acceleration was identified as the venting force of the Flash Evaporator System (FES) [9]. The FES is a component of the Orbiter Active Thermal Control Subsystem (ATCS) [10]. Along with the radiators and ammonia boilers, the FES acts to meet total system heat rejection requirements during flight. Tt is also used to dump excess potable water in flight. The FES is located in the Orbiter aft fuselage and is composed of a high-load and topping system contained in one envelope. Steam generated from the topping evaporator is ejected through two opposing sonic nozzles on each side of the aft Orbiter: (1506", +128", 305") in structural coordinates, see Fig. 34. The high-load evaporator is not normally used on orbit because it has a propulsive vent; it was not used on orbit during USML-l [Q. Carelock, personal communication].

During USML-l, two nozzle FES operations, in topping mode, occurred with about a 28 hour periodicity. The FES removed water at about 10.5 lb hr-1 for 14 hours, followed by a 14 hour off period, see Fig. 35. USML-1 FES operations caused total thrust along the X-body axis of -0.03 lbf and along the Z-body axis of 0.018 lbf [9]. The resultant linear accelerations caused by the FES activity are gx=-1.2x10-7 g, gz=7.6x10-8 g, where g_x and g_z are acceleration in the X-body and Z-body directions. Y-body accelerations due to FES operations cancel due to the opposing nozzle configuration.

Figs. 36 and 37 show the average orientation of the residual acceleration vector recorded by OARE when FES was off and on [11]. The data represented here were extrapolated to the CGF location [2] and the signs have been adjusted to transform the data into an Orbiter fixed reference frame. Note that the -Xb, +Zb nature of the FES venting force influences the acceleration vector.

Fig. 38 shows the average orientation of the residual acceleration vector recorded by PAS in the Flight Deck and extrapolated to the CGF location [1 l]. All PAS Flight Deck measurements were taken while the FES was on. Note that the vector orientation indicated by PAS is consistent with that shown by OARE when the FES was on.

The Orbiter Food Water and Waste management Subsystem provides basic life support functions for the flight crew. Two components of this system provide storage and dumping capabilities for potable and waste water. Three waste water dumps occurred during Spacelab operations on USML-1. The contributions of these water dumps and the FES contribution are discussed in more detail in an attached preprint in Appendix 2.

Vibrational Environment : The vibrational environment on-board a manned orbiting laboratory is influenced greatly by both spacecraft operations and crew activity. Large magnitude disturbances caused by Orbiter Reaction Control System firings and crew exercise, especially if not isolated, are propagated throughout the craft as vibrations at Orbiter, carrier, and subsystem structural modes. Oscillatory disturbances from spacecraft fans, motors, and pumps also cause excitation of structural modes. On a smaller scale, localized vibrations at experiment component structural modes can be excited by Orbiter operations and by experiment specific operations. In the remainder of this section we discuss the vibrational environment on USML- 1 as caused by Orbiter Reaction Control System activity and crew exercise.

The Orbiter Reaction Control System (RCS) provides thrust for attitude (rotational) maneuvers and small velocity changes (translations) when the Orbiter is above 21,336 m [10]. RCS modules are located in the forward fuselage nose area and in the left and right OMS/RCS pods, attached to the aft fuselage. The forward RCS has 14 primary and 2 vernier RCS engines; the aft RCS has 12 primaries and 2 verniers in each pod. Primary RCS (PRCS) engines provide 870 lb of thrust each; vernier RCS (VRCS) engines provide 24 lb of thrust each. Both RCS engine types can be used in steady-state thrusting mode for one to 125 sec or in pulse mode with a minimum pulse time of 0.08 sec.

On average, 125 RCS thrusters fired per hour between MET day 3 and MET day 7 on STS-50. This is the count of total firings and does not take into account the fact that several thrusters often fire at the same time for attitude control. If simultaneous multiple firings are considered as a single event, the average number of firings per hour decreases by about 65%. Fig. 39 is a histogram of the total RCS count from MET 92 hr to MET 184 hr. Note that the attitude deadband was changed from 0.5° to 0.1° at approximately 120 hr. RCS activity increases by about 98% after this change.

Instantaneous linear accelerations produced by a VRCS firing would be about lx10-4 g. Instantaneous linear accelerations produced by a PRCS firing would be about 3.5x10-3 g. Various engine firing durations, simultaneous firings of opposing and/or complementary jets, the excitation of structural modes, and acceleration data sampling rates make it difficult to identify a single acceleration value from accelerometer data.

RCS activity for attitude control is generally necessary because the Orbiter tends to drift out of a desired attitude. Such drifting is due, for example, to orbit degradation related to aerodynamic drag and attitude instability. In addition, Orbiter induced accelerations will require attitude correction. An example of this which occurred during USML- l involves supply water dumps.

Potable and waste water accumulated in flight is stored in 74 kg capacity tanks which can be dumped overboard via vents on the port side of the Orbiter: potable water ports at (620", -105.5", 342") and waste water ports at (620", -105.5", 336"), in structural coordinates, see Fig. 34. Three waste water dumps occurred during Spacelab operations on USML-1. Each water dump lasted one hour. The 0.09 lbf venting thrust along the Y-body axis caused linear accelerations of approximately g_y=3.8x10-7 g. Because of the vent configuration, X-body and Z-body accelerations are negligible. RCS data for a water dump at MET 6/17 indicate that thruster activity increased from about 30 firings an hour prior to the dump, to about 30 firings a half hour during the dump, Fig. 40. This increase in activity was in response to Orbiter motion caused by the port side waste water dump which causes the orbiter to yaw. Fig. 41 shows an acceleration vector magnitude for the period shown in Fig. 40. Note that transient acceleration magnitudes related to VRCS activity are in the 1-4x10-4 g range.

Fig. 42 shows OARE data for an earlier waste water dump. The acceleration magnitudes are different than the Fig. 41 SAMS data because of the different filtering applied to the data. Note, however, that the Yb and Zb (Fig. 32 lb & c) data clearly show the response of the Orbiter to the negative yaw VRCS jets fired to counteract the water dump torque [9].

Another vibration source which existed during USML-1 was crew use of exercise equipment. During this mission, ergometer exercise occurred in three configurations: with the cycle ergometer hard-mounted to the Flight Deck, with the cycle ergometer attached to the Ergometer Vibration Isolation System (EVIS) in the mid-deck, and with the cycle ergometer suspended by bungees in the aft Flight Deck area. A comparison of vibration levels among the three exercise configurations on USML-l is presented in Ref. [4]. Vibration levels related to exercise are not particularly noticeable above the general background in SAMS Head B (CGF) data. Fig. 43 shows a period during which bungee isolated exercise occurred. Exercise begins approximately 15 minutes into the plot. The pedalling frequency of about 1.2 Hz is easily seen in Fig. 43c. Excitation of Orbiter/Spacelab 3.5, 3.7, and 4.7 Hz structural modes can be seen, although no comment about the power in these modes can be made because this is above the SAMS filter cut-off frequency. These modes may, in part, be excited because of their coincidence with upper harmonics of the exercise frequency.

5.4 Conclusions

The three accelerometer systems flown on the First United States Microgravity Laboratory mission together provide a working characterization of the quasi-steady acceleration and vibration environment experienced by experiments during the mission. The OARE provided a measure of the quasi-steady acceleration environment over the extent of the mission. The PAS provided a more real-time spot check of the environment for up to 20 minute periods. The data sets resulting from these two systems give consistent values for the residual acceleration vector magnitude and appear to give a consistent estimate of the vector direction. Comparisons of the OARE and PAS data sets can only be made for the times when PAS was used. It is important to note that all PAS measurements were taken when the Flash Evaporator System was venting excess water.

Acceleration magnitudes obtained from OARE and SAMS cannot be directly compared because of the different filtering and processing applied to the data. The two data sets can be used, however, to confirm activity that both record. The OARE and the SAMS data sets both indicate that waste water venting forces at the port side vent site require increased RCS jet activity to counteract Orbiter torquing. RCS data from the mission also support this increase of RCS activity.

SAMS data collected during USML-1 also provide an indication of the vibration levels related to crew exercise. This subject has been covered quite thoroughly in the literature [4] and in this meeting. Neither OARE nor PAS is designed to measure exercise related vibration magnitudes or frequencies.

OARE and PAS accelration measurements taken during USML-1 indicate that some force acting on the orbiter produced an "extra" acceleration component which cannot be accounted for by atmopsheric drag, radial and tangential (Euler) effects. Quasi-steady acceleration measurements made by OARE and PAS and extrapolated to the CGF region are consistent. Both instruments indicate that the gravity gradient component in the negative X_b direction was augmented by an acceleration of about 0.5×10^{-6} g and that the atmospheric drag was smaller than 0.5×10^{-6} g. Venting forces related to FES and water dump activities contribute accelerations on the order of 10^{-7}g. FES activity has a periodicity of about 28 hours and this is manifested in the OARE data. These venting contributions do not account for the total difference between measured and modelled quasi-steady accelerations for USML-1 (see also Appendix 2). The discrepancy may be due to an error in estimating the venting forces of the FES nozzles. Other potential sources are still under investigation.

As far as the impact on solute transport conditions in the CdZnTe melt is concerned, the overall quasi-steady magnitudes would not be expected to contribute significantly to

lateral composition nonuniformity is concerned even though the orientation of the acceleration vector often deviated considerably from the desired axial orientation. Thruster firings of significant duration (0.5-2.0 seconds) occurred at regular intervals (4-8 minutes) for a large portion of the GCRC experiments. Simulation of the CdZnTe melt's response to these firings suggests that resulting perturbations to the melt composition fields will be negligible.

5.5 References

[1] Blanchard, R. C., M. K. Hendrix, J. C. Fox, D. J. Thomas, J. Y. Nicholson, Orbital Acceleration Research Experiment. J. Spacecraft and Rockets 24 (1987) 504-511.

[2] Blanchard, R. C., J. Y. Nicholson, J. R. Ritter, Preliminary OARE Absolute Acceleration Measurements on STS-50. NASA Technical Memorandum 107724, February 1993.

[3] Blanchard, R. C., J. Y. Nicholson, J. R. Ritter, STS-40 Orbital Acceleration Research Experiment flight results during a typical sleep period, Microgravity Sci. Technol. V/2 (1992) 86-93.

[4] Baugher, C. R., G. L. Martin, R. DeLombard, Low-Frequency Vibration Environment for Five Shuttle Missions, NASA Technical Memorandum 106059, March 1993.

[5] Rogers, M. J. B., C. R. Baugher, R. C. Blanchard, R. DeLombard, W. W. Durgin, D. H. Matthiesen, W. Neupert, P. Roussel, A comparison of low-gravity measurements on-board Columbia during STS-40. Microgravity Sci. Technol., in print (1993).

[6] Alexander, J. I. D. and C. Lundquist., Residual motions caused by micro-gravitational acceleration, J. Astronautical Sci. 35 (1987) 193-211.

[7] Alexander, J. I. D. and C. Lundquist, Motions in fluids caused by microgravitational acceleration and their modification by relative rotation, AIAA Journal 26 (1988) 34-39.

[8] Hamacher, H. Simulation of Weightlessness, in: Materials Sciences in Space, B. Feuerbacher, H Hamacher, R. J. Naumann (eds.), Springer-Verlag (1986) 31-52.

[9] Rogers, M. J. B., B. P. Matisak, J. I. D. Alexander, Venting force contributions: Quasisteady acceleration on STS-50, Microgravity Sci. Technol., submitted.

[10] Shuttle Operational Data Book, Volume I, JSC-08934, Rev. E, Johnson Space Center, Houston, TX, January 1988.

[11] Alexander, J. I. D. and M. J. B. Rogers, A note on the extrapolation of PAS and OARE acceleration measurements to the CGF location on STS-50 (USML- 1), Center for Microgravity and Materials Research, University of Alabama in Huntsville, September 1993.

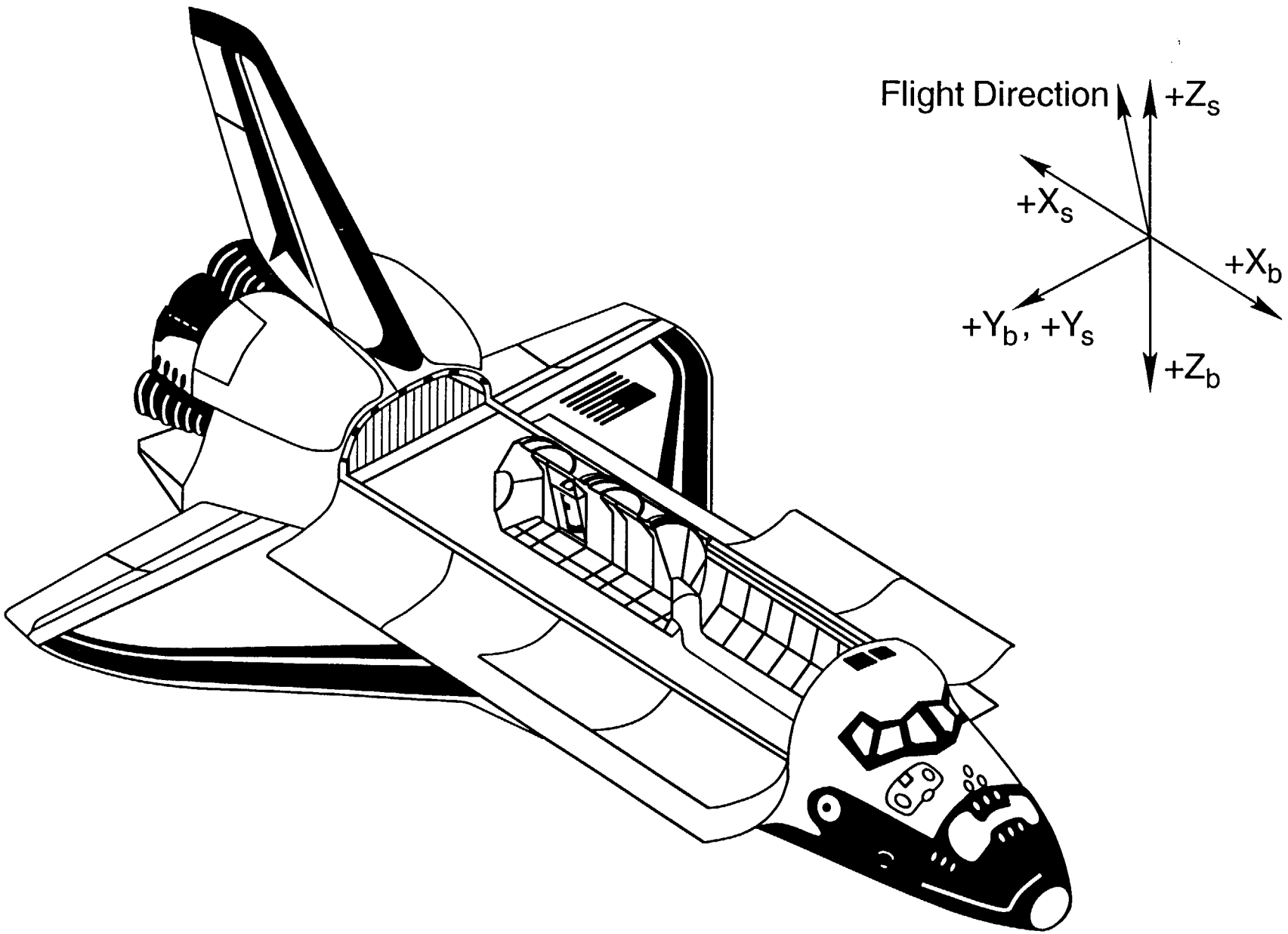

Figure 32 Cutaway view of Spacelab in Orbiter payload bay. Orbiter body coordinate system designated (X_b, Y_b, Z_b); Orbiter structural coordinate system designated (X_s, Y_s, Z_s).

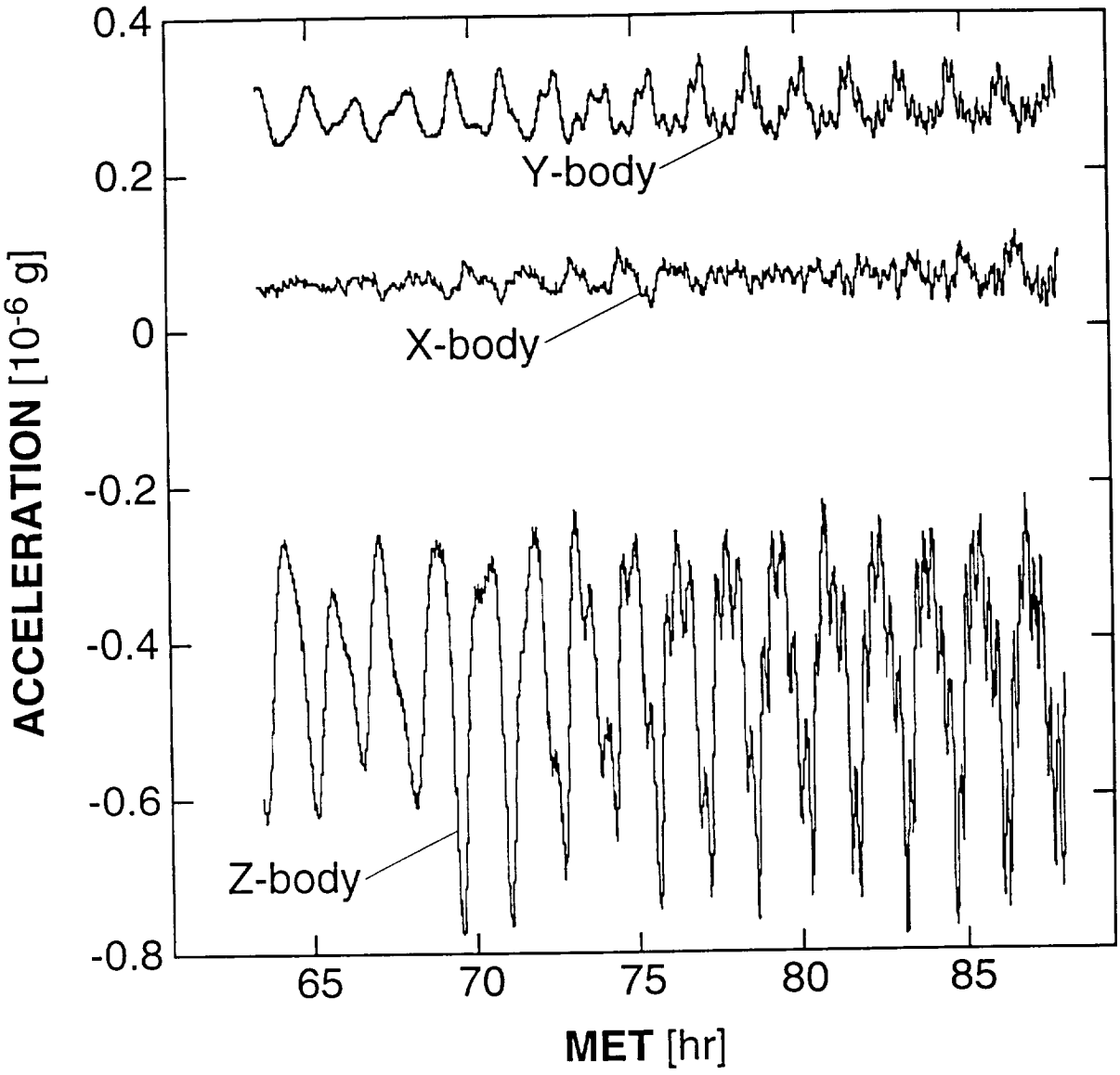

Figure 33 Modelled quasi-steady acceleration on USML-1 (aerodynamic drag, gravity gradient. tangential, and radial components). Accelerations at the Crystal Growth Furnace location modelled using actual Orbiter state vector data from MET 63 hr to 89 hr.

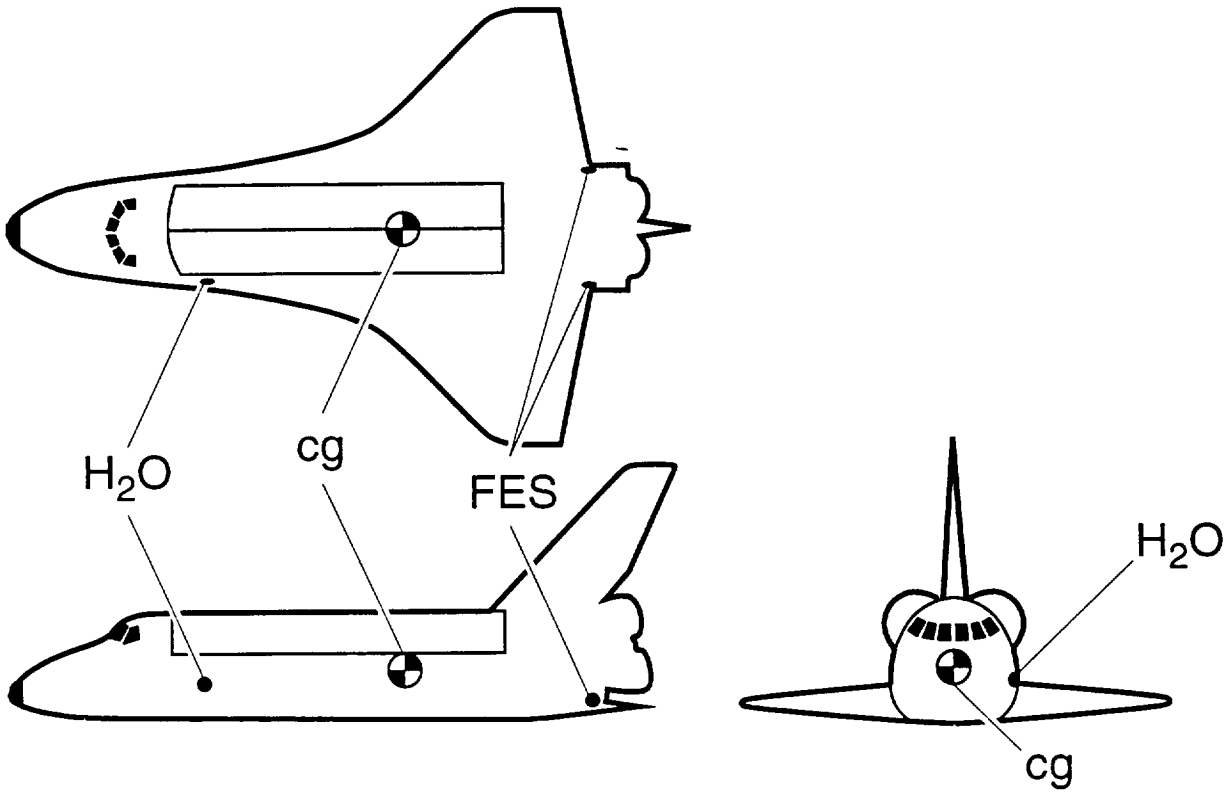

Figure 34 Approximate locations of Orbiter cg, waste and potable water vents (H_20), and Flash Evaporator System vents (FES). See text for coordinates.

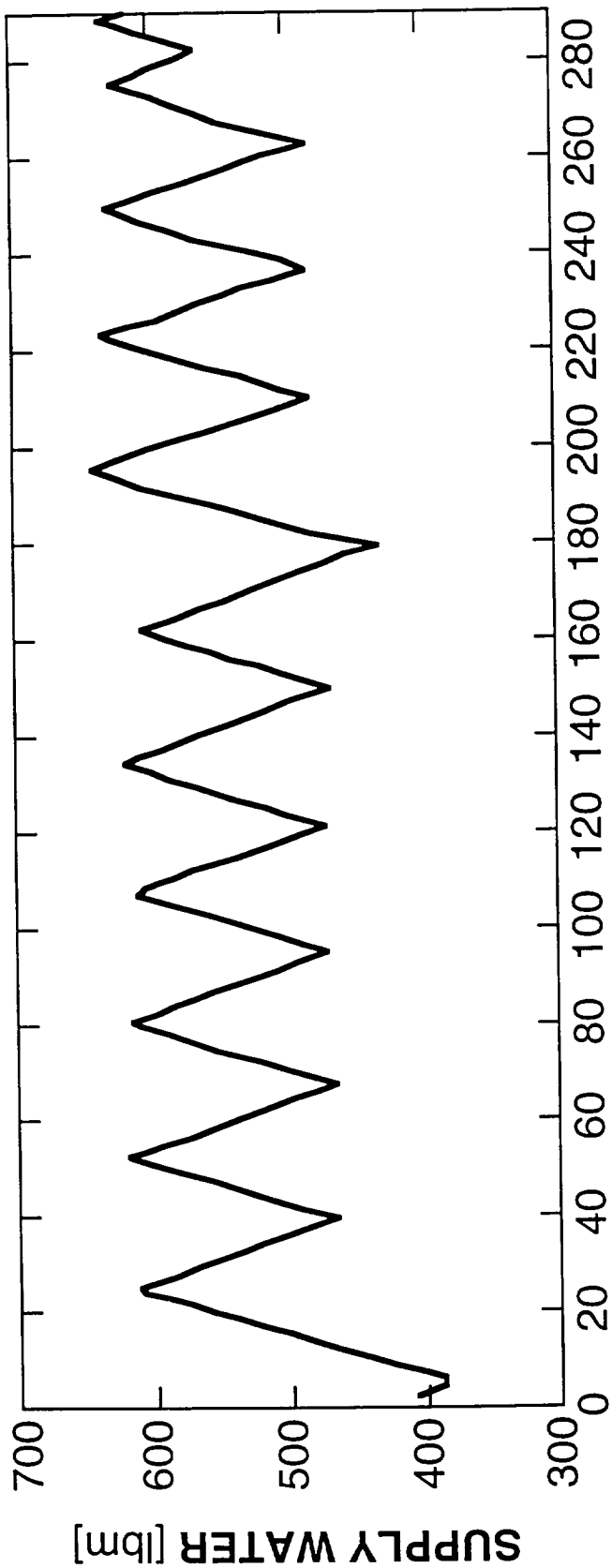

Figure 35 Supply water quantity history for STS-50. Downgoing segments of plot indicate water loss via FES activity. Note ~28 hr periodicity of venting.

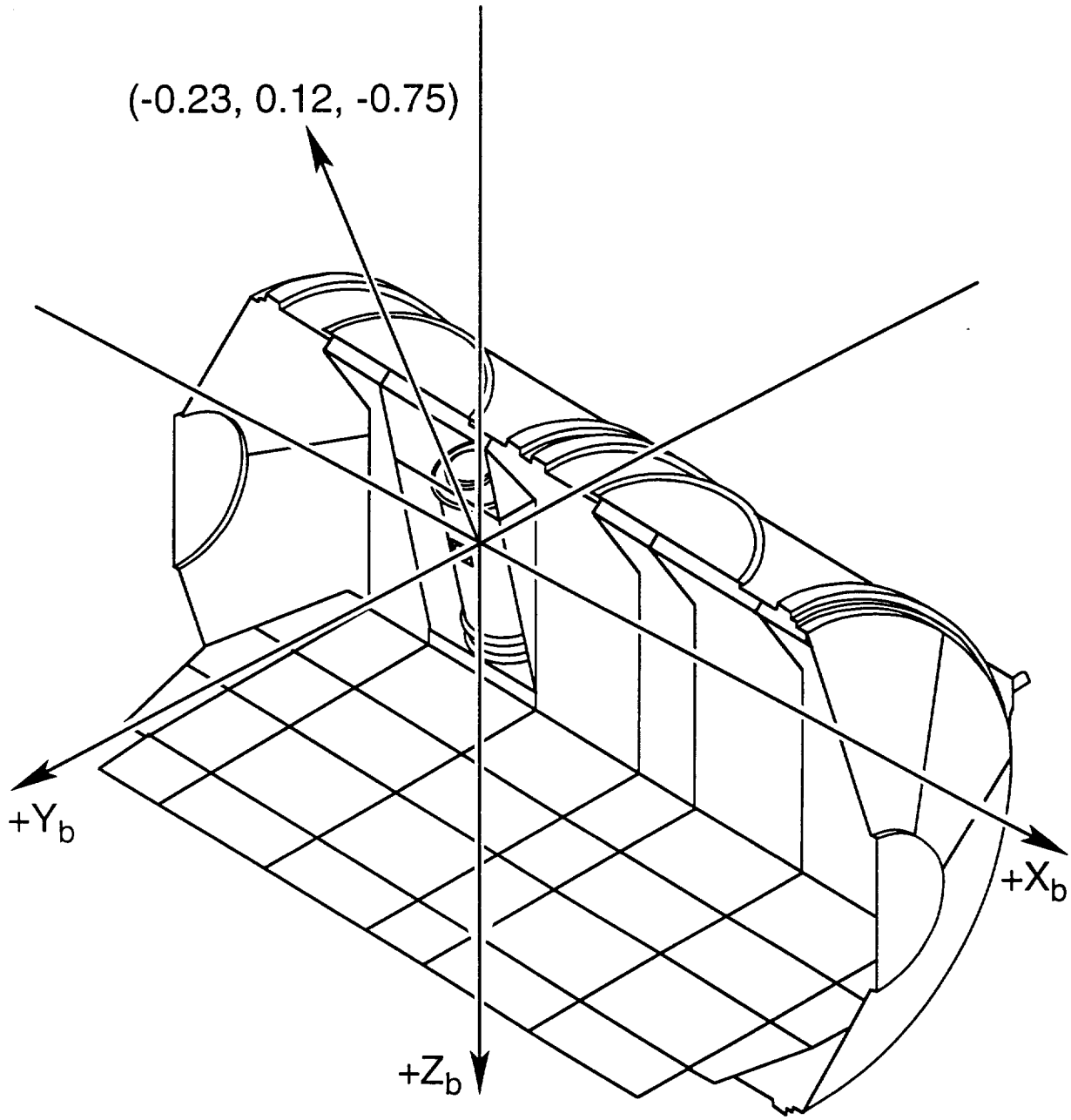

Figure 36 Average orientation of residual acceleration vector recorded by OARE when FES was off. Data recorded at OARE location and extrapolated to CGF location. From [11].

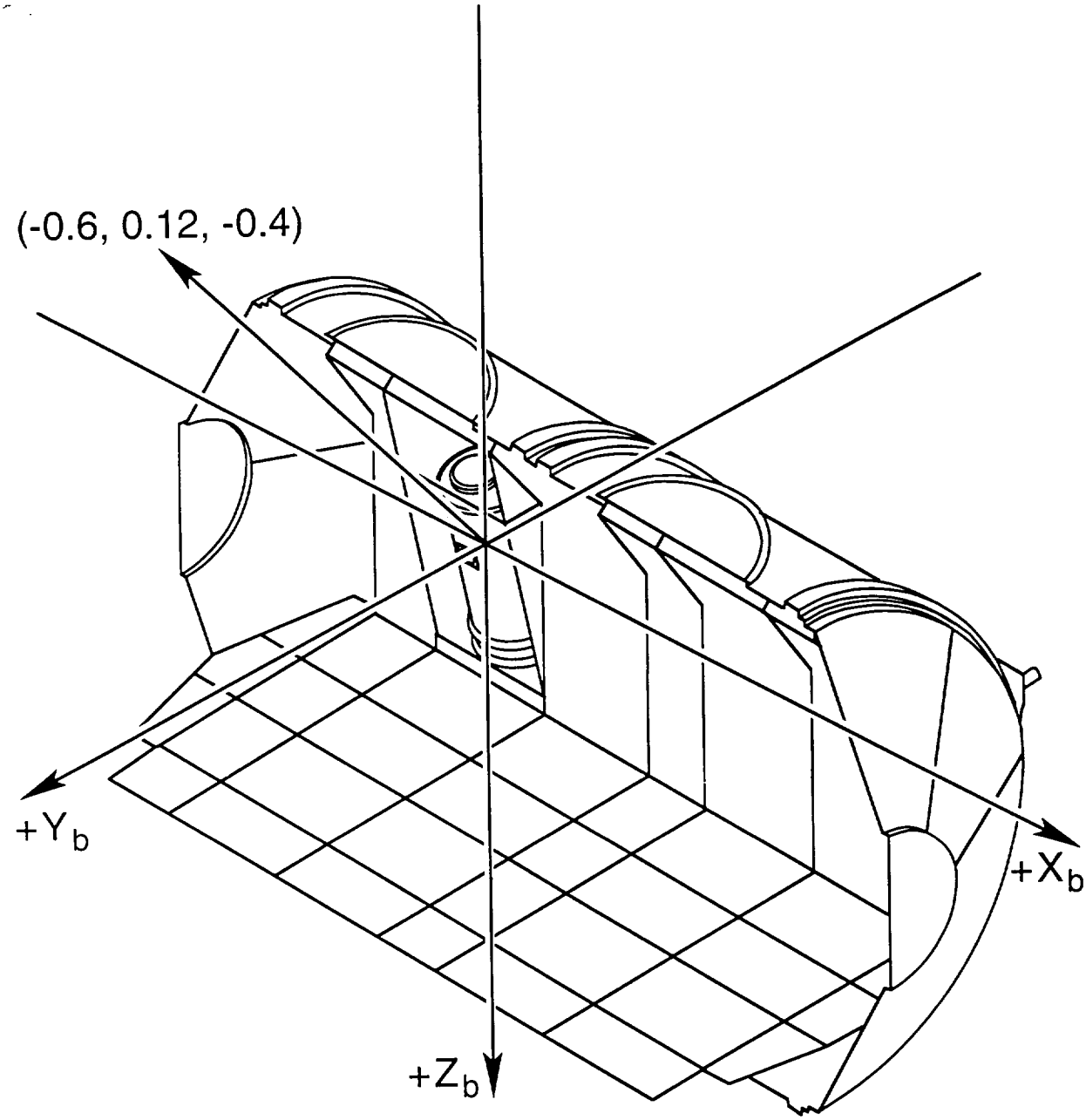

Figure 37 Average orientation of residual acceleration vector recorded by OARE when FES was on. Data recorded at OARE location and extrapolated to CGF location. From [11].

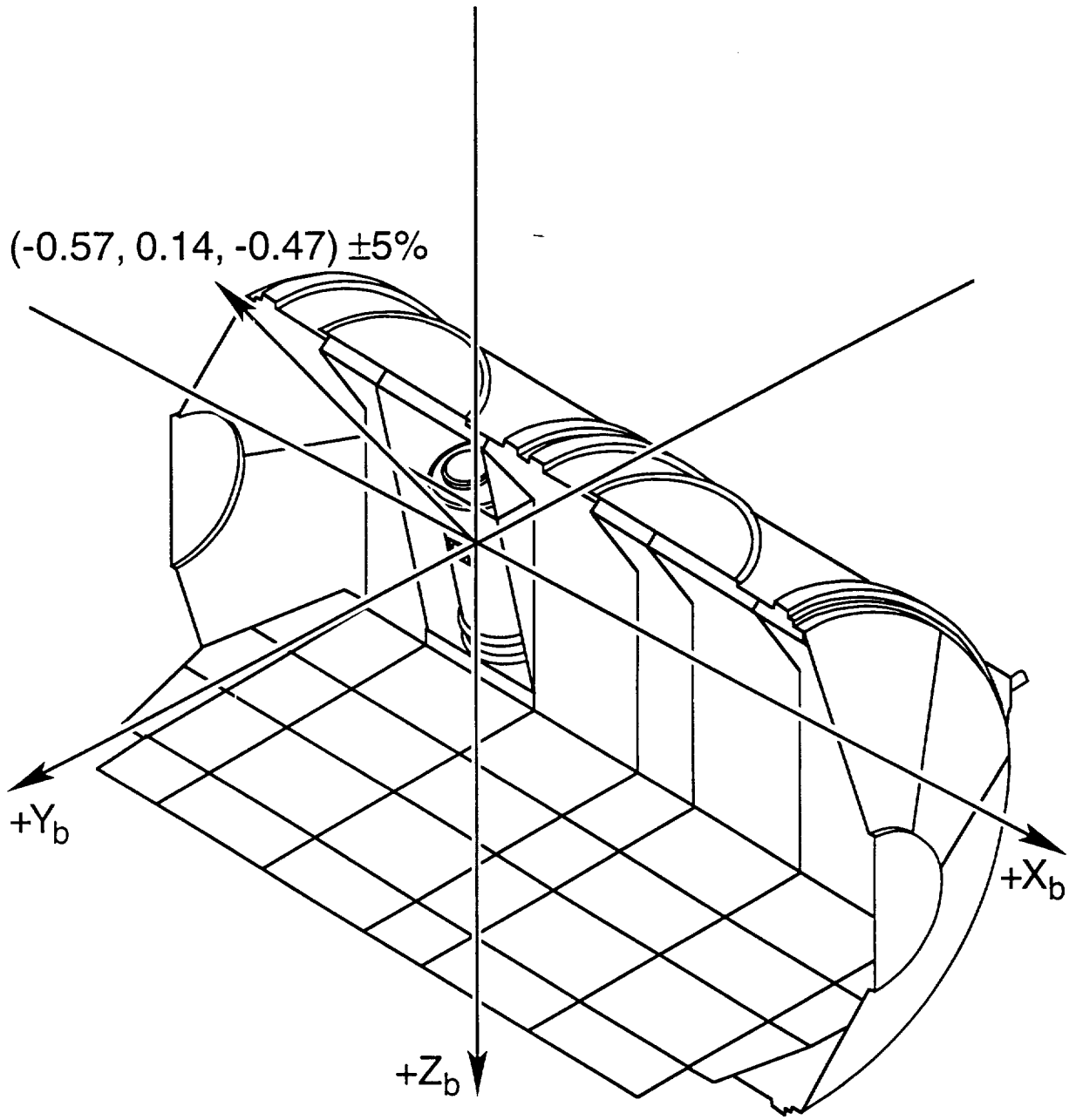

Figure 38 Average orientation of residual acceleration vector recorded by PAS when FES was on. Data recorded in Flight Deck and extrapolated to CGF location. From [11].

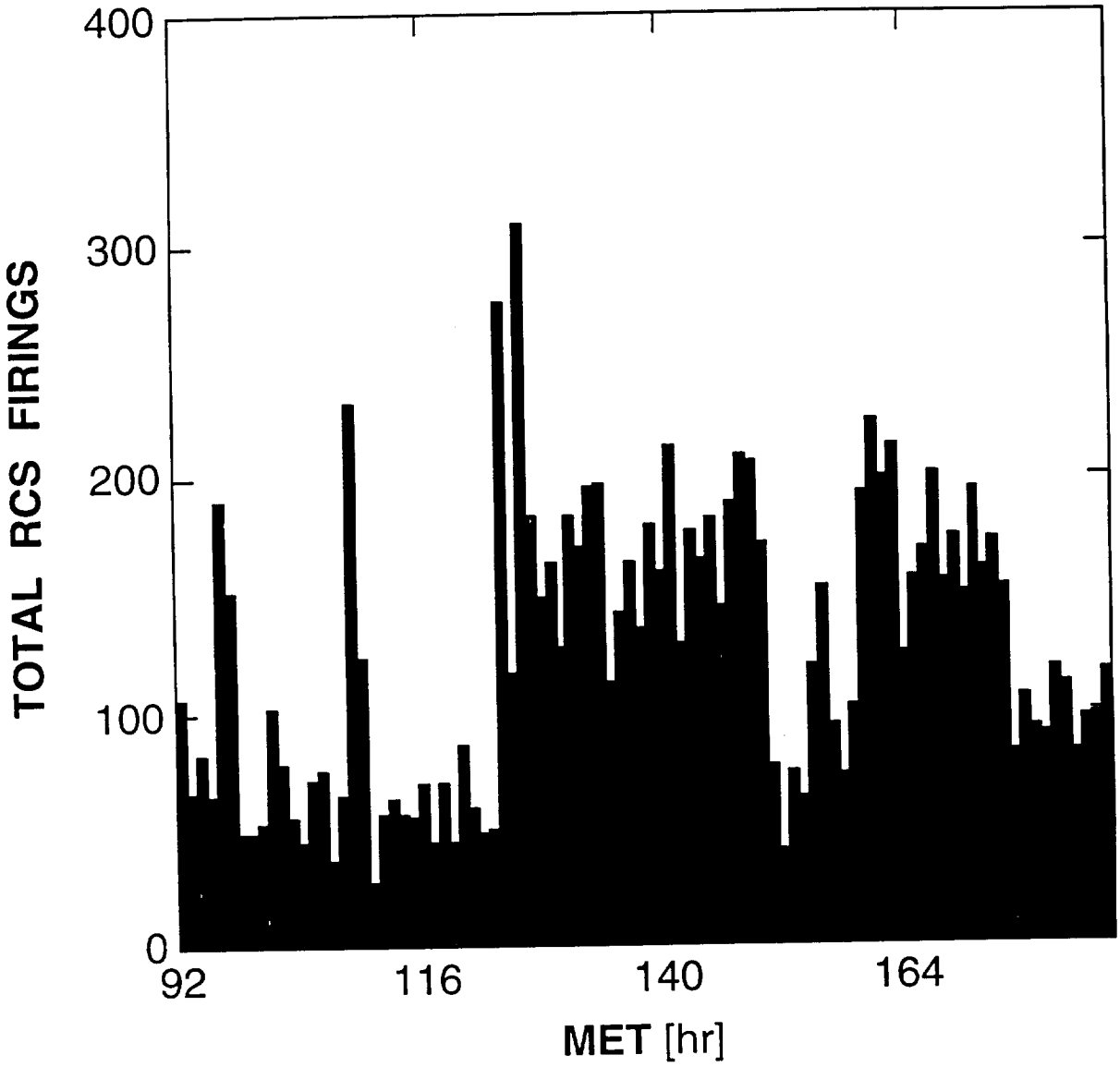

Figure 39 Total number of RCS jets fired in one hour periods. Note that simultaneous firings are considered as multiple events and that all firings are of VRCS jets.

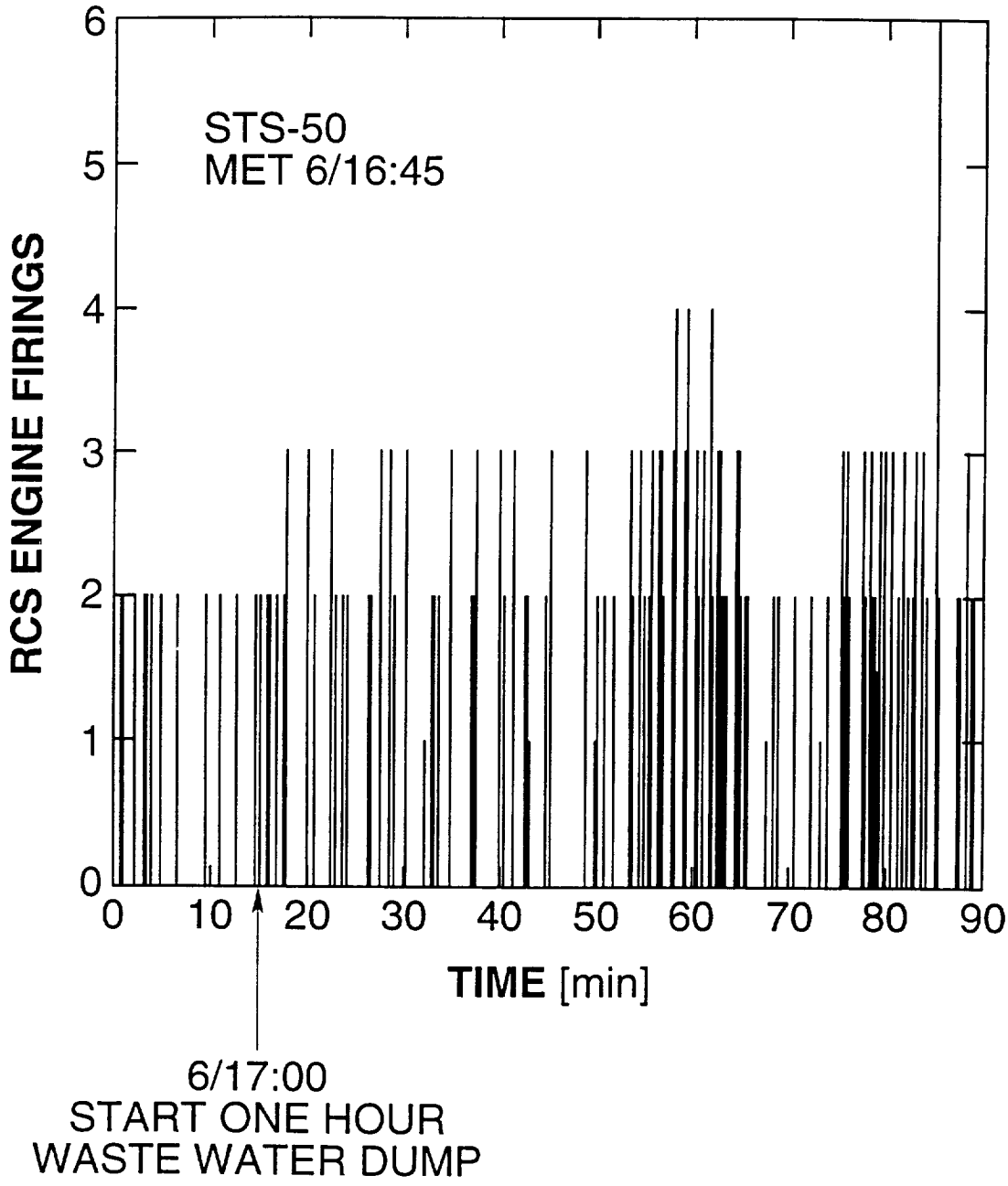

Figure 40 VRCS jet firing history before and during waste water dump. Plot shows jet firing occurrences versus time. For example, a bar of height 2 indicates that 2 VRCS engines fired. Width of bar indicates relative firing length and/or temporal spacing of firings.

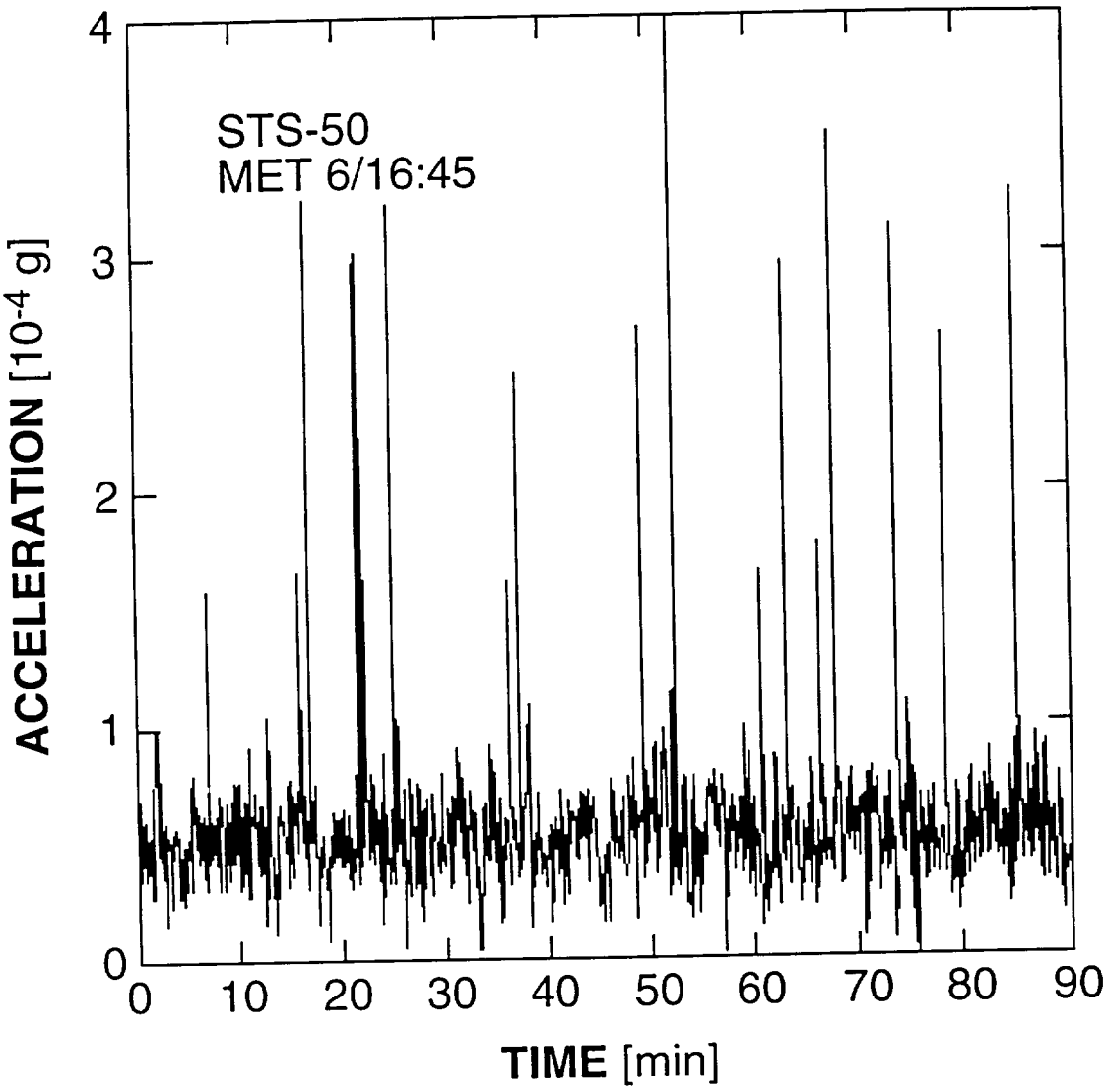

Figure 41 SAMS Head B (CGF) data plotted as vector magnitude for time shown in Fig. 40. Note acceleration transients related to thruster activity.

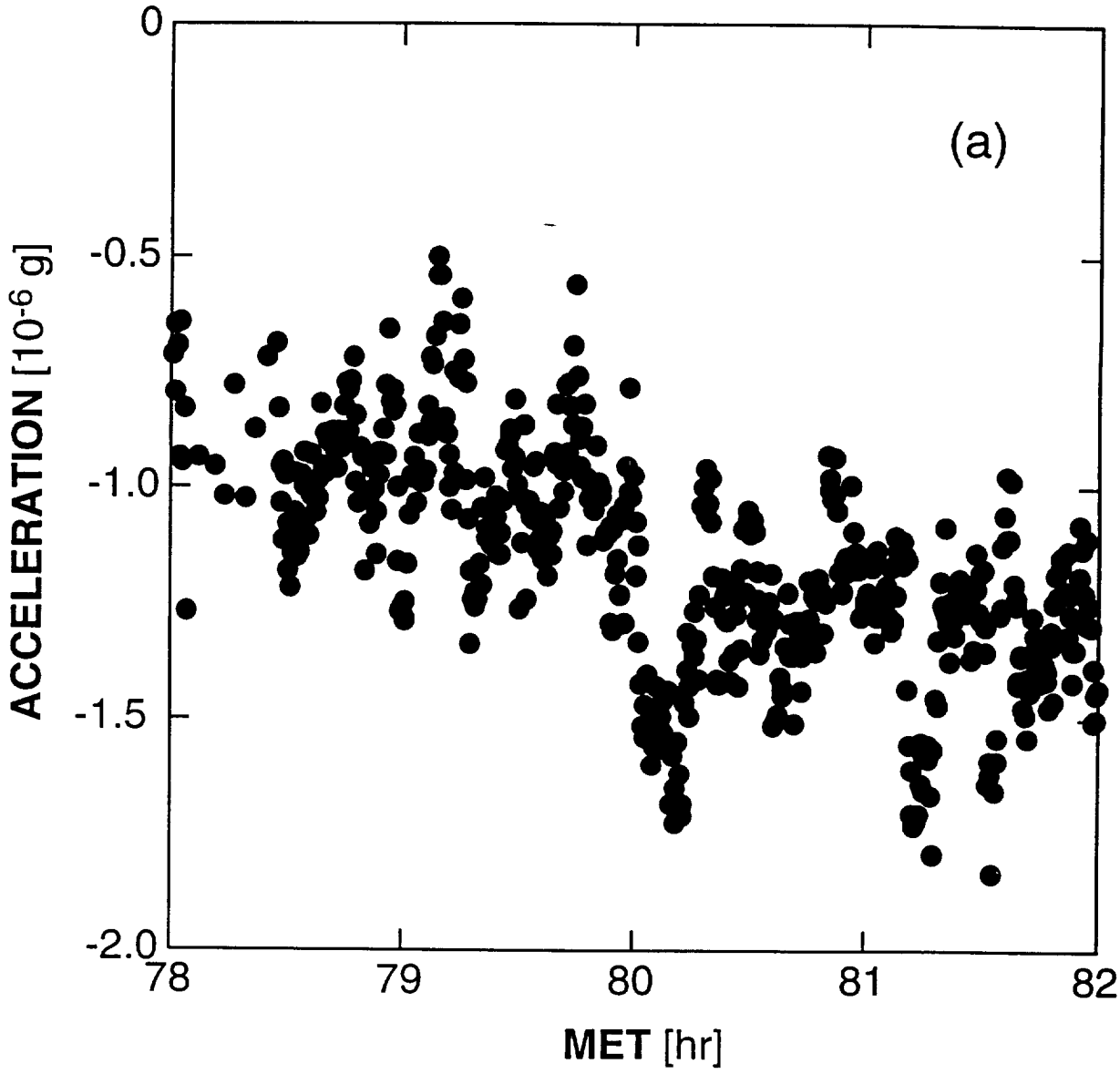

Figure 42 OARE data recorded during waste water dump activity (an earlier event than shown in Figs. 40 and 41). (a) X_b, (b) Y_b, (c) Z_b Note response to thrusters, most evident in (b) and (c).

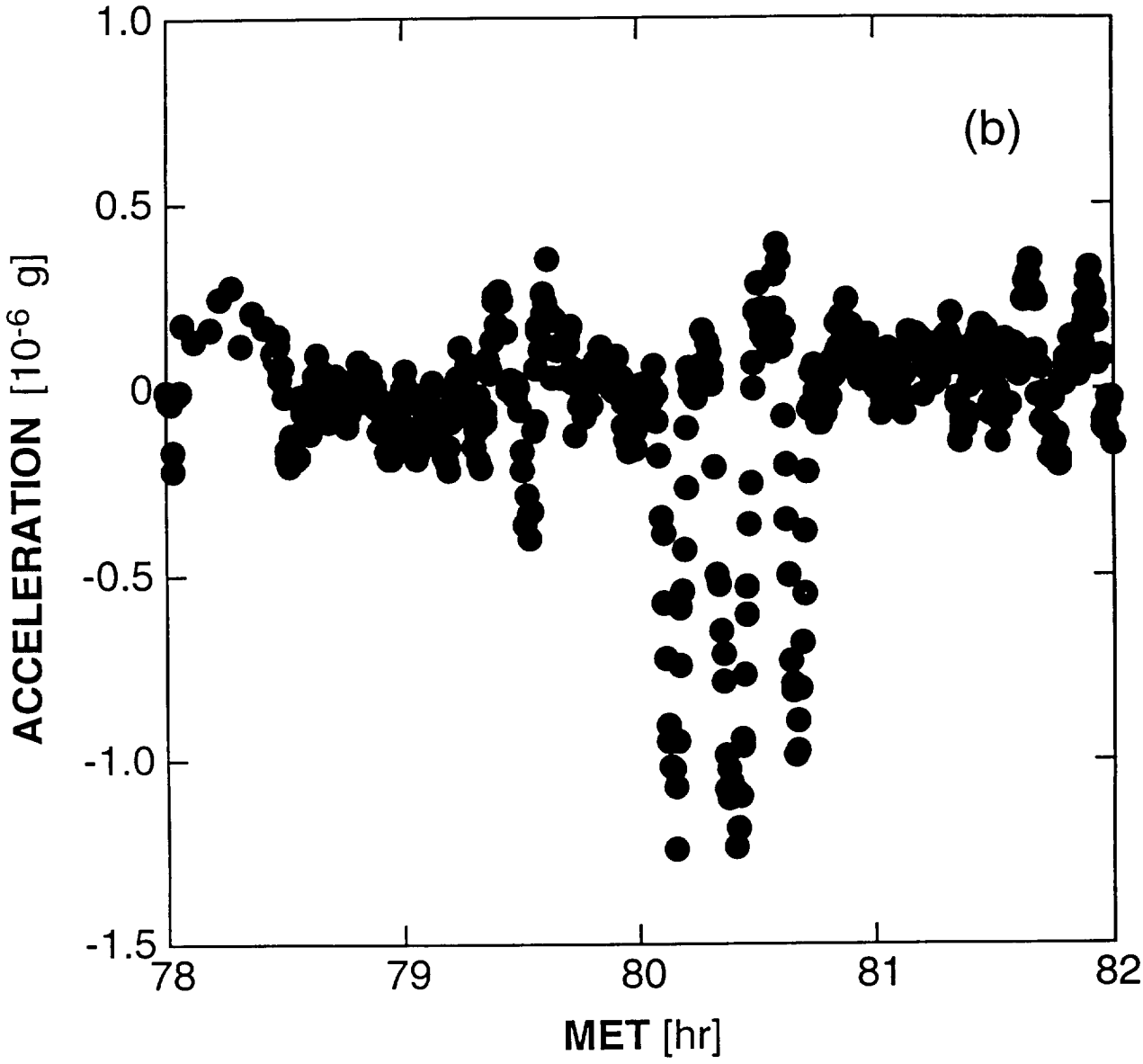

Figure 42 Continued

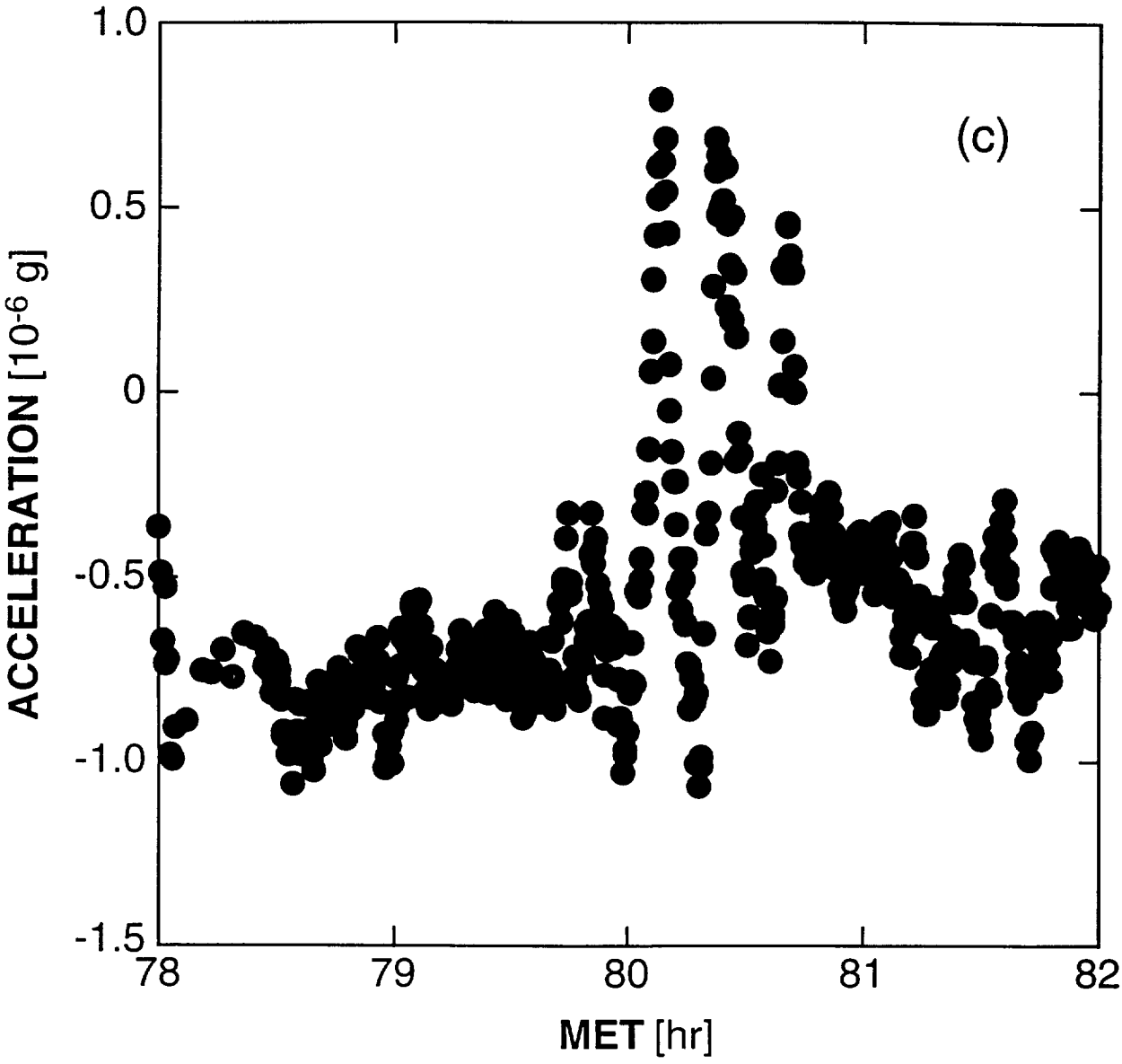

Figure 42 Continued

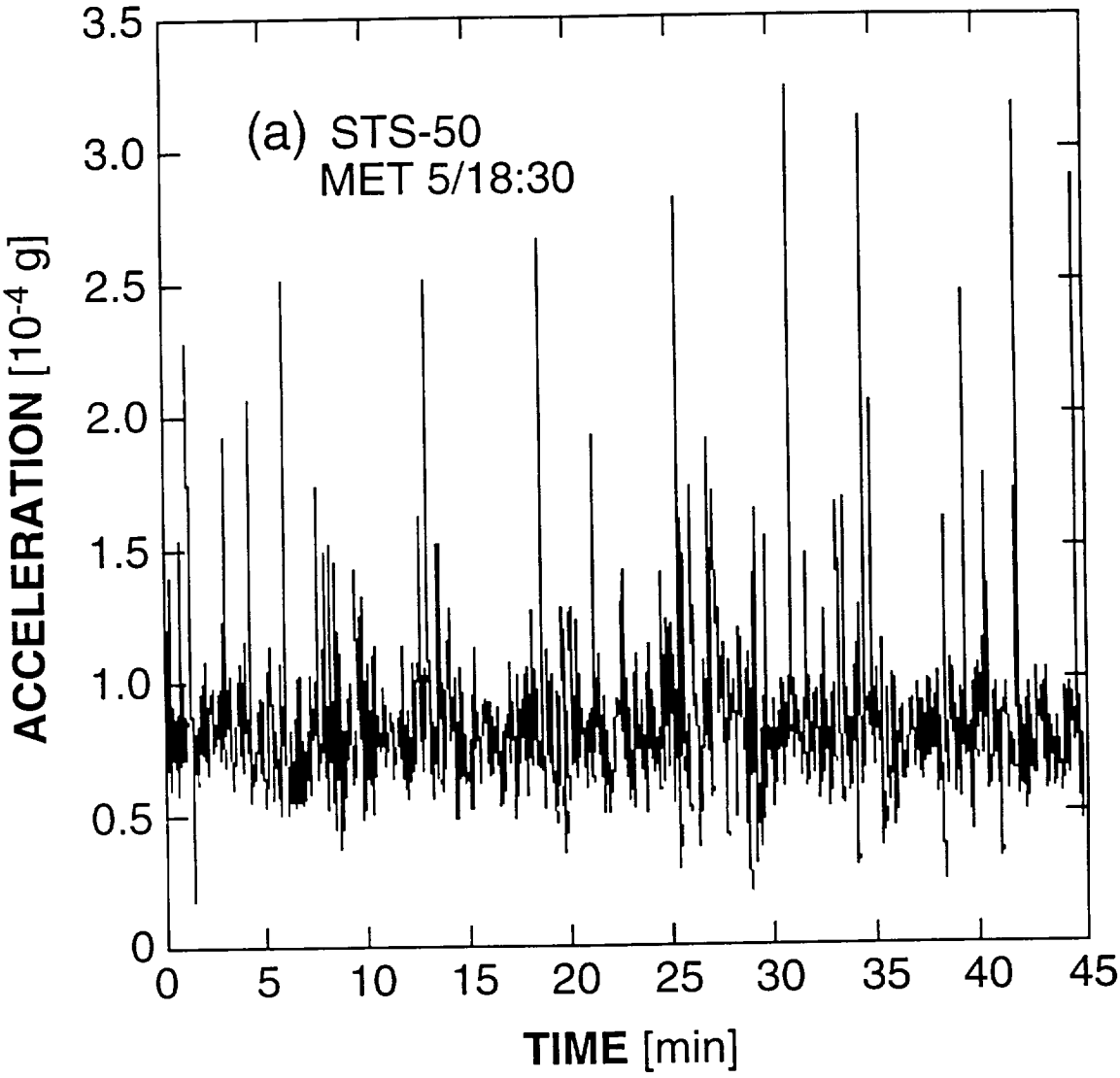

Figure 43 SAMS Head B (CGF) data during bungee isolated exercise. (a) Vector magnitude, exercise begins about 15 minutes into plot. (b) Combined amplitude spectrum, pre-exercise. (c) Combined amplitude spectrum, during exercise. Note excitation of 1.2 Hz pedalling frequency in (c).

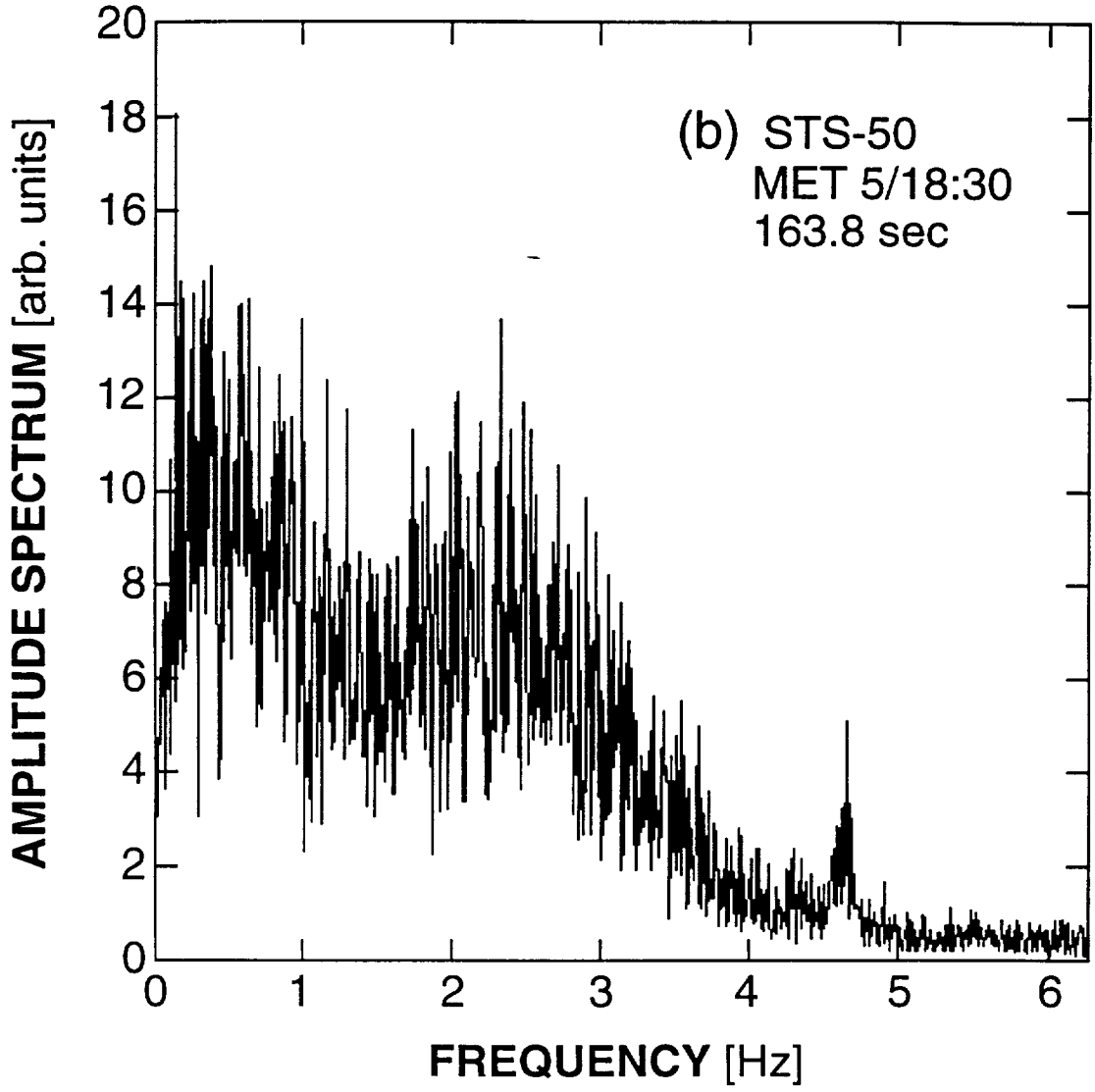

Figure 43 Continued

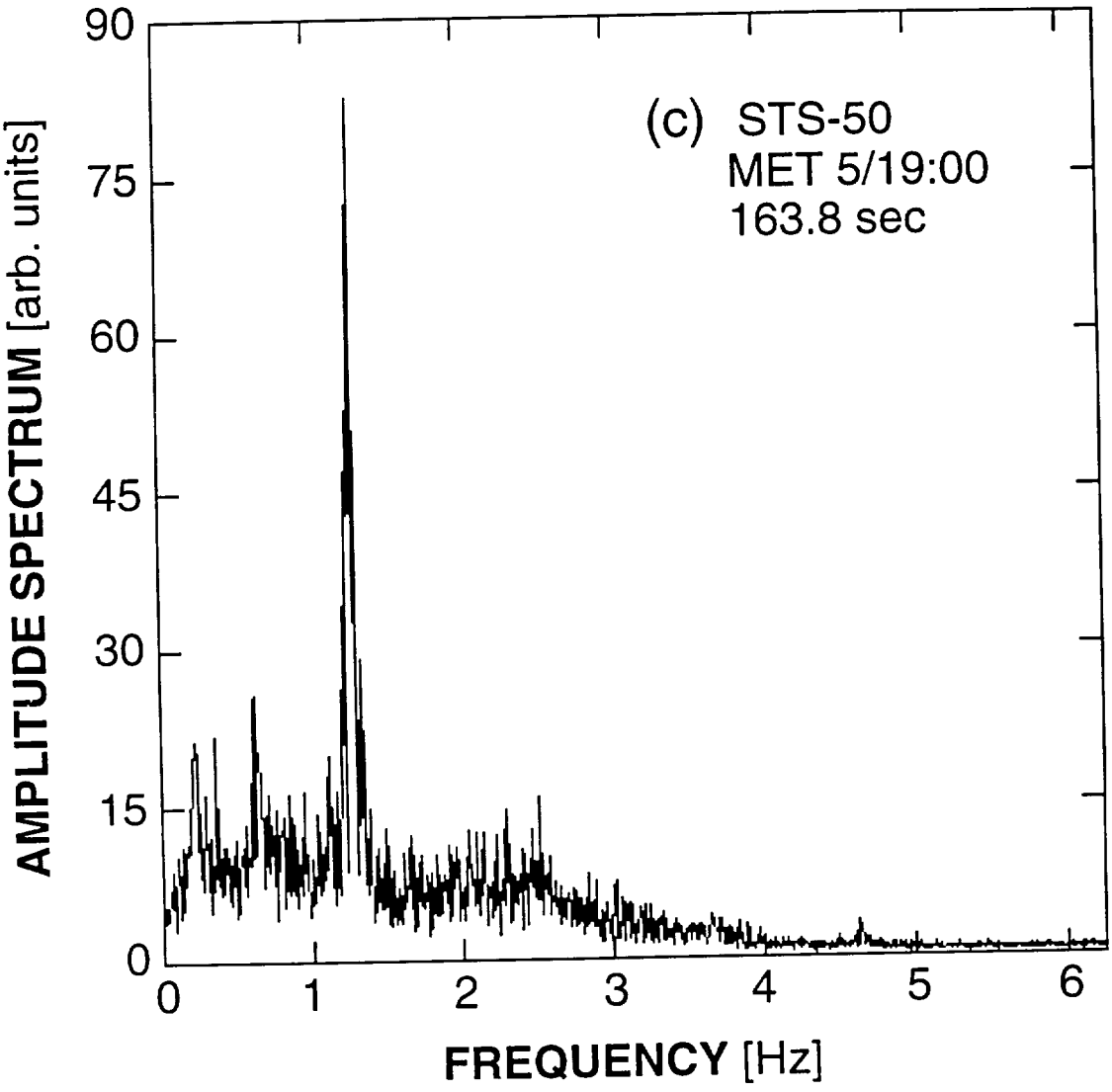

Figure 43 Continued

6. *PUBLICATIONS AND PRESENTATIONS*

6.1 Presentations

Results of our work during the period of performance of this contract have been the subject of the following presentations at conferences , workshops and colloquia:

M. J. B. Rogers, R. P. Wolf and J.I.D. Alexander, "Correlation of acceleration data on STS-50", Joint "L+1" Science Review for USML-1 and USMP-1 , Huntsville Alabama, September, 22-24, 1993.

J.I.D. Alexander, "Analysis of Experiment Sensitivity to Residual Acceleration" Invited presentation at the International Symposium on Microgravity Science and Application, Beijing, China, May 10-12, 1993

J.I.D. Alexander, "Modelling or Muddling? Analysis of Buoyancy Effects on Transport under Low Gravity Conditions," World Space Congress, Washington D.C. August 28-September 5, 1992.

A. Fedoseyev and J.I.D. Alexander, Modelling of Solidification fronts in Ampoules under Low Gravity Conditions", Alabama Materials Science Conference, Sept. 1993, Huntsville Al.

P. Larroude, J. Ouazzani and J.I.D. Alexander, "Flow Transitions in a 2D Directional Solidification Model," Proceedings of the 6th Material Science Symposium, European Space Agency, Brussels, Belgium, 1992.

S. Amiroudine, "Vibrational Convection and Transport Under Low Gravity Conditions," S.E. Conference on Theoretical and Applied Mechanics (SECTAM) XVI, April 12-14, 1992, Nashville, Tennessee.

J.I.D. Alexander,"Numerical Analysis of the Effects of Low Gravity on Convection and Transport," Case Western Reserve University, Department of Mechanical Engineering, February 6, 1992.

J.I.D. Alexander, "Numerical Simulation of Low-g Fluid Transport," AIAA Short Course on Low-Gravity Fluid Mechanics, January 10-12, 1992, Reno, Nevada

J.I.D. Alexander, "The Effects of Vibration on Convection and Transport During Directional Solidification," University of Erlangen, September 10, 1991.

J.I.D. Alexander, "Numerical Analysis of the Sensitivity of Experiments to Spacecraft Low Gravity Environments", April 9, 1991, Clarkson University, Department of Mechanical Engineering, Potsdam, New York.

J.I.D. Alexander, "Vibrational Convection and Transport Under Low Gravity Conditions," Society of Engineering Science 28th Annual Technical Meeting, November 6-7 1991, Gainesville, Florida.

S. Amiroudine,"Sensitivity of Bridgman-Stockbarger Crystal Growth to Residual Acceleration," 5th Annual Alabama Materials Research Conference, September 25-26, 1991, Birmingham, Alabama.

J.I.D. Alexander, "Numerical Analysis of the Sensitivity of Crystal Growth Experiments to Spacecraft Residual Acceleration," IUTAM Symposium on Microgravity Fluid Mechanics, September 2-6, 1991, Bremen, Germany.

J.I.D. Alexander, "Numerical Analysis of the Sensitivity of Crystal Growth Experiments to Spacecraft Residual Acceleration," Gordon Conference on Gravitational Effects in Physico-Chemical Systems, (Poster) Plymouth State College, June 16-21, Plymouth, New Hampshire.

J.I.D. Alexander, "Residual Acceleration Effects on Low Gravity Experiments," Institute de Mécanique des Fluides de l'Université d'Aix-Marseille II, January, 1991, Marseille, France.

M. J. B. Rogers, R. P. Wolf and J.I.D. Alexander, "Correlation of acceleration data on STS-50", Joint "L+1" Science Review for USML-1 and USMP-1 , Huntsville Alabama, September, 22-24, 1993.

6.2 Papers published:

J.I.D. Alexander, "Analysis of Experiment Sensitivity to Residual Acceleration", to appear in **Microgravity Science and Technology**.

M.J.B. Rogers, B. P. Matisak and J.I.D. Alexander, "Venting force contributions: Quasi-steady acceleration on STS-50", to appear **Microgravity Science and Technology.**

M. J. B. Rogers, R. P. Wolf and J.I.D. Alexander, "Correlation of acceleration data on STS-50", **Joint "L+1" Science Review for USML-1 and USMP-1 ,** Huntsville Alabama, September, 22-24, 1993.

P. Larroude, J. Ouazzani and J.I.D. Alexander, "Symmetry Breaking Flow Transitions and Oscillatory Flows in a 2D Directional Solidification Model," in press, **European Journal of Mechanics**, 1993.

J.P. Pulicani, S. Krukowski, J.I.D. Alexander, J. Ouazzani, and F. Rosenberger, "Convection in an Asymmetrically Heated Cylinder,"**International Journal of Heat and Mass Transfer**, 35, 2119-2130, 1992.

6.3 Theses

Sakir Amiroudine, "Bridgman-Stockbarger Crystal Growth in Low Gravity: Numerical Analysis of the Effects of Steady Oscillatory Residual Acceleration on Dopant Uniformity." M.S. Thesis, University of Alabama Department of Mechanical Engineering, 1992.

REPORT DOCUMENTATION PAGE

Form Approved
OMB No. 0704-0188

1. AGENCY USE ONLY *(Leave blank)*	2. REPORT DATE	3. REPORT TYPE AND DATES COVERED
	September 1998	Contractor Report

4. TITLE AND SUBTITLE
"Shuttle Mission STS-50: Orbital Processing of High-Quality CdTe Compound Semiconductors Experiment." Subtitle: "Final Flight Sample Characterization Report"

5. FUNDING NUMBERS
Contract Number:
NAS8-38147

6. AUTHOR(S)
Principal Investigator: D. J. Larson, Jr.
Co-investigators: L. G. Casagrande, D. Di Marzio, J. I. D. Alexander, F. Carlson, T. Lee, M. Dudley, & B. Raghathamachar

7. PERFORMING ORGANIZATION NAME(S) AND ADDRESS(ES)
Northrop Grumman Corporation
Advanced Systems & Technology
Bethpage, New York 11714

8. PERFORMING ORGANIZATION REPORT NUMBER

9. SPONSORING/MONITORING AGENCY NAME(S) AND ADDRESS(ES)
National Aeronautics and Space Administration
George C. Marshall Space Flight Center
Marshall Space Flight Center, Alabama 35812

10. SPONSORING/MONITORING AGENCY REPORT NUMBER

11. SUPPLEMENTARY NOTES
MSFC Technical Monitor: Linda Jeter
Final Report

12a. DISTRIBUTION/AVAILABILITY STATEMENT
Unclassified
Availability: NASA MSFC

12b. DISTRIBUTION CODE

13. ABSTRACT *(Maximum 200 words)*

The Orbital Processing of High-Quality Doped and Alloyed CdTe Compound Semiconductors program was initiated to investigate, quantitatively, the influences of gravitationally dependent phenomena on the growth and quality of bulk compound semiconductors. The objective was to improve crystal quality (both structural and compositional) and to better understand and control the variables within the crystal growth production process. The empirical effort entailed the development of a terrestrial (one-g) experiment baseline for quantitative comparison with microgravity (μ-g) results. This effort was supported by the development of high-fidelity process models of heat transfer, fluid flow and solute redistribution, and thermo-mechanical stress occurring in the furnace, safety cartridge, ampoule, and crystal throughout the melting, seeding, crystal growth, and post-solidification processing. In addition, the sensitivity of the orbital experiments was analyzed with respect to the residual microgravity (μ-g) environment, both steady state and g-jitter. CdZnTe crystals were grown in one-g and in μ-g. Crystals processed terrestrially were grown at the NASA Ground Control Experiments Laboratory (GCEL) and at Grumman Aerospace Corporation (now Northrop Grumman Corporation). Two μ-g crystals were grown in the Crystal Growth Furnace (CGF) during the First United States Microgravity Laboratory Mission (USML-1), STS-50, June 24 - July 9, 1992.

14. SUBJECT TERMS
Orbital processing, compound semiconductors, CdTe, crystal growth, microgravity, process models, fluid flow, solute redistribution, thermo-mechanical stress, seeding, convection, macrosegregation, synchrotron, x-ray topography, Space Shuttle, USML

15. NUMBER OF PAGES
145

16. PRICE CODE

17. SECURITY CLASSIFICATION OF REPORT	18. SECURITY CLASSIFICATION OF THIS PAGE	19. SECURITY CLASSIFICATION OF ABSTRACT	20. LIMITATION OF ABSTRACT
Unclassified	Unclassified	Unclassified	Unlimited

AT01S 0 2
TURNER J/PUBLICATION
MARSHALL SPACE FLIGHT CENTER
HUNTSVILLE AL.

DELETIONS OR CHANGES 544-4494
RETURN ADDRESS AT01D
Document Code: 2444